Atomistic Characterization and Modeling of the Deformation and Failure Properties of Asphalt-Aggregate Interface

Yang Lu

Dissertation submitted to the faculty of
Virginia Polytechnic Institute and State University
in partial fulfillment of the requirements for the degree of
Doctor of Philosophy

in

Civil Engineering

Linbing Wang, Chair
Ishwar K. Puri
Elisa D. Sotelino
George M. Filz

April 20, 2010

Blacksburg, Virginia

Keywords: Atomistic Modeling, Asphalt-aggregate Interface, Moisture Damage, High Performance Parallel Computing, Multiscale Image Characterization

ATOMISTIC CHARACTERIZATION AND MODELING OF THE DEFORMATION AND FAILURE PROPERTIES OF ASPHALT-AGGREGATE INTERFACE

Yang Lu

ABSTRACT

This dissertation is dedicated to develop models and methods to bridge atomistic and continuum scales of deformation processes in asphalt-aggregate interfacial composite materials systems. The deformation and failure behaviors, e.g. nanoscale strength, deformation, stiffness, and adhesion/cohesion at asphalt-aggregate interfaces are all evaluated by means of atomistic simulations. The atomistic modeling approach is employed to simulate mechanical properties, which is connected by their common dependence on the nanoscale bonding and their sensitive dependences on mechanics and moisture sensitivity. Specifically, CVFF-aug forcefield is employed in the atomistic calculations to study the fundamental failure processes that appear at the interface as a result of a mechanical deformation. There are five primary aspects to this dissertation.

First, the multiscale features of asphalt concrete materials are characterized by using nanoscale characterization & fabrication devices, e.g. High Resolution Optical Microscope (HROM), Environmental Scanning Electron Microscope (ESEM), Transmission Electron Microscope (TEM), Focused Ion Beam (FIB), and Atomistic Force Microscope (AFM).

Second, based on the multiscale devices characterization of the interfaces, a 2-layer atomistic bitumen-rock interface structure is constructed. Interface structure evolution under uniaxial tension is performed with various deformation rates. Comparison is made between both theoretical and experimental characterizations of interface configuration. Molecular dynamics (MD) simulations are used to investigate potential relationships between interface structure and morphology. Influences of deformation rate and temperature factors are discussed in terms of interface region stress-strain relation and loading time duration.

Third, molecular dynamics simulations are also performed to provide a characterization of atomic scale mechanical behaviors for a 3-layer confined shear structure which leads to interfacial shear failure. In addition, atomistic static simulation approach is employed to calculate a couple of mineral crystals' elastic constants. Furthermore, molecular dynamics simulations are also used to predict the static, thermodynamic, and mechanical properties of three asphalt molecular models.

Fourth, the high performance parallel computing technology is extensively employed throughout this dissertation. In addition to use the large-scale MD program, LAMMPS, the author developed a high performance parallel distributive computing program, MPI_multistress, to implement the multiscale understanding/predicting of materials mechanical behaviors.

Finally, this research also focuses on the evaluation of the susceptibility of aggregates and asphalts to moisture damage through understanding the nano-mechanisms that influence adhesive bond between aggregates and asphalt, as well as the cohesive strength and moisture susceptibility of the specific asphalt-aggregate interfaces. Surface energy theory and pull-out simulation are used to compute the adhesive bond strength between the aggregates and asphalt, as well as the cohesive bond strength within the binder.

In general, this dissertation has focused on the development of nanoscale modeling methods to assess asphalt-aggregate interfacial atomistic deformation and failure behaviors, as well as moisture effects on asphalt mixture strength. Simulation results provide valuable insights into mechanistic details of nanoscale interactions, particularly under conditions of various deformation rates and different temperatures. The results obtained show that a reasonable agreement between the theoretical and pavement industry observations is satisfactory. We conclude that the theoretical calculations presented here are useful in asphalt concrete industry for predicting the mechanical properties of asphalt-aggregate interfaces, which are difficult to obtain experimentally because of their small size.

ACKNOWLEDGMENTS

I would like to thank my family, particularly my wife Helen Lau, for all of the devotions they made while I worked on this research.

I would like to thank Prof. Linbing Wang, Prof. Ishwar K Puri, Prof. Elisa Sotelino, and Prof. George M Filz for serving on my thesis committee. I would like to thank my advisor, Prof. Linbing Wang, for providing me the opportunity to pursue this research full-time. I appreciate the advice and direction they gave in regards to both my research and future career endeavors. I would like to thank all of the graduate students in the Transportation Infrastructure Engineering group who provided help and friendship during my time at Virginia Tech.

The course I took under Prof. Puri on Molecular Modeling and Simulation is one of the best courses I have taken at Virginia Tech, which not only account for a major part of my knowledge but also strongly fuel my interest in these directions as this dissertation shows.

I am grateful to Virginia Tech, especially Civil and Environmental Engineering Department, for admitting me as a graduate student in 2006. To me, Virginia Tech is a very special place, and I thank all those who contribute to and are in stewardship of this unique and wonderful environment. The support to this work by National Science Foundation under Award #0625927 is gratefully acknowledged.

I would like to thank Dr Edward J. Garboczi (NIST) and Prof. Mircea Grigoriu (Cornell University) for their hospitality during my guest visit to the National Institute of Standards and Technology (NIST), where I learned the techniques of Spherical Harmonic-Based Non-Gaussian Random Fields for Generating Virtual Aggregates. I would like to thank Nanoscale Characterization and Fabrication Lab of Institute for Critical Technology and Applied Science (ICTAS) at Virginia Tech for their close collaborations and support. I would like to thank Advanced Research Computing Center at Virginia Tech, the SystemX high performance parallel cluster, on which most of my computation was performed.

Lastly, Prof. Linbing Wang has been my mentor for four years, without whose wisdom, guidance and support this work and my other achievements would have been impossible.

Table of Contents

List of Figures

List of Tables

Chapter 1
Introduction

When asphalt pavement is under external traffic loading, the evolution of crack-tip microstructure is a complex and highly nonlinear phenomenon central to the understanding of strength and failure of materials. Of fundamental interest are debonding processes in a crack-tip stress field and their role in controlling the brittle versus ductile behavior [1-5]. Traditionally, brittle-to-ductile transition in metals is believed to be governed by dislocation nucleation [6], whereas in a crystal material such as mineral it is thought to be controlled by dislocation mobility [7-8]. Despite the many attempts to elucidate the fundamental nature of crack-tip plasticity, our knowledge of the asphalt pavement mechanistic details at the atomic level is still primitive because of limited method of experiments, and the limited ability of computer simulation to probe sufficiently long time and length scales.

The mechanical deformation and failure of asphalt concrete materials are inherently multiscale phenomena in that the observed macroscale material behavior is governed by processes that occur on many different lengthscales and timescales. In this research, we are concerned with the atomistic modeling and simulation of asphalt-aggregate materials' multiscale behaviors that bridge the interfacial from the nanoscale atomistic motions to the macroscale mechanical properties. At the small lengthscale of Angstroms, quantum mechanical interactions and atomic structure provide an underlying framework for the elastic deformation of materials and, more importantly, for the formation of a wide variety of nano-defects in interfacial zones. Although nanometer scale defects such as vacancies, impurities, nanopores, and voids correspond to specific atomic configurations involving many atoms, they can also be viewed as individual mechanical entities with specific properties. The deformation fields associated with these defects leads to defect interactions at even larger scales. Typically, nanoscale behavior is the fundamental scale which directly leads to macroscale phenomenon. Macroscopic

behavior is a manifestation of the interaction and organization to these statistical defects within an atomistic group that may range in size from microns to millimeters. Currently available multiscale analyses attempt to bridge lengthscales by providing different physics-based models that can appropriately represent damage mechanisms at each scale. At the nanoscale, quantum mechanics, classical molecular dynamics (MD), and molecular mechanics (MM) methods are all used to simulate fundamental material processes by using computational chemistry and provide an understanding of deformation and fracture processes of materials at the atomic level.

With the current state-of-the-art computing technology, massively parallel supercomputer simulations can handle about 10^9 atoms. The modern computers along with new simulation algorithms and more refined, high quality available experimental data on structural properties of porous materials have contributed to a better understanding of the macroscopic behaviors of these materials, and hence to a more reliable interpretation the experimental results. Researchers focus on the mathematical procedures to obtain reliable pore size distributions, as well as investigate on the most meaningful quantities to reliably characterize micro-, nano-, and meso-porous materials, including the surface area, the pore size heterogeneity, the pore wall distribution and the energy distribution function.

In this study, atomistic modeling is performed to study the deformation and failure behaviors of organic-inorganic composite materials in asphalt concrete within the interfacial regions. The modeling lies in the mechanisms associated with debonding using bi-material geometries by (1) addressing interface evolution and nanopore generation at various temperatures, (2) considering large-scale interface models and (3) proposing models for the deformed structure of specific interfaces using either adhesive or cohesive failure. The development of proposed models for the deformed interface structure is possible because energy minimization is performed on the interface models prior to the application of a mechanical deformation. As a result, the interface structure is well characterized in terms of atomistic structural nature.

We employ multiscale modeling approach which involves the interpreting of critical information obtained from atomic-scale models to continuum properties. At the atomic level, elastic constants, plastic properties, and other properties of defect-free

crystals can be extracted from atomistic models because constitutive material property could be input into continuum models in our future research. Simulations are performed using both uniaxial tension and interface confined shear boundary conditions, which are considered as common cases for deformation in nanoscale systems. Uniaxial tension boundary conditions involve the application of deformation at various constant strain rates normal to the interface plane, while the lateral boundaries are prescribed as stress free. Interface layer confined shear boundary conditions involve the application of deformation at a constant strain rate parallel to the interface plane, while the lateral boundaries in that dimension are not changed. Thus, these simulations consider stresses parallel to the boundary plane during the tensile deformation process. Important inelastic properties include the peak tensile strength, the displacement associated with peak tensile strength and the virial potential values of separation. Interface stress is calculated using the virial stress definition [9] averaged over a small region around the boundary. Much more detail will be given regarding each loading case and atomistic model later in this work.

Accounting for the large variation of asphalt mixes, resulting from variations of constituents and compositions, a multiscale scheme for characterizing asphalt-aggregate interface from nanoscale is currently developed in this research. The multiscale concept allows one to link macroscopic materials' properties of asphalt-aggregate interface to materials' phenomena/properties of atomic-scale observation. Starting with the characterization of the multiscale structures and components, advanced characterization devices e.g. HDOM, AFM, ESEM, FIB and TEM, are employed to characterize the asphalt-aggregate interfacial atomistic structure, topography, and components. The obtained results could serve as input for upscaling the atomic scale model to the composite materials behaviors at the next-higher scale, e.g. mesoscale or macroscale.

1.1 Asphalt Mixture Terminology

Pavement designed using Hot Mix Asphalt (HMA) is referred to as flexible pavements and HMA is classified as bituminous mixtures. HMA consists mainly of aggregate (approximately eighty-five percent by volume), asphalt binder, additives, and

air-voids. According to the American Society of Testing and Materials (ASTM) Designation, Standard Terminology Relating to Materials for Roads and Pavements (1997), bitumen is defined as a class of black or dark-colored cementitious substances, natural or manufactured, composed principally of high molecular weight hydrocarbons. Asphalt is a dark brown to black cementitious material in which the predominating constituents are bitumen that occur in nature or are obtained in petroleum processing.

Bituminous mixture is a general term for asphalt mixture and they are used interchangeably. The top wearing surface and the load bearing layer of a flexible pavement are constructed with compacted asphalt mixture. Asphalt binder describes the principal binding agent in HMA which includes the asphalt cement and any added materials used to modify the original asphalt properties. Aggregate is the general term for granular material of mineral composition such as sand, gravel, and crushed stone. Aggregate can be classified as coarse or fine. The term mastic represents the combination of asphalt binder and mineral fillers.

1.2 Interfacial Adhesive Failure

Adhesives present a complex problem for asphalt concrete. Here, the word, adhesives, refers to the interfacial asphalt thin layer. Progress has primarily occurred for adhesives with weak interfacial strength. Such adhesives typically do not have strong chemical bonds across the interface. Only relatively weak van der Waals interactions exist at these interfaces. The nature of the interface between the adhesive and a rigid adherend, refers to aggregate, is especially important as this region tends to be the weak link. Fracture mechanics methods have been used to analyze the interfacial failure in such systems. However, the interface system is comprised by organic-inorganic composite materials which make it hard to be evaluated by classic fracture mechanics. A more robust theory requires additional knowledge about the physical phenomena occurring at the interface distinct from the bulk. The difficulty of measuring properties of interfaces has been a major obstacle in understanding interfacial adhesion issues. In addition, the number of chemical bonds at the interface is varied.

So far, there is very limited research achievement about mechanisms for

interfacial failure in asphalt glued onto mineral rock surfaces. Still less work exists for molecular simulation of asphalt-rock interface adhesion properties. Interfacial bonding strength is influenced by the interfacial nonbonded interaction between the adhesives and the various solid surfaces.

1.3 Definition of Moisture Damage

Asphalt pavement failures are typically classified as load stability or durability related failures. Moisture damage is signified by loss of strength or durability in an asphalt pavement due to the effects of moisture and may be measured by the asphalt mixture's loss of mechanical properties. The integrity of an asphalt concrete pavement depends on the bond between aggregate and asphalt cement. Moisture in the form of liquid or vapor can degrade this bond and lead to the first stage of failure which is deterioration of the asphalt-aggregate bond or 'stripping' followed by the second stage which is premature failure of the pavement structure.

Stripping typically begins at the bottom of the compacted bituminous layer where tensile stresses are greatest due to cyclic traffic loading. The stripping then progresses upward to the surface. The surface layer can be replaced; however stripping in the load bearing layer does not provide support, so the effective compacted bituminous layer thickness is decreased. This may lead to pavement cracking and surface rutting and to loss of serviceability [10]. There are four 'essential ingredients' that encourage stripping: presence of water, high air void content, high temperature, and high stress.

Moisture damage is a complex process that is influenced by material factors, their combinations, construction, and external effects such as environment and loading. These factors influence physical properties of an asphalt mixture such as air void content, mechanical strength, and stiffness. When moisture is introduced and transported through the mixture and individual materials, deterioration may appear in the form of detachment, displacement, spontaneous emulsification, pore pressure, or hydraulic scour [11-13].

As a result, major pavement failure modes may present such as debonding and permanent deformation.

1.4 Motivation

Asphalt concrete is a kind of widely used composite pavement material, which is a commonly used stone-based material and it's composed by bitumen and rock minerals. It's a common sense that interfaces play a very important role in overall strength of any composite material. Premature rutting, raveling, permanent deformation, and wear are often observed in many pavements. Distress and deterioration in large number of pavements as a result of bitumen-rock interface debonding is an indication of the significance and the severity of the problem. Debonding is defined in the literature as the physical separation of asphalt and aggregate produced by adhesion failure [14]. It can be understood as the separation between the thin bituminous film, formed during the mixing stage at elevated temperatures, and the aggregate particle. Based on the current definition of the debonding phenomena, researchers have adopted adhesion theories that describe the bond between bitumen and mineral aggregates [15-18]. A number of debonding mechanisms have been proposed to describe the effect moisture has on the bitumen-rock bond [11, 13-15, 19]. Despite of these findings, quantification of debonding potential prior to the mix-design stage, based on the variables described by the adhesion theories, remains difficult. Laboratory test methods used after the mix-design state are unreliable and cannot predict susceptibility of stripping. Therefore, an effective approach which can precisely characterize the interfacial debonding mechanism and predict long term performance is needed.

Basically, debonding damage at the interface of bitumen-rock can be generally classified into two mechanisms: loss of adhesion and loss of cohesion. The loss of adhesion is due to environmental effects of factors, e.g. temperature, water, aging, etc. getting between the interfaces and stripping away the asphalt film. The loss of cohesion is due to softening of asphalt concrete mastic. The two mechanisms are interrelated and a debonding damaged pavement may be a result of both mechanisms. Furthermore, the interface debonding is a function of several other factors like the changes in asphalt binders, decreases in asphalt binder content to satisfy rutting associated with increases in traffic, changes in aggregate quality, increased widespread use of selected design features, and poor quality control.

Previously, researchers adopted classical fracture mechanics, based on a continuum mechanics description of material domains and fracture behavior described in terms of empirical parameters (K_{IC}, J-R curves, crack-tip opening angle (CTOA), etc.), to study materials' failure. However, the nature of bitumen-rock interface failure initiation, microscale stripping mechanisms and nanoscale interface interactions have not yet been thoroughly understood, because nanoscale details are hard to obtain from experiments given the fact that fracture process must be interrupted in order to probe the microstructure. Moreover, it is hard to be conveniently predicted by continuing FEM analyses, due to the fact that failure is originated from particle dislocation and bond rupture. Therefore it is rational to study micromechanical behavior using atomistic modeling method. The emerging field of nanomechanics is providing a new focus in the study of the mechanics of materials, particularly, that of simulating fundamental atomic mechanisms involved in the initiation and evolution of damage. It provides a more complete understanding of the interface deformation and failure.

Pavement materials are composed by bitumen and minerals aggregates. Typically, crystals are the major components of minerals, while bitumen is amorphous material without a periodic crystal structure. Bitumen is a complex chemical mixture of molecules that are predominantly hydrocarbons with a small amount of structurally analogous heterocyclic species and functional groups. The precise composition varies according to the source of the crude oil from which the asphalt originates.

Asphalt concrete deformation and failure phenomena are hard to be addressed in standard continuum calculations. These phenomena include the influence of free surfaces, buried interfaces, internal material defects, and nonlocal interactions that become dominant for structures with very small feature sizes. This presents the situation where continuum mechanics theory, employing constitutive laws developed from macroscale property measurements, may fail to properly describe the mechanics of such features.

In order to achieve this, atomic scale models must be able to define and quantify relevant thermomechanical quantities. To focus our discussion, we consider the classical molecular dynamics (MD) method. 'Classical' MD means atoms are explicitly resolved and the electronic degrees of freedom are not considered. Note that quantum mechanics models that address electronic degrees of freedom (e.g. methods considered as ab initio,

such as density functional theory) are computationally expensive, and such that system sizes are typically limited to a few hundred atoms. Considering that a cube, 10 nm on edge, is comprised of tens of thousands of atoms, it is easy to see that methods resolving electronic degrees of freedom cannot address such length scales. Nonetheless, ab initio and related methods are critical for understanding reactivity, bonding energy, and other fundamental aspects of atomic interaction.

The accuracy of classical MD is often assessed (in the absence of experimental data) by comparing to more rigorous predictions from some level of quantum mechanics theory. While discussion here focuses on classical simulations, corresponding expressions can be derived for ab initio methods and an example for calculating surface stress is presented in [20]. Classical MD is well suited to model structures with nanometer length scale features. As a result, in recent years, practitioners of mechanics have increasingly used MD techniques as models for exploring mechanical behavior of very small objects. This implies the method is desired to calculate stress and other thermomechanical quantities in such models. A key challenge is to compute meaningful quantities in sub-system volume elements in order to address stress or distributions in thermomechanical quantities. In this dissertation, stress and thermomechanical calculation procedures are according to the method proposed by Zhou [21].

It is widely accepted that the strength of materials is largely influenced by defects. The reason is that upon application of an external load to the material, these imperfections lead to a magnification of the local stresses, and thereby induce failure since the forces between atoms become so large that the chemical bonds are sheared or ruptured. This occurs collectively over larger lengthscales. If a large number of interatomic bonds are compromised, the material undergoes permanent shape change or begins to fracture. The details, how exactly these bonds respond to extreme loading conditions, control the overall material behavior. It all starts at the atomic scale. So in order to understand materials failure, it is not simply possible to average over microscopic features. The presence of a tiny defect in the material can make a huge difference, because it is the source for steady growth of a fracture that will eventually destroy the entire material or structure.

The properties of asphalt concrete materials are determined from complex

interaction of individual scale-specific properties and their interactions. To date it remains unclear how different properties interact, and which are most important, but it is believed that the hierarchical scale plays a vital role. In particular, bitumen-rock interfaces are poorly understood in terms of their nanoscale mechanical behavior, and fundamental failure and deformation theories are needed, especially those including the effects of the hierarchical scale. Our goal is to develop such theoretical understanding of the cross-scale relationships between nanoscale and macroscopic scale.

We hypothesize that such cross-scale interactions can play a significant role in determining the mechanical behavior of asphalt concrete materials and utilize such principles systematically. However, these concepts are not yet understood within the context of scientific or engineering principles. So far, no atomic-scale consistent studies have been carried out on asphalt concrete interface with the aim of elucidating its fundamental properties such as response to tensile stretching and the interaction of several asphalt molecules with each other. The lack of such studies motivates the investigations reported in this thesis, aiming at an atomistic based, fundamental development of mechanics of asphalt concrete.

1.5 The Need for Atomistic Simulations

In the continuum viewpoint, materials are treated without explicitly considering the underlying inhomogeneous microstructure. The basic assumption is that matter can be divided indefinitely, without a change of the material properties. Only a few special cases of continuum models can be solved analytically and written in closed-form solutions. Many problems require a numerical solution of the governing partial differential equations, for instance by finite difference methods, boundary element or finite element approaches. Many numerical methods used to solve continuum problems thereby require the discretization of the domain into integration points (e.g., mesh generation the FEM). A higher density of integration points provides a more accurate solution of the problem, and higher densities of integration points must be used in regions of large gradients of stresses and deformation.

However, phenomena that are not addressed in standard continuum calculations,

such as the influence of free surfaces, buried interfaces, internal material defects, and nonlocal interactions become dominant for structures with very small feature sizes. This presents the situation where continuum mechanics theory, employing constitutive laws developed from macroscale property measurements, may fail to properly describe the mechanics of such features. There are some limitations of continuum approaches. One limitation is the reduction of characteristic material lengthscales to the sub-100nm regime. In this regime, continuum mechanical methods become questionable, as the material in-homogeneities reach lengthscales comparable to the overall size of the structure. Thus, the basic assumption of continuum theories that material can be divided without changing the material properties does not hold any more. Another important area is the introduction of complex nano-structural features and the existence of complex chemistry. That involves discrete reactions which can severely influence the behavior of a material, making it impossible to neglect the discrete nature of molecules.

Hence, atomistic simulation is a natural choice to study materials failure at the atomic level. The atomic level provides the most fundamental description of the failure processes. Consider, for instance, an array of nanometer scale islands assembled on the surface of a substrate. Constructing this from specific materials and with appropriate islands sizes results in quantum dot arrays-structures possessing unique optical, electronic, and magnetic properties. These properties depend critically on the stress state in the islands. For such geometry, the role of free surfaces and interfaces must be included to properly describe the mechanics of the array. Crystal defects, if present, will significantly affect stress in the island array. These influences are not captured in traditional continuum approaches, while material constitutive laws may be developed to address such situations. Moreover, experiments do not exist with sufficient resolution to measure needed quantities for such laws. One example of such a quantity is the thermodynamic surface stress: as the two dimensional analog to stress, it represents the energetic penalty associated with increasing free surface area via elastic distortion [1, 4]. For very small structures, the magnitude of surface stress, which varies significantly for different crystallographic surfaces, will greatly influence mechanical response. Surface stress has been measured for some thin film systems [5–7], but how such properties manifest for very small feature sizes remains unclear. Facing such obstacles, continuum

mechanics approaches appear to be intractable at this scale. However, atomistic models have been used to develop new material force laws that were input to a continuum framework [8–10].

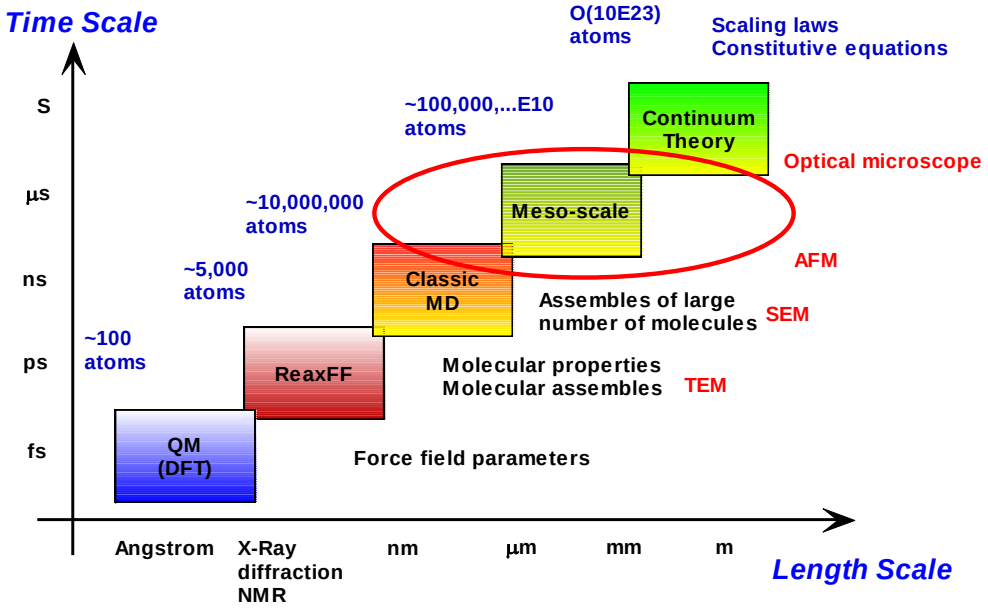

Figure 1-1 Multiscale Tools for characterization and modeling of materials deformation and failure

Typical, an overview of the most prominent materials simulation techniques is shown in Figure 1-1. In this figure, we also indicate which lengths and timescales can be reached with the various methods. The experimental methods include ESEM, TEM, AFM, Optical microscope, etc. Theoretical and simulation tools include quantum mechanics/density functional theory (QM/DFT), molecular dynamics (MD), coarse-grained models, and mesoscale atomically informed continuum theories, as well as continuum methods.

Quantum-mechanical-based treatments are typically limited to very short time- and length- scales, on the order of a few nanometers and picoseconds. The assumption of empirical interactions in classical molecular dynamics scheme significantly reduces the computational burden, the lengths and timescales that can be reached are dramatically increased, approaching micrometers and several nanoseconds. For comparison, we include also continuum mechanics-based simulation tools that can treat virtually any length scale, but they may lack a proper description at small scales, and they are therefore often not suitable to describe materials failure processes in full details. Mesoscopic

simulation methods such as discrete dislocation dynamics can bridge the gap between molecular dynamics and continuum theories by generating an intermediate scale at which clusters of atoms or small crystals are treated as a single particle [22-23].

It was not until the 1980s that scientists and engineers began to include atomistic descriptions into models of materials' failure and plasticity. Over the last decades, there has been a new realization that understanding the nanoscale behavior is required for understanding how materials fail. It opens great opportunities to provide new design methods for materials from the bottom up. Hence, the significance of atomistic processes to describe deformation and failure of materials is apparent.

Basically, the continuum and atomistic viewpoints provide two fundamentally different approaches in modeling materials, with different appeal and significance for specific applications. For many applications, the two views are complementary and joint use of the approaches can provide much insight into the behavior of materials. The atomistic models provide a fundamental description of material properties and processes, which enables one to communicate data of such studies seamlessly to concepts from other scientific disciplines. Atomistic methods provide a rather general description of matter, since the same atomistic model of solving the dynamical evolution of equilibrium and nonequilibrium processes provides detailed insight into the physics of elementary processes.

In atomistic modeling, the discreteness of matter at the atomic scale is explicitly considered. An example is the discreteness of an atomic lattice in the metal, where atoms are glued to their equilibrium crystal positions. Therefore in atomistic modeling no spatial discretization is necessary, since this is given by the atomic distances. Each atom is considered to be an individual particle that cannot be divided further. Atomistic models can rarely be solved analytically; therefore most models are implemented in numerical simulations that model the motion of each atom in the material over the course of the simulation time span. The simulation thereby carries out a step-by-step integration to successively progress the timescale during a study. The collective behavior of the atoms allows one to understand how the material undergoes deformation, observe phase changes, or investigate many other phenomena. The observed phenomena in a larger ensemble of atoms provide the links between the atomic scale to mesoscopic or

macroscopic phenomena. However, since the basic information of an atomistic simulation is comprised of atomic positions, velocities, and forces. The interpretation of these numbers can be quite challenging.

A fundamental challenge of any model and simulation implementation is the determination of parameters. This is important for continuum approaches, because many atomistic or molecular mechanisms (e.g., the generation of dislocations, diffusion, and creep) are not explicitly described at the relevant scale of the underlying physics, but treated by empirical relations that mimic the overall collective effect of these processes. Important parameters for continuum approaches include elastic constants and cohesive laws that describe the separation behavior of interfaces to this problem, because they are capable of capturing the elementary physical mechanisms of failure.

It is generally accepted that the nano-indentation and nano-scratch based experimental techniques combined with high-resolution imaging (e.g. electron microscopy) are currently the most reliable and accurate methods for studying and quantifying the effect of nanotubes on the deformation behavior of polymer-matrix composites [24]. It is also generally recognized that atomic level calculations based on the high-fidelity multi-body quantum-mechanics based forcefields to account for the inter- and intra-molecular interactions is critical for obtaining a better understanding of the phenomena controlling the nature, as well as the level of nanotube-induced stiffening/strengthening (e.g. interfacial bonding and matrix-to-reinforcement load transfer mechanisms) in polymer-matrix composites (e.g. [25-26]).

One of the strengths and the reasons for the great success of atomistic methods is its very fundamental viewpoint of materials behavior. The only physical law that is put into the simulations is Newton's law and a definition of how atoms interact with each other. Despite this very simple basis, very complex phenomena can be simulated. Unlike many continuum mechanics approaches, atomistic techniques require no assumption on the defect dynamics. A drawback of atomistic simulations is the difficulty of analyzing results and the large computational resources necessary to perform the simulations. This becomes more evident as the simulation sizes increase to systems with billions of atoms [27-28]. Even with today's largest computers, system sizes with only a few billion atoms can be simulated, whereas a cubic centimeter of material already contains more than 10^{23}

atoms. Another drawback is that once the atomic interactions are chosen, the complete material behavior is determined. In some cases, it is difficult to find the correct potential for a specific material.

The significance of including nanoscale mechanisms is also due to the increasing trend toward miniaturization. Once the dimensions of materials reach the submicron lengthscale, full atomistic information about the material state is often necessary to study relevant materials phenomena. In addition to the significance of nanoscopic phenomena for deformation, engineers can now also design materials at the nanoscale. The ability to create nanostructures by design has reached a level of perfection that now enables us to make almost arbitrary structures and shape at ultra-small scales, either through self-assembly or by utilizing small-scale material manipulation and cutting techniques (such as focused ion beam, FIB). This ability opens a new era in the design of materials, forming bottom up and enabling new functions, properties, and behaviors for very rich set of applications. However, these advances also require new theoretical concepts to describe the materials behavior, as it can be quite different from what is conventionally know from larger scale materials. Atomistic models are often quite suitable to capture these and other effects.

Moreover, the atomistic viewpoint has another quite important aspect: it allows for the seamless communication of various scientific disciplines with one another, in particular during the study of deformation and fracture. The reason is that the term of the ‘chemical bond’ is a concept with which many disciplines can be linked. In this sense, chemistry is the most fundamental language of materials science and related disciplines. Additionally, atomistic models typically contain extremely large numbers of particles, even though the actual physical dimension may be quite small. For example, even a crystal with dimensions below a few micrometers side length has several tens of billions of atoms. Predicting the behavior of such large many particle systems under explicit consideration of the trajectory of each particle is only possible by numerical simulation, and must typically involve large computational facilities.

Furthermore, macroscopic tensile tests used to study the elastic/plastic deformation and fracture behavior of the asphalt-aggregate composite materials suffer from a number of limitations. There are two important points: (a) insufficient load and

displacement resolutions to capture the changes in stress/strain behavior at the micro and nano scale and; (b) fabrication of the macroscopic tensile test specimens can often introduce surface flaws, hence undesirable stress concentrations will appear.

Therefore, atomistic modeling technique is needed to capture the asphalt-aggregate interface materials phenomena from nanoscales to macroscales. It enables the integration of computational and theoretical methods with experimental analysis and characterization methods.

1.6 Merger of Structure and Material

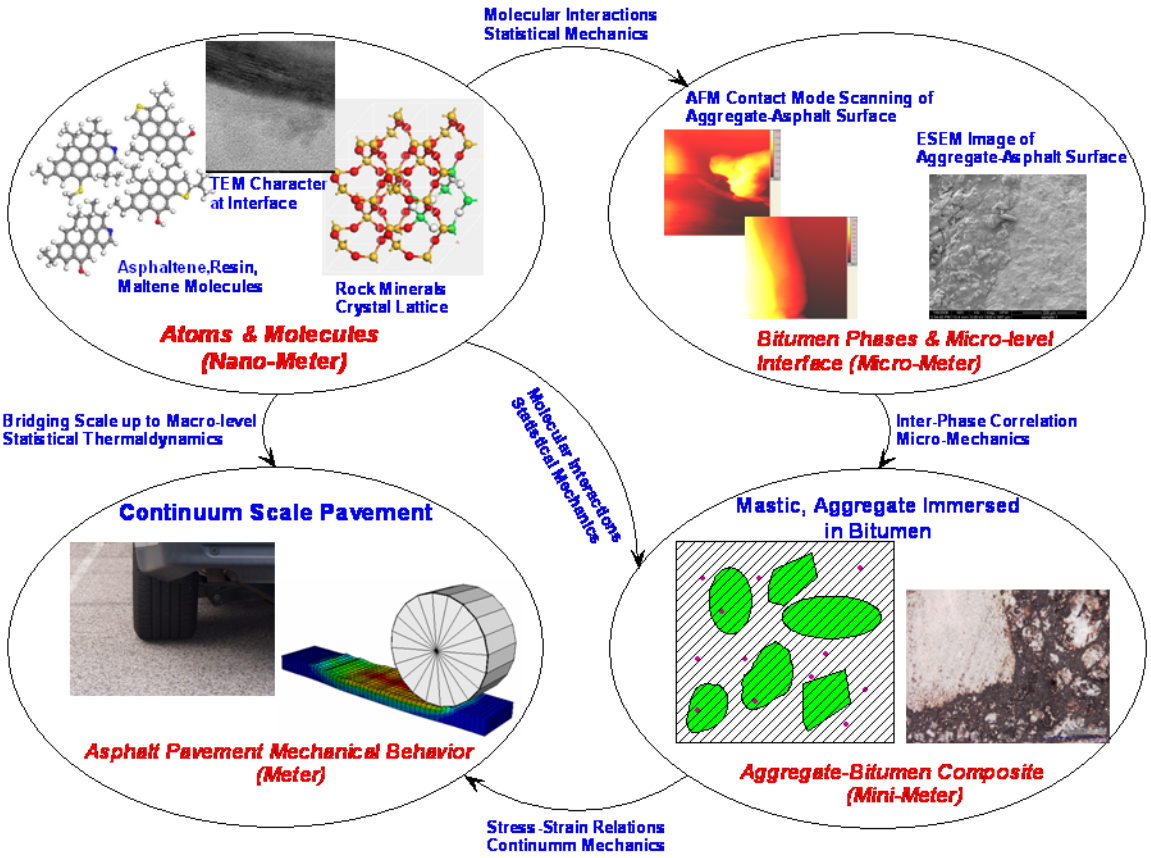

Figure 1-2 Deformation and failure of the multiscale characterization and modeling relationship defined for asphalt aggregate interface composite materials.

Atomistic characterization of asphalt-aggregate interface materials provides a foundation for the integration of structures and materials. Thereby, it enables the inclusion of molecular- and multi-scale features in the pavement material design process.

Figure 1-2 illustrates the atomistic based hierarchical multiscale modeling of the composite asphalt-aggregate interface materials. The hierarchical multi-scale simulation scheme enables us to develop an atomistic based description of the interface materials. The upper left part of the figure indicates nanoscale pavement materials interface structure, e.g. asphaltene molecule or mineral crystal lattice, which is characterized by Transmission Electron Microscope. It is connected to mesoscale interface by using Atomic Force Microscope contact mode scanning and Environmental Scanning Electron Microscope characterization. At this scale, coarse-graining approach is used in the development of mesoscale models, illustrating the representation of full-atomistic description of asphalt concrete materials molecule by a collection of 'super-atoms' or beads, reaching length scales and timescales several orders larger. Keeps on upscale to the mini-meter scale, microscale mastic and fine aggregate immersed in bitumen can be characterized. Consequently, the lower left part of the figure indicates classes or scales of pavement materials in asphalt pavement mechanical behavior that can be studied with continuum scale technique. In order to achieve the above hierarchical multiscale modeling, researchers use an interdisciplinary approach for the analysis that combines computational chemistry, high performance distributive computing, and multi-scale modeling technologies with the theoretical model development.

In pavement engineering fields, asphalt concrete materials and their structures play an essential role for their properties and applications. We are particular interested in the combination of disparate properties in composite materials. Especially, one may interest in building a bridge from atomistic composition, materials components, and nanoscale structure to the macroscale strength, stiffness, elasticity, adaptability, and adhesion, etc. Its fundamental, theoretical, and scientific understanding is the primary goal of the research carried out so far. For example, a better understanding of the failure mechanisms of materials has high impact in preventing failure of existing structures. Development of new materials may lead to better designs and could replace classical designs, for example by using eco-friendly additives.

1.7 Objective and Scope

Asphalt concrete composites consist of various elements such as asphalt binder, fillers, coarse and fine aggregates. Significant considerations in understanding the mechanical behaviors of the asphalt concrete composites include the nature of the deformation and failure of the interfaces between these constituent elements and their interaction. Development of advanced asphalt composite materials with improved toughness and durability requires a fundamental understanding of the characteristics of the interfaces. Physical and chemical properties of aggregates at a macro and micro scale influence the performance of asphalt mixes.

The objective of the present work is to carry out a series of molecular dynamics calculations in order to understand and quantify the mechanical properties of 2-lyaer and 3-layer atomistic bitumen-rock composite material. It should be noted that the shear or tensile loading condition can be modeled by sidewall loading mode. Consequently, interface layer mechanical properties can be analyzed by statistical mechanics. Based on the simulation results, deformation rate effect is generally believed to yield better load transfer between the asphalt and the rock aggregates. On the other hand, interface asphalt molecule structure and rock aggregate atom types are also major factors that may contribution to bulk and interface mechanical properties.

In my research, an atomistic level bitumen-quartz and bitumen-calcite composite materials models for the purpose of investigating deformation and failure behaviors are developed. Influences that may concentrate/mitigate interface anti-debonding factors are also evaluated in this research. For asphalt matrix rock composite materials, a good load transfer between the asphalt matrix and the rock minerals is critical. Hence, the role of interface layer structure, chemistry components, interface interaction force (energy), and surface free energy on the asphalt-aggregate interface moisture damage are all evaluated in this research.

Discoveries from this research will provide guides for optimization of the binder-mineral filler combination in asphalt concrete mix design, which may consequently result in asphalt-aggregate mixture designs that will last longer and perform better. The broader impact of my research is that it will result in a general understanding the failure of stone-

based infrastructure materials, e.g. geotechnical, pavement, and structural materials, at atomic scale.

1.8 Dissertation Outline

This is a study of the microstructural influences on the mechanical behavior of asphalt-rock minerals interface behaviors using computer simulation. We describe atomistic modeling and simulation studies of the deformation and failure in bitumen-rock mineral interface systems with original contributions in both theoretical and applied aspects. The work is organized in five parts.

First, we present a review on atomistic modeling theory and analysis tools, including a summary of recent research activities in the field. It is followed by a comprehensive discussion of atomistic elasticity theory. Consequently, the parallel implementation of atomistic modeling, parallel algorithm, and distributive postprocess tools will be introduced. Second, this dissertation characterized multiscale features of asphalt concrete materials interface by using nanoscale characterization & fabrication devices. Third, based on the multiscale devices characterization, a 2-layer atomistic bitumen-rock interface structure is constructed. The interface structure evolution under uniaxial tension is performed with various deformation rates. Fourth, the molecular dynamics simulations are performed to provide a characterization of atomic scale mechanical behaviors for a 3-layer interface structure under confined shear which leads to interfacial shear failure. In addition, atomistic static simulation is employed to calculate several mineral crystals' elastic constants. Furthermore, molecular dynamic simulations are also used to predict the static, thermodynamic, and mechanical properties of three asphalt molecular models. Finally, this research also focuses on the evaluation of the susceptibility of aggregates and asphalts to moisture damage. Results of the atomistic calculations are utilized to motivate forms for continuum interface separation potentials.

Chapter 2
Molecular dynamics simulation fundamentals

Among various methodologies for atomic-level simulation, molecular dynamics (MD) is one of the most popular tools to investigate mechanical behaviors of materials. Provided well-defined descriptions of model problems are available, molecular dynamics is promising, especially for the problems that the model size is too big for quantum simulation to be used, but the atomic resolution has to be maintained. Quantum simulations are not capable of this large size of problems, and at the same time, the continuum simulations cannot provide the atomic details which were kept by a specific potential in this research. This demonstrates the crucial role of molecular dynamics in the field of computational nanomechanics of materials.

2.1 Basics of Molecular Dynamics

Molecular dynamics (MD) was first used in thermodynamics and physical chemistry to calculate the collective or average thermochemical properties of various physical systems including gases, liquids, and solids. It has been recently applied to simulate the instantaneous atomic behavior of a material system. There are two basic assumptions made in standard molecular dynamics simulations [29]:

1) Molecules or atoms are described as a system of interacting material points, whose motion is described dynamically with a vector of instantaneous positions and velocities. The atomic interaction has a strong dependence on the spatial orientation and distances between separated atoms. This model is often referred to as the soft sphere model, where the softness is analogous to the electron clouds of atoms.
2) No mass changes in the system. Equivalently, the number of atoms in the system remains the same. The simulated system is usually treated as an isolated domain system with conserved energy. However, non-conservative techniques are also

available which model the dissipation of the kinetic energy into the surrounding media.

2.1.1 Lagrange Equations of Motion

The equations of motion of a system of interacting material points (particles or atoms), having s degrees of freedom in total, can be generally written in terms of a Lagrangian [30],

$$\frac{d}{dt}\frac{\partial L}{\partial \dot{q}_\alpha} - \frac{\partial L}{\partial q_\alpha} = 0, \quad \alpha = 1, 2, ..., s \tag{2-1}$$

where q's are the generalized coordinates, the observables uniquely defining spatial positions of atoms, and the superposed dot denotes time derivatives.

The molecular dynamics simulation typically runs with the reference to the Cartesian coordinate systems, where equation (2-2) are simplified to yield

$$\frac{d}{dt}\frac{\partial L}{\partial \dot{r}_i} - \frac{\partial L}{\partial r_i} = 0, \quad i = 1, 2, ..., N \tag{2-2}$$

where $r_i = (x_i, y_i, z_i)$ is the position vector of atom i and N is the total number of atoms. The spatial volume occupied by these N atoms is usually referred to as the MD domain.

Due to the homogeneity of time and space, and also isotropy of space in inertial systems, the Lagrange equations of motion must not depend on the choice of initial time of observation, the origin of the coordinate system, and directions of its axes. These basic principles are equivalent to the requirements that the Lagrangian function cannot explicitly depend on time, directions of the position and velocity vectors, and it can only depend on the absolute value of the velocity vectors. In order to provide identical equations of motions in all inertial coordinate systems, the Lagrangian must also comply with the Galilean relativity principle. One function satisfying all these requirements reads [31]

$$L = \sum_{i=1}^{N} \frac{m_i}{2}\left(\dot{x}_i^2 + \dot{y}_i^2 + \dot{z}_i^2\right) \equiv \sum_{i=1}^{N} \frac{m_i \dot{r}_i^2}{2} \tag{2-3}$$

for a system of free, non-interacting, particles; m_i is the mass of particle i. Interaction

between the particles can be described by adding to equation (2-3) a particular function of atomic coordinates U, depending on properties of this interaction. Such a function is defined with a negative sign, so that the system's Lagrangian acquires the form

$$L = \sum_{i=1}^{N} \frac{m_i \dot{r}_i^2}{2} - U\left(r_1, r_2, ..., r_N\right) \tag{2-4}$$

This gives the general structure of Lagrangian for a conservative system of interacting material points in Cartesian coordinates. It is important to note two features of this Lagrangian: the additivity of the kinetic energy term and the absence of explicit dependence on time. The fact that the potential energy term only depends on spatial configuration of the particles implies that any change in this configuration results in an immediate effect on the motion of all particles within the simulated domain. The inevitability of this assumption is related to the relativity principle. Indeed, if such an effect propagated with a finite speed, the former would depend on the choice of an inertial system. In this case the laws of motion (in particular, the MD solutions) would be dissimilar in various systems; that would contradict the relativity principle.

By substituting the Lagrangian to equation (2-4), the equations of motion can finally be written in the Newtonian form,

$$m_i \ddot{r}_i = -\frac{\partial U\left(r_1, r_2, ..., r_N\right)}{\partial r_i} \equiv F_i, \quad i = 1, 2, ..., N \tag{2-5}$$

The force F_i is usually referred to as the internal force, for example, the force exerted on atom i due to specifics of the environment it is exposed to equation (2-5) is further solved for a given set of initial conditions to get trajectories of the atomic motion in the simulated system.

An important issue arising in MD simulations is accounting for a mechanism of the conduction of heat away from a localized area of interest. The MD domain is usually far too small to properly describe this process within a conservative system. Modern computer power allows modeling domains with a maximum of several billion atoms (when a very simple model of interatomic potential is used); that corresponds to a material specimen size of only about $0.1 \times 0.1 \times 0.1 \mu m^3$.

MD simulations are most often performed using periodic boundary conditions,

implying that the total energy in the system remains constant. Artificial damping forces can also be applied to a group of atoms along the boundaries of the MD domain. That is known as the heat bath technique. However, this approach cannot capture the true mechanism of dissipation in real systems. Furthermore, the potential energy term shown in equation (2-5), having no explicit dependence on time, implies the use of conservative models. Non-conservative models can also be constructed, using this basic form of the Lagrangian and implementing the so-called 'wave-transmitting' boundary conditions to describe energy dissipation from the molecular dynamics domain into the surrounding media. The basic idea of such an approach is to calculate the response of the outer region to excitations originating from the MD domain at each time step of the simulation. The outward heat flow is then cancelled due to the negative work done by the corresponding response forces applied to boundary atoms within the localized area of interest.

The classical Lagrangian formulation, discussed in this subsection, is typically used for those molecular dynamics simulations aimed on the analysis of detailed atomic motion, rather than on obtaining averaged (statistical) characteristics [29].

2.1.2 Integrating the Equations of Motion

A simple solution strategy is to develop a stepping method that gives new coordinates and velocities from the old ones, for each particle i, such as

$$\mathbf{r}_i(t_0) \rightarrow \mathbf{r}_i(t_0 + \Delta t) \rightarrow \mathbf{r}_i(t_0 + 2\Delta t) \rightarrow \mathbf{r}_i(t_0 + 3\Delta t) \ldots \tag{2-6}$$

A numerical scheme can be constructed by considering the Taylor expansion of the position vector $\mathbf{r}_i$:

$$\mathbf{r}_i(t_0 + \Delta t) = \mathbf{r}_i(t_0) + \mathbf{v}_i(t_0)\Delta t + \frac{1}{2}\mathbf{a}_i(t)\Delta t^2 + \ldots \tag{2-7}$$

and

$$\mathbf{r}_i(t_0 - \Delta t) = \mathbf{r}_i(t_0) - \mathbf{v}_i(t_0)\Delta t + \frac{1}{2}\mathbf{a}_i(t)\Delta t^2 + \ldots \tag{2-8}$$

Adding these two equations together yields

$$\mathbf{r}_i(t_0+\Delta t) = -\mathbf{r}_i(t_0-\Delta t) + 2\mathbf{r}_i(t_0) + \mathbf{a}_i(t)\Delta t^2 + \ldots \quad (2\text{-}9)$$

The above equation provides a direct link between new positions at $(t_0+\Delta t)$ and the old positions and accelerations at (t_0). The accelerations can be obtained from the forces by considering Newton's law, $\mathbf{a}_i = \frac{\mathbf{F}_i}{m}$. This updating scheme is referred to as the Verlet central difference method.

There exist many other integration schemes that are frequently used in molecular dynamics implementations. In the following few sections we summarize a few additional popular algorithms.

In Velocity Verlet algorithm, the positions are updated as

$$\mathbf{r}_i(t+\Delta t) = \mathbf{r}_i(t) + \mathbf{v}_i(t)\Delta t + \frac{1}{2}\mathbf{a}_i(t)\Delta t^2 + \ldots \quad (2\text{-}10)$$

where $\mathbf{v}_i(t+\Delta t) = \mathbf{v}_i(t) + \frac{1}{2}(\mathbf{a}_i(t) + \mathbf{a}_i(t+\Delta t))\Delta t$

MD allows accurate predictions of interactions between constituent phases at the atomic scale. It involves the determination of the time evolution of a set of interacting atoms, followed by integration of the corresponding equations of motion. The equations of motion are given by Newton's second law. MD is a statistical mechanics method, where a set of configurations is distributed according to a statistical ensemble or statistical distribution function. The trajectories of the motion of the atoms are calculated under the influence of interaction forces of the atoms in a phase space with 6 N dimensions; three degrees of variation for position and three degrees of variation of the momentum for each atom.

Calculation of physical quantities by MD simulation is obtained by arithmetic averages of instantaneous energy values from individual simulation steps. MD simulations, if run for a sufficiently long time, can completely sample the phase space; however, in practice, simulation times are limited. Physical quantities are obtained after the molecular system reaches a thermodynamic equilibrium. The MD simulations in this dissertation are all based on the sort of calculations done with molecular dynamics, which include understanding the deformation of interface structures under the loading of

external force.

2.2 Interatomic Potentials and Force Fields

According to equation (2-5), the general structure of the governing equations for molecular dynamics simulations is given by a straightforward second order ordinary differential equation. However, the potential function for equation (2-5) can be a very complicated part, when accurately representing the interatomic interaction in the system to be simulated. The nature of this interaction is due to complicated quantum effects taking place at the subatomic level that are responsible for chemical properties such as valence and bond energy; quantum effects also are responsible for the spatial arrangement of the interatomic bonds, their formation and breakage. In order to obtain reliable results in molecular dynamic simulations, it is desired for the classical interatomic potential to accurately account for the quantum mechanical processes, though in an averaged sense.

The issues related to the form of the potential function for various classes of atomic systems have been extensively discussed in literature. The general structure of this function is presented by the following

$$U\left(r_1, r_3, ..., r_N,\right) = \sum_i V_1\left(r_i\right) + \sum_{i,j>1} V_2\left(r_i, r_j\right) + \sum_{i,j>i,k>j} V_3\left(r_i, r_j, r_k\right) + ... \qquad (2\text{-}11)$$

where r_N is the position vector of the N-th particle, and the function V_m is called the m-body potential. The first term of equation (2-11) represents the energy due to an external force field, such as gravitational or electrostatic, into which the system is immersed; the second term shows pairwise interaction of the particles, the third term gives the three-body components, etc. In practice, the external field term is usually ignored, while all the manybody effects are incorporated in order to reduce the computational expense of the simulations.

At the subatomic level, the electrostatic field due to the positively charged atomic nucleus is neutralized by the negatively charged electron clouds surrounding the nucleus. Within the quantum mechanical description of electron motion, a probabilistic approach

is employed to evaluate the probability densities at which the electrons can occupy particular spatial locations. The term 'electron cloud' is typically used in relation to spatial distributions of these densities. The negatively charged electron clouds, however, experience cross-atom attraction, which grows as the distance between the nuclei decreases. On reaching some particular distance, which is referred to as the bond length, this attraction is equilibrated by the repulsive force due to the positively charged nuclei. A further decrease in the inter-nuclei distance results in a quick growth of the resultant repulsive force.

There exists a variety of mathematical models to describe the above physical phenomena. In 1924, Jones proposed the following potential function to describe pairwise atomic interactions,

$$V\left(r_{ij}\right)=V\left(r\right)=4\varepsilon\left[\left(\frac{\sigma}{r}\right)^{12}-\left(\frac{\sigma}{r}\right)^{6}\right] \tag{2-12}$$

This model is currently known as the Lennard-Jones (LJ) potential [32], and it is used in simulations of a great variety of atomistic systems and processes. Here, r_{ij} is the interatomic distance vector, σ is the collision diameter, the distance at which $V\left(r\right)=0$, and ε shows the bonding/dislocation energy, for example, the minimum of function equation (2-12) to occur for an atomic pair in equilibrium.

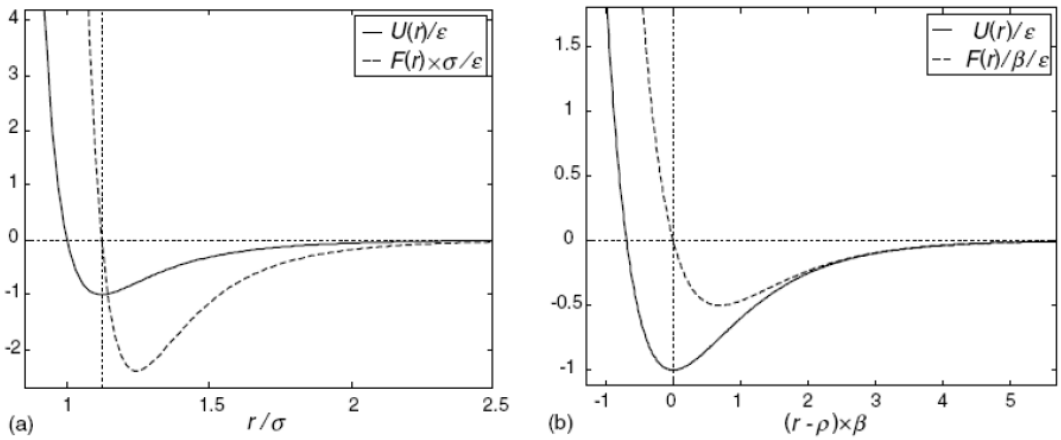

Figure 2-1 Pairwise potentials and interatomic forces: (a) Lennard-Jones and (b) Morse potentials [32]

The first term of this potential represents atomic repulsion, dominating at small

separation distances while the second term shows attraction (bonding) between two atoms. Since the square-bracketed quantity is dimensionless, the choice of units for V depends on the definition of ε. Typically, ε is the order of $10^{-19} \sim 10^{-18}$ (J), therefore it is more convenient to use a smaller energy unit, such as electron volt (eV), rather than joules. $1(eV) = 1.602 \times 10^{-19}$(J), which represents the work done if an elementary charge is accelerated by an electrostatic field of a unit voltage. The energy ε represents the amount of work that needs to be done in order to remove one of the two coupled atoms from its equilibrium position ρ to infinity. The value ρ is also known as the equilibrium bond length, and it is related to the collision diameter. In a typical atomistic system, the collision diameter ε is equal to several angstrom ($\mathring{A}$), $1(\mathring{A}) = 10^{-10}(m)$. The corresponding force between the two atoms can be expressed as a function of the interatomic distance,

$$F(r) = -\frac{\partial V(r)}{\partial r} = 24\frac{\varepsilon}{\sigma}\left[2\left(\frac{\sigma}{r}\right)^{13} - \left(\frac{\sigma}{r}\right)^{7}\right] \tag{2-13}$$

This potential and corresponding force functions are plotted in terms of the interatomic distance in Figure 2-1(a), using dimensionless quantities. Another popular model for pairwise interaction is known as the Morse potential given in Figure 2-1(b),

$$V(r) = \varepsilon\left[e^{2\beta(\rho - r)} - 2e^{\beta(\rho - r)}\right], \quad F(r) = 2\varepsilon\beta\left[e^{2\beta(\rho - r)} - 2e^{\beta(\rho - r)}\right] \tag{2-14}$$

where ρ and ε are the equilibrium bond length and dislocation energy respectively; β is an inverse length scaling factor. Similar to the Lennard-Jones model, the first term of this potential is repulsive and the second is attractive, which is interpreted as representing bonding. The Morse potential has been adapted for modeling atomic interaction in various types of materials and interfaces. The Lennard-Jones and Morse potentials are most commonly used in molecular dynamics simulations, based on the pairwise approximation, in chemistry, physics and engineering.

The higher order terms of the potential function, equation (2-11), are typically employed in simulations of solids and complex molecular structures to account for chemical bond formation, their topology and spatial arrangement, as well as the chemical

valence of atoms. However, practical implementation of the many-body interaction can be involved. As a result, all the many-body terms of the order higher than three are usually ignored. Essentially, the three-body potential V_3 is intended to provide contributions to the potential energy due to the change of angle between radius vectors $r_{ij} = r_i - r_j$, in addition to the change of absolute values $r_{ij} = |r_i - r_j|$. This accounts for changes in molecular shapes and bonding geometries in atomistic structure.

However, the general three-body potentials, such as V_3 in equation (2-11), have been criticized for their inability to describe the energetics of all possible bonding geometries [33], while a general form for a four- and five-body potential appears intractable, and would contain too many free parameters. As a result, a variety of advanced two-body potentials have been proposed to efficiently account for the specifics of a local atomistic environment by incorporating some particular many-body dependence inside the function V_2, known as bond-order functions, rather than introducing the many-body potential functions $V_m > 2$. These terms implicitly include the angular dependence of interatomic forces by introducing the bond-order function, while the overall pairwise formulation is preserved. Also, these potentials are usually treated as short-range ones, for example, accounting for interaction between a current atom and several neighbors only. Some of the most common models of this type are the following: the Tersoff potential [33] for a class of covalent systems, such as carbon, silicon and germanium, the Brenner [34] and Reactive Empirical Bond Order (REBO) [35] potentials for carbon and hydrocarbon molecules.

Many force fields have been developed to describe crystalline systems, including metals and ceramics. These are typically separated into pair potentials and multi-body potentials. In pair potentials, the total potential energy of the system is expressed as the sum over all pairs of bonds. In multi-body potentials, the strength of the pair wise interactions is modulated dependent on the atomic environment. Examples for pair potentials are the Lennard-Jones potential and the Morse function. Examples for popular multi-body potentials are the Tersoff potential and the Stillinger-Weber potential to model covalent interactions, or the EAM and MEAM potentials suitable for metals.

Because today's computers are still not fast enough to give a complete quantum

mechanical description of large molecules like proteins. Therefore, in order to be able to study the binding of ligands to large molecules like proteins, it is still necessary to make use of methods making even greater approximations than the semiempirical quantum mechanical methods. Whereas the latter use a set of parameters describing only the core orbitals, with force field methods molecules are solely described by parameterized potential functions. These methods are not quantum mechanical methods, since force field methods do not deal with an electronic Hamiltonian or wave function or an electron density. Instead, molecules are treated as a set of masses (atoms) held together by springs (bonds). The interaction between these atoms is described with potential energy functions, which are constructed as a function of atomic coordinates, making use of parameters for describing bond stretching and bond-bending and allowing for interactions between non-bonded atoms. So, the potential energy surface itself (in simplified form) is the starting point for the Molecule Mechanics approach, whereas the quantum mechanical approach requires mapping out the potential energy surface for the molecule in question.

Potential energy functions are constructed as a function of atomic coordinates, making use of parameters for describing bond stretching, bond-bending, and allowing for interactions between non-bonded atoms. Functional forms of potential energy functions are shown in equation (2-15). Generally, force-field methods describe the potential energy surface of molecules as a sum of bond stretching (V_{str}), bond-angle bending (V_{bend}), out-of-plane bending (V_{oop}), internal rotation (torsion) about bonds (V_{tors}), interactions between these kinds of motion (V_{cross}), van der Waals attractions and repulsions between non-bonded atoms (V_{vdW}), and electrostatic interactions between non-bonded atoms (V_{el}):

$$V = V_{str} + V_{bend} + V_{oop} + V_{tors} + V_{cross} + V_{vdW} + V_{el} \qquad (2\text{-}15)$$

2.2.1 Bond Stretching

In a public forcefield, bond length is described by a harmonic potential, which is based on Hooke's law. Like in all spectroscopic force fields, the potential is calculated as the force needed to stretch a particular bond between atoms i and j with respect to its

equilibrium length b_0:

$$V_{str} = \sum_{i>j} k_{B,ij} \left(b_{ij} - b_{ij}^0 \right)^2 \tag{2-16}$$

where k_B denotes force constant of the bond length B [$kcal \cdot mol^{-1} \cdot rad^{-2}$].

Although the form of (2-16) is relatively simple, it has been shown, that it suits very well for the description of large molecules, as long as many different atom types with specific parameters are used. However, in order to achieve higher accuracy in the treatment of small molecules, it is often more advantageously to define less atom types, but using more computationally expensive potential functions. Since the some public forcefields are originally developed for proteins, however, the bond stretching potential is calculated by a simple quadratic form given in equation (2-15) with the definition of many different parameters.

Bond lengths can also be calculated more correctly by including Morse [29] potentials. Because of the considerable extra computational cost of calculating these potentials, however, these potentials have been neglected throughout the work presented here.

2.2.2 Bond Bending

The potential energy V_{bend} of bond bending is taken as the sum of potential energies V_{bend} for bending each bond angle between atoms i, j and k contained in the molecule. Like the stretching potential, the bending potential has a harmonic form as well:

$$V_{bend} = \sum k_{B,ijk} \left(\theta_{ijk} - \theta_{ijk}^0 \right)^2 \tag{2-17}$$

where

θ_{ijk} = the actual value of the bond angle between atoms i, j and k

θ_{ijk}^0 = the equilibrium value of the bond angle between atoms i, j and k

2.2.3 Torsional Energy

The term V_{tors} is taken as the sum of terms V_{tors} over all 1 through 4 atom pairs:

$$V_{tors} = \sum k_{\tau} \left[1 + \cos\left(n\varphi_{ijkl} - \varphi^{0}_{ijkl} \right) \right] \tag{2-18}$$

where

k_{τ} = torsional barrier [$kcal \cdot mol^{-1}$]

n = number of minima over 360 º(periodicity)

φ_{ijkl} = actual torsional angle between atoms i, j, k and l

φ^{0}_{ijkl} = reference value of torsional angle between atoms i, j, k and l

2.2.4 Out-of-plane Energy

To ensure planarity of a sp^2 hybridized carbon atom an out-of-plane bending term is added to the expression of the total energy. In a public forcefield, this out-of-plane term has the following form:

$$V_{oop} = \sum k_{oop} \left[1 + \cos\left(n\chi_{ijkl} - \chi^{0}_{ijkl} \right) \right] \tag{2-19}$$

where k_{oop} denotes the out-of-plane torsional parameter.

Since the functional form of $V_{oop,ijk}$ is similar to that of $V_{tors,ijkl}$ the out-of-plane term is often referred to as improper torsion. Like the torsional energy term it is defined by four atoms, but now the four atoms have to be positioned in the same plane.

2.2.5 Van der Waals Interactions

Whereas the energy terms mentioned above only account for neighboring atoms contained in one and the same molecule, additional terms describing nonbonded and 1,4, 1,5, 1,6 ….atom-pair interactions are also required in the force field to describe molecular interaction as accurately as possible. These essentially nonbonded interactions are usually assumed to be of the same form as the interactions between rare gas atoms [36], for example, a long range R^{-6} attraction due to induced dipole-induced dipole interaction (London dispersion interaction) and a short-range R^{-12} (Pauli) repulsion resulting from the overlap of electron clouds. Both types of interaction are contained in the Van der

Waals energy term (the 1,2 and 1,3 Van der Waals and electrostatic interactions are considered to be implicitly included in the bondstretching and bond-bending parameters described above). The resulting Van der Waals energy term is therefore usually expressed as the Lennard-Jones 12-6 potential:

$$V_{vdW} = \sum_{i<j} \varepsilon_{IJ} \left[\left(\frac{R_{IJ}^*}{R_{ij}} \right)^{12} - 2 \left(\frac{R_{IJ}^*}{R_{ij}} \right)^{6} \right] = 4 \sum_{i<j} \varepsilon_{IJ} \left[\left(\frac{\sigma_{IJ}^*}{R_{ij}} \right)^{12} - 2 \left(\frac{\sigma_{IJ}^*}{R_{ij}} \right)^{6} \right] \qquad (2\text{-}20)$$

where R_{IJ} is the distance between atoms i and j, ε_{IJ} is the value of $V_{vdW,ij}$ at the minimum in the interaction curve, R_{IJ}^* is the equilibrium distance between atoms i and j, and σ_{IJ} is the distance at which $V_{vdW,ij}$ is zero.

2.2.6 Electrostatic Interactions

The electrostatic term V_{el} is taken as the sum of Coulombic interactions between the partial atomic point charges of the system under study, except for the 1,2 and 1,3 pairs:

$$V_{el} = \sum_{i<j} \frac{Q_i Q_j}{\varepsilon_r R_{ij}} \qquad (2\text{-}21)$$

where Q_i, Q_j are the atomic charges of atoms i and j respectively, ε_r is the dielectric constant of the medium, and R_{ij} is the distance between atoms i and j.

Although very fast, one of the major drawbacks of using force fields is that one has to derive new parameters for each bond type not previously included in the parameter list.

2.2.7 Characterize the Interface by Using CVFF-aug Forcefield

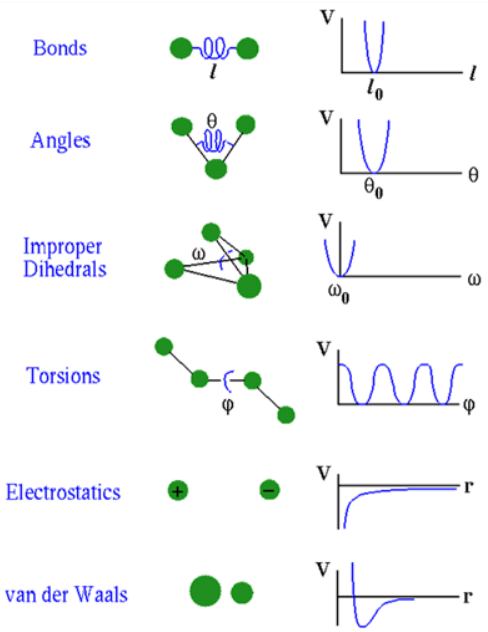

$$V_{bond} = \frac{1}{2} k_l (l - l_0)^2$$

$$V_{angle} = \frac{1}{2} k_\theta (\theta - \theta_0)^2$$

$$V_{improper} = k_\omega (1 - \cos 2\omega)$$

$$V_{torsion} = A_n \left[1 + \cos\left(n\varphi - \varphi_0 \right) \right]$$

$$V_{elec} = \frac{q_i q_j}{4\pi\varepsilon_0 r_{ij}}$$

$$V_{vdW} = 4\varepsilon_{ij} \left[\left(\frac{\sigma_{ij}}{r_{ij}} \right)^{12} - \left(\frac{\sigma_{ij}}{r_{ij}} \right)^{6} \right]$$

Figure 2-2 Potential energy functions of CVFF-aug forcefield

The consistent-valence forcefield (CVFF) is a generalized valence forcefield [37]. Parameters are provided for amino acids, water, and a variety of other functional groups. The augumented CVFF includes non-bond parameters for additional forcefield types that are useful for simulation of silicates, aluminosilicates, clays and aluminophosphates. These added parameters were derived using Ewald summation for nonbond interactions between the additional atom types.

In the following the analytical form of the terms given in equation (2-15) will be briefly described. Although implemented in the CVFF-aug, the cross potentials (V_{cross}), which represent couplings between deformations of internal coordinates, are not used in the work presented.

The energy functions of CVFF-aug forcefield, as shown in Figure 2-2, include internal coordinate terms and pairwise nonbond interaction terms. The total energy can be expressed by the equation:

$$Energy = E_{bond} + E_{angle} + E_{torsion} + E_{oop} + E_{elec} + E_{vdW} \tag{2-22}$$

$$\begin{aligned} E_{vdW} &= LJ(r) && r < r_{in} \\ &= S(r) * LJ(r) && r_{in} < r < r_{out} \\ &= 0 && r > r_{out} \end{aligned} \tag{2-23}$$

$$E_{elec} = C(r) \qquad r < r_{in}$$
$$= S(r) * C(r) \quad r_{in} < r < r_{out} \tag{2-24}$$
$$= 0 \qquad r > r_{out}$$

$$LJ(r) = 4\varepsilon\left[\left(\frac{\sigma}{r}\right)^{12} - \left(\frac{\sigma}{r}\right)^{6}\right] \tag{2-25}$$

$$C(r) = \frac{Cq_i q_j}{\varepsilon r} \tag{2-26}$$

$$S(r) = \frac{\left[r_{out}^2 - r^2\right]\left[r_{out}^2 + 2r^2 - 3r_{in}^2\right]}{\left[r_{out}^2 - r_{in}^2\right]^3} \tag{2-27}$$

The equation (2-22) denotes the general form of the total energy, including bonded and nonbonded terms. Equation (2-23) shows the Van der Waals interaction potential term. Equation (2-24) denotes the electrostatic interaction energy. Equation (2-26) and equation (2-27) are both decaying factors that used to characterize a smooth transition of Van der Waals and electrostatic interaction potentials.

CVFF-aug forcefield is used in this research to simulate the mechanical properties of SiO_2 portion of interface structure. Here, r_{ij} is the distance between tow atoms, q_i is the charge on atom i, C is the dielectric constant and ε, σ are material parameters. The first term models short-range interactions; the second term considers the long-range Coulomb interactions due to electric charges. Atom-atom interactions include both the long-range and short-range terms. Calculation of the long-range Coulomb force is carried out using the Ewald sum, which is computationally efficient and unconditionally converging. The periodicity required for the Ewald sum is introduced using a supercell concept, in which the simulation box is defined considerably larger than the nano-sample.

2.3 Energy Minimization --- Molecular Mechanics (MM)

Energy minimization is an approach during which the potential energy of the system, at zero temperature, is minimized. Energy minimization corresponds to the physical situation of cooling down a material to the absolute zero point. The method in

which the deformation behavior of a material or structure is probed during continuous energy minimization is also referred to as molecular statics. Such approaches have been used to study dislocation nucleation from crack tips or the deformation of carbon nanotubes. It mimics a quasistatic experiment, albeit neglecting the effect of finite temperature.

A variety of algorithms exist to perform energy minimization, most notably conjugate gradient methods or steepest descent methods. Figure 2-3 depicts an asphaltene molecule result during energy minimization, showing how the potential energy of the system decreases systematically with the number of iteration steps and finally converges to a finite value.

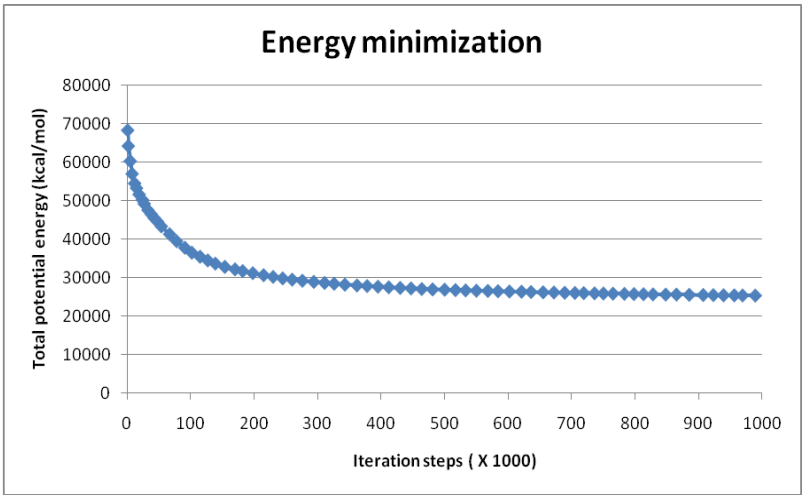

Figure 2-3 Example procedure of an energy minimization, here an example of minimizing the structure of an asphaltene molecule. As the number of iterations progresses, the total potential energy decreases, until it converges and reaches a constant value

The aim of energy minimization of a molecule is to locally explore the potential energy surface in order to find a point in the configuration space where the net force on each atom vanishes. These points are energetic minima. By using molecular mechanics the starting conformation of a molecule is often chosen arbitrarily, which means that the potential energy of the molecule is not optimal. With energy minimization methods the nearest minimum on the potential hypersurface (local minimum) can be found. This does not necessarily have to be the global minimum.

The nearest local minimum can be found using iterative procedures, which

calculate the gradient of the potential hypersurface, according to which new atomic positions are calculated of a lower-energy structure. Most methods apply the line search method, which seeks the nearest local minimum in the hyperpotential surface by stepwise generation of vectors, which represent the direction in which the energy decreases fastest. Since the direction in which the minimization is continued is perpendicular to the search line at this point, each line search is orthogonal to the previous one. Some examples of minimization algorithms include the steepest descent, the conjugate gradient, the Newton-Raphson and the simplex methods. Because here only the first two methods have been applied, they will be briefly described in the following. Both are gradient methods.

The steepest descent method starts with defining the direction of the local downhill gradient. Obviously, this method may be rather inefficient on energy surfaces having narrow valleys. LAMMPS, however, uses a slightly modified procedure, in that the position of the trial point is continuously updated along the direction of the gradient. This way line searches can be truncated, leading to a considerable decrease in the number of function evaluations. Nevertheless, the method remains rather inefficient due to the orthogonality of each new step. Because this is only useful at the beginning of the minimization procedure (oscillation results when the minimum is approached), this method is often used for an initial relaxation of poorly defined structures.

Conjugate gradients, however, calculate a new direction vector by incorporating the gradient at the endpoint of the line search, which is added to the gradient from the previous direction. As a result, the resulting gradient is orthogonal to the previous one, and the next direction is conjugate to all previous directions. Because convergence toward the minimum is achieved more efficiently than with steepest descent, conjugate gradient is the method of choice for large molecular systems.

2.4 Thermodynamic Ensembles and Their Numerical Implementation

When the equations reviewed in the previous section are integrated, the resulting thermodynamical ensemble is NVE, which means that the particle number N, the system volume V, and the total energy of the system E remain constant throughout the

simulation. Molecular dynamics simulations may be performed under a variety of conditions and constraints, corresponding to different ensembles in statistical mechanics. These conditions are always true for any closed mechanical system. Modifications of the MD algorithm allow use of the canonical (constant NVT) or isothermal-isobaric (constant NPT) ensembles. Most of the simulations discussed here used NVT or NPT conditions.

To illustrate the approach of modifying the equations of motion to obtain a specific thermodynamical ensemble, here we briefly review a simple algorithm to enable an NVT ensemble, the Berendsen thermostat. The approach is based on the idea to change the velocities of the atoms so that the temperature (which is a direct function of the atomic velocities) approaches the desired value, mimicking the effect of a heat bath. This is realized by calculating a rescaling parameter λ

$$\lambda = \sqrt{1 + \frac{\Delta t}{\tau}\left(\frac{T}{T_{set-1}}\right)} \tag{2-28}$$

where Δt is the molecular dynamics time step and τ is a parameter called 'rise time' that describes the strength of the coupling to the hypothetical heat bath. The velocities are then rescaled according to this parameter, where the new velocity vectors are given by

$$\mathbf{v}_{new,i} = \lambda \mathbf{v}_i \tag{2-29}$$

for each atom i.

Other approaches to enable the NVT ensemble include methods based on Langevin dynamics and the Nose-Hoover scheme. For NPT ensembles, the Parrinell-Rahman approach provides a popular choice for an algorithm. In this method, in addition to adjusting the temperatures to approach the desired control value, the pressure is adjusted by changing the cell size of the simulated system.

States with high energy will occur less often, states with low energy more often. Each microscopic state has a certain probability associated with the corresponding energies. During the integration of the equations of motion, molecular dynamics naturally samples these microscopic configurations and provides a collection of snapshots that after averaging correspond to the proper macroscopic state. The obtained trajectories can then be used to calculate thermodynamical properties by simply averaging over the sampled configuration without further weighting.

2.5 Periodical Boundary Condition

One of the principal difficulties in MD simulation is that the number of atoms is always much smaller than the Avogadro number, N_A, characteristic of macroscopic systems. Many atoms are, thus, located near enough to the edge of the simulation cell that their potential fields reflect conditions outside the cell, and edge effects can significantly distort the results. Therefore, most workers use periodic boundary conditions to minimize edge effects and simulate more closely the system's bulk macroscopic properties. In practice, the application of periodic boundary conditions assumes the basic simulation box to be surrounded by identical boxes infinitely in all three dimensions. Thus, if a particle leaves the box through one side, its identical image enters simultaneously through the opposite side.

Whether the properties of this relatively small, infinitely periodic system and the equivalent macroscopic system are the same depends in part on the length scale over which the intermolecular potentials act and the property under investigation. For short-range interactions, either spherical or 'minimum image' cutoff criteria are commonly used [38]. The latter means that each molecule interacts only with the closest image of all other particles in the simulation cell or its periodic replicas. However, all realistic potentials for ionic species in solids or aqueous solutions contain long-range electrostatic (Coulombic) interactions, which decay only as 1/r, where r is the interatomic distance. Ewald summation is considered the most satisfactory method for treating these long-range interactions [38].

MD simulations involve averages taken over computational runs with finite sizes and times and are thus subject to statistical errors. It is essential to estimate these in evaluating the results. The statistical uncertainties of simulated properties are usually estimated by the method of block averages [38]. The MD trajectory is subdivided into several non-overlapping blocks of equal length, and the averages of the desired properties are computed for each block. If $\langle A \rangle$ is the mean value of a property A computed for block i, the variance δA of the mean value $\langle A \rangle$ for the entire simulation can be estimated as

$$(\delta A)^2 = \frac{1}{M}\sum_{i=1}^{M}\left[\langle A\rangle_i - \langle A\rangle\right]^2 \tag{2-30}$$

where M is the number of blocks. Strictly speaking, Equation (2-30) is valid only if all $\langle A\rangle_i$ are statistically independent and show a normal Gaussian distribution. Thus, if the simulation is of insufficient length, these estimates should be taken with caution, especially for the properties calculated from fluctuations.

2.6 Exploring the Molecular Configuration Space

Molecular mechanics preliminary methodologies give a simplified representation of the real microscopic world. In order to connect results derived from these methods with physically measurable macroscopic properties, it is necessary to include the central concept of statistical mechanics when describing a molecular system. This concept states that the most probable configuration of a microscopic system can be described by the Boltzmann distribution factor:

$$\frac{n_j^*}{N} = \frac{e^{-\beta\varepsilon_i}}{e^{-\beta\varepsilon_j}} \tag{2-31}$$

where n_j^* is the number of particles in the most probable (equilibrium) state, N is the total number of particles, β is $1/kT$ (called Boltzmann factor), ε_j is the energy of configuration i, and j is the total number of configurations. So, it is necessary to explore the configurational space of the system.

Therefore, we can say that Boltzmann distribution equation is one possible way to verify whether the system equilibrium state reached by using certain type of forcefield, such as CVFF, CVFF-aug, COMPASS, CFF, AMBER, etc.

However, with static molecular mechanics methods usually only the nearest local minimum with energy U can be found, which is related to the physically measurable free energy G by the enthalpy H as follows:

$$\Delta H = \Delta U - p\Delta \tag{2-32}$$

$$\Delta G = \Delta H - T\Delta S \tag{2-33}$$

where, p is the pressure, V is the volume of the system.

Since the volume change can be neglected under normal circumstances, calculation of the energies U of different conformations enables calculation of ΔG with experimentally obtained values.

Since the energy minimization methods can only find the nearest minimum on the potential hypersurface (local minimum), which is a roughly global minimum. The critical approach have been developed for exploring the configurational space for global minimum is Molecular Dynamics Simulation

2.7 Thermodynamic Property Calculation

In previous section we have focused attention on the simulation itself, that is, on computing the phase-space trajectory for a system of model molecules. In this section, we turn our attention to the analysis of computed trajectories. The analysis involves evaluating macroscopic properties-properties that pertain, not individual molecules, but to an entire system of molecules. The properties we consider in this section are thermodynamic quantities and static structure.

We divide thermodynamic properties into three classes: (1) simple functions of the Hamiltonian, (2) the thermodynamic response function, which are derivatives of the simple functions, and (3) the entropy and free energies. Generally, as we move from class 1 to class 3, these properties become more difficult to evaluate accurately.

For a system of N particles, the phase-space trajectory is represented by the set of numbers

$$\left\{\left[\mathbf{r}^N\left(k\Delta t\right), \mathbf{p}^N\left(k\Delta t\right)\right], k = 1, \ldots, M\right\} \tag{2-34}$$

Here $\mathbf{r}^N$ is the set of N position vectors and $\mathbf{p}^N$ is the set of N momentum vectors. The trajectory has been obtained from a simulation performed over M discrete times using the time-step Δt. Form this trajectory the time average $\langle A \rangle$ of some function of the

trajectory can be estimated by the sum

$$\langle A \rangle = \frac{1}{M} \sum_{k=1}^{M} A\left[\mathbf{r}^N (k\Delta t), \mathbf{p}^N (k\Delta t) \right] \tag{2-35}$$

the finite interval average is an approximation to the infinite time average as below

$$\langle A \rangle = \lim_{t \to \infty} \frac{1}{t} \int_{t_0}^{t_0 + t} A\left(\mathbf{r}^N, \mathbf{p}^N \right) d\tau \tag{2-36}$$

In this research, statistical thermodynamics method is employed to calculate system properties from molecular dynamics simulations. We introduce definitions and numerical procedures for the following material properties:

- Temperature T (thermodynamic property)
- Pressure P (thermodynamic property)
- Radial distribution function g(r) (structural information)
- Mean square displacement function (measure for mobility of atoms, relates to diffusivity)
- Velocity autocorrelation function (transport properties)

2.7.1 Temperature Calculation

MD simulation trajectories describe the positions, velocities, forces, etc on every atom for every time step. From this information, collective analyses of atomic properties allows one to extract macroscale thermodynamic quantities. This was already alluded to above in the description of atomic velocity assignment when initializing a MD simulation. Assuming there is zero net system momentum or, more generally that the system is in thermodynamic equilibrium, then the atomic kinetic energy can be directly related to the system temperature according to Maxwell-Boltzmann statistics. That is, at any instant in time t during a simulation, the atomic velocities give the system T via

$$T(t) = \frac{1}{3Nk_B} \sum_{\alpha=1}^{N} m^{\alpha} \left(v^{\alpha} \right)^2 \tag{2-37}$$

In this expression, k_B is Boltzmann's constant, m^α is the mass of atom α and v^α is the magnitude of atom α's velocity. MD simulation is inherently associated with properties of discrete atoms and the expression from statistical mechanics above is readily calculable in such a model. In this review, we generally restrict discussion to thermomechanical property definitions which are calculable from quantities inherent to MD simulation.

2.7.2 Pressure Calculation

The pressure P is given by

$$P = Nk_BT - \frac{1}{3V}\sum_{i=1}^{N}\sum_{j=1,j<i}^{N}\left\langle r_{ij}\frac{d\phi}{dr_{ij}}\right\rangle \tag{2-38}$$

The first term stems from the kinetic contributions of particles hitting the wall of the container, and the second term stems from the interatomic forces, expressed as the force vector contribution multiplied by the distance vector component between particles i and j.

2.7.3 Radial Distribution Function

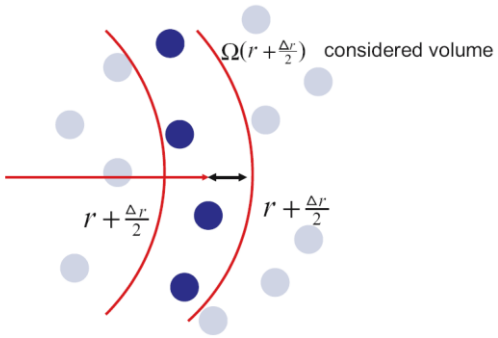

Figure 2-4 Method to calculate the radial distribution function g(r)

The radial distribution function g(r) measures how atoms organize themselves around one another -- 'local structure'. Specifically, it is proportional to the probability of finding two atoms separated by distance $r \pm \Delta r$. The function $g(r)$ plays a central role in statistical mechanical theories of dense substances, and for atomic substances. It is used

in predicting the pair distribution function theory of dense fluids and provides a signature for identifying the lattice structure of the crystalline solids. Since molecular dynamics provides positions of individual atoms as functions of time, g(r) can be readily computed from molecular dynamics trajectories.

The radial distribution function (RDF), g(r), is defined as

$$g(r) = \frac{\rho(r)}{\rho_0} \tag{2-39}$$

where $\rho(r)$ is the local density at r, and $\rho_0 = N/V$ is the averaged atomic volume density. A possible numerical strategy to calculate g(r) is depicted in Figure 2-4. For such a discrete estimate,

$$g(r) = \frac{N\left(r \pm \frac{\Delta r}{2}\right)}{\Omega\left(r \pm \frac{\Delta r}{2}\right)\rho_0} \tag{2-40}$$

where $N\left(r \pm \frac{\Delta r}{2}\right)$ is the number of particles in the volume shell with volume $\Omega\left(r \pm \frac{\Delta r}{2}\right)$. A detailed derivation of RDF is listed in the Appendix.

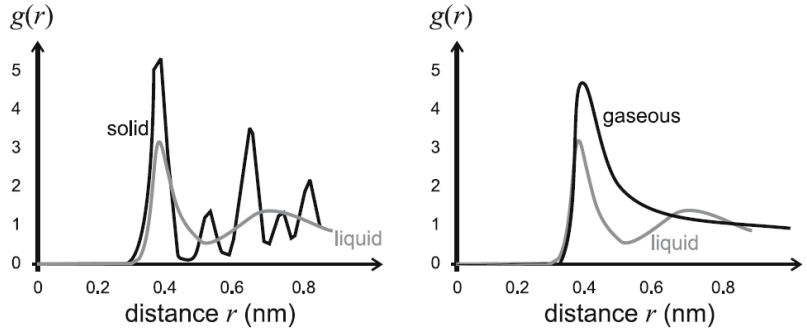

Figure 2-5 Radial distribution function g(r) for various atomistic configurations, including a solid (crystal), a liquid and a gas

An example is shown in Figure 2-5. The RDF enables to perform quantitative analysis of atomic structure and can elucidate if a system is in solid, liquid, or gas state. Moreover, the RDF provides detailed information about the type of crystal structure or

includes precise signatures of the specific atomic arrangement of a liquid. It also provides a means to compare quantitatively with experimental results (e.g., obtained using neutron-scattering techniques) and can thereby assist in developing new potential formulations.

2.7.4 Mean Square Displacement Function

The dynamics of molecules has them colliding and re-colliding with each other, and observation of the trajectory of any given molecule will find that it meanders erratically and randomly through the available volume. Although there is no directed motion, a molecule will not remain indefinitely in the vicinity of its present position. The mean square displacement (MSD) is a measure of the average distance a molecule travels. It is defined

$$MSD(t) = \left\langle \Delta r^2 \right\rangle = \frac{1}{N} \sum_{i=1}^{N} \left(r_i(t) - r_i(0) \right)^2 \tag{2-41}$$

In this equation, $r_i(t) - r_i(0)$ is the distance traveled by molecule i over some time interval of length t, and the squared magnitude of this vector is averaged over many such time intervals. Often this quantity is averaged also over all molecules in the system, summing i from 1 to N and dividing by N.

If the molecule encountered no other molecules, traveling ballistically, then the distance it traveled would be proportional to the time interval---distance equals velocity times time---and the MSD would increase quadratically with t. In denser phases, quadratic behavior holds only for a very short time interval, of the order of the mean collision time. Beyond this time the motion is better described as a random walk, for which the MSD increases only linearly with time. The rate of growth of the mean square displacement depends on how often the molecule suffers collisions. At higher density, it will take longer to diffuse a given distance, as other molecules continually impede its progress.

The limiting slope of $MSD(t)$, considered for time intervals sufficiently long for it to be in the linear regime, is related to the self-diffusion constant D.

$$D = \frac{1}{2d} \lim_{t \to \infty} \frac{d}{dt} \left\langle \Delta r^2 \right\rangle \tag{2-42}$$

where d is the dimension of the space.

If averaged over all particles, the mean square displacement function provides the square distance that particles have moved during time t. The mean square displacement function is zero at t = 0, and it grows with increasing time. In a solid, it is expected that the mean square displacement function grows to a characteristic value and then saturates at a constant value. In a liquid, all atoms move continuously through the material, as in Brownian motion. Diffusivity in liquids is related to the linear variation of the mean square displacement function with time t.

2.7.5 Velocity Autocorrelation Function

The velocity autocorrelation function (VAF) is defined as

$$\left\langle v(0)v(t) \right\rangle = \frac{1}{N} \sum_{i=1}^{N} \frac{1}{N} \sum_{j=1}^{N} v_i(t_0) v_i(t_0 + t) \tag{2-43}$$

where v_i refers to the magnitude of the velocity vector of particle i. The velocity autocorrelation function gives information about the atomic motions of particles in the system. Since it is a correlation of the particle velocity at one time with the velocity of the same particle at another time, the information refers to how a particle moves in the system, such as during diffusion. The diffusion coefficient can be calculated as

$$D = \frac{1}{3} \int_{t'=0}^{t'=\infty} \left\langle v(0)v(t) \right\rangle dt' \tag{2-44}$$

Autocorrelation functions can be used to calculate other transport coefficients such as thermal conductivity or the shear viscosity. These expressions derived based on the Green-Kubo relations can provide links between correlation functions and material transport coefficients (also applicable to thermal conductivity, shear viscosity, and other material transport properties).

In addition to the diffusivity D, the VAF also provides information about structural properties of an atomic system. For liquids or gases, under relatively weak

molecular interactions, the magnitude of the VAF reduces gradually under the influence of weak forces. This is because the velocity decorrelates rapidly with time. This is the same concept as stating the atom loses its memory about what its initial velocity was. For example, in the case of a gas, the VAF plot is a simple exponential decay, revealing the presence of weak forces slowly destroying the velocity correlation.

In a solid, under relatively strong interactions, the atomic motion is an oscillation, vibrating backwards and forwards, reversing their velocity at the end of each oscillation. Therefore, the VAF corresponds to a function that oscillates strongly from positive to negative values and back again, while the magnitude of the oscillations decay in time. This leads to a function resembling a damped harmonic motion. Figure 2-6 plots the VAF for different cases.

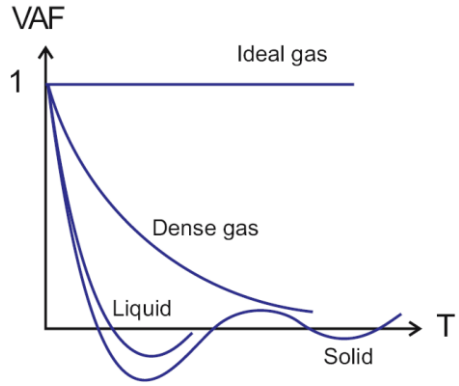

Figure 2-6 Velocity autocorrelation function (VAF) for a gas, liquid, and solid

2.7.6 Application of Mechanical Boundary Conditions

The application of boundary conditions in atomistic and molecular systems is essential, in particular for studies of the mechanical behavior.

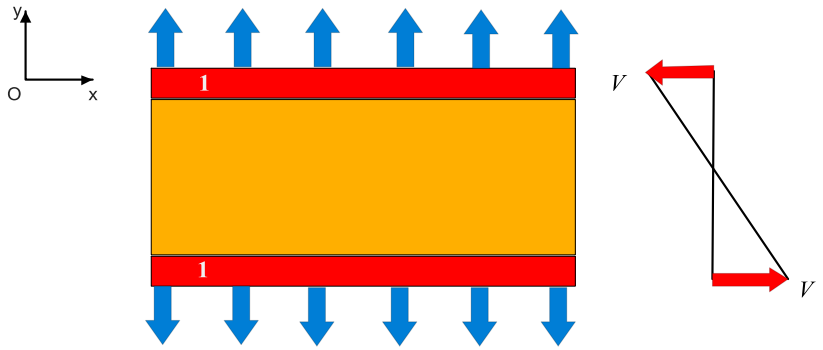

Figure 2-7 Simulation method of domain decomposition by the method of virtual atom types. The atoms in region 1 do not move according to the physical equations of motion, but are displaced according to a prescribed displacement history. An initial velocity gradient as shown in the right half of the plot is used to provide smooth initial conditions

Most straightforward are approaches to apply displacement boundary conditions. In these applications, the dynamics of corresponding atoms (or groups of atoms forming a physical domain whose displacement is prescribed) is altered so that this group of atoms follows a prescribed motion rather than following the dynamics according to the equations of motion.

To model different interatomic interactions in different regions of the simulation domain, one can assign a virtual type to particular groups of atoms. On the basis of the type definition of interacting pairs of atoms, it is possible to calculate different interatomic interactions. For instance, this enables one to model an atomically sharp crack tip by removing any atomic interaction across a material plane (effectively describing this part as a free surface). An example for this type of domain decomposition is shown in Figure 2-7. To apply mechanical load by controlling the displacement, a linear velocity gradient is established prior to simulation to avoid shock wave generation from the boundaries shown in Figure 2-7.

To strain the system, a few layers of atoms at the boundary of the crystal slab are not moved according to the natural equations of motion (e.g., by the Verlet algorithm), but are instead displaced in each step, according to the prescribed displacement, with the velocity that matches the initial velocity field. This procedure has been used in several atomistic studies of dynamic fracture. It is possible to stop the increase of loading after a prescribed loading time, from which on the boundaries are kept fixed. In an alternative method, the system can be strained prior to the beginning of the simulation (according to

the particular loading direction), and the outermost material layers are then kept fixed during the simulation (that is, atoms in this group do not move at all).

The application of stress or pressure boundary conditions can be more challenging, but it can be achieved by utilizing appropriate ensemble schemes, as for instance the Parinel-Rahman method. This approach enables one to prescribe a particular stress tensor to the system. By changing the prescribed value of the stress tensor one can simulate slow loading conditions.

To apply the forces to the molecule that induce deformation, steered molecular dynamics (SMD) has evolved into a useful tool. Steered molecular dynamics is based on the concept of adding a harmonic moving restraint to the center of mass of a group of atoms. This leads to the addition of the following potential to the Hamiltonian of the system:

$$U\left(\mathbf{r}_1\mathbf{r}_2,\ldots,t\right)=\frac{1}{2}k\left(\mathbf{v}t-\left(\mathbf{r}\left(t\right)-\mathbf{r}_0\right)\cdot\mathbf{n}\right) \tag{2-45}$$

where $\mathbf{r}\left(t\right)$ is the position of restrained atoms at time t, $\mathbf{r}_0$ denotes original coordinates and v and **n** denote pulling velocity and pulling direction, respectively. The net force applied on the pulled atoms is

$$F\left(\mathbf{r}_1\mathbf{r}_2,\ldots,t\right)=k\left(\mathbf{v}t-\left(\mathbf{r}\left(t\right)-\mathbf{r}_0\right)\cdot\mathbf{n}\right) \tag{2-46}$$

By monitoring the applied force (F) and the position of the atoms that are pulled over the simulation time, it is possible to obtain force-vs.-displacement data that can be used to derive the mechanical properties such as bending stiffness or the Young's modulus (or other mechanical properties). SMD studies are carried out in this dissertation to calculate the interfacial mechanical properties.

2.8 Parallel Molecular Dynamics

Large-scale molecular-dynamics simulations often require an enormous amount of computer power. Based on the concept of concurrent computing, modern parallel computers are made out of hundreds or thousands of PC working simultaneously on

different parts of the same problem. Information between these small computers is shared by communicating, which is achieved by message-passing procedures (MPI) [39].

Parallel molecular-dynamics is relatively straight-forward to implement with great efficiency in a message-passing environment. It is important to have an effective algorithm for handling the summations of N interacting particles. If summations had to be carried out for each particle over all particles, the problem would scale with N^2. This is a computational catastrophe for large systems. However, if the interactions between particles are short ranged, the problem can be reduced so that the execution time scales linearly with the number of particles (that is, execution time scales with N). The computational space is divided up into cells such that in searching for neighbors interacting with a given particle, only the cell in which it is located and the next-nearest neighbors have to be considered. Since placing the particles in the correct cells scales linearly with N, the problem originally scaling with N^2 can therefore be reduced to N. With a parallel computer whose number of processors increases with the number of cells (the number of particles per cell does not change), the computational burden remains constant.

The speedup factor S is defined as the ratio of execution time on one processor (T_s) over the execution time on p processors (T_p):

$$S = \frac{T_s}{T_p} \tag{2-47}$$

The perfectly efficient parallel computer would exhibit linear speedup. This would mean that the computation time for p processors is 1/p times the execution time on one processor. However, the speedup depends strongly on the fraction of the work done in parallel. For more information about parallel algorithm, one can refer to Plimpton's algorithms for molecular-dynamics with short-range forces [40].

Parallel computing requires decomposing the computation into subtasks and mapping them to multiple processors. For MD simulations, the divide-and-conquer strategy based on spatial decomposition is commonly used. The total volume of the system is divided into P subsystems of equal volume, and each subsystem is assigned to a node in an array of P processors. The data associated with atoms of a subsystem are

assigned to the corresponding processor. In order to calculate the force on boundary atoms in a subsystem, the coordinates of the atoms in the boundaries of neighbor subsystems need to be cached from the corresponding processor.

2.9 LAMMPS Parallel MD Algorithm

2.9.1 Introduction

For all of the calculations used in this dissertation, we used the LAMMPS molecular dynamics code designed for large-scale atomistic simulations. This code is written in C++ and also parallelized with MPI.

The parallel nature of MD simulations has long been recognized. Assuming the Coulombic term in equation can be computed in the order of O(N) time, then on P processors, the overall calculation should scale as N/P. For general molecular systems simulated on message-passing machines, most parallel implementations have used the replicated-data technique, where a copy of all N atomic positions is stored on each of P processors. This enables easy computation and load-balancing of the nonbonded terms. However at each timestep, the inter processor communication needed to globally update a copy of the N-vector of atom positions scales as N, independent of P. Thus replicated-data methods do not scale to large numbers of processors. An alternative known as force-decomposition scales as $N/\sqrt{P}$, but is still sub-optimal. For large N/P ratios, spatial-decomposition methods are clearly the best algorithmic choice. By subdividing the physical volume among processors, most computations become local and communication is minimized so that optimal N/P scaling can be achieved. Such methods have been extensively used for atomic simulations, and less so for general molecular systems. A chief difficulty is how to compute the bonded terms in parallel. In the next section we describe how LAMMPS is structured to enable parallelization of bonded interactions with a spatial-decomposition of molecular connectivity information.

2.9.2 Parallel Decomposition Methods

Three classes of parallel algorithms are suitable for short-range MD force fields: so-called atom-, force-, and spatial-decomposition algorithms. Atom-decomposition methods assign a subset of atoms permanently to each processor, force-decomposition methods assign a subset of pairwise force computations to each proc, and spatial-decomposition methods assign a sub-region of the simulation box to each processor.

The spatial (or domain) decomposition algorithm represents a powerful approach to parallel molecular dynamics simulations that use short-ranged potentials. The algorithm uses a spatial decomposition of the simulation box as indicated in Figure 2-8, where we can define a hierarchy consisting of a domain (whole system), n-regions (one for each processor) and individual cells within the regions. The cubical cells of Figure 2-8 are defined so that the smallest length of a cell is always larger than the cutoff on the non-bonded potential. This means that an atomic can only interact with another site if that site is present in the same cell, or present in a neighbor cell.

The advantages of this approach stem from the fact that each processor is able to act independently in calculating forces for most sites in its own region. The only exception arises from sites that appear in the cells on the boundary of a region. For these sites, message passing must take place to communicate vital data from neighboring processors. However, the quantity of data that must be communicated is small compared to that required in the large global sums of the force array in the replicated data method. This means that the domain decomposition algorithm can work pretty efficiently with minimal communications overheads.

The algorithm scales well with the number of particles in a system. As each region gets larger, the relative proportion of particles in cells on the boundary of a region becomes smaller, and so the relative contribution of communications the overall simulation time diminishes.

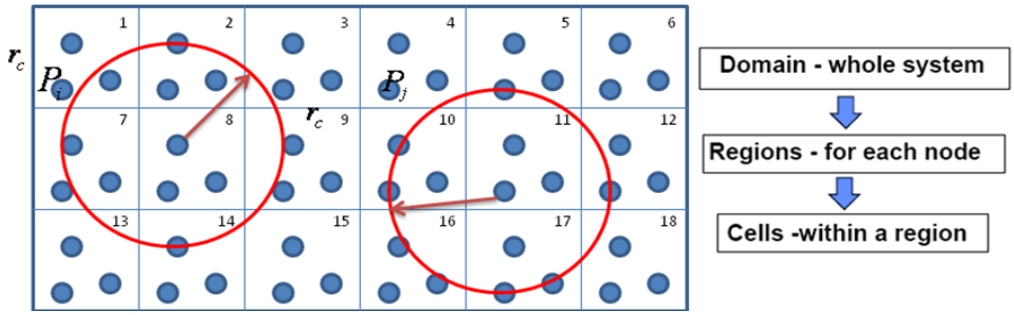

Figure 2-8 The division of the 2-D periodic simulation box (domain) into regions and cells among 18 processors in a spatial-decomposition algorithm. With this force cutoff distance r_c (arrow), processor P_i or P_j only need communicate with the 9 nearest-neighbor processors.

The domain decomposition algorithm is outlined in Figure 2-9. It assumes z represent the ID of any processor, processor z owns the box labeled D_z and will update the positions X_z of the atoms in its box. To compute forces on its atoms a processor will need to know not only X_z but also positions Y_z of atoms owned by processors whose boxes are within a cutoff distance r_c of its box. As it computes the forces f_z on its atoms, it will also compute components of forces g_z on the nearby atoms.

(1) **Compute** non-bonded forces in D_z, summing results into f_z and g_z	$\frac{N}{P}$
(2) **Compute** bonded forces in D_z, summing results in f_z and g_z	$\frac{N}{P}$
(3) **Share** g_z with neighboring processors, summing received forces into my f_z	Δ
(4) **Update** atom positions in x_z using f_z	$\frac{N}{P}$
(5) **Share** x_z with neighboring processors, using received positions to update y_z	Δ
(6) Move atoms to new processors as necessary	Δ

Figure 2-9 Single timestep of the spatial-decomposition algorithm for processor Pz

We assume that current X_z and Y_z positions are known by each processor at the beginning of the timestep. With these definitions, steps (1) and (2) of the algorithm are the computations of non-bonded and bonded forces for interactions involving the processor's atoms. These steps scale as the number of atoms N/P in each processor's box. In step (3) the g_z forces computed on neighboring atoms are communicated to processors owning neighboring boxes. The received forces are summed with the previously computed f_z to create the total force on a processor's atoms. The scaling of this step depends on the length of the force cutoff relative to the box size. We list it as Δ and discuss it further below. Step (4) updates the positions of the processor's atoms. In step (5) these positions are communicated to processors owning neighboring boxes so that all processors can update their y_z list of nearby atoms. Finally in step (6), periodically (usually when neighbor lists are created), atoms which have left a processor's box must be moved to the appropriate new processor.

The computational scaling of steps (1), (2) and (4) is the optimal N/P. The scaling of the communication steps (3), (5), and (6) is more complex. In the limit of large N/P ratios, Δ scales as the surface-to-volume ratio $(N/P)^{2/3}$ of each processor's box. If each processor's box is roughly equal in size to the force cutoff distance, then Δ scales as N/P and each processor receives N/P atom positions from each of its neighboring 8 processors (in 2D), as in Figure 2-8.

In practice, however, there can be several obstacles to minimizing Δ and achieving high parallel efficiencies for a domain decomposition method in MD simulations of molecular systems. There are some inefficiencies of domain decomposition method. They are listed as follows:

(A) Molecular systems are often simulated in a vacuum or with surrounding solvent that does not uniformly fill a 3D box. In this case it is non-trivial to divide the simulation domain so that every processor's box has an equal number of atoms in it and yet keep the inter-processor communication simple. Otherwise, the load-imbalance is the result.

(B) Because of the 1/r dependence of Coulombic energies, long cutoffs are often used in simulations of organic materials. Thus a processor's box may be much smaller than the

cutoff. The result is considerable extra communication in steps (3) and (5) to acquire needed atom positions and forces, i.e. Δ no longer scales as N/P, but as the cube of the cutoff distance, r_c.

(C) As atoms move to new processors in step (6), molecular connectivity information must be exchanged and updated between processors. The extra coding to manipulate the appropriate data structures and optimize the communication performance of the data exchange subtracts from the parallel efficiency of the algorithm.

In general, domain decomposition methods are more difficult to integrate into large, existing codes than are replicated-data or even force decomposition methods. This fact, coupled with the potential for other parallel inefficiencies just outlined (A-C), has made domain decomposition implementations less common than replicated-data for macromolecular MD codes. However, in terms of their optimal communication scaling they are clearly the method of choice for very large simulations. Additionally, for MD codes that include long-range force interactions via multipole methods, domain decomposition methods are a natural choice for performing the near field pairwise computations.

We distinguish between two types of atoms, those within a processor's box that are 'owned' by the processor, and those atoms that are nearby which are owned by 'other' processors. For other atoms, only a minimal set of information necessary to compute force interactions with those atoms is stored - position, charge, atom type, and global tag (a number from 1 to N). By contrast, for owned atoms, all of the molecular connectivity information is also stored in addition to the usual positions, velocities, global tag, etc. This data is initialized when the molecular topology is input at the beginning of the simulation. Each bond, angle, and dihedral interaction is permanently assigned to one of the 2, 3, or 4 atoms involved. The processor owning that atom stores the global tags of all atoms in the bonded interaction as well as a pointer to the set of numerical coefficients needed to compute the interaction.

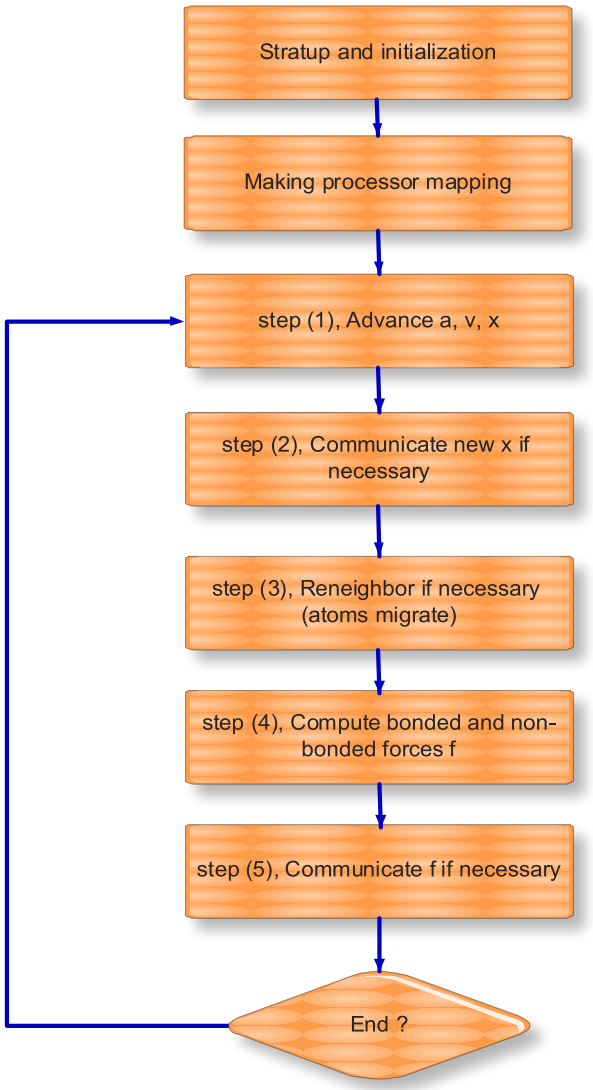

Figure 2-10 Flow chart illustrate the sequence of steps required in the domain decomposition algorithm for the evaluation of the forces

In general, a parallel sequence of steps required in the domain decomposition algorithm for the evaluation of interatomic forces is shown in Figure 2-10. After a simulation is started, LAMMPS will automatically partition the domain and mapping each box domain to a specific processor.

The simulation will start from step (1). Velocities are advanced half a timestep and used in the half step to advance the positions a full timestep. Each processor performs these operations only on its owned atoms. To compute bonded and non-bonded forces on its atoms, each processor will need to know the current positions of other atoms in

neighboring boxes. These positions are communicated in step (2) which can be done rapidly by 6 swaps with neighboring processors on a 3D stencil. Neighbor lists are used to efficiently compute the non-bond forces. As atoms move, these lists must be reformed every few timesteps in step (3) using both owned and other atoms. Reneighboring atoms is necessary because of atoms migration. At the same time atoms that have entered/exited a processor's box are moved to the new owning processor. When this occurs, all of the owned atom information including molecular connectivity must migrate with the atom. Now in step (4) all the forces of equation can be computed. If Newton's third law is used to only compute a force interaction once when 2 (or more) atoms reside in different boxes, then processors will have accumulated partial forces on other atoms at the end of step. These forces are communicated in step (5), an operation similar to step (2). Finally velocities of owned atoms are advanced and the simulation goes to the next loop. Consequently, the final half step in step (1) uses the new forces to calculate the acceleration of each atom.

Chapter 3
Atomistic Elasticity Theory: Linking Atoms and Continuum

This chapter is dedicated to provide a link between the atomistic models and continuum theoretical concepts of stress and strain. I review the basic thermo-dynamical concepts that enable a rigorous link between atomistic systems and corresponding continuum theoretical concepts. The discussion includes a review of entropic and energetic contributions to elasticity, free energy models.

During each of the molecular dynamics simulation in this dissertation, before finite temperature, dynamical calculations are performed, we carry out an energy minimization for several thousand steps, making sure that convergence is achieved, thus relieving any potential overlap in vdW. In the second step, we anneal the molecule after heating it up to a temperature, e.g. $T = 298K$. The heat up rate is $\Delta T = 25K$ every 1000 timesteps, and we keep the temperature fixed after the final temperature, e.g. $T = 298K$, is achieved (then we apply a temperature control in a NVT ensemble). We also ensure that the energy remains constant after the annealing procedure.

Depending on the details of the loading case, we then apply mechanical forces using various types of constraint and investigate the response of the molecule due to the applied loading. Typically, we obtain force, position, and velocity data of each atom, which is then used to extract mechanical quantities such as stress and strain. Steered MD is used, which based on the concept of adding restraint force to groups of atoms by extending the Hamiltonian by an additional restraint potential.

3.1 Thermodynamics as Bridge between Atomistic and Continuum Viewpoints

The link between atomistic models and concept of elasticity used in continuum mechanical theories can be most directly established by considering concepts of thermodynamics: by calculating how the free energy of a system changes due to deformation, one can calculate the stress state. Thermodynamics provides this link since both a statistical mechanics approach and continuum theory can be related to thermodynamical concepts. In this sense, thermodynamics is the glue between atomistic methods and continuum theories, linking microscopic states with a macroscale system.

This concept can be used to link atomic interactions with concepts of stress and strain. Such handshaking concepts also lay the foundation for some multiscale simulation techniques, as they allow transcend throughout distinct scales. However, it is emphasized that during the transition from microscale to macroscale, some information may lose: the atomistic scale provides a deterministic description of the atomistic state, but the averaged continuum description does not. Some of the most fundamental concepts of thermodynamics tell us that many microscopic states refer to the same macroscopic state. This represents an important issue in the case when a transition is to be made from microscale to macroscale and vice versa. Statistical concepts can be used in the case of equilibrium phenomena (e.g., by assigning random atomic velocities due to a specific temperature, following an appropriate Boltzmann distribution), but this is a tremendously challenging task for nonequilibrium systems.

The need to advance methods that connect atomistic and continuum analysis is becoming increasingly compelling with rapid advance in computational resources. In order to compare atomistic simulations with continuum analysis level, it is necessary to use methods that allow information passing between the two levels of descriptions [41]. Of particular interest is the relationship between interatomic potentials and associated elastic properties.

3.2 Review of Atomic Scale Approaches to Continuum Properties

Statistical mechanics establishes ties between atomic scale behavior and thermodynamic properties observed at continuum scales. Based on the notion of ensembles, rigorous paths are defined mathematically connecting collective atomic behavior to thermodynamic equilibrium. An underlying notion behind equilibrium MD is that one establishes a well described ensemble and allows the finite collection of atoms to sample accessible microstates. With sufficient sampling, thermodynamic averages can be obtained with good accuracy (statistical mechanics also proves equivalence between ensemble descriptions in the thermodynamic limit).

Though based on the same underlying physics, continuum theory does not address discrete atomic behavior and so a lot of research has been applied to understanding connections between continuum thermomechanical quantities and the corresponding atomic quantities that, manifest as an ensemble, define macroscale equilibrium. The challenge is to establish quantities calculable in an atomic ensemble that accurately map to the corresponding continuum quantity.

As stated above, a key issue of multiscale mechanical modeling is the development of definitions for continuum variables that are calculable within an atomic system. Connections between continuum variables and microscopic quantities originate from long-time, equilibrium ensemble averages giving rise to macroscopic balance equations. The instantaneous atomic contributions to these averages do not have the same physical interpretation as the corresponding 'point-wise' continuum quantities. However, if we use the limit theorem, the instantaneous atomic contributions to these averages can be extended to a limited domain average. A classic example is the Cauchy stress, or true stress and the ensemble stress defined by the virial theorem (VT). Because the expression developed is a time and spatial averaged quantity, the virial stress expression has become an invaluable computational diagnostic tool for evaluating simulations of materials science phenomena such as void formation during thin film growth [42], internal stress fields due to inhomogeneous precipitates [43] and finite deformation leading to atomicscale plasticity [44].

There have been several efforts to modify the VT by developing definitions for stress that satisfy the equation for balance of linear momentum for a dynamic continuum. Irving and Kirkwood [45] were the earliest to use expressions for mass, momentum and energy densities that are defined for a spatial point at an instant of time based on the statistical distribution of particles nearer to the point chosen. Their resulting formula for stress contains several expressions that require integration over phase space of quantities weighted by a probability distribution function. One of these quantities is an infinite series expansion of differential operators. While their pioneering effort is indeed note worthy, the end product is difficult to implement within a standard particle simulation. Schofield and Henderson [46] also noted that the expression developed by Irving and Kirkwood is non-unique due to an ensemble average being considered in regions of inhomogeneity.

A different approach to deriving a local stress tensor was taken by Tsai [9], who used considerations of forces acting across, and motion through, a spatial boundary to develop an expression for stress within a one-dimensional atomic chain. Cheung and Yip [47] later revisited this approach to calculate the normal stress on each atomic plane for a relaxed crystal with planar free surfaces. They showed that the local virial stress expression produces a physical oscillation in normal stress for the atomic plane at the free surface and the nearest adjacent planes while their modification of Tsai's expression correctly yields zero normal stress. This approach has also been used to examine interplanar stress across strained interfaces [48]. Therefore, this approach certainly appeals to the mechanical intuition for a definition of stress.

3.3 Physical Foundations of Atomistic Mechanical Elasticity

Elasticity stems from the change of the free energy due to the collective interactions of atom and their bonds under deformation, and thus it is intimately linked to the chemistry that defines the atomic interaction energies. Depending on what material is considered, these chemical interactions are more or less complex. In metals, for example, bonding is primarily non-directional, and can be characterized by positive ions embedded in a gas of electrons. Other materials show much greater chemical complexity - often

featuring many different chemical bonds with varying strength. In amorphous bitumen materials, it is vital to consider various types of chemical interactions, including:

- Ionic interactions (electro-static columbic interactions),
- Covalent bonds (due to overlap of electron orbitals),
- Hydrogen-bonds, and
- Weak or dispersive van der Waals (vdW) interactions.

In general, the elastic properties of materials can be expressed as the partial derivative of the free energy density with respect to the strain tensor that characterizes the deformation. Based on the free energy

$$G = U - TS \tag{3-1}$$

where G, U, T, and S represent free energy, internal energy, absolute temperature, and entropy, respectively.

We can define the free energy density (V denotes the volume) by,

$$\Psi = \frac{G}{V} \tag{3-2}$$

the stress is then given by

$$\sigma_{ij} = \frac{\partial^2 \Psi}{\partial \varepsilon_{ij}} \tag{3-3}$$

and

$$C_{ijkl} = \frac{\partial^2 \Psi}{\partial \varepsilon_{ij} \partial \varepsilon_{kl}} \tag{3-4}$$

Equation (3-3) is written as a tensor equation, considering all 21 independent elastic coefficients C_{ijkl} and all independent entries in the stress and strain tensor. Note that stress and strain are related by Hooke's law, $\boldsymbol{\sigma} = \mathbf{C}\boldsymbol{\varepsilon}$.

This finding is quite significant: if one can calculate the free energy density of an atomistic system for various deformation states, then one can estimate the stress as well as Young's modulus. Provided that an accurate model for the atomic interactions is used, this provides a theoretical strategy to predict the elastic properties of materials.

These equations inform us that the change of the energy of a system controls the elastic properties, and thus the elastic properties are strongly influenced by the actual contributions to the free energy, G. For instance, the free energy density of crystalline material temperatures is primarily controlled by energetic changes of the internal energy. Therefore in many crystalline materials the entropic term can be neglected, so that equation (3-3) and (3-4) can be directly substituted by U/V, the internal energy, and therefore

$$\Psi \approx \frac{U}{V} \tag{3-5}$$

In natural and biological materials, the free energy density is dominated by entropic contributions. In polymers, entropic contributions can dominate the elasticity, in particular for small deformation, and therefore Ψ can be substituted by $-TS/V$, so that

$$\Psi \approx -\frac{TS}{V} \tag{3-6}$$

The dominance of entropic behavior is a well-known and well-studied phenomenon in many polymers.

3.3.1 Energetic Elasticity Theory

Usually, researchers use energetic elasticity theory to link molecular or atomistic properties with overall elastic modulus. Energetic elasticity is characterized by the stretching of atomic bonds, metallic, covalent or ionic bonds, that lead to a change in potential energy in the material volume. Many techniques have been proposed to link micro-structural deformation with macroscopic concepts of elasticity.

A prominent example is the Cauchy-Born (CB) rule, which relates microscopic deformation fields with macroscopic stresses and strains [49]. The CB rule or different implementations is the basis for several multi-scale modeling algorithms, including the quasi-continuum method [50] or the virtual internal bond method [51]. A limitation of these methods is that they are largely limited to zero temperature studies, and that the technique is only applicable far from defects or large stress and strain gradients.

Recently, the CB rule has been extended to capture entropic effects as well, thus

overcoming some of the limitations of the classical CB rule, and making such multi-scale techniques applicable to finite temperature studies [52].

3.3.2 Cauchy Stress in Atomic Scale

The challenge of defining an atomistic-based stress measure is how to relate the continuum stress with atomistic stress. The virial stress needs to be averaged over space and time to converge to the Cauchy stress tensor. While continuum properties are valid at any random material point, this is not true for atomistic quantities due to the discrete nature of atomic microstructure. As most atomistic quantities, the stress tensor coefficients must be averaged in space and time in order to be compared with continuum concepts. Thus, the virial needs to be averaged over space and time to converge to the Cauchy stress tensor.

The virial theorem (VT) permits determination of the stress field applied to the surface of a fixed volume V containing interacting particles. Extension of VT to MD simulations provides the instantaneous ensemble stress.

The average stress of the specific region in the atomistic simulation, σ_{ij}, on the j plane and in the i direction is calculated by virial formula [53]

$$\sigma_{ij} = -\frac{1}{N}\sum_{i=1}^{N_s}\left(\frac{m_i v_i \otimes v_i}{V_i} + \frac{1}{2V_i}\sum_{j=1}^{N_s} r_{ij} \otimes F_{ij}\right) \tag{3-7}$$

where m_i is the mass of the atom i, V_i denotes the volume assigned to atom i, N_s denotes the number of particles contained in the region of atomic interaction, r_{ij} denotes the vector from atom j to atom i, F_{ij} is the force acting on atom i due to interaction with atom j. The first term of the right-hand side of equation (3-7) represents the kinetic effect associated with atomic motion, and is related to temperature. The second term represents the effect of atomic interaction, and it is related to the interatomic forces and the separation between the atoms.

Note that the finite timestep equilibrium simulations demonstrate fluctuations in system properties about the equilibrium average. For an infinite system, the macroscale thermodynamic quantities equal the system averages at every instant in time, by

definition. However, for finite size systems, e.g. MD ensembles, the definitions for temperature and stress above must typically be averaged over some of a simulation time (e.g. some duration of ensemble trajectory) in order to obtain a good description of the system equilibrium average. With time averaging over the right hand side of equation (3-7), the VT expression for stress is obtained.

3.3.3 Virial Strain

The strain field is a measure of geometric deformation of the atomic lattice. The local atomic strain is calculated by comparing the local atomic strain which is calculated by comparing the local deviation of the lattice from a reference configuration [54]. Usually, the reference configuration is taken to be the un-deformed lattice. In the atomistic simulations, the information about the position of every atom is readily available. The virial strain is relatively straightforward.

We define the following tensor for atom l

$$q_{ij}^{l} = \frac{1}{N}\sum_{k=1}^{N}\left(\frac{\Delta x_i^{kl}\Delta x_j^{kl}}{r_0^2}\right) \tag{3-8}$$

where $\Delta x_i^{kl} = x_i^l - x_i^k$ and $\Delta x_j^{kl} = x_j^l - x_j^k$; i and j refer to 1,2,3. The quantity N refers to the number of nearest neighbors considered. Here k denotes the ID of atoms included in the neighbor list; r_0 denotes the distance between atoms k and l on the un-deformed lattice from a reference configuration. The left Cauchy-Green strain tensor is given by

$$b_{ij}^{l} = \frac{N}{\lambda}q_{ij}^{l} = \frac{1}{N}\sum_{k=1}^{N}\left(\frac{\Delta x_i^{kl}\Delta x_j^{kl}}{r_0^2}\right) \tag{3-9}$$

where λ is a pre-factor depending on the lattice considered. For a two-dimensional triangular lattice with nearest neighbor interaction, $\lambda = 3$ and $\lambda = 2$ denote for a square lattice with nearest neighbor interaction and $\lambda = 4/3$ denotes for a face-centered cubic lattice.

This definition provides an expression for a measure of deformation defined using continuum mechanics and in terms of atomic positions. The Eulerian strain tensor of

atom l is obtained from equation, $e_{ij}^{l} = \frac{1}{2}\left(\delta_{ij} - b_{ij}^{l}\right)$. One can calculate the engineering strain $\boldsymbol{\varepsilon = \sqrt{b} - 1}$. The atomic strain is valid instantaneously in space and time.

3.4 Formula for Mechanical Properties

3.4.1 Local Mechanical Properties

The local mechanical properties can be determined by dividing the simulation cell into smaller cubes of length l [55]. In order to find the local elastic constants, a local stress must be defined. By performing a microscopic momentum balance flux balance on a cube m, the following expression for the local stress tensor can be derived:

$$\sigma_{ij}^{m} = \rho^{m} k_B T \delta_{ij} - \frac{1}{l^3} \sum_{a<b} \left(\frac{\partial U}{\partial r^{ab}} \right) \frac{r_i^{ab} r_j^{ab}}{r^{ab}} \frac{q^{ab}}{r^{ab}} \tag{3-10}$$

where ρ^{m} is the number density of cube m, k_B is Boltzmann's constant, T is the temperature of the system, and δ_{ij} is the Kronecker delta. Subscripts denote Cartesian coordinates; U is the pairwise additive potential energy function and r^{ab} is the distance between two interaction sites a and b. If the vector joining a and b, r_i^{ab}, passes through cube m the fraction of the line segment that lies inside the cube defines the variable q^{ab}. If the vector does not pass through the cube, then $q^{ab} = 0$. Integration of σ_{ij}^{m} over the entire volume gives the internal stress tensor of the bulk system.

The local elastic modulus tensor, C_{ijkl}^{m}, is related to the internal stress fluctuations through the second derivative of the free energy with respect to the strain [55],

$$C_{ijkl}^{m} = C_{ijkl}^{Bm} - C_{ijkl}^{Sm} + C_{ijkl}^{Km} \tag{3-11}$$

Where

$$C_{ijkl}^{Bm} = \frac{1}{l^3} \left\langle \sum_{\alpha<\beta} \left(\frac{\partial U}{\partial r^{ab^2}} - \frac{1}{r^{ab}} \frac{\partial U}{\partial r^{ab}} \right) \frac{r_i^{ab} r_j^{ab} r_k^{ab} r_l^{ab}}{\left(r^{ab}\right)^2} \frac{q^{ab}}{r^{ab}} \right\rangle \tag{3-12}$$

$$C_{ijkl}^{Sm} = \frac{V}{k_B T}\left[\left\langle \sigma_{ij}^{m}\sigma_{kl}\right\rangle - \left\langle \sigma_{ij}^{m}\right\rangle\left\langle \sigma_{kl}\right\rangle\right] \tag{3-13}$$

$$C_{ijkl}^{Km} = 2\left\langle \rho^{m}\right\rangle k_B T\left(\delta_{il}\delta_{jk} + \delta_{ik}\delta_{jl}\right) \tag{3-14}$$

and where V is the volume of the system. The brackets denote a canonical ensemble average; C_{ijkl}^{Bm} represents the instantaneous elastic modulus for any given configuration under a uniform, infinitesimally small strain (the so-called Born term). The contributions of internal particle motions (caused by the thermal fluctuations) to the elastic modulus are accounted by the stress-fluctuation term, C_{ijkl}^{Sm}. The contribution of the kinetic energy to the modulus is denoted by C_{ijkl}^{Km}.

3.4.2 Crystalline Elastic Constants

Two classes of methods calculating elastic constants were available in the published articles. Consistently, static method based molecular mechanics was found more favorable than the dynamic one based molecular dynamics. In this research, a constant-strain minimization method (static method) was applied to the equilibrated system. After an initial energy minimization, a very small strain (remain within elastic limits, ±0.001) was applied to the system and another energy minimization was started. Stiffness matrix was calculated from the second derivative of potential energy U with respect to strain ε as follows:

$$C_{ij} = \frac{1}{V}\frac{\partial^2 U}{\partial\varepsilon_i\partial\varepsilon_j} = \partial\sigma_i / \partial\sigma_j = \left(\sigma_+ - \sigma_-\right)/2\varepsilon_j \tag{3-15}$$

where s calculated from the first derivative of potential energy per unit volume with respect to strain was stress component under tension for ‘‘+’’ or compression for ‘‘−’’. Lame constants λ, μ for the structure can in turn be calculated from the stiffness matrix related to

$$\begin{aligned}\lambda &= \frac{1}{3}\left(C_{11} + C_{22} + C_{33}\right) - \frac{2}{3}\left(C_{44} + C_{55} + C_{66}\right)\\ \mu &= \frac{1}{3}\left(C_{44} + C_{55} + C_{66}\right)\end{aligned} \tag{3-16}$$

Once the two Lame constants have been obtained, several related mechanical properties can be derived from them:

$$E = \mu\frac{3\lambda + 2\mu}{\lambda + \mu} \qquad G = \mu$$
$$B = \lambda + \frac{2}{3}\mu \qquad \nu = \frac{\lambda}{2(\lambda + \mu)} \tag{3-17}$$

where E, G, B and ν n represent Young's modulus, shear modulus, bulk modulus and Poisson's ratio, respectively. An intensive description of the method can be referred to the original articles written by Theodorou and Suter [42].

For a periodic simulation cell characterized in some reference state by the three column vectors $\mathbf{a}^0$, $\mathbf{b}^0$, $\mathbf{c}^0$, and by the vectors **a**, **b**, **c** in the deformed state, the strain tensor is given by:

$$\boldsymbol{\varepsilon} = \frac{1}{2}\left[\left(\mathbf{h}_0^T\right)^{-1} G\mathbf{h}_0^{-1} - 1\right] \tag{3-18}$$

where $\mathbf{h}_0$ denotes the matrix formed from the three column vectors $\mathbf{a}^0$, $\mathbf{b}^0$, $\mathbf{c}^0$, **h** denotes the corresponding matrix formed from **a**, **b**, **c**, *T* denotes the matrix transpose, and **G** denotes the metric tensor $\mathbf{h}^T\mathbf{h}$.

Generally, the overall mechanical properties of materials comprising different domains cannot be estimated without detailed knowledge of the morphology of the material. For minerals, this is usually done by either assuming some simplifying distribution of features or applying a theoretical solution, or numerically, starting from a configuration known in detail. Atomistic simulations are not similar to calculations on crystals: observed on a macroscopic level, most materials are homogeneous, but if observation focuses on ever smaller lengthscales, they become heterogeneous at some point. Even for amorphous polymers are heterogeneous, if only on a scale of few nanometers. This heterogeneity controls itself in simulation when different realizations of an amorphous cell are employed to simulate properties. The simulated values differ from cell to cell, sometimes substantially, and a single cell usually is not perfectly isotropic in its characteristics. In the following, we will show how to do get elastic constants with sets of values obtained by simulation.

We represent the isothermal elastic constants, statistical-mechanical defined as the

elements of the fourth-rank tensor of second derivatives of Helmholtz free energy A (per unit volume) with the tensor components of strain ε (or, employing the statistical-mechanical definition of strain, by the strain dependence of the material stress tensor σ [49])

$$C_{ijkl} = \frac{1}{\langle V \rangle} \frac{\partial^2 A}{\partial \varepsilon_{ij} \partial \varepsilon_{kl}}\bigg|_{T,[\varepsilon_{ij}][\varepsilon_{kl}]} = \frac{\partial \sigma_{ij}}{\partial \varepsilon_{kl}}\bigg|_{T,[\varepsilon_{kl}]} \qquad (3\text{-}19)$$
$$\{i,j,k,l\}^4 \in \{1,2,3\}^4$$

In the contracted matrix form, by

$$\boldsymbol{\varepsilon} = \left[\varepsilon_{11}\ \varepsilon_{22}\ \varepsilon_{33}\ 2\varepsilon_{23}\ 2\varepsilon_{13}\ 2\varepsilon_{12}\right]^T \qquad (3\text{-}20)$$

$$\mathbf{s} = \left[\sigma_{11}\ \sigma_{22}\ \sigma_{33}\ \sigma_{23}\ \sigma_{13}\ \sigma_{12}\right]^T \qquad (3\text{-}21)$$

$$\mathbf{C} = \begin{bmatrix} C_{1111} & C_{1122} & C_{1133} & C_{1123} & C_{1113} & C_{1112} \\ C_{1122} & C_{2222} & C_{2233} & C_{2223} & C_{2213} & C_{2212} \\ C_{1133} & C_{2233} & C_{3333} & C_{3323} & C_{3313} & C_{3312} \\ C_{1123} & C_{2223} & C_{3323} & C_{2323} & C_{2313} & C_{2312} \\ C_{1113} & C_{2213} & C_{3313} & C_{2313} & C_{1313} & C_{1312} \\ C_{1112} & C_{2212} & C_{3312} & C_{2312} & C_{1312} & C_{1212} \end{bmatrix} \qquad (3\text{-}22)$$

Where $\boldsymbol{\varepsilon}$ is the 'strain matrix', $\boldsymbol{\sigma}$ is the 'stress matrix', and $\mathbf{C}$ is the 'stiffness matrix'. The inverse $\mathbf{S} = \mathbf{C}^{-1}$ is the 'compliance matrix' and $\boldsymbol{\sigma} = \mathbf{C}\boldsymbol{\varepsilon}$, $\boldsymbol{\varepsilon} = \mathbf{S}\boldsymbol{\sigma}$. The strain tensor ε_{ij} is symmetric by construction and the reduction to $\boldsymbol{\varepsilon}$ does not involve a loss of information; the stress tensor σ_{ij} is only symmetric in mechanical equilibrium and contracted matrix representation $\boldsymbol{\sigma}$ only fully represents the stress tensor if mechanical equilibrium is established. This can happen in a static situation (e.g. for an energy-minimized single structure), or when the investigated material executes symmetric fluctuations around a mechanically equilibrated average configuration (e.g. when sufficiently many structures are considered that represent fluctuations). Due to the symmetry of ε_{ij} and σ_{ij} (in the mechanically equilibrated case), the tensor of elastic constants C_{ijkl} is pair-wise symmetric in i,j and k,l and there are at most 21 independent tensor elements --- typically these are identified with the 21 independent

elements of the stiffness (or compliance) matrix. The elastic deformation energy is $\frac{1}{2}\boldsymbol{\varepsilon}^T\boldsymbol{\sigma} = \frac{1}{2}\boldsymbol{\sigma}^T\boldsymbol{\varepsilon} = \frac{1}{2}\boldsymbol{\varepsilon}^T\mathbf{C}\boldsymbol{\varepsilon} = \frac{1}{2}\boldsymbol{\sigma}^T\mathbf{S}\boldsymbol{\sigma}$ (where the superscript 'T' denotes the transpose, i.e. 1×6 matrices), and, since this energy must be positive, the stiffness matrix as well as the compliance matrix are positive definite.

The elements of **C** and **S** are addressed with their matrix subscripts, e.g. C_{2213}. The traditional modulus, i.e. the elastic modulus E_i, the shear modulus G_i, and Poisson's ratios ν_{ij} are defined as follow:

$$E_i = \frac{1}{S_{ii}}, \quad G_i = \frac{1}{S_{kk}}, \quad \nu_{ij} = \frac{S_{ij}}{S_{jj}} \qquad \{i, j\} \in \{1,2,3\}, \quad k = i+3 \tag{3-23}$$

E_i is the Young's modulus along axis i

G_{ij} is the shear modulus in direction j on the plane whose normal is in direction i

ν_{ij} is the Poisson's ratio that corresponds to a contraction in direction j when an extension is applied in direction i.

For estimating the composite elastic constants of a material composed of domains with different elastic properties, we follow [56] and [57] who treat elastic deformations of materials consisting of agglomerates of homogeneous solid domains firmly bonded together, i.e. 'composites', in unbounded phases. Each domain has its own set of elastic constants and the volume of interest is 'representative', i.e. sufficiently large that the heterogeneities of structure are averaged and volume appears 'macroscopically uniform'. The approach chosen is one typical for 'homogenization theories' [58-59].

3.4.3 Elastic Modulus Calculation Approaches

To date, reported attempts to estimate the elastic modulus has adopted one of three approaches. The first approach, originating in the work of Theodorou and Suter [60], uses a static method. Briefly, the author performed a detailed theoretical study of the various factors contributing to the elastic constants, as formally defined by equation (3-19). They concluded that contributions originating from changes in configurational entropy on deformation, and from the strain dependence of the vibrational frequencies

ought to be negligible for glassy polypropylene. In consequence, it should be possible to estimate the elastic stiffness coefficients from numerical estimates of

$$\frac{d^2U}{d\varepsilon_i d\varepsilon_j} (= \frac{d\sigma_i}{d\varepsilon_j}) \tag{3-24}$$

Thus, having constructed an energy-minimized series of atomistic structures confined to a periodic cube, each structure is subjected to twelve deformations; three pairs in uniaxial tension/compression and three pairs involving pure shear, followed by a reminimization to restore a state of detailed mechanical equilibrium.

Each of these deformations corresponds to setting one of the components of the strain vector equation (3-20) to some small value (for example ε = 0.001), while keeping all other components fixed at zero. The elastic stiffness coefficients can then be obtained by estimating the second derivatives of the deformation energy with respect to strain using a finite difference formula (for the diagonal components only), and by calculating $\Delta\sigma_i / \Delta\varepsilon_j$ for each of the six pairs of applied strains, where $\Delta\sigma_i$ represents, in vector notation. Another method is to calculate the elements of the stress tensor by analytically using the virial theory. Although both of these methods gave good agreement for the diagonal elements C_{ii} of the stiffness matrix for the glassy polypropylene samples studied in the [60] original work, generally it should be assumed that numerical estimation of second derivatives (of the energy) will be less precise than estimation of the first derivatives (of the stress). Therefore, the latter method is preferred.

A second approach for obtaining elastic modulus involves using constant stress molecular dynamics to measure the stress-strain behavior of a material subjected to an applied load. This approach has been used to investigate the stress-strain behavior and estimate the modulus of samples of amorphous polyethylene modeled using a united-atom approach. Brown and Clarke [61] modified the constant stress dynamics method [62] to ensure the matrix **h** made up from the cell vectors **a**, **b**, **c** remains symmetric during the simulation. The simulation consisted of increasing the magnitude of an applied tensile stress at a constant rate of either 1 MPa/ps or 5 MPa/ps. The resulting longitudinal and average lateral strain were then monitored during the simulation and used to estimate the Young's modulus, Poisson's ratio and yielding behavior of the material at various

temperatures. It should also be noted that the Berendsen thermostat approach, which does not correspond to any of the ensembles encountered in statistical thermodynamics, was chosen in preference to the theoretically more rigorous approach [63] which generates the constant stress ensemble. Because it is relatively free from unphysical oscillatory fluctuations of the cell. These arise because the difference between internal stress and applied stress is coupled to the first derivative of the cell vectors with respect to time rather than to the second derivative.

One potential advantage of the dynamics approach over the static method described above is that the entropic effects ignored by the latter are implicitly included. Moreover, the dynamics approach in principle allows study of yielding, albeit under conditions of extremely rapid rate of application of stress. However, using molecular dynamics has a number of significant disadvantages. Firstly, it typically requires long duration simulations. Secondly, the strain fluctuates with time even when the system is subjected to a non time-dependent stress. Consequently, there are uncertainties in its measurement. These are further amplified in a dynamical experiment in which the stress is increased at a constant rate. We might attempt to eliminate this artifact by increasing the stress stepwise, waiting until the strain equilibrates before incrementing the stress. However, experimentalists will be familiar with the fact that the strain may increase on the time scale of seconds to days after application of a stress.

The third approach for obtaining stiffness coefficients, which also implicitly captures entropic effects, uses fluctuation formulas applied to simulations in different ensembles. The simplest formula, applicable when simulations have been performed in the constant stress ensemble, is as follows [63]:

$$C_{ik} = \frac{kT}{\langle V \rangle} \langle \varepsilon_i \varepsilon_j \rangle^{-1} \tag{3-25}$$

In practical applications, convergence of this expression tends to be relatively slow. As pointed out by reference [64], alternative fluctuation formulas exist for ensembles in which the shape of the simulation cell is held fixed. While these methods do show improved convergence behavior, the formulas are more difficult to apply in practice due to the presence of terms which depend on the second derivatives of the energy with respect to atomic positions.

In general, taking into consideration the general desirability of averaging property measurements for amorphous polymers over as many independent samples as possible, the static method probably offer the most desirable approaches available at the present work. Therefore, such method is employed in Chapter 4 to calculate mineral crystals' elastic constants.

3.5 MPI Distributive Computing of Interfacial Atomistic Stress

3.5.1 Introduction

Calculating the effective properties of atomistic simulation production trajectories is not a trivial procedure. Due to their large volume, random composition, and widely varying timesteps, these properties cannot be determined analytically, but instead necessitate a numerical computation. But before any computing may begin, detailed trajectory information must be saved along the simulation.

One application in this research, the regional instant stress is interpreted from the trajectories. Atomistic models built in this research can contain 2 to 3 distinct individual layers in the interface system. The nominal size of data sets is a matrix with dimension of $12\times6\times6000$ for each timestep output. Even though it appears to be a large system, we would like to increase the potential problem size and increase the simulation cell size. But the possible overall sizes of problems have been ultimately bound by the available computational resources of a serial based machine. In addition, the RAM of a PC is limited by 4GB and it makes even a medium computation impractical. So the original serial program always stops since running out memory.

Using parallel processing allows one to have the power and storage capacity of several processors. It is then possible to divide a large dataset exactly across multiple processors and, in essence, each processor operates on a dataset of reduced size. In addition, any large arrays calculated in the serial version only have their corresponding sections calculated on each processor as well. The overall functionality of the program is not compromised by operating on smaller sections, but one can gain huge memory space

and speed-up of execution time on an order of the number of processors used, so we are able to handle large problems.

Parallel processing also supports data transfer, e.g. send and receive mechanisms, between the processors. This is important for calculations involving nearest neighbors. Split the data across P processors by direct consequence of the split of the timesteps. Of course, it is necessary to know which data is needed by which processor and when in order to have a successfully operating program.

It allows the input data file to read into memory in stages (slices), therefore, the ROOT node does not need to read the entire data file in all at once. This reduces the amount of memory that ROOT needs to allocate. This is important when the initial data file is too large to fit onto one node at once.

3.5.2 Program Theory

This rest of this chapter will examine the basics behind the parallel versions by discussing their data models, memory management, and algorithms.

Briefly, these programs operate by performing a series of matrix operations (additions and multiplications) on very large arrays, dimensioned as large as the original data set or greater, in order to calculate the true stress of the interface region.

The serial case defines these trajectories as 2-D matrix and then operates or computes each step sequentially and therefore independently from each other. This is a good behavior for a program to have if the parallel adaptation is to be made. In fact, it ensures that the operations can proceed in a parallel fashion. Therefore, it is necessary to give each processor a stage of the original data matrix and most of the calculations can proceed independently until special cases of communication are needed. It is important to reduce the amount of time one spends communicating to gain the maximum time savings from parallel computations.

So we developed a parallel algorithm to implement the nano-to-macro stress-strain properties interpretation according to theories provided in the equations (3-7), (3-9) and (3-10).

3.5.3 Non-Parallel I/O for a MPI Program

MPI-1 library does not have any explicit support for parallel I/O. Therefore, MPI applications developed over the past few years have had to do their I/O by relying on the features provided by the underlying operating system, typically Linux/Unix. The most straightforward way of doing this is just to have one process do all I/O. In this section by illustrating this technique, I/O of our program is diagrammed in Figure 3-1.

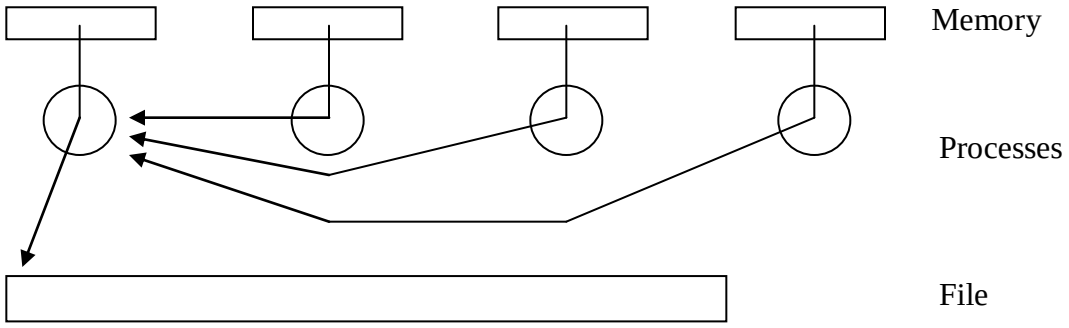

Figure 3-1 Sequential I/O from a parallel program

The program begins with each process initializing its portion of the array. After finish the computation of each stage, all processes but process 0 send their section back to process 0. Process 0 first writes its own section and then receives the contributions from the other processes in turn (the rank is specified in MPI_Recv) and writes them to the file.

This is often the first way that I/O is done in a parallel program that has been converted from a sequential program, since no changes are made to the I/O part of the program. There are a number of other reasons why I/O in a parallel program may be done this way.

- The parallel machine on which the program is running may support I/O only from one process.
- One can use sophisticated I/O libraries, perhaps written as part of a high-level data-management layer, that do not have parallel I/O capability.
- The resulting single file is convenient for handling outside the program.

3.5.4 Distributive Algorithm Implementation

Below is a description of the structure of the parallel implementation for the

postprocess algorithm for a distributed memory multi-processor.

Step 1: Initialization of Slave Processes

The master process initiates all of the required slave processes. The slaves then compute their interaction and inverse interaction lists. Each slave then process pre-computes constant matrix used, and allocates memory to hold the atom and cell data structures.

Step 2: Domain Distribution

The master process sends the atom position, velocity, and force data to each of the slave processes. Each slave receives data for only the particles in the cells owned by that slave. Each slave process sends atom data to the other slave processes that require the data for their direct calculations. The contents of the messages are determined from the inverse interaction lists sent to each slave.

Step 3: Calculate the effective radius

For each cell at the lowest tree level, the slave process computes the effective radius of each atom due to all atoms within that box. No communication or synchronization is necessary as each process relies only on data already assigned to that specific slave.

Step 4: Calculate the virial stress

Starting at the lowest tree level, the slave process computes the virial stress of each atom due to all atoms within that box, and then calculates the interface area true stress. Thereafter, true stress of each step owned by the slave process is accumulated and saved in a matrix.

Step 5: Message Passing

Each slave process passes the true stress information of each step to master process.

Step 6: Collect Results

After each slave process sends the true stress information to the master process, the master process receives this information, which concludes the processing.

The key to performance of the parallel algorithm is the interleaving of message passing and computation. By performing as much computation as possible between the

time messages are sent and received, the effect of message passing latency can be well hidden.

3.5.5 Parallel Multiscale Stress Program Highlights

A FORTRAN molecular dynamics stress calculation code, MPI_multistress.f90, parallelized by Message Passing Interface is developed for the true stress calculation. We use the IBM XL FORTRAN Compiler for SystemX for compilation of the source code. Most simulations are carried out on SystemX nodes in the Virginia Tech Advanced Research Computing Center in Blacksburg. This supercomputer consists of 1100 nodes with 2 CPUs each in a shared memory environment, with 4 GByte RAM each.

The following lists the highlights of our distributive computing program, MPI_multistress.f90.

1. Domain decomposition method is adopted in this program for parallel computation job partitioning. An automatic partition algorithm is developed in this program to partition the computational load evenly for each slave node. This will eventually results in better parallel efficiency.
2. Object oriented programming is adopted, which can speed up further code development time and made the code easy to extend for further access.
3. Encapsulate 2 modules for global use, which is a most commonly used programming development technique.
4. Fortran95 allocatable array is used in this program, which can be applied to infinite huge data post-processing, as well as no waste of memory volume.
5. Self-defined argument type (use objected oriented programming technology) is applied in this code, which make this code easy to reference.
6. With this program architecture constructed, huge data input/output can be implemented by using this code's interface. This makes it suitable for doing MD simulation trajectory postprocess.
7. From the per-atom trajectory data, one can get collective instant mechanical properties, e.g. stress and strain of any specific region, can be obtained. In addition, the code can output scalar value e.g. temperature, pressure, volume, as well as vector value like per-atom value, in a customized manner.

8. In order to reach a higher parallel efficiency, the master node is also set to be a work node that is assigned its own computational work which has no need for message massing when collecting results.

Chapter 4
Atomistic-Modeling of Mineral Aggregate

Construction aggregate, or simply ‘aggregate’, is a broad category of coarse particulate material used in construction, including sand, gravel, crushed stone and geo-synthetic aggregates. Aggregates are a component of stone based composite materials such as concrete and asphalt concrete; the aggregate serves as reinforcement to add strength to the overall composite material. Due to the relatively high hydraulic conductivity value as compared to most soils, aggregates are widely used in drainage applications such as foundation, retaining wall drains, and road side edge drains. Aggregates are also used as base material under foundations, roads, and railroads. To put it another way, aggregates are used as a stable foundation or road/rail base with predictable, uniform properties (e.g. to help prevent differential settling under the road or building), or as a low-cost extender that binds with more expensive cement or asphalt to form concrete.

The American Society for Testing and Materials publishes an exhaustive listing of specifications for various construction aggregate products. In this list, minerals are categorized by their individual structure and are suitable for specific construction purposes. These products include specific types of coarse and fine aggregate designed for such uses as additives to asphalt and concrete mixes, as well as other construction uses. State transportation departments further refine aggregate material specifications in order to tailor aggregate use to the needs and available supply in their particular locations.

Since aggregate plays such an important role in pavement materials, this chapter is dedicated to calculate the bulk mechanical properties of several commonly used mineral aggregates by using atomistic modeling method.

4.1 Mineral Composition of Aggregate Rocks

A main determining factor in the formation of minerals in a rock is the chemical composition of the mass. For a certain mineral, it can be formed only when the necessary elements are present in the rock. Calcite is the prevalent components in limestone, as it is in consistent essentially of calcium carbonate; quartz is common in sandstones and certain igneous rocks which contain a high percentage of silica.

Other factors are of equal importance in determining the natural association of rock-forming minerals, principally the mode of the origin of the rock and the stages through which it has passed in attaining its present condition. Two rock masses may have very much the same bulk composition but consist of entirely different assembly of minerals. The tendency is always for those compounds to be formed which are stable under the conditions that the rock mass originated. A granite arises by the consolidation of a molten magma at high temperatures and great pressures and its component minerals are those stable under such conditions. Exposed to moisture, carbonic acid, and other substantial agents at the ordinary temperatures of the Earth's surface, some of these original minerals, such as quartz and white mica are relatively stable and remain unaffected; others are replaced by new combinations due to weather or decay. The feldspar passes into kaolinite and quartz, and any mafic minerals such as pyroxenes, amphiboles or biotite are also present. Later, they are often altered to chlorite, epidote, rutile and other substances. These changes are accompanied by disintegration, and the rock falls into a loose, incoherent, earthy mass which may be regarded as a sand or soil. The materials thus formed may be washed away and deposited as sandstone or siltstone. The structure of the original rock is now replaced by a new one; the mineralogical constitution is profoundly altered; but the bulk chemical composition may not be very different. The sedimentary rock may again undergo metamorphism. If penetrated by igneous rocks it may be recrystallized or, if subjected to enormous pressures with heat and movement during mountain building, it may be converted into gneiss. The gneiss is not very different in mineralogical composition though radically different in structure to the granite which was its original state.

4.2 Mineral Definition and Classification

To be classified as a true mineral, a substance must be a solid and have a crystalline structure. It must also be a naturally occurring, homogeneous substance with a defined chemical composition. Traditional definitions excluded organically derived material. However, the International Mineralogical Association in 1995 adopted a new definition: a mineral is an element or chemical compound that is normally crystalline and that has been formed as a result of geological processes.

The chemical composition may vary between end members of a mineral system. For example the plagioclase feldspars comprise a continuous series from sodium and silicon-rich albite ($NaAlSi_3O_8$) to calcium and aluminium-rich anorthite ($CaAl_2Si_2O_8$) with four recognized intermediate compositions between.

A crystal structure is the orderly geometric spatial arrangement of atoms in the internal structure of a mineral. There are 14 basic crystal lattice arrangements of atoms in three dimensions, and these are referred to as the 14 ‘Bravais lattices’. Each of these lattices can be classified into one of the seven crystal systems, and all crystal structures currently recognized fit in one Bravais lattice and one crystal system. This crystal structure is based on regular internal atomic or ionic arrangement that is often expressed in the geometric form that the crystal takes. Even when the mineral grains are too small to see or are irregularly shaped, the underlying crystal structure is always periodic and can be determined by X-ray diffraction. Chemistry and crystal structure together define a mineral. In fact, two or more minerals may have the same chemical composition, but differ in crystal structure (these are known as polymorphs). For example, pyrite and marcasite are both iron sulfide, but their arrangement of atoms differs. Similarly, some minerals have different chemical compositions but the same crystal structure: for example, halite (made from sodium and chlorine), galena (made from lead and sulfur) and periclase (made from magnesium and oxygen) all share the same cubic crystal structure.

Crystal structure greatly influences a mineral's physical properties. For example, though diamond and graphite have the same composition (both are pure carbon), graphite is very soft, while diamond is the hardest of all known minerals. This happens because

the carbon atoms in graphite are arranged into sheets which can slide easily past each other, while the carbon atoms in diamond form a strong, interlocking three-dimensional network.

There are currently more than 4,000 known minerals, according to the International Mineralogical Association, which is responsible for the approval of and naming of new mineral species found in nature. Of these, perhaps 100 can be called ‘common’, 50 are ‘occasional’, and the rest are ‘rare’ to ‘extremely rare’.

4.3 Fundamentals of Crystals

The fundamental difference between single crystal, polycrystalline, and amorphous solids is the length scale over which the atoms are related to one another by translational symmetry (periodicity or long-range order). Single crystals have infinite periodicity, polycrystals have local periodicity, and amorphous solids (and liquids) have no long-range order.

- An ideal single crystal has an atomic structure that repeats periodically across its whole volume. Even at infinite length scales, each atom is related to every other equivalent atom in the structure by translational symmetry.
- A polycrystalline solid or polycrystal is comprised of many individual grains or crystallites. Each grain can be thought of as a single crystal, within which the atomic structure has long-range order. In an isotropic polycrystalline solid, there is no relationship between neighbor grains. Therefore, on a large enough length scale, there is no periodicity across a polycrystalline sample.
- Amorphous materials, like window glass, have no long-range order at all, so they have no translational symmetry. The structure of an amorphous solid (and indeed a liquid) is not truly random. The distances between atoms in the structure are well defined and similar to those in the crystal. This is why liquids and crystals have similar densities. They both have short-range order that fixes the distances between atoms, but only crystals have long-range order.

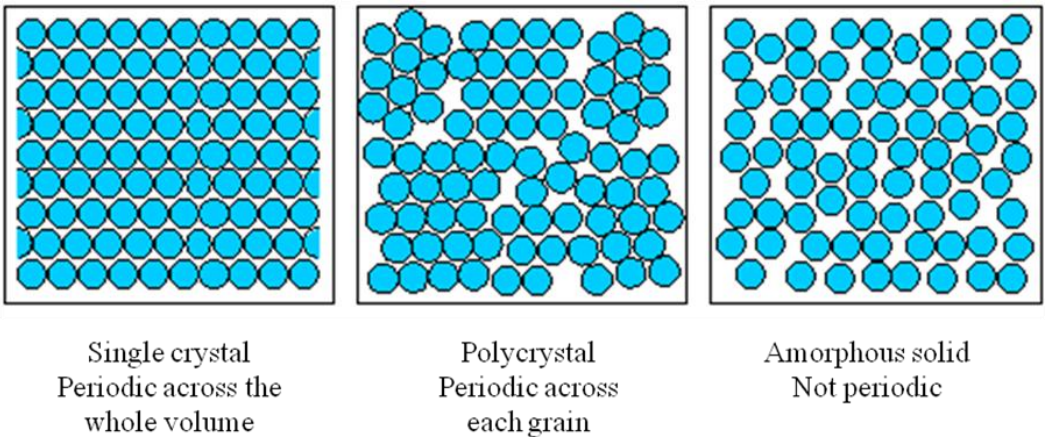

Figure 4-1 Depiction of single crystal, polycrystal, and amorphous solid (from Wikipedia)

The range of crystalline order distinguishes single crystals, polycrystals and amorphous solids. Figure 4-1 shows how the periodicity of the atomic structure of each type of material compares.

Many characteristic properties of materials, such as mechanical, optical, magnetic and electronic behavior, can be attributed to the difference in structure between these three classes of solid. Natural rock minerals are polycrystals, while asphalts are amorphous colloids that different significantly from origins.

In this chapter for simplicity, 4 most widely spread and representative mineral crystals are selected in this study to perform atomistic calculation of bulk mechanical properties.

4.4 Mineral Mechanical Properties Calculation

Based on the calculation theory stated in Chapter 3, simulations are carried out in two steps, (1) relaxation followed by (2) molecular mechanics minimization. After relaxation, the structure displays the characteristics of various mineral rock crystal structures in agreement with experiment [65].

Potential parameters for the mineral aggregates were based on the augmented Consistent Valence Force Field (CVFF-aug). Intra-molecular motion (bond stretching) was allowed for all species and for hydroxyl groups at the upper kaolinite surface. The

potential energy component for nonbonded interactions consists Coulombic and van der Waals terms between atoms i and j at a separation of r.

Where applicable, atomic parameters were taken from CVFF-aug shown in Table 4-1, which is a nonbonded version for simulations of oxide minerals available. For quartz silicon and oxygen atoms, CVFF-aug values were used for the Lennard-Jones parameters, and partial charges were also assigned by the forcefield. For Si, we used a partial charge of 2.100 e. Oxygen atoms in quartz, including those at the upper surface, were assigned a charge of -1.1688 e so that the SiO2 unit is electroneutral. In order to maintain consistency, partial charges for all hydrogen atoms were assigned the same value, except at the bottom quartz surface as discussed above. Likewise, van der Waals parameters for hydroxide oxygen were assigned the same value as oxygen in water.

The same forcefied parameters assign rules for Granite, Quartz, Calcite, and Kaolinite crystals are all typed with specific nonbond parameters according to CVFF-aug forcefield shown in Table 4-1.

Table 4-1 Nonbond Parameters for the CVFF-aug ForceField

species	symbol	Charge (e)	D_0 (kcal/mol)	R_0
water hydrogen	h*	0.4100		
hydroxyl hydrogen	ho	0.4250		
water oxygen	o*	-0.8200	0.1554	3.5532
hydroxyl oxygen	Oh	-0.9500	0.1554	3.5532
bridging oxygen	Ob	-1.0500	0.1554	3.5532
bridging oxygen with octahedral substitution	Obos	-1.1808	0.1554	3.5532
bridging oxygen with tetrahedral substitution	Obts	-1.1688	0.1554	3.5532
bridging oxygen with double substitutioin	Obss	-1.2996	0.1554	3.5532
hydroxyl oxygen with substitution	Ohs	-1.0808	0.1554	3.5532
tetrahedral silicon	St	2.1000	1.8405 X 10e-6	3.7064
octahedral aluminum	Ao	1.5750	1.3298 X 10e-6	4.7943

tetrahedral aluminum	At	1.5750	1.8405 X 10e-6	3.7064
octahedral magnesium	Mgo	1.3600	9.0298 X 10e-6	5.9090
hydroxide magnesium	Mgh	1.0500	9.0298 X 10e-6	5.9090
octahedral calcium	Cao	1.3600	5.0298 X 10e-6	6.2484
hydroxide calcium	Cah	1.0500	5.0298 X 10e-6	6.2428
octahedral iron	Feo	1.5750	9.0298 X 10e-6	5.5070
octahedral lithium	Lio	0.5250	9.0298 X 10e-6	4.7257
aqueous sodium	Na	1.0000	0.1301	2.6378
aqueous potassium	K	1.0000	0.1000	3.7423
aqueous cesium	Cs	1.0000	0.1000	4.3002
aqueous calcium	Ca	2.0000	0.1000	3.2237
aqueous barium	Ba	2.0000	0.0470	4.2840
aqueous chloride	Cl	-1.0000	0.1001	4.9388

4.5 Crystal Mineral Atomistic Structure Modeling

4.5.1 Granite

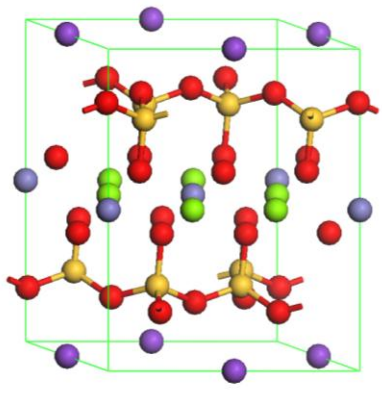

Figure 4-2 Granite structure of unit cell

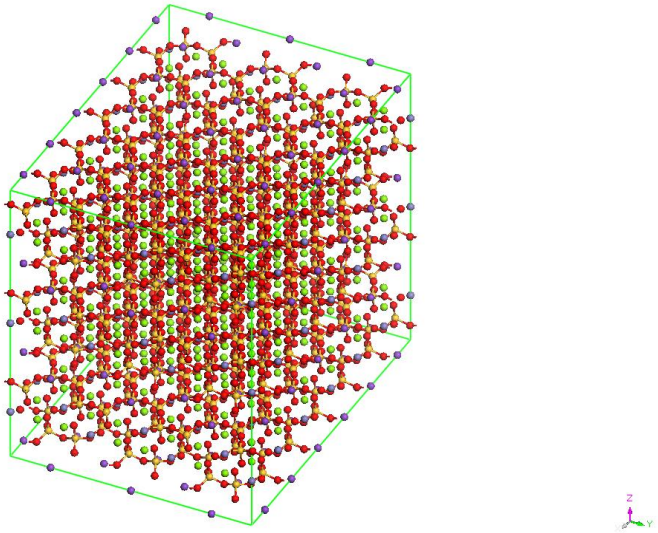

Figure 4-3 Granite structure of $6\times3\times3$ supercell cell

Granite is nearly always massive (with various crystal structures), hard and tough, and therefore it has gained widespread use as a pavement construction stone. The average density of granite is 2.75 g/cm^3. Here we use the granite model from American Mineralogist Crystal Structure database [65]. The unit cell of granite is given in Figure 4-2 with side lengths of a=5.36 Å, b=9.25 Å, c=10.25 Å and angles of α=90°, β=100.15°, and γ = 120°. It belongs to C12/m1 space group. The unit cell volume is 499.63 Å^3. As shown in Figure 4-3, the MD simulation model for granite contains $6\times3\times3$ crystallographic unit cells in the x-, y-, and z-directions of the Cartesian coordinate system, respectively. The supercell size of granite model is at side lengths of a = 32.13 Å, b = 27.753 Å and c = 30.738 Å and angles of α=90°, β=90°, γ = 120°. The granite supercell consists of 2580 atoms for total. The three-dimensional periodic boundary conditions are applied on this model for simulation.

4.5.2 Quartz

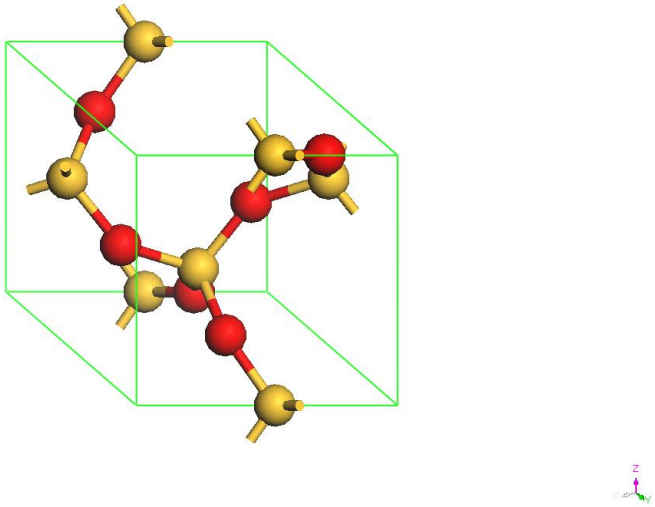

Figure 4-4 Quartz structure of unit cell

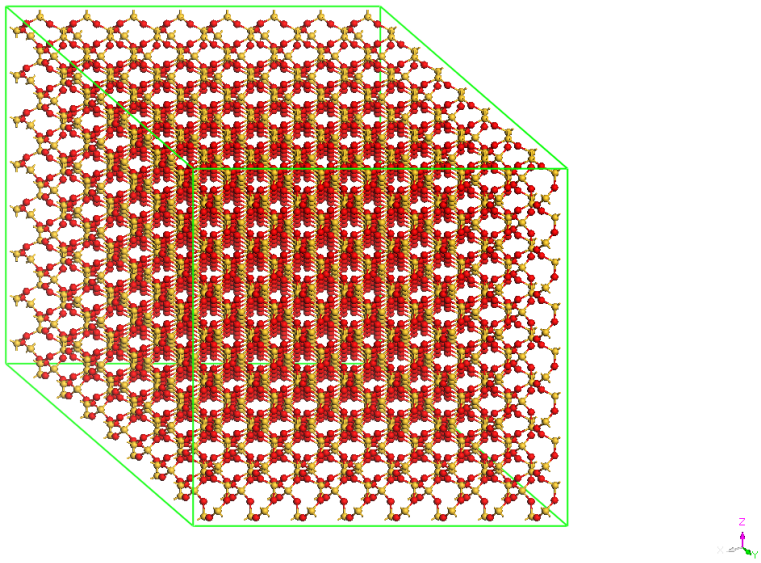

Figure 4-5 Quartz structure of $8\times8\times8$ supercell cell

Quartz is a major rock-forming mineral in many geologic environments. For example, quartz makes up nearly one-third of reservoir rock. Also, quartz has a relatively simple composition and experimental data available. Quartz belongs to the rhombohedral crystal system. It has a density of 2.65 g/cm ^{3} The ideal crystal shape is a six-sided prism terminating with six-sided pyramids at each end. In nature, quartz crystals are often twinned, distorted, or intergrown with adjacent crystals of quartz. It only shows part of this shape, or to lack obvious crystal faces altogether. Structure properties of quartz [66]

at pressure P = 1 ATM is illustrated in Figure 4-4. The lattice parameters are: a=4.916 Å, b=4.916 Å, c=5.410 Å, α=90°, β=90°, γ = 120°. It belongs to $P3_221$ space group, with 12 atoms per unit cell, 4 silicon atoms and 8 oxygen atoms, respectively. As shown in Figure 4-5, the MD simulation model for quartz contains 8×8×8 crystallographic unit cells in the x-, y-, and z-directions of the Cartesian coordinate system, respectively. The supercell size of quartz model is at side lengths of a = b = 39.304 Å and c = 43.2416 Å and angles of α=90°, β=90°, γ = 120°. The quartz supercell consists of 5896 atoms for total. The three-dimensional periodic boundary conditions are applied on this model for simulation.

4.5.3 Calcite

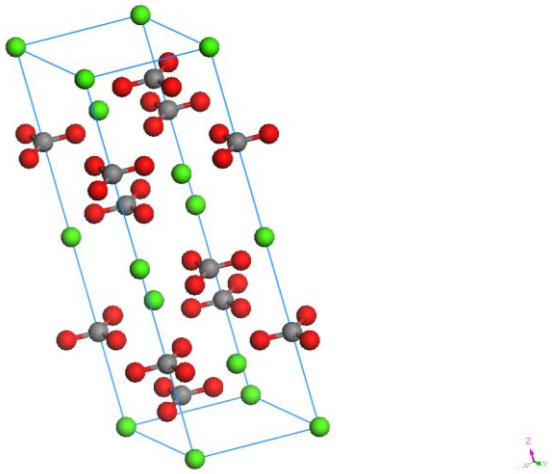

Figure 4-6 Calcite structure of unit cell

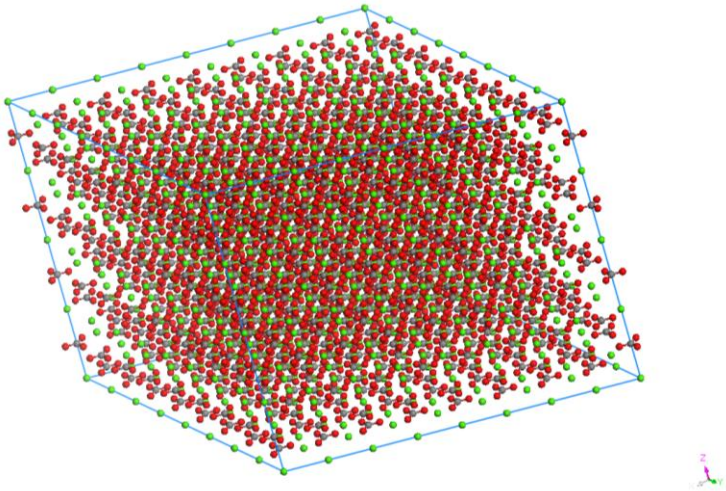

Figure 4-7 Calcite structure of $8\times8\times2$ supercell cell

Calcite belongs to the Trigonal-Hexagonal crystal system, though actual calcite rhombohedra are rare as natural crystals. However, they show a remarkable variety of habits including acute to obtuse rhombohedra, tabular forms, prisms, or various scalenohedra. Calcite exhibits several twinning types adding to the variety of observed forms. It may present as fibrous, granular, lamellar, or compact. Cleavage is usually in three directions parallel to the rhombohedron form. It has a density of 2.71 g/cm^3. Unit cell of calcite is illustrated in Figure 4-6. The lattice parameters are: a=b=4.99 Å, c=17.061 Å, and α=90°, β=90°, γ = 120°. It belongs to R3c space group. As shown in Figure 4-7, the MD simulation model for calcite contains 8×8×2 crystallographic unit cells in the x-, y-, and z-directions of the Cartesian coordinate system, respectively. The supercell size of quartz model is at side lengths of a = b = 39.92 Å and c = 34.12200 Å and angles of α=90°, β=90°, γ = 120°. The quartz supercell consists of 3840 atoms for total. The three-dimensional periodic boundary conditions are applied on this model for simulation.

4.5.4 Kaolinite

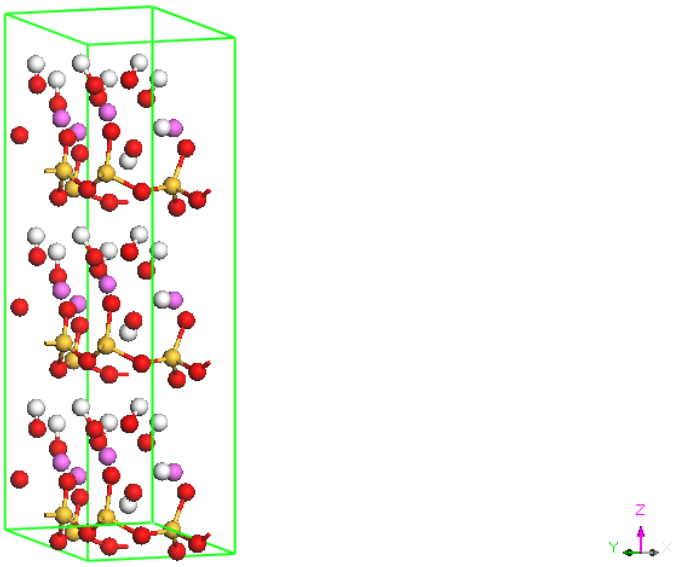

Figure 4-8 Kaolinite structure of unit cell

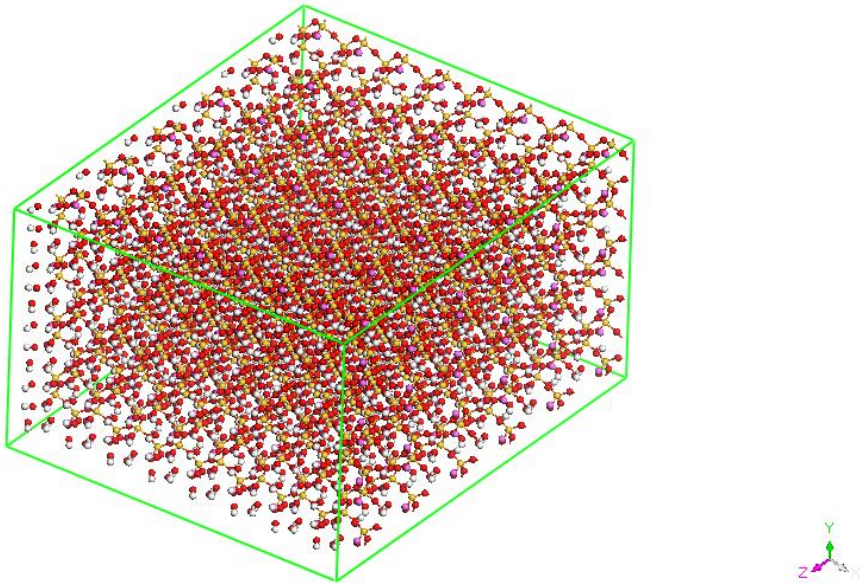

Figure 4-9 Kaolinite structure of $8\times4\times6$ supercell cell

Kaolinite (china clay) is a hydrated aluminium silicate crystalline mineral formed over many millions of years by the hydrothermal decomposition of granite rocks. Kaolinite belongs to the Triclinic-Pedial crystal system. It has a density of 2.62 g/cm^3. A unit cell structure property of kaolinite is illustrated in Figure 4-8. The lattice parameters are: a=5.15 Å, b=8.93 Å, c=7.384 Å, α=91.93°, β=105.042°, γ = 89.791°. As shown in Figure 4-9, it belongs to the P1 space group. The MD simulation model for calcite contains $8\times4\times6$ crystallographic unit cells in the x-, y-, and z-directions of the Cartesian coordinate system, respectively. The supercell size of quartz model is of side lengths at a = 41.192 Å, b = 35.736 Å, c = 44.304 Å and angles of α=91.93°, β=105.042°, γ = 89.791°. The quartz supercell consists of 7080 atoms for total. The three-dimensional periodic boundary conditions are applied on this model for simulation.

4.6 Results and Discussion

The atomistic simulations described here were carried out with LAMMPS MD code, which is compiled with IBM XL C++ compiler on the SystemX (high performance parallel computing center at Virginia Tech). Visualization is done by the visual molecular dynamics software (VMD) [67].

The static method mentioned in Chapter 3 is employed to the equilibrated systems, as shown in 4 mineral crystals supercell models constructed above. After an initial energy minimization, a very small strain (remain within elastic limits, e.g. ± 0.003) is applied to the system and energy re-minimization is applied. In the following tables, we present the result of our calculation of the stiffness matrix in Table 4-2, Table 4-5, Table 4-8, and Table 4-11, the compliance matrix in Table 4-3, Table 4-6, Table 4-9, and Table 4-12, as well as the modulus and Poisson ratios in Table 4-4,

Table 4-7, Table 4-10, and Table 4-13.

4.6.1 Granite

Table 4-2 Granite elastic stiffness constants C_{ij} (GPa)

591.4628	766.8829	428.0272	55.1123	1.2187	-126.7157
766.8829	703.3607	799.5609	-73.7918	112.1436	-1.4587
428.0272	799.5609	508.9904	78.7918	12.9736	22.2488
55.1123	-73.7918	78.7918	-23.9733	34.1915	142.2299
1.2187	112.1436	12.9736	34.1915	107.8153	-31.6896
-126.7157	-1.4587	22.2488	142.2299	-31.6896	46.7011

Table 4-3 Granite elastic compliance constants S_{ij} (1/TPa)

5.195	-0.9563	-3.6609	5.0384	-0.1057	0.3936
-0.9563	1.5508	3.4027	-0.432	0.6056	-2.5374
-3.6609	3.4027	0.3054	-4.4313	-1.3662	2.5962
5.0384	-0.432	-4.4313	3.2226	2.0657	7.3558
-0.1057	0.6056	-1.3662	2.0657	8.0183	-0.4674
0.3936	-2.5374	2.5962	7.3558	-0.4674	-1.555

Table 4-4 Granite Young's modulus, Poisson ratios, Lame constants, Modulus

Young Modulus (GPa)		**Poisson Ratios**			
X =	192.49	Exy =	0.18	Exz =	0.70
Y =	644.82	Eyx =	-0.61	Eyz =	2.19
Z =	644.82	Ezx =	11.98	Ezy =	-11.14
Lame constants (GPa) (assuming material is isotropic)					
λ =	514.24	μ =	43.5143		
		calculated	**Experimental**		
Bulk modulus (GPa) =		643.64	NA		

Shear modulus (GPa)=	13.40	NA

As to granite, the absolute magnitude of the non-diagonal terms for strain within the layers is generally reasonable in comparison to experimental data for other minerals [68]. We note that C11 is 591.46 and C22 is at a higher value of 703.36. The results indicate that the **b** direction is more rigid than the **a** direction. As we expected, the granite crystal is most readily deformed along **c** corresponding to C33.

However, the mechanical property of granite depends on its various sources. The mechanical properties of results have shown that the Young's Modulus of granite macro-crystals is 192.49 GPa in **a** direction, while it is of 644.82 GPa in **b** and **c** directions. The bulk modulus calculated is 643.64 GPa and the shear modulus is 13.40 GPa. However, the experimental value is not available for comparison, because of the various sources of granite compositions.

4.6.2 Quartz

Table 4-5 Quartz elastic stiffness constants C_{ij} (GPa)

92.8794	27.7973	4.3211	-0.0123	-13.2486	-0.1904
27.7973	94.583	4.2702	0.0077	12.8044	0.2924
4.3211	4.2702	81.8213	0.0292	0.0372	0.0774
-0.0123	0.0077	0.0292	43.1925	0.0026	14.8236
-13.2486	12.8044	0.0372	0.0026	48.2651	-0.0364
-0.1904	0.2924	0.0774	14.8236	-0.0364	32.0452

Table 4-6 Quartz elastic compliance constants S_{ij} (1/TPa)

12.7573	-4.3602	-0.4484	-0.0445	4.659	0.1425
-4.3602	12.484	-0.4191	0.0552	-4.5086	-0.1695
-0.4484	-0.4191	12.2674	0.0017	-0.0214	-0.0293
-0.0445	0.0552	0.0017	27.5217	-0.038	-12.7319
4.659	-4.5086	-0.0214	-0.038	23.194	0.1128
0.1425	-0.1695	-0.0293	-12.7319	0.1128	37.0981

Table 4-7 Quartz Young's modulus, Poisson ratios, Lame constants, Modulus

Young Modulus (GPa)		**Poisson Ratios**			
X =	78.38	Exy =	0.3418	Exz =	0.0351

Y =	80.10	Eyx =	0.3493	Eyz =	0.0336
Z =	81.51	Ezx =	0.0366	Ezy =	0.0342
Lame constants (GPa) (assuming material is isotropic)					
λ =	7.4260	μ =	41.1676		
		calculated	**Experimental**		
Bulk modulus (GPa) =		36.96	38 ~ 98		
Shear modulus (GPa)=		34.53	44		

The predicted anisotropy in the mechanical stiffness of quartz shown in Table 4-5, Table 4-6, and Table 4-7 is in consistent with experimental observations [69]. The bulk modulus is calculated to be 36.96 GPa. Experimentally, bulk modulus values for quartz is 38-98 GPa [70]. The shear modulus was calculated to be 34.53 GPa. Experimentally, bulk modulus values for calcite is 44.53 GPa [70], which is a little bit lower than the calculated value. The Young's modulus calculated for quartz is 78.38 GPa, 80.10 GPa, and 81.51 GPa in three directions, respectively. The experimental values obtained are ranged from 76 to 97 GPa. Thus, our calculated value is in reasonable agreement with experimental values for quartz crystal structure.

For the purpose of comparison, the major component of granite is the quartz structure. But the results from our calculation are quite different for quartz and granite. This behavior could be due to the transformation of the granite structure to a mixture of amorphous alumina, kalium, and silica. Those materials are with higher mechanical properties. The obtained granite after minimization is an intermediary phase for the crystallization, which could be hard compounds desired in the formulation of ceramics.

4.6.3 Calcite

Table 4-8 Calcite elastic stiffness constants C_{ij} (GPa)

173.4891	64.1595	97.4627	5.6451	-107.1023	-88.4127
64.1595	454.8568	-165.5746	-40.0059	326.636	-46.7829
97.4627	-165.5746	0.6333	-5.8651	112.2354	-8.6348
5.6451	-40.0059	-5.8651	-342.4477	-21.5847	139.9773
-107.1023	326.636	112.2354	-21.5847	-186.4615	-89.0982
-88.4127	-46.7829	-8.6348	139.9773	-89.0982	-93.2084

Table 4-9 Calcite elastic compliance constants S_{ij} (1/TPa)

5.1992	0.9681	-6.1146	-1.0015	-3.3473	-3.1555
0.9681	1.374	-6.1075	-2.0741	0.7383	-4.8627
-6.1146	-6.1075	23.8105	1.2368	5.3981	3.357
-1.0015	-2.0741	1.2368	-2.3648	-2.2818	0.5062
-3.3473	0.7383	5.3981	-2.2818	3.5022	-4.47
-3.1555	-4.8627	3.357	0.5062	-4.47	-0.5727

Table 4-10 Calcite Young's modulus, Poisson ratios, Lame constants, Modulus

Young Modulus (GPa)		**Poisson Ratios**			
X =	192.33	Exy =	-0.1862	Exz =	1.1761
Y =	72.78	Eyx =	-0.7046	Eyz =	4.4451
Z =	41.99	Ezx =	0.2568	Ezy =	0.2565
Lame constants (GPa) (assuming material is isotropic)					
λ =	321.1670	μ =	207.3725		
		calculated	**Experimental**		
Bulk modulus (GPa) =		126.9725	129.6		
Shear modulus (GPa)=		89.1558	35		

As for calcite, the absolute magnitude of the non-diagonal terms for strain within the layers is generally reasonable in comparison to experimental data for other minerals [68]. We note that C11 is 173.4891 and C22 is at a higher value of 454.85, indicating that the **b** direction is slightly rigid than the **a** direction. As expected, the calcite crystal is most readily to deform along **c** direction, corresponding to C33. The predicted anisotropy in the mechanical stiffness of calcite shown in Table 4-8, Table 4-9, and Table 4-10 is in consistent with experimental observations [69]. The bulk modulus was calculated to be 126.97 GPa. Experimentally, bulk modulus values for calcite is 129.6 GPa [70]. The shear modulus was calculated to be 89.1558 GPa. Experimentally, bulk modulus values for calcite is 35 GPa [70], which is much lower than the calculated value. The Young's modulus we obtained are 192.33 GPa, 72.78 GPa, and 41.99 GPa in **a**, **b**, and **c** directions, respectively. Whereas the experimental values are range from 72.35 to 88.19 GPa. This could be due to the pure calcite structure is a porous structure and it is very rarely found in nature. Therefore, it is reasonable to get larger elastic parameters than experimental values. Thus, our calculated values are reasonable.

4.6.4 Kaolinite

Table 4-11 Kaolinite elastic stiffness constants C_{ij} (GPa)

140.7005	70.9451	29.7989	0.6935	-21.2575	0.5789
70.9451	141.3128	29.3017	0.344	-10.0213	-4.4146
29.7989	29.3017	54.5118	4.4829	5.7971	2.8078
0.6935	0.344	4.4829	10.941	0.2664	-6.413
-21.2575	-10.0213	5.7971	0.2664	11.6168	-2.1107
0.5789	-4.4146	2.8078	-6.413	-2.1107	36.2027

Table 4-12 Kaolinite elastic compliance constants S_{ij} (1/TPa)

15.8921	-3.4089	-10.7524	4.369	31.914	2.7987
-3.4089	10.1656	-4.534	3.0906	5.1765	2.495
-10.7524	-4.534	32.804	-16.4423	-41.0758	-8.2326
4.369	3.0906	-16.4423	110.3469	20.3911	22.318
31.914	5.1765	-41.0758	20.3911	172.0569	16.95
2.7987	2.495	-8.2326	22.318	16.95	33.4619

Table 4-13 Kaolinite Young's modulus, Poisson ratios, Lame constants, Modulus

Young Modulus (GPa)		**Poisson Ratios**			
X =	62.92	Exy =	0.21	Exz =	0.68
Y =	98.37	Eyx =	0.34	Eyz =	0.45
Z =	30.48	Ezx =	0.33	Ezy =	0.14
Lame constants (GPa) (assuming material is isotropic)					
λ =	73.0013	μ =	9.5869		
		calculated	**Experimental**		
Bulk modulus (GPa) =		46.57	35		
Shear modulus (GPa)=		11.93	23		

The bulk modulus, shear modulus, and the elastic constants tensors of kaolinite were calculated using Molecular Mechanics calculations and are shown in Table 4-11, Table 4-12, and Table 4-13. The absolute magnitude of the non-diagonal terms for strain within the layers is generally reasonable in comparison to experimental data for other minerals [68]. We note that C11 is 3% less than C22, indicating that the **a** direction is slightly more flexible than the **b** direction. As we expected, the crystal is most readily deformed along **c** direction, corresponding to C33. The predicted anisotropy in the mechanical stiffness of kaolinite is in consistent with the experimental observations shown in reference [69]. The bulk modulus was calculated to be 46.57 GPa.

Experimentally, bulk modulus values for kaolinite have ranged between 21 and 55 GPa [70]. Thus, our calculated value is in reasonable agreement with experimental values.

Surprisingly, however, both the calculated and experimental Kaolinite values are significantly higher than the experimental value reported for quartz of 92.88 GPa [71]. Thus, it would appear that quartz is less rigid than kaolinite. The lower bulk modulus of kaolinite may be attributed to the structural misfit between the octahedral and tetrahedral sheets and the fact that the interlayer hydrogen bonds in kaolinite between the aluminum octahedral layer and the opposing siloxane surface are fundamentally different from the interlayer interactions in gibbsite that, in turn, lowers the resistance to an external force. The Young's modulus of kaolinite calculated are 62.92 GPa, 98.37 GPa, and 30.48 GPa in the **a**, **b**, and **c** directions, respectively. These values are within the scope of the experimental values of 92 GPa, 170 GPa, and 31 GPa in the **a**, **b**, and **c** directions, respectively.

Note that, ideally, the non-diagonal components should be zero for isotropic materials. Although the non-diagonal components are not zero, common characteristics of isotropic material remain in Figure 4-11. The diagonal components are much higher than the non-diagonal ones and the entire matrixes are roughly symmetrical along the diagonal components. The bulk modulus, Young's modulus and shear modulus are consistently a little about 15% higher than the corresponding experimental values. The parameters trend as higher than those of obtained from experiments have also been reported by other groups [71-73]. This may partly result from the fact that the models for calculation represent perfect structure while realistic systems have voids or defects in the structures. A little lower conversion compared to the experimental value may be also responsible for it. From these results, the Molecular Mechanics method produced reasonable well mineral mechanical parameters. Good agreements between the calculated elastic constants and the experimental values confirmed that the models developed on the basis of the newly developed method are representative.

In general, the elastic properties of granite, quartz, calcite, and kaolinite were obtained by Molecular Mechanics simulation methodology. Elastic constant tensors were determined for the optimized structure. Full elastic stiffness constant tensors were determined using the stress tensors generated from each strain pattern. The bulk modulus,

shear modulus, and the Young's modulus of each mineral were also calculated from the elastic constants tensors.

4.7 Summary

As can be observed from the results, ideally, in stiffness matrix the non-diagonal components should be zero for isotropic materials. Although the non-diagonal components are not zero, common characteristics of isotropic material remain in stiffness matrixes of the 4 minerals: the diagonal components are much higher than the non-diagonal ones and the entire matrix is roughly symmetrical along the diagonal components. Contrarily, the calculated elastic constants have both positive and negative values, which mean highly anisotropic elastic properties of quartz structure will appear from atomistic scale.

It is an interesting finding that the mineral crystal has negative Poisson's ratios for the loadings along certain directions. Its magnitude ranges variously over all crystal directions. Negative Poisson's ratio corresponds to volume expansion/contraction under shear strain. Thus, granite, calcite, and kaolinite retain elastic anisotropy from nanoscale point of view, the property also presents for macroscopically isotropic mineral, quartz.

Since a reasonable agreement between the theoretical and experimental values is satisfactory, we conclude that the theoretical calculations as presented here are useful in asphalt concrete nanoscale modeling research for predicting the mechanical properties of asphalt-rock interface that are difficult to obtain experimentally.

Chapter 5
Atomistic Modeling of Asphalt Binder's Physical and Mechanical Properties

5.1 Asphalt Molecules Model

Bitumen is often characterized chemically by its hydrocarbon class compositions such as saturates-aromatics-resins-asphaltenes (SARA) contents [74]. Asphaltenes are a solubility class defined as insolubles in light aliphatic solvent (e.g., n-pentane or n-heptane) and soluble in aromatic solvent (e.g., toluene). Asphaltenes are not a chemical class by definition, but there is a large body of literature on asphaltene structure [75-81]. Although the chemical and physical properties of asphaltenes have been investigated for decades using wide range of techniques such as Vapor pressure osmometry (VPO), Near-infrared chemical imaging (NIR), Nuclear magnetic resonance spectroscopy (NMR), Fluorescence depolarization, Spectral fluorescence microscopy, rheology, interfacial tension, their molecular structure and thermodynamic state in various systems are still debated.

The molecular weight of asphaltenes is the subject of long-standing controversy. The reported average molecular mass of asphaltenes ranges from 400 to 10,000 g/ml depending on the technique used to determine molecular weight [75-77, 82]. According to most recent studies, the average molecular weight of asphaltenes is around 750 [77]. Geoenzin and Mullins [83] gave the idealized molecular structures for asphaltenes as depicted in Figure 5-1. According to Figure 5-1, the asphaltene molecules possess, on average, about seven fused aromatic rings and diameters of asphaltene molecules varies from 8 to 15 Angstrom.

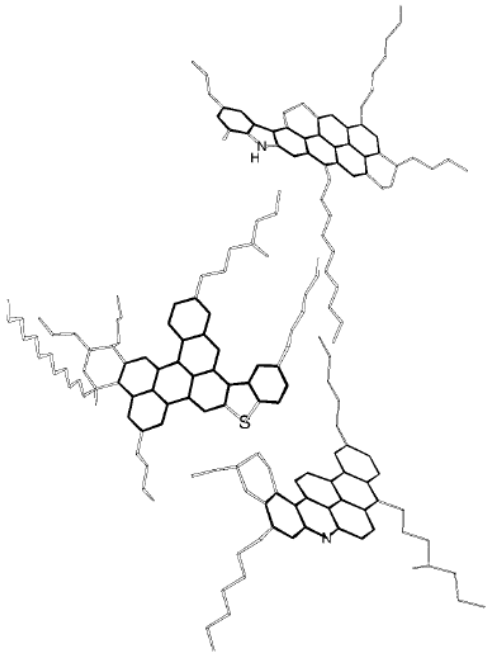

Figure 5-1 Idealized molecular structures for asphaltenes consistent with overall molecular size, aromatic ring systems, and chemical speciation. The aromatic rings are shown with darker lines.

The configuration of the internal structure of asphalt is largely determined by the chemical constitution of the molecular species present. Bitumen is a complex chemical mixture of molecules that are predominantly hydrocarbons with a small amount of structurally analogous heterocyclic species and functional groups containing sulphur, nitrogen and oxygen atoms. Bitumen also contains trace quantities of metals such as vanadium, nickel, iron, magnesium and calcium, which occur in the form of inorganic salts and oxides structures. Elementary analysis [84] of bitumens manufactured from a variety of crude oils shows that most bitumens contain:

- Carbon 82-88%
- Hydrogen 8-11%
- Sulphur 0-6%
- Oxygen 0-1.5%
- Nitrogen 0-1%

The precise composition varies according to the source of the crude oil from which the bitumen originates, modification induced by semi-blowing and blowing during

manfacture and ageing in service.

The chemical composition of bitumen is extremely complex. Thus, a complete analysis of bitumen would be extremely laborious. The correlation of the rheological properties with a large quantity of the data would be impractical. However, it is possible to separate bitumen into two broad chemical groups called asphaltenes and maltenes. The maltenes can be further subdivided into saturates, aromatics and resins. The four groups are not well defined and there is some overlap between the groups. However, this does enable bitumen rheology to be set against broad chemical composition.

The methods available for separating bitumens into fractions can be classified as:

- Solvent extraction
- Adsorption by finely divided solids and removal of un-adsorbed solution by filtration
- Chromatography
- Molecular distillation used in conjunction with one of the above techniques.

Solvent extraction is attractive as it is a relatively rapid technique but the separation obtained is generally poorer than the results from using chromatography where a solvent effect is combined with selective adsorption. Similarly, simple adsorption methods are not as effective as column chromatography in which the eluting solution is constantly re-exposed to fresh adsorbent and different equilibrium conditions as it progresses down the column. Molecular distillation is lengthy and has limitations in terms of the extent to which type separation and distillation of high molecular weight components of bitumen can be effected. Chromatographic techniques have, therefore, been most widely used to define bitumen constitution. Using this technique, bitumens can be separated into the four groups: asphaltenes, resins, aromatics and saturates. The main characteristics of these four broad component groups and metallic constituents are now discussed.

5.1.1 Asphaltenes

Asphaltenes are n-heptane insoluble black or brown amorphous solids containing

some nitrogen, sulphur and oxygen, in addition to carbon and hydrogen. Asphaltenes are generally considered to be highly polar and complex aromatic materials of fairly high molecular weight. Different methods of determining molecular weights have led to different values ranging widely from 600 to 300000 depending on the separation technique employed. However, the majority of test data indicates that the molecular weights of asphaltenes range from 1000 to 100000; they have a particle size of 0.5 to 30 nm and hydrogen/carbon (H/C) atomic ratio of about 1:1. The asphaltene content has a large effect on the rheological characteristics of bitumen. Increasing the asphaltene content produces a harder, more viscous bitumen with a lower penetration, higher softening point and, consequently, higher viscosity. Asphaltenes constitute 5 to 25% of the bitumen.

5.1.2 Resins

Resins are soluble in n-heptane. Like asphaltenes, they largely composed of hydrogen and carbon. They contain small amounts of oxygen, sulphur and nitrogen. They are dark brown in color, solid or semi-solid and, being polar in nature. They are strongly adhesive. Resins are dispersing agents or peptisers for the asphaltenes. The proportion of resins to asphaltenes governs the solution or gelatinous type character of the bitumen. Resins separated from bitumens are found to have molecular weights ranging from 500 to 50000, a particle size of 1 to 5 nm and H/C atomic ratio of 1:3 to 1:4.

5.1.3 Aromatics

Aromatics comprise the lowest molecular weight naphthenic aromatic compounds in the bitumen and represent the major proportion of the dispersion medium for the peptized asphaltenes. They constitute 40 to 65% of the total bitumen and are dark brown viscous liquids. The average molecular weight range is in the region of 300 to 2000. They consist of non-polar carbon chains in which the unsaturated ring systems dominate and they have a high dissolving ability for other high molecular weight hydrocarbons.

5.1.4 Saturates

Saturates consist of straight and branch chain aliphatic hydrocarbons together

with alkyl-naphthenes and some alkyl-aromatics. They are non-polar viscous oils which are straw or white in color. The average molecular weight range is similar to that of aromatics and components include both waxy and non-waxy saturates. This fraction forms 5 to 20% of the bitumen.

5.1.5 Bitumen structure

Bitumen is traditionally regarded as a colloidal system consisting of high molecular weight asphaltene micelles dispersed or dissolved in a lower molecular weight oily medium (maltenes). The micelles are considered to be asphaltenes together with an absorbed sheath of high molecular weight aromatic resins which act as a stabilizing solvating layer. In the presence of sufficient quantities of resins and aromatics of adequate solvating power, the asphaltenes are fully peptized and resulting micelles have good mobility within the bitumen. If the aromatic/resin fraction is not present in sufficient quantities to peptize the micelles, or has insufficient solvating power, the asphaltenes can associate together further. This can lead to an irregular open packed structure of linked micelles in which the internal voids are filled with an inter micellar fluid of mixed constitution.

The colloidal behavior of the asphaltenes in bitumens results from aggregation and salvation. The degree to which they are peptized will have a considerable influence on the resultant viscosity of the system. Such effects decrease with increasing temperature and GEL character of certain bitumens may be lost when they are heated to high temperatures. The viscosities of saturates, aromatics, and resins depend on the molecular weight distribution. The higher the molecular weight, the higher the viscosity would be. The viscosity of the continuous phase, e.g. the maltenes, imparts an inherent viscosity to the bitumen that is increased by the presence of the dispersed phase, such as the apshaltens. The fraction of saturates decreases the ability of the maltenes to solvate the asphaltenes because high saturate contents can lead to agglomeration of the asphaltene. Accordingly, an increase in GEL character and a temperature dependence for bitumens results not only from the asphaltene content but also from the saturate content.

5.1.6 Cautions with Molecular Models

In general, molecular models can be an excellent aid to understand process chemistry and physics. As long as the model allows the predictability of process behavior, use of the model is warranted. However, caution is also advised. Because of the complexity of the asphaltene fraction, there is no one method that will guarantee the development of a suitable molecular model.

The effort must be multidimensional taken into account all of the properties and characteristics of the materials. Especially, caution is advised when average structures are used. Averages can be misleading especially when molecular weight data can be a major limitation to the development of the average structure.

Indeed, even when a multidimensional approach is employed for the derivation of a model, there is no guarantee that the model is a true reflection of the molecular types in asphaltene fraction. It must also be recognized that any model developed may not be the only, or final, answer to the problem. As techniques improve and knowledge evolves, the model must be as well.

Recognition of the fact that it is not possible to compose a model that represents all of the properties of asphaltenes is a major achievement. The molecular size, as deduced from molecular weight measurements, prohibits this. Therefore, it is more preferable to design models that are representative of the various constituent fractions of an asphaltene.

5.2 Average Molecular Structures of Core Asphalts

The molecular structures of asphalt components vary extensively from those which might be entirely aromatic to those with no conjugated entities at all. Differences in the range of molecular weight, the content of functional groups containing hetero atoms, the extent of substitution and branching of chains will also be found.

Indeed, the degree of variability itself may be important to asphalt characteristics. It is necessary to keep these points in mind even while discussing the concept of an ‘average molecule’ of asphalt cement.

An ‘average molecule’ is a structure derived from the average molecular weight, chemical analysis, and NMR data. It may not represent an existent molecule but provides

a valuable visual means of describing the overall characteristics of a specific type of asphalt material. Average structures have been derived only for the eight core asphalts, but with some additional data, could be derived for fractions such as those from ion exchange chromatography.

As shown in Figure 5-2, we choose a well-known chemical structure of an 'average' asphalt molecule [79]. Construction of a model of this molecule requires specialist model building and visualization tools, which are available in the VMD software. During asphalt molecule construction, the model was begun by drawing the aromatic core to accommodate the required number of aromatic carbon atoms plus sulfur and aromatic hydrogen.

The average asphalt model for the latter use could be very useful in understanding asphalt behavior. In addition, heteroatoms posed a special problem in constructing average molecular structures because they are present in very low concentrations. As a matter of convention, if the molecular formula indicated the presence of greater than 0.5 atoms of a heteroelement, an appropriate functional group was included in the structure. Nitrogen was included as a substituent usually in an aliphatic chain or a saturated ring, although it could certainly be present in an aromatic system.

Sulfur was included in an aromatic ring in most cases. If the possibility of a second sulfur was indicated, it was placed as an aliphatic sulfide. There are a number of considerations in constructing an average molecule and it must be stressed that the structures shown in Figure 5-2 are in no way unique. A number of ways could be found to draw other structures based on the same data.

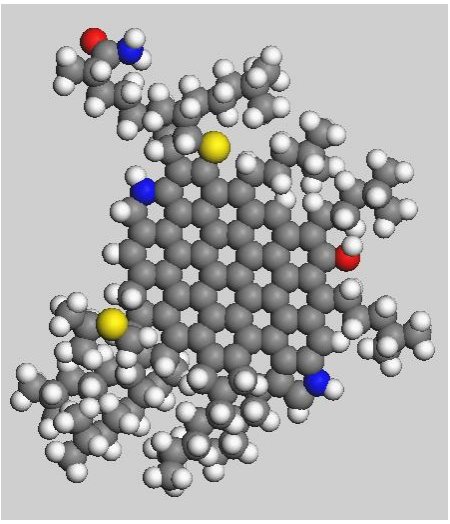

Average Asphalt Chemical Structure Average Asphalt Molecular Structure

Figure 5-2 An all-atom average molecular model of asphalt

Before studying the average structure, the limitations of the concept must be stressed. The variability in molecular structures in a specific type of asphalt is very wide. An average structure of necessity features only the most common traits. Other characteristics, a carboxylic acid group, for example, do not appear in an average structure because their concentrations are not large enough to make them 'average'. However, that is not to say that such groups may not be important to the behavior of the asphalt. One further caution relates to the fact that aliphatic and aromatic characteristics are combined in the average molecule when in fact they may be more widely separated.

5.3 Devise Asphalt Mixtures Model

Different model has different strength and weakness in providing representative features. For the purpose of comparison, two asphalt mixture models in representing various components of specific asphalt molecules are also built in this Chapter.

Since asphalt is a composite mixture, analyzing the physical properties of asphalt using molecular simulation needs to devise model asphalt mixtures of reasonable compositions, with different compounds representing each constituent (asphaltene, resin and maltene). Several compounds are chosen in this section to represent two asphalt

mixtures models, rather than just a single ‘average’ molecule in order to incorporate the diversity of chemistries and polarities [85-86] found in real asphalts.

Each component is represented using one molecule type. Molecule choice was based on measurements of Storm and co-workers [87]. Two asphaltene structures are chosen to make two bitumen models.

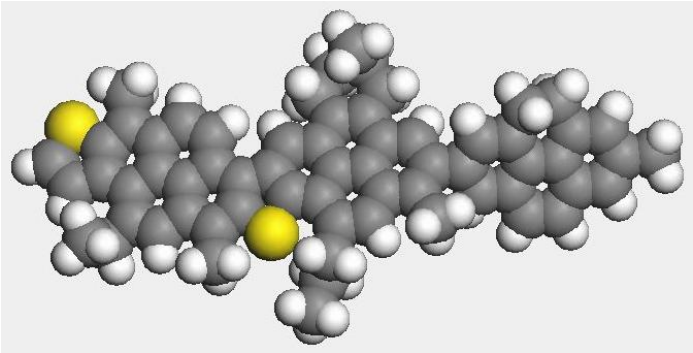

Figure 5-3 Molecule structure of asphaltene_1

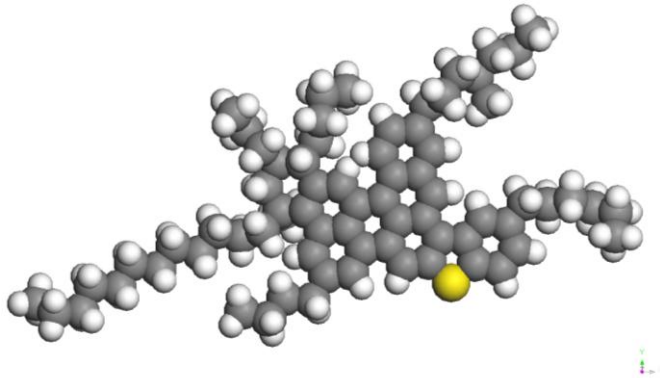

Figure 5-4 Molecule structure of asphaltene_2

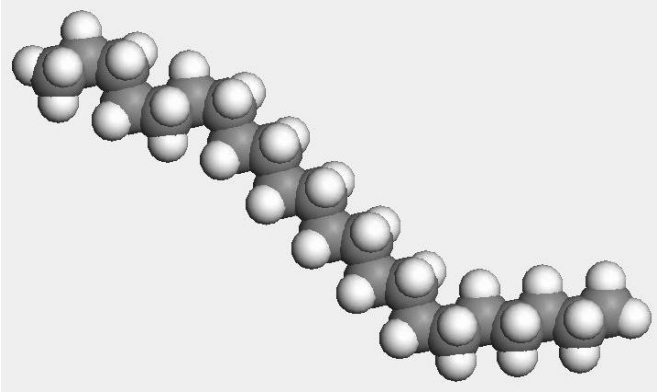

Figure 5-5 Molecule structure of n-C22

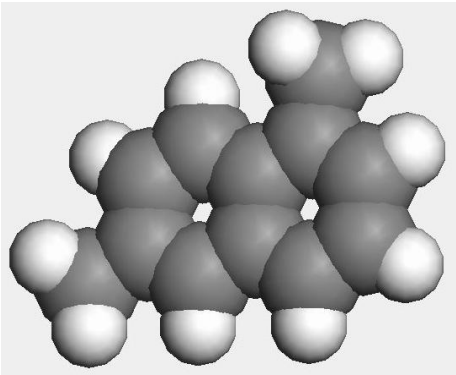

Figure 5-6 Molecular structure of 1,7-dimethyl naphthalene

In this dissertation, n-docosane (n-C22H46), as shown in Figure 5-5, is chosen as a representative saturate. A chain length of 22 is near the middle of this range. Kowalewski et al. [88] reported that n-C22 is the normal alkane with the highest concentration in the asphalt that they considered. Its melting point T_m = 44 ℃ and boiling point T_b = 369 ℃ are consistent with this saturate being a waxy component of an overall asphalt.

1,7-Dimethylnaphthalene, as shown in Figure 5-6, is chosen to be a representative naphthene aromatic. Its 16.7:83.3 alkane/aromatic ratio differs from the overall 58:42 balance reported [89] for one resin, but it does resemble some molecules depicted earlier for asphaltenes. The number of aromatic rings and side chains makes it intermediate between saturates and asphaltenes. Its size is relatively small compared to a reported overlap in resin and asphaltene molecular-weight distribution [77].

The concentrations of n-C22 and dimethylnaphthalene were chosen based on the alkane/aromatic carbon ratio ($72.2:27.8 \approx 8:3$) reported by [89] for the oil components, thus treating dimethylnaphthalene within both the oil and resin categories. This led to mixtures with 59 wt % n-C22 and 20 wt % 1,7-dimethylnaphthalene. If more molecules were desired for each subsection of the asphalt, an alternative would have been to use the overall oil/resin/asphaltene balance reported for this mixture [90] (71.0/7.5/ 21.5) in conjunction with the alkane and aromatic carbon speciations for resin and oil.

Two proposed asphaltene structures were chosen from examples in the literature and are shown in Figure 5-3 and Figure 5-4. The first contains a moderate-size aromatic

core with small branches. It is taken from NMR studies by [91]; they proposed a collection of sample molecules that in total represent statistics of molecular asphaltenes. The second, taken from discussions by Groenzin and Mullins [77] of their fluorescence depolarization studies, contains a somewhat smaller aromatic core and much longer alkane side branches. It is also a molecule from a collection of proposed asphaltenes. These models were chosen because they represent different proposed styles for the kinds of bonding patterns present in asphaltenes. Rogel and Carbognani [92] chose asphaltenes with much larger aromatic rings (10 to 20 fused rings) for their simulations.

Two model asphalt mixtures were created, using these asphaltene, saturate, and naphthene aromatic molecules. The overall mixture composition was guided by the measurements in [87]. An asphaltene mass fraction of 21% was selected, similar to the 22 wt% reported for Ratawi vacuum residual. The overall compositions and corresponding molecular characterizations of model mix1 and mix2 are listed in Table 5-1 and Table 5-2, respectively. The mix1 model is constructed using asphaltene_1, whereas the mix2 model is constructed using asphaltene_2.

Table 5-1 Overall Composition of Mixtures Based on the Asphaltene_1 model

	Asphaltene	1,7-dimethyl naphthalene	n-C_{22}
Number molecules	5	27	41
Mass fraction	20.7	19.7	59.6

Table 5-2 Overall Composition of Mixtures Based on the Asphaltene_2

	Asphaltene	1,7-dimethyl naphthalene	n-C_{22}
Number molecules	5	30	45
Mass fraction	21.1	19.8	59.1

5.4 Simulation Procedures

In this subsection, to represent asphalt structure a single average molecule as shown in Figure 5-2 and the two asphalt mixtures models are employed in the MD

simulations. By using these model asphalts, the MD simulations will be performed to quantify the overall bulk physical property. All of the three models will be chosen to make a comparison in the MD simulation. Efforts will be made to reflect the sensitivity to molecular architecture. The CVFF-aug forcefield parameters, illustrated in Table 5-3 are employed in these simulations. The potential energy terms for bonded interactions of asphalt molecules consists angle bending, bond stretching terms, and torsional term, as well as nonbonded terms.

Table 5-3 CVFF-aug ForceField Parameters for Asphalt models

Species	**Symbol**	**Charge (e)**	D_0 **(kcal/mol)**	R_0
water hydrogen	h*	0.4100		
hydroxyl hydrogen	ho	0.4250		
water oxygen	o*	-0.8200	0.1554	3.5532
hydroxyl oxygen	Oh	-0.9500	0.1554	3.5532
bridging oxygen with octahedral substitution	Obos	-1.1808	0.1554	3.5532
bridging oxygen with tetrahedral substitution	Obts	-1.1688	0.1554	3.5532
hydroxyl oxygen with substitution	Ohs	-1.0808	0.1554	3.5532

Bond Stretching: $E_{ij} = k_1(r - r_0)$ for the potential energy $E\left(kcal \cdot mol^{-1}\right)$, Bond stretch force constant k_1, and Equilibrium Bond Length r_0

bond	k_1	r_0
S-O	1000.00	1.80
O*-h*	1106.00	1.00
Os-h*	1312.00	1.25
Oh-h*	1106.00	1.00

Angle Bending: $E_{ij} = k_2(\theta - \theta_0)^2$ for the Potential Energy E($kcal \cdot mol^{-1}$), Angle Bend Force Constant $k_2\left(kcal \cdot mol^{-1} \cdot rad^{-2}\right)$, and Equilibrium Angle $\theta_0(\deg)$

angle	θ_0	k_2
c-S-c	180.00	300.00
h*-c*-h*	109.47	91.50
C-C-C	126.00	160.00

5.4.1 Average Asphalt Model System Run

In task-1, an average asphalt model system is constructed. The average asphalt molecule is relatively rigid, and no saturate components included in the model system. To the purpose of running stably, a simulation protocol is made and it is different from that used in mixture model.

In this simulation, MD (constant-NPT MD and constant-NVT MD) simulations were employed for simulating the motions of all atoms in the average molecules system over time under some appropriate thermodynamic conditions. The constant-NPT MD represented constant number of atoms or molecules, constant pressure, and constant temperature, which was primarily used to bring the systems into equilibrium suggested by energy and density stability. And the constant-NVT MD was performed at constant number of atoms or molecules, constant volume, and constant temperature for further equilibrating and collecting data for property analysis of structure, energy, and dynamics.

After the initial microstructure was generated, the minimization of the potential energy of the model system was carried out, where CVFF-aug forcefield was used. Next, 100 ps constant-NVT MD simulation was performed at 600 K to relax the average molecule structure, followed by 500 ps constant-NPT MD simulation to obtain optimized density. The system was then cooled stepwise to 273.15 K with the rate of 50 K/600 ps. At each temperature, a constant-NVT MD simulation of 100 ps and a constant-NPT MD simulation of 500 ps with time step 1 fs were carried out. It can be observed that the time-averaged densities at all temperatures tend to be in steady states at the latter stage.

Finally, the resulting configurations with the experimental densities appropriate for the temperatures were used to initiate constant-NVT dynamics for a period of 2 ~ 3 ns. For higher temperatures (298 K), 2 ns constant-NVT dynamics was performed,

whereas for lower temperatures (273 K), 3 ns constant-NVT dynamics was performed. This is due to the fact that the model system relaxes more slowly to equilibrium at the lower temperatures. In terms of non-bonding interaction treatments, separate methods were employed for the van der Waals interactions and Columbic interactions. For the former, atom-based direct cutoff of 9.5Å and a buffer of 0.5 Å were used, whereas for the latter Eward summation were employed in constant-NVT MD and constant-NPT MD simulations, respectively, depending on the accuracy and efficiency of the computation. Velocity Verlet algorithm with a time step of 1.0 fs was used for the integration of the atom motion equations throughout all MD simulations. Nose-Hoover method and Andersen method were adopted for controlling the temperature and pressure, respectively.

5.4.2 Mixture Model System Run

In task-2, we employed 2 three-component systems as simple computational models of asphalt. We chose two model asphaltene molecules from the literature [76, 78, 91, 93] to represent an asphaltene component, 1,7-dimethylnaphthalene to represent resin naphthene aromatic, and n-C22 to represent a saturate component. In the mix_1 asphalt system, we used 5 asphaltene_1 molecules suggested by Artok et al. [91], 27 of 1,7-dimethylnaphthalene, and 41 of n-C22 molecules, whereas in the mix_2 asphalt system, we used 5 asphaltene_2 molecules suggested by Groenzin and Mullins [83], 35 of 1,7-dimethylnaphthalene, and 45 of n-C22 molecules.

For the simulations, an explicit atom representation for each molecule was used. This is computationally more expensive than representing many atoms as a single site (united atom model) but can lead to more accurate estimates of intermolecular packing. The CVFF-aug force field supplied required parameters for each atom. Asphalt molecules are organic large molecules, so there are chemical bindings, called connectivity, between organic atoms. Required forcefield parameters, including nonbonded and bonded interaction parameters are listed in Table 5-3. Bonded interaction parameters are built on CHARMM potential, a commonly used potential function for organics. The well known high performance parallel MD software, LAMMPS [40], is employed in all of the simulation in this research. In order to analyze the temperature dependent thermodynamic

properties of the model asphalt systems, 2 different temperatures were chosen: 273.15 and 298.15 K, respectively, in this study.

Molecular configurations were initialized in the model construction. Each asphalt model systems were packed into a 3D periodic cell box according to condensed compact theory [94]. We applied molecular dynamics at constant volume and temperature NVT using the velocity rescaling method for 120 ps. This can dissipate initially high energies and helps to keep the system stable. Then we continued in the isothermal-isobaric NPT ensemble using the Nosé-Hoover thermostat and barostat for at least 2 ns to shrink system volume. After reaching the sampling state, in which systems showed consistent and steady instantaneous volume fluctuations around the average volume, we continued with NVT simulation Nosé-Hoover at the average volume using a 1.0 fs time step. We simulated in the sampling state for 10 ns, depending on temperature the lower the temperature, the longer the simulation time, collecting atom position data every 1 ps.

The time step size is critical in MD simulation. Here, the time step size is chosen by comparing energy drifts in NVE simulations at different average temperatures. Our results showed that a large energy drift occurred with a time step of 2.0 fs or more. While the total energy drifted much less with a time step of 1.5 fs but still showed large energy fluctuations. Time steps of 1.0 and 0.5 fs led to similar energy conservation. In the NPT system, we used a time step of 0.5 fs to ensure system stability and keep the system from energy explosion. In production runs we chose a 1.0 fs timestep to access longer production times. NVT simulation was chosen for sampling dynamics since a barostat has been shown to influence dynamics results. Flexible bond lengths and angles were used since constraints can affect chain dynamics.

At higher temperatures, the simulation procedure leads to better products, because the total simulation time exceeds the asphalt relaxation time at 293.15 and 273.15 K values. In addition, the 2 ns at constant pressure exceed the relaxation time of the dimethylnaphthalene and n-C22. The relaxation of each asphaltene molecule thus occurs in an equilibrated environment of large molecules. At lower temperatures, only dimethylnaphthalene relaxes completely over the time scale of the simulation.

5.5 Asphalt Dynamic Properties from MD Simulations

Thermodynamic properties like the cohesive-energy density, the viscosity (in NPT ensemble) or the pressure (in NVT ensemble) are also explored in the MD simulations. The pressure information can be introduced into asphalt systems by the so-called ramp correction. Since the initially optimized structure yield a pressure different from the one at which the atomistic simulation are performed.

5.5.1 Cohesive Energy Densities

In atomistic simulations, the cohesive energy is defined as the increase in energy per mole of a material if all intermolecular forces are eliminated. The cohesive energy density corresponds to the cohesive energy per unit volume. Mixing energy, ΔE^M, of two liquids molecules as:

$$\Delta E^M = const\left(\left[\left(E_{CED,1}\right)^{\frac{1}{2}} - \left(E_{CED,2}\right)^{\frac{1}{2}}\right]\right)\phi_1\phi_2 \qquad (5\text{-}1)$$

where ϕ_i denotes volume fractions of the two species, E_{CED} is the cohesive energy density (CED).

Accordingly, making the assumption that the entropy of mixing is purely combinatorial and using equation (5-1) for the heat of mixing should, in principle, allow calculation of the phase diagram for any mixture system given only a knowledge of the volume fractions and cohesive energy densities of the components.

In practice, this initial expectation has proved to be oversimplified for most mixtures of small molecules. However, cohesive energies for mixtures of liquids from different classes are still used as an approximate guide in solubility prediction, especially when the entropy of mixing is largely combinatorial. Moreover, the concept of cohesive energy has found uses in predicting other aspects of behavior such as mechanical properties.

When calculating the cohesive energy density for each asphalt model, it is important to ensure that the effect of truncation of the non-bond potential has been taken into account. Hence, the cohesive energy is given by an ensemble average of the quantity:

$$E_{CED} = U_{intra} - (U_{calc} + \delta U_{tail}) \tag{5-2}$$

where U_{intra} denotes the intra-molecular energy of the parent molecules, U_{intra} is the energy given by the simulation (with cutoffs), and δU_{tail} is given by

$$\delta U_{tail} = \frac{1}{2}\sum_{\alpha=1}^{\nu} N_\alpha \sum_{\beta=1}^{\nu} \rho_\beta 4\pi \int_{r_c}^{\infty} r^2 g_{\alpha\beta}(r) U_{\alpha\beta}(r) dr \tag{5-3}$$

where the N_α denote numbers of atoms of the specified type and the ρ_α and ρ_β denote number densities.

5.5.2 Viscosity

Shear viscosity often referred to as simply viscosity, describing the reaction to applied shear stress. Simply put, it is the ratio between the pressure exerted on the surface of a fluid, in the lateral or horizontal direction, to the change in velocity of the fluid as you move down in the fluid.

Time dependent correlation functions are used to measure how the value of a given dynamic quantity, $A(t)$, may be related to the value of another quantity $B(t)$, these functions can be computed directly from molecular dynamics data.

Here we give a definition of time correlation function. If $A(t)$ and $B(t)$ represent two time-dependent signals, then the time correlation function is defined by

$$C(t) = \lim_{x\to\infty} \frac{1}{\tau} \int_{t_0}^{x} A(t_0) B(t_0 + t) dt \tag{5-4}$$

where A is sampled at the time origin t_0 and B is sampled after a time delay, t. The correlation function, $C(t)$, depends on the time delay but is independent of the time origin-correlations of this type are said to be stationary.

Specifically, in this study, stress autocorrelation function (SACF) is defined by:

$$SACF = \langle P_{ij}(t) P_{ij}(0) \rangle \tag{5-5}$$

where $\langle ... \rangle$ denotes a statistical average over time origins and where $P_{ij}(t)$ is the off-diagonal component of the pressure tensor.

In equilibrium molecular dynamics (EMD), the shear viscosity is obtained from

pressure or momentum fluctuations based on the Green-Kubo (GK) relations. Application of the GK method to the shear viscosity gives the following relation between shear viscosity and the time correlation functions involving the off diagonal components of the pressure tensor:

$$\eta = \frac{V}{kT}\int_0^\infty \left\langle P_{ij}(t) P_{ij}(0) \right\rangle dt \tag{5-6}$$

where V denotes the system volume, T denotes the system temperature, and k denotes Boltzmann constant.

The bulk viscosity η_v is related to the decay of fluctuations in the diagonal elements of the stress tensor as follows:

$$\eta_v = \frac{V}{kT}\int_0^\infty \left\langle \delta P(t) \delta P(0) \right\rangle dt \tag{5-7}$$

The viscosities of asphalt and structural changes under shear flow are of great practical importance in manufacturing and processing of pavement asphalts. Viscosity measurements have been employed for many years as a technique for evaluating asphalts. Atomistic calculation of shear and bulk viscosities in this research are both explored by using Green-Kubo method [95], which is an integral over the stress autocorrelation function (SACF).

5.6 Results

MD simulations were performed to estimate a couple of properties of the 3 model asphalts. Thermodynamic quantities, such as temperature, Radial Distribution Function (RDF), density concentration profile, Mean Square Displacement (MSD), stress auto-correlation function, shear viscosity, bulk viscosity, are extracted from MD trajectories for interpreting asphalt bulk mechanical behaviors of various models.

5.6.1 Average Asphalt Structure Model

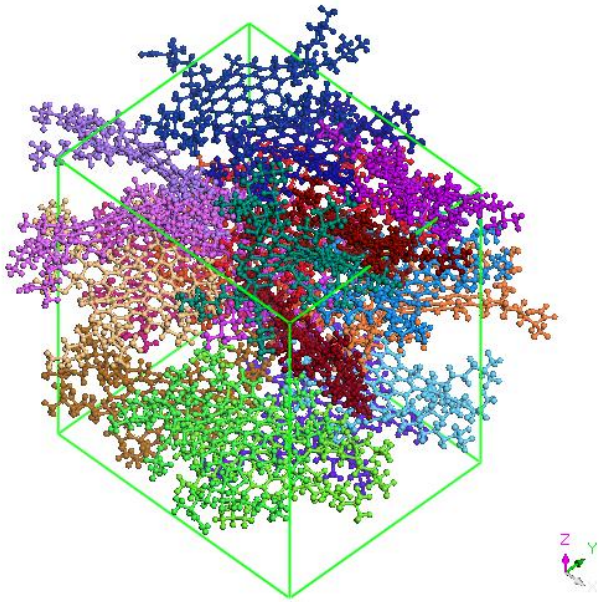

Figure 5-7 Visualization of the relaxed average asphalt model

In this subsection, the MD simulations are carried out on the average asphalt system. MD simulations are performed on the average asphalt model shown in Figure 5-7, with NVT ensemble at 298.15 K and 273.15 K, respectively. This model size is of a=39.30 Å, b=32.43 Å, c=46.52 Å, α=90°, β=90°, γ = 90 °. There are 20 molecules, 5760 atoms, 6200 bonds, 12180 angles, and 19340 torsions involved in this simulation. Long range Coulomb and electric calculation are adopted. Pressure and energy tail corrections are added to all subsequent energy evaluations.

5.6.1.1 RDF (Static Properties)

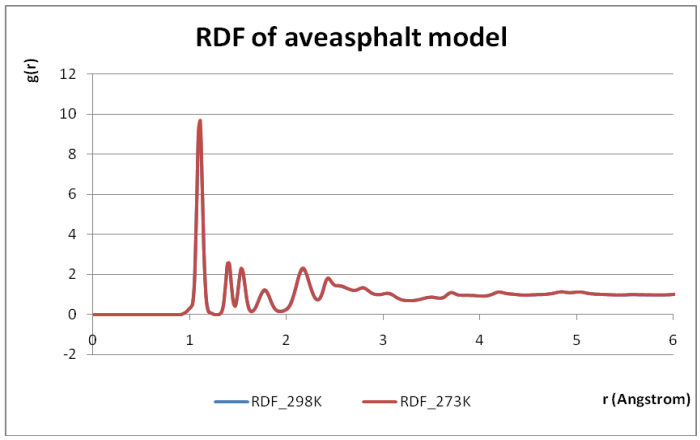

Figure 5-8 RDF of average asphalt model with 298K and 273K, respectively

The structural properties of the average asphalt molecules are most conveniently described by distributions of geometric quantities, which can be intramolecular or intermolecular. The intramolecular properties can be distances between two adjacent atoms, angles between three subsequent atoms, dihedral angles between four subsequent atoms, principal values of the radius of gyration tensor and so forth. The intermolecular properties involve distances between the atoms belonging to different molecules. All these properties have to be calculated upon the available MD trajectories.

In statistical mechanics, a radial distribution function (RDF), g(r), describes how the atomic density varies as a function of the distance from one particular atom. More precisely, if there is an atom at the original point O, and if n = N/V is the average number density, then the local density at distance r from O is $n \cdot g(r)$. A detailed derivation of RDF is demonstrated in the Appendix.

Firstly, the structural aspects of the average model were examined using radial distribution functions (RDFs). Calculated RDFs at two temperatures 273.15 K and 293.15 K are shown in Figure 5-8 for the average asphalt model bulk system. All atoms and the last 1000 configurations from constant-NVT MD simulations were included in these calculations. Common features are demonstrated for the two different temperatures. The first peak at around 1.1 Å corresponds to the bond distance between hydrogen and other atoms. The second peak at around 1.45 Å comes from the bond distance between carbon and non-hydrogen atoms. The third peak at around 1.65 Å is attributed to the distance between the two hydrogen atoms in the aromatic ring group. The subsequent intramolecular peaks result from distances between atoms two bonds apart, such as hydrogen and carbon.

Among these peaks, the atom pairs associated with polar atoms are not expected to exhibit an important contribution because of the much lower fraction. Other peaks up to 4 Å are of intramolecular origin and reflect mainly relative positions and interactions between non-bond atoms separated by bonds. Note that any sharp peaks at distances greater than 4 Å are absent and the RDFs tend to 1, which is generally regarded as the proof of the amorphous nature of the asphalt system. The intermolecular contributions to the total RDFs, shown in Figure 5-8, provide another proof in that no sharp peaks are

observed in this distance range, which is consistent with the absence of long-range order. The presence of some small sharp peaks at distance less than 4 Å is due to the artificial treatments of constructing the model, e.g. some chemical bonds in the central cell crossover the periodic boundary with those in the image cells.

As far as the temperature dependence is concerned, the total RDFs exhibit the same quantities of the system at two temperatures. Such accordance represents the less temperature dependence behavior for the average asphalt model, which give a rigid property by it structural nature.

5.6.1.2 Potential Energy

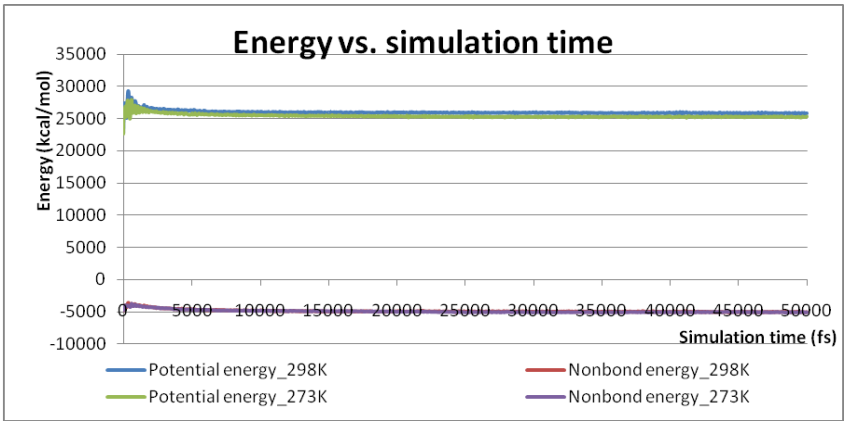

Figure 5-9 Potential energy and Nonbond energy of average asphalt model at 298K and 273K, respectively

Based on the potential energy and nonbond energy plotted in Figure 5-9, after a short fluctuation at the first 5ps the system potential energy advances smoothly at both 298K and 273K. As far as the temperature dependence is concerned, the Potential energy exhibit slight variations in the height of the initial stage peaks and along the simulation progress. The Nonbond energy at 298 K is slightly higher than that at 273 K. As depicted in Figure 5-9, the nonbond energy at two temperatures is roughly in accordance with each other, which reveals little change in nonbond interaction of the average asphalt model system at such a little temperature difference.

5.6.1.3 MSD (Dynamic Properties)

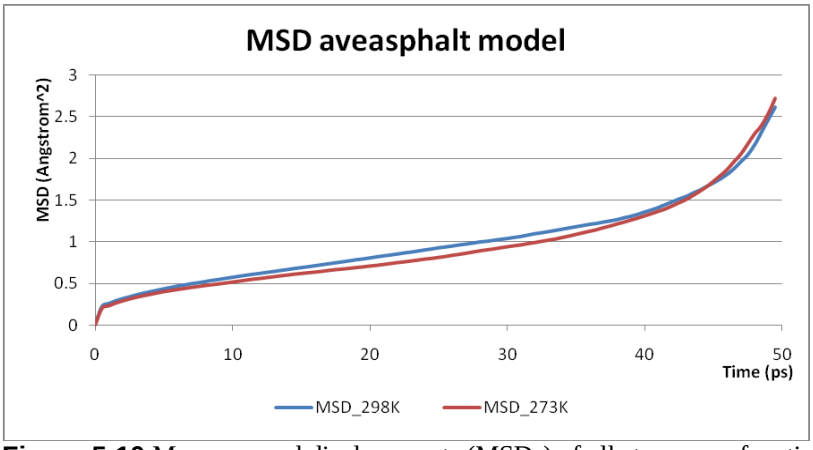

Figure 5-10 Mean squared displacements (MSDs) of all atoms as a function of time with 298K and 273K, respectively

Generally, the rigid average asphalt molecules exhibit much lower mobility than the mixture asphalt model due to topological constraints. These differences can be characterized by calculating mean squared displacements (MSDs) according to the following relation

$$MSD = \frac{1}{3N}\sum_{i=0}^{N-1}\left\langle \left|\vec{R}_i(t) - \vec{R}_i(t)\right|^2 \right\rangle \tag{5-8}$$

where R is the position of the atom, N is the total number of the atoms of a given type, and the broken brackets denote averaging over all choices of time origin.

On the basis of the trajectory outputs of the average model from the 200-ps MD simulations, the mean-square displacement (MSD) is calculated. The MSD values for all atoms were calculated according to equation (5-8) by preparing time-series data items of length Δt (1.0 fs in this study), and averaging the data items on the basis of the number of atoms. Figure 5-10 displays time dependency of the MSD for all atoms. Only the first 50 ps out of 1000 ps are plotted because of two reasons: the motion was generally very slow and most movements were finished in the former several hundred picosecond intervals.

From the computed MSD, a 200-ps running period was found to be long enough for the average asphalt MD model, as shown in Figure 5-10 by the MSD. With NVT ensemble, the MSD of average model start with a slope at the beginning of simulation. Then MSD is followed by a smooth increase, which means the MD system is under a

relax procedure, but the displacement is not that large. It is not until 47-ps, the MSD curve grows up sharply and ends at the highest point, which corresponds to a optimal potential point for the entire system. The MSD provides a full description of model molecules diffusion properties during equilibrium.

Based on the MD simulations conducted in this study, the mechanism of asphalt molecules diffusion, semi-liquid and temperature-dependent properties can be reasonably explained. The motion of the relatively rigid average molecular model is expected to be quite different from that of the chain molecules.

5.6.1.4 Concentration Profile

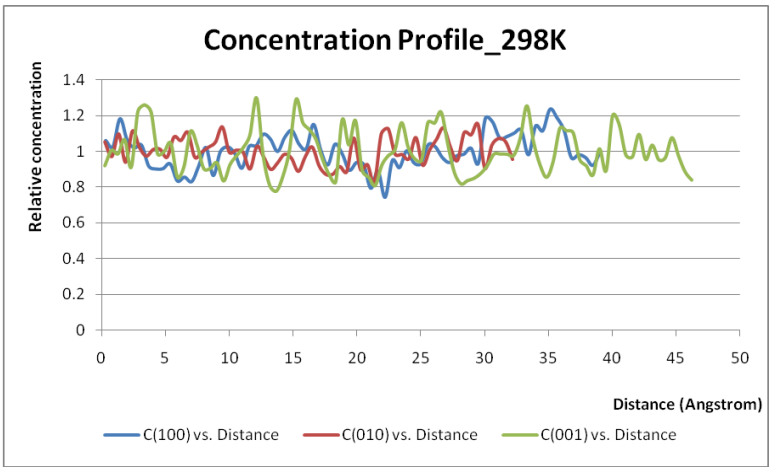

Figure 5-11 Concentration profile of aveasphalt model at 298K

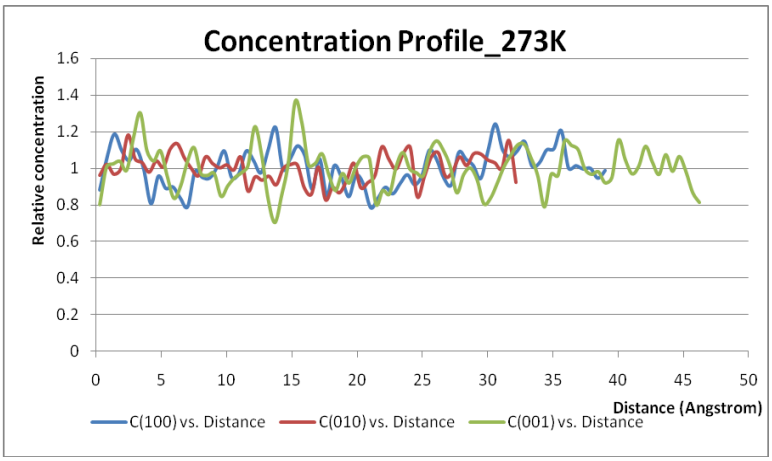

Figure 5-12 Concentration profile of aveasphalt model at 273K

Concentration profiles take coordinate information as input and plot the relative concentration of the specified atoms in layers parallel to specific planes.

The concentration profile results for average asphalt model at two different temperatures are shown in Figure 5-11 and Figure 5-12. Concentration at both temperatures in all three directions, (100), (010), and (001) show slightly fluctuation around a stable value of 1. This is in good agreement with our expected features, because the average model in of a roughly relaxed structure before the MD-NVT performed. The temperature-dependent concentration profiles also provide confidence that simulations based on the simulation protocol can lead to reasonable results for the constructed model average asphalt model.

5.6.1.5 Stress Autocorrelation Function

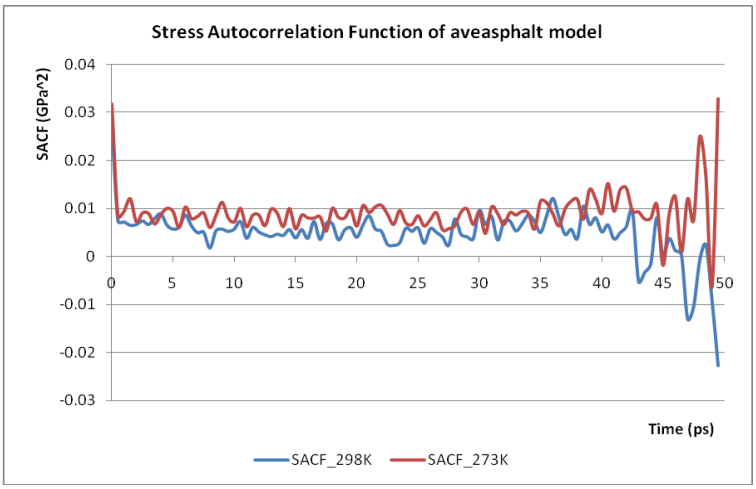

Figure 5-13 Stress Autocorrelation Function of aveasphalt model

The Stress Autocorrelation Function, shown in Figure 5-13, and the Viscosity, shown in Table 5-4 are studied for the average asphalt model. This model has rigid aromatic rings with more cohesive features, so we need to calculate its viscosity results with more precision in a less computation time.

Much of the decay of the SACF often takes place within 50 ps, the presence of slowly decaying components means that averaging must be performed over simulations of long duration to obtain accurate results.

Table 5-4 Bulk and Shear viscosity of aveasphalt model at 298K and 273K, respectively (Poise)

	273K	298K
Bulk viscosity	3.90547	1.25663
Shear viscosity	2.5005	1.2751

The model viscosity is calculated using the Green-Kubo method at temperatures of 273.15 and 298.15 K as a function of increasing integration time, and the results are shown in Table 5-4. As can be seen from the Table 5-4, shear viscosity of 2.5005 Poise at 273K is higher than that of 1.2751 Poise at 298K. The same temperature dependency properties are also shown in bulk viscosity of 3.90547 Poise at 273K, which is higher than that of 1.25663 Poise at 298K. Hence the reasonable temperature dependences of viscosity can be drawn from MD simulation.

5.6.1.6 Cohesive Energy Density

The cohesive energy density (CED) of average asphalt model at 273K is found to be $2.247\times10^{8} J/m^{3}$, while it is $2.238\times10^{8} J/m^{3}$ at 298K. The calculated instant CED of average asphalt model is given in Figure 5-14. During the evolution of CED curve, the same temperature dependency properties are also shown in cohesive energy density. The CED of 273K is a little bit higher than that of CED at 298K. This is a reasonable temperature dependence of asphalt semi-liquid properties, since with the temperature increases a little asphalt will show its trend to liquid.

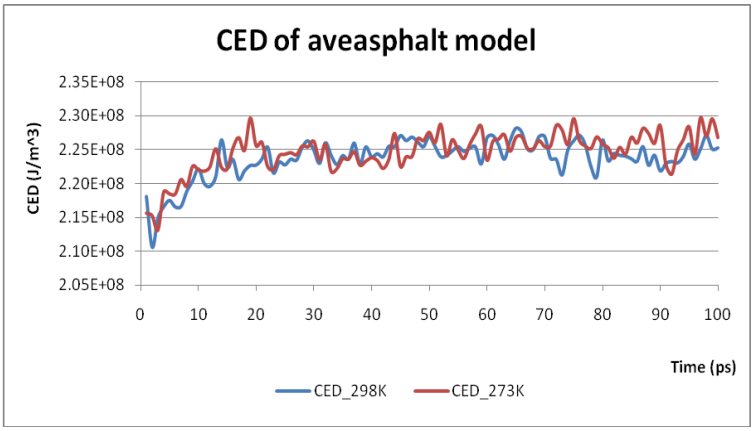

Figure 5-14 CED of aveasphalt model at 273K and 298K, respectively

5.6.2 Asphalt_mix1

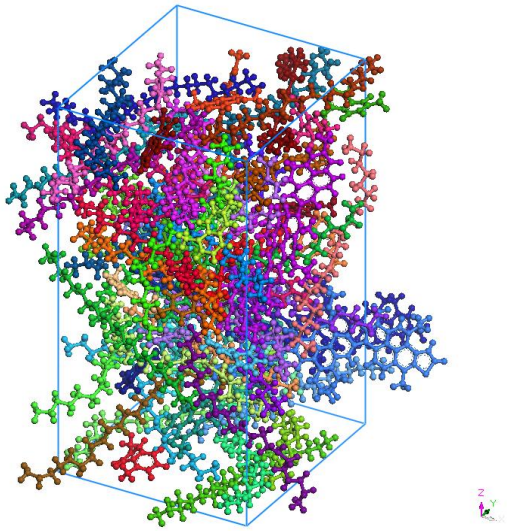

Figure 5-15 Visualization of the relaxed asphalt_mix1 model

MD simulation is performed on asphalt_mix1 model shown in Figure 5-15, with NVT ensemble at 298.15 K and 273.15 K, respectively. This model size is of a=24.57 Å, b=27.03 Å, c=48.64 Å, α=90°, β=90°, and γ = 90 °. There are 73 molecules, 4026 atoms, 4082 bonds, 7756 angles, and 11121 torsions included in this simulation. Long range Coulomb and electric calculation are adopted. Pressure and energy tail corrections are added to all subsequent energy evaluations.

5.6.2.1 RDF (Static Properties)

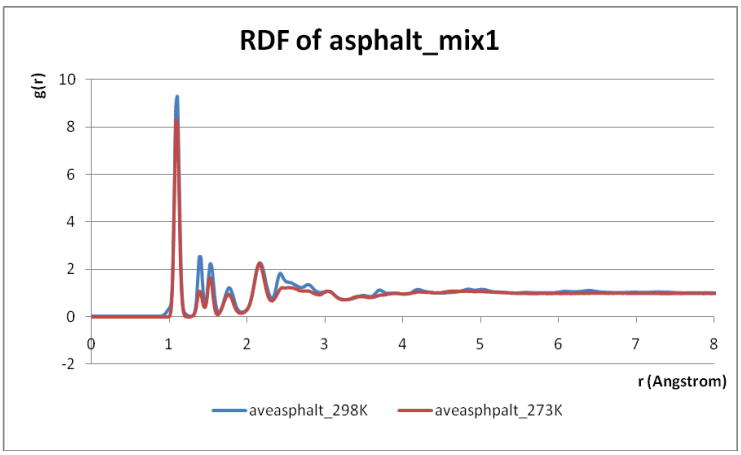

Figure 5-16 RDF of asphalt_mix1 model with 298K and 273K, respectively

Calculated RDFs at two temperatures 273.15 K and 293.15 K are shown in Figure 5-16 for this bulk system. All atoms and the last 1000 configurations from constant-NVT MD simulations were included in these calculations. Common features are demonstrated for the two different temperatures. Asphalt_mix1 demonstrates the RDF properties in a similar manner shown in average asphalt model. The first peak also appears at around 1.1 Å, which corresponds to the bond distance between hydrogen and other atoms. The second peak also appears at around 1.45 Å, and it comes from the bond distance between carbon and non-hydrogen atoms. The third peak at around 1.65 Å is attributed to the distance between the two hydrogen atoms in the aromatic ring group as well. The subsequent intramolecular peaks result from distances between two atoms with bonds apart, such as hydrogen and carbon.

As far as the temperature dependence is concerned, the total RDFs only exhibit slight variations in the height of the first and second peaks and along the simulation progress. The all atoms intermolecular RDF at 298.15 K is slightly higher at the first 4 peaks than that at 273.15 K, which reveals the change in density of the asphalt_mix1 system.

5.6.2.2 MSD

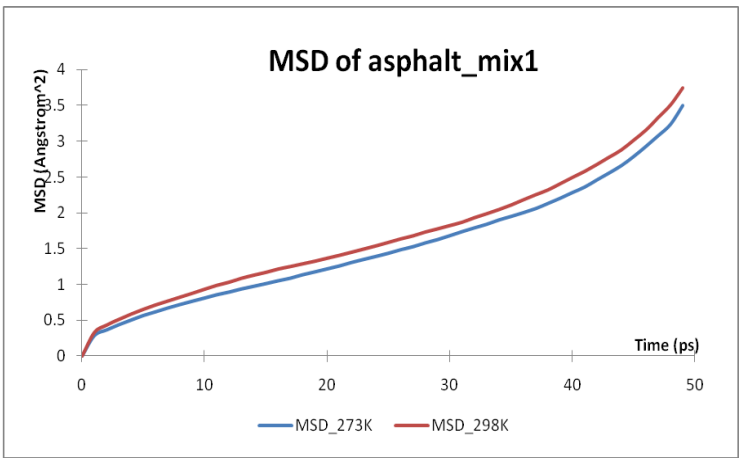

Figure 5-17 MSD for asphalt_mix1 model of all atoms as a function of time

Figure 5-17 displays time dependences of the MSD for all atoms. With NVT ensemble, the MSD of asphalt_mix1 model starts with a small slope at the beginning of

simulation. Then MSD is followed by a smooth increase, which means the MD system is under a relax procedure, but the displacement is limited. It is not until 47-ps, the MSD curve grows up sharply and ends at the highest point, which corresponds to a optimal potential point for the entire system. The MSD provides a full description of model molecules diffusion properties during equilibrium.

Considering the temperature dependence property, the total MSD of asphalt_mix1 only exhibits slight growth along the simulation progress. The all atoms MSD at 298.15 K is slightly higher at the first 4 peaks than that at 273.15 K, which reveals the higher thermal dynamic transportation properties in asphalt_mix1 system.

5.6.2.3 Temperature

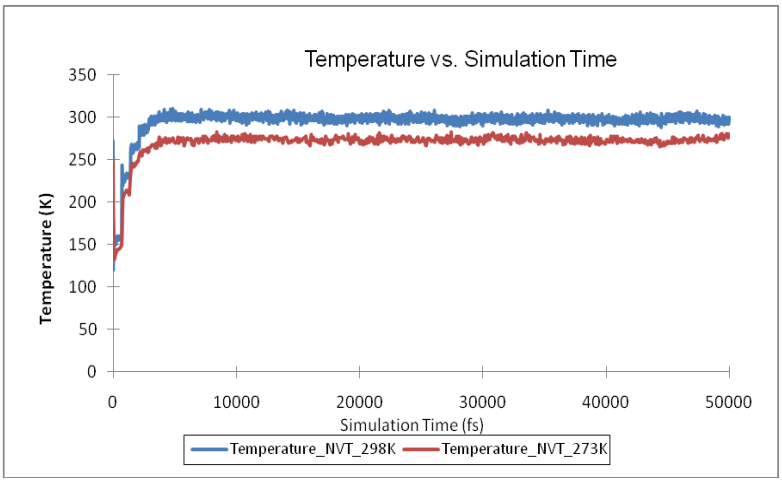

Figure 5-18 Temperature-time curve of asphalt_mix1 system

After the system enters into a stable state, simulation trajectories are analyzed. Temperature-time curve of asphalt_mix1 system under 298K and 273K is shown in Figure 5-18. As far as the temperature dependence is concerned, the system temperature exhibit slight variations in the first stage of the MD simulation, then followed by a smooth and stable state. The system temperature at with NVT-ensemble at 298.15 K is slightly higher than that at 273.15 K throughout the simulation process. Thus, the system represents pretty stable temperature features, through the running procedure.

5.6.2.4 Potential Energy

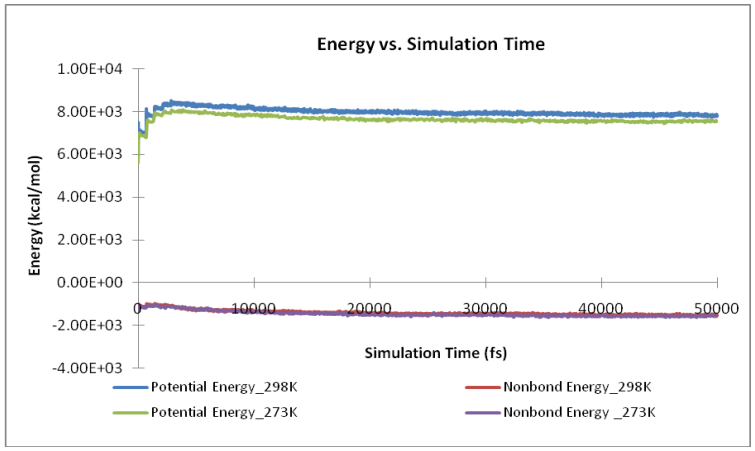

Figure 5-19 Energy-time curve of asphalt_mix1 system

Energy-time curves of asphalt_mix1 system under 298K and 273K are shown in Figure 5-19. As far as the temperature dependence is concerned, the total Potential Energy only exhibit slight variations in the first stage of the MD simulation, then followed by a gradually stable state. The Potential energy at 298.15 K is slightly higher than that at 273.15 K throughout the simulation process. As depicted in Figure 5-19, the intermolecular Nonbonded energy at 298.15 K is slightly higher than that at 273.15 K.

5.6.2.5 Concentration Profile

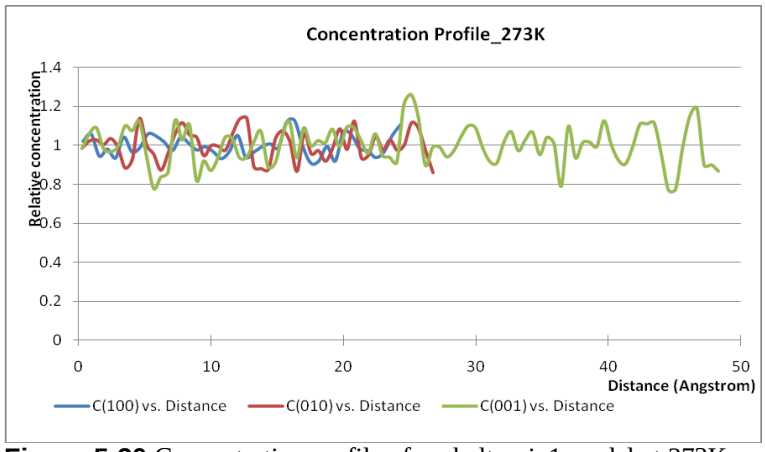

Figure 5-20 Concentration profile of asphalt_mix1 model at 273K

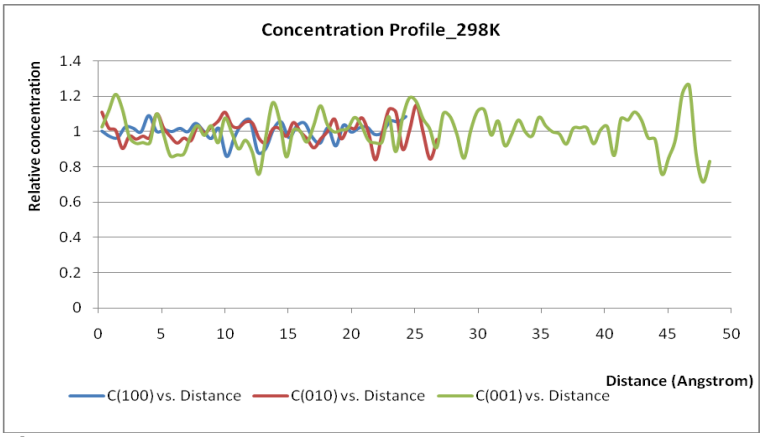

Figure 5-21 Concentration profile of asphalt_mix1 model at 298K

The concentration profile results for average asphalt model at two different temperatures are shown in Figure 5-20 and Figure 5-21. Concentration at both temperatures in all three directions, (100), (010), and (001) show slightly fluctuation around a constant value of 1. The temperature-dependent concentration profiles also provide confidence that simulations based on the simulation protocol can lead to reasonable results for the asphalt_mix1 model.

5.6.2.6 Stress Autocorrelation Functions

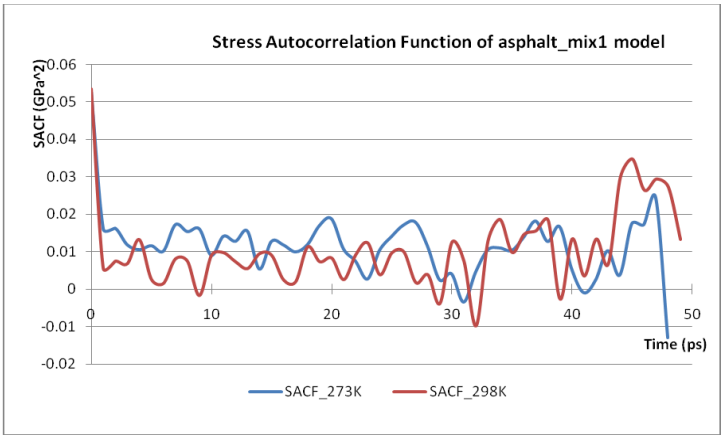

Figure 5-22 Stress autocorrelation function of asphalt_mix1 model at 298K and 273K, respectively

The Stress Autocorrelation Function, shown in Figure 5-22, and the Viscosity shown in Table 5-5 are studied for the asphalt_mix1 model.

Table 5-5 Bulk and Shear viscosity of asphalt_mix1 model at 298K and 273K, respectively (Poise)

	273K	298K
Bulk viscosity	0.892	0.149
Shear viscosity	1.678	1.207

The model viscosity is calculated using the Green-Kubo method at temperatures of 273.15 and 298.15 K, respectively, as a function of increasing integration time, and results are shown in Table 5-5. As can be seen from the table, shear viscosity of 1.678 Poise at 273K is higher than that of 1.207 Poise at 298K. The same temperature dependency properties are also shown in bulk viscosity of 0.892 Poise at 273K, which is higher than that of 0.149 Poise at 298K. Hence the reasonable temperature dependences of viscosity can be drawn from MD simulation.

5.6.2.7 Cohesive Energy Density

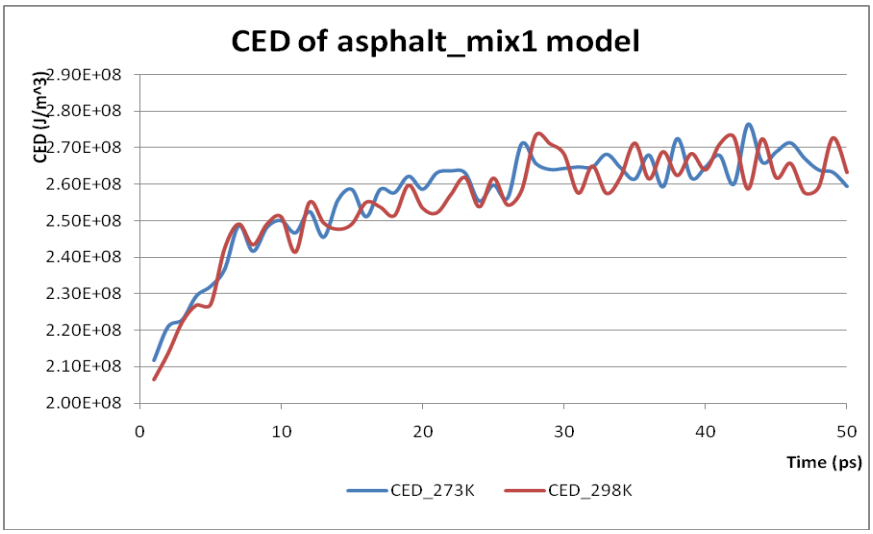

Figure 5-23 CED of asphalt_mix1 model at 273K and 298K, respectively

The cohesive energy density (CED) of asphalt_mix1 model at 273K is found to be $2.566\times10^{8}\,J/m^{3}$, while it is $2.551\times10^{8}\,J/m^{3}$ at 298K. The calculated instant CED of average asphalt model is given in Figure 5-23. During the evolution of CED curve, the same temperature dependency properties are also shown in cohesive energy density. The CED

of 273K is a little bit higher than that of CED at 298K. This is a reasonable temperature dependence of asphalt semi-liquid properties, since with the temperature increases asphalt will show its trend to liquid.

5.6.3 Asphalt_mix2

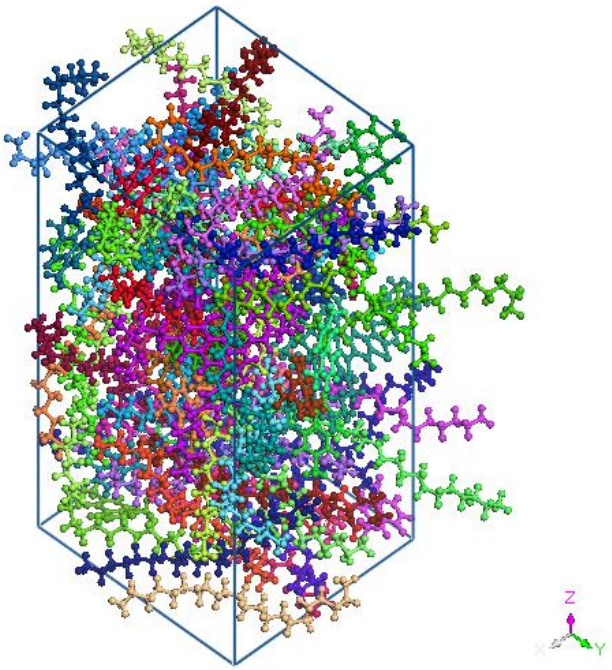

Figure 5-24 Visualization of the relaxed asphalt_mix2 model

The same simulation protocol is also applied on asphalt_mix2 model. MD simulation is performed with NVT ensemble at 298.15 K and 273.15 K, respectively, on asphalt_mix2 model shown in Figure 5-24, with NVT ensemble at 298.15 K and 273.15 K. This model size is of a=24.57 Å, b=27.03 Å, c=54.22 Å, α=90°, β=90°, and γ = 90 °. There are 80 molecules, 4635 atoms, 4660 bonds, 8915 angles, 12785 torsions included in this simulation. Long range Coulomb and electric calculation are adopted. Pressure and energy tail corrections will be added to all subsequent energy evaluations.

5.6.3.1 RDF (Structural Properties)

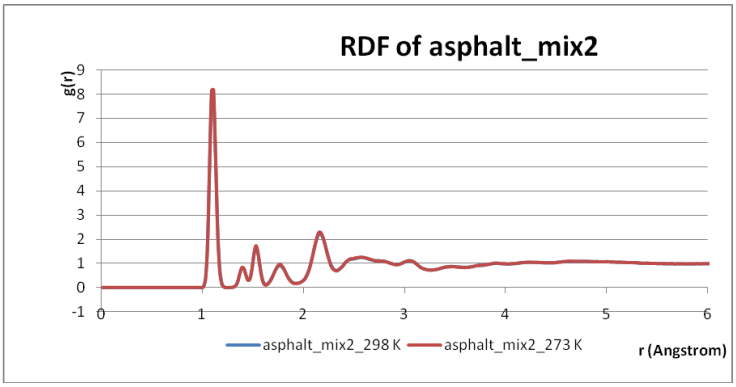

Figure 5-25 RDF of asphalt_mix2 model with 298K and 273K, respectively

Calculated RDFs at two temperatures 273.15 K and 293.15 K are shown in Figure 5-25 for asphalt_mix2 model. The same peak values are almost in agreement with those in asphalt_mix1 model.

As far as the temperature dependence is concerned, the RDF depicts the same quantities of the system at two temperatures. Such agreement represents the less temperature dependence behavior for the asphalt_mix2 than the asphalt_mix1 model. This is something related with the asphaltene structure and model composition in asphalt_mix2 model.

5.6.3.2 MSD

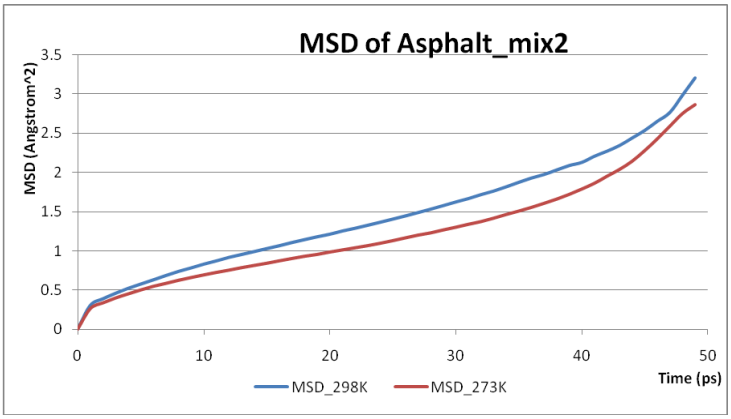

Figure 5-26 MSD for asphalt_mix2 model of all atoms as a function of time with 298K and 273K, respectively

Instant MSD values are displayed in Figure 5-26. With NVT ensemble, the MSD

of asphalt_mix2 model start with a small slope at the beginning of simulation. Then MSD is followed by a smooth increase, which means the MD system is under a relax procedure, but the displacement is limited. Gradually, the MSD curve grows up and ends at the highest point, which corresponds to an optimal potential point for the entire system. The MSD provides a full description of model molecules diffusion properties during equilibrium.

Considering the temperature dependence property, the total MSD of asphalt_mix2 only shows a slight growth along the simulation progress. The all atoms MSD at 298.15 K is slightly higher than that at 273.15 K, which reveals the higher thermal dynamic transportation properties in asphalt_mix1 system.

5.6.3.3 Temperature

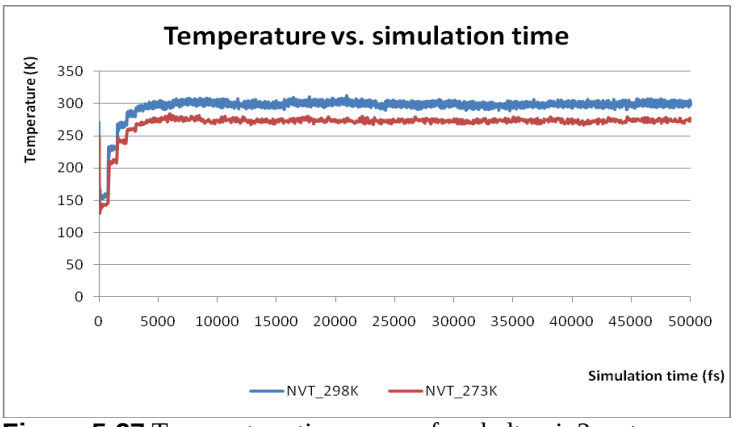

Figure 5-27 Temperature-time curve of asphalt_mix2 system

Temperature-time curve of asphalt_mix2 system under 298K and 273K, respectively, is shown in Figure 5-27. The system temperature exhibits slight variations in the first stage of the MD simulation followed by a smooth and stable state. The system temperature with NVT-ensemble at 298.15 K is slightly higher than that at 273.15 K throughout the simulation. Hence, good system thermodynamic properties can be drawn from the represents pretty stable temperature features, through the running procedure.

5.6.3.4 Potential Energy

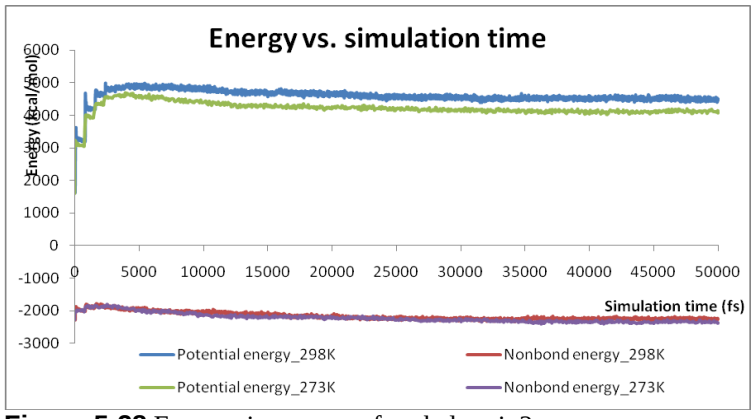

Figure 5-28 Energy-time curve of asphalt_mix2 system

Energy-time curves of asphalt_mix2 system under 298K and 273K are shown in Figure 5-28. As far as the temperature dependence is concerned, the total Potential Energy only exhibit slight variations in the first stage of the MD simulation, then followed by a gradually stable state. The Potential energy at 298.15 K is a little bit higher than that at 273.15 K throughout the simulation process. As depicted in Figure 5-28, the intermolecular Nonbonded energy at 298.15 K is slightly higher than that at 273.15 K.

5.6.3.5 Concentration Profile

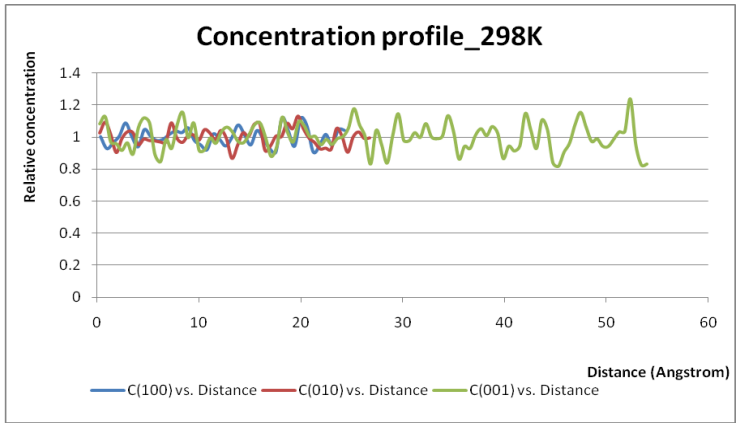

Figure 5-29 Concentration profile of asphalt_mix2 model at 273K

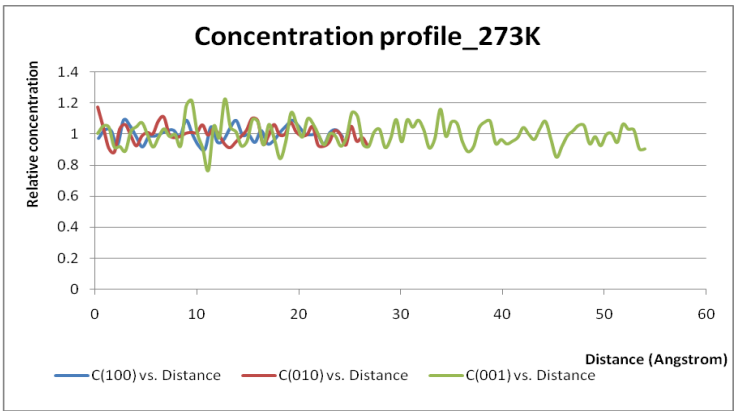

Figure 5-30 Concentration profile of asphalt_mix2 model at 273K

The concentration profile results for average asphalt model at two different temperatures are shown in Figure 5-29 and Figure 5-30. Concentration at both temperatures in all three directions, (100), (010), and (001) show slightly fluctuation around a constant value of 1. The temperature-dependent concentration profiles also provide confidence that simulations based on the simulation protocol can lead to reasonable results for the asphalt_mix2 model.

5.6.3.6 Stress Auto-correlation Functions

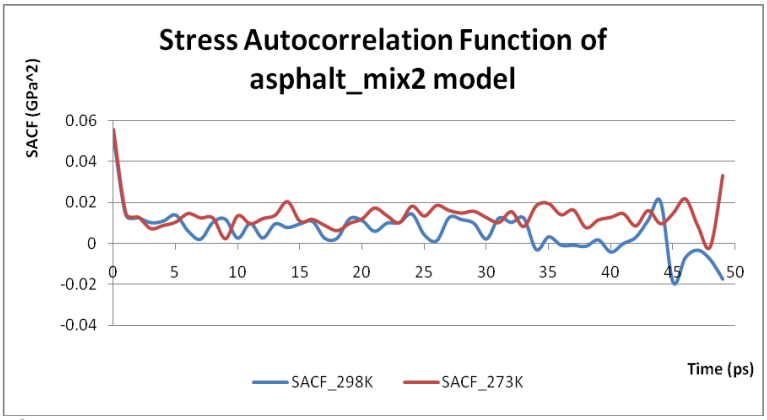

Figure 5-31 Stress autocorrelation function of asphalt_mix2 model at 298K and 273K, respectively

The Stress Autocorrelation Function, shown in Figure 5-31, and the Viscosity shown in Table 5-6 are calculated for the asphalt_mix2 model.

Table 5-6 Bulk and Shear viscosity of asphalt_mix2 model at 298K and 273K, respectively (Poise)

	273K	298K
Bulk viscosity	0.159	0.111
Shear viscosity	2.001	0.872

The model viscosity is calculated using the Green-Kubo method at temperatures of 273.15 and 298.15 K as a function of increasing integration time, and results are shown in Table 5-6. As can be seen from the table, shear viscosity of 2.00023 Poise at 273K is higher than that of 0.871786 Poise at 298K. The same temperature dependency properties are also shown in bulk viscosity of 0.159436 Poise at 273K, which is higher than that of 0.110855 Poise at 298K. The Reasonable temperature dependences of viscosity can be drawn from MD simulation.

5.6.3.7 Cohesive Energy Density

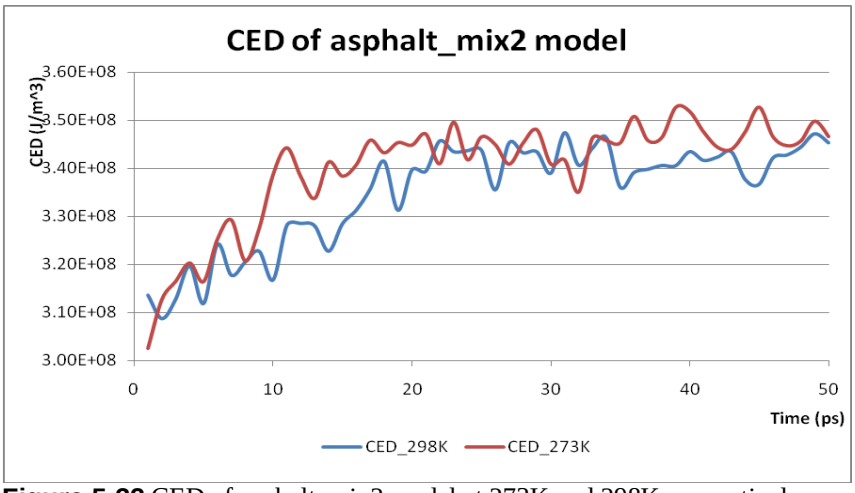

Figure 5-32 CED of asphalt_mix2 model at 273K and 298K, respectively

The cohesive energy density (CED) of asphalt_mix2 model at 273K is found to be $3.401\times10^{8}\,J/m^{3}$, while it is $3.349\times10^{8}\,J/m^{3}$ at 298K. The calculated instant CED of average asphalt model is given in Figure 5-32. During the evolution of CED curve, the same temperature dependency properties are also shown in cohesive energy density. The CED of 273K is a little bit higher than that of CED at 298K. But roughly the asphalt_mix2 model shows less temperature dependency properties in CED. This is could be due to the composition and molecular structures of the asphalt_mix2 model.

5.7 Discussion

Direct comparison with experimental measurements is not presently possible. All of the molecular models, including the average asphalt model and 2 asphalt mixture models, discussed here have a size of about 3~6 nm which is much smaller than typically treated experimentally. In comparison to macroscopic systems, the simulations correspond to the small region near the surface.

From the results obtained, it is illustrated the 3 models that RDF and MSD have temperature dependency properties. This is in accordance with thermodynamics. SACF and viscosity of three models demonstrate that the average asphalt model has the highest viscosity than the other two mixture models. Because average model is composed by only one type of rigid molecules, the fluidity of this large and rigid asphalt is relatively less than those of mixture models, which are composed by many soft and small molecules.

We make a comparison between mix1 and mix2 models. At 273K, mix1 model's shear viscosity is of 1.67795 Poise, which is less than that of mix2 at 2.00023 Poise. The same relation also appears at 298K. This may due to the fact that mix2 model has a larger asphaltene model than mix1. Based on the shear viscosity presented in Table 5-4, Table 5-5, and Table 5-6, average model has 2.5005 Poise at 273K and 1.2751 Poise at 298K, respectively. Mix1 model has 1.67795 Poise at 273K and 1.20712 at 298K, while Mix2 model has 2.00023 Poise at 273K and 0.871786 at 298K, respectively. Hence, viscosities of all 3 models show good agreement with the temperature dependency properties. Based on the bulk viscosity contained in Table 5-4, Table 5-5, and Table 5-6, they are in reasonable accordance with the temperature dependency properties.

In a similar manner, the temperature dependency properties appear in CED results as well. Average model has cohesive energy density of $2.247\times10^{8} J/m^{3}$ at 273K, while it is $2.238\times10^{8} J/m^{3}$ at 298K. Cohesive energy density of mix2 model is $3.401\times10^{8} J/m^{3}$ at 273K and $3.349\times10^{8} J/m^{3}$ at 298K, respectively. Mix1 model has $2.566\times10^{8} J/m^{3}$ at 273K and $2.551\times10^{8} J/m^{3}$ at 298K, respectively. The reason that CEDs of average model is small than those of mixture models lies in that much more space occurs in the average model. Because one simulation cell composed by only one type of big and rigid molecules cannot be condensed. Hence, a lot of free space is shown in relaxed average

model. On the contrary, in asphalt mixture models, large asphaltene molecules take the responsibility of big frame, while small size and soft molecules, e.g. aromatic rings, saturates, and resins act as fillers. This kind of size range makes a mixture model performing better than the average model. Thus, CEDs of mixture model are bigger than that of average model. Table 5-5 and Table 5-6 also depict that the model composition and structure of mix2 model is better than mix1 model. The reason could be mix2 model has relatively soft asphaltene_2 than asphaltene_1 in mix1 model. Furthermore, the mix2 model has more fillers (30 of 1,7-dimethyl naphthalene and 45 of n-C22) than those comprised in mix1 model (27 of 1,7-dimethyl naphthalene and 41 of n-C22 27), as illustrated in Table 5-1 and Table 5-2. Therefore, good ingredients and fraction of molecules plus a relatively soft asphaltene molecule may result in good cohesive energy density values.

5.8 Summary

In summary, based on the comprehensive analysis upon the relations between structure and properties, detailed MD simulations using CVFF-aug forcefield have been performed on one average model and two mixture asphalt models depend on real composition, density, and temperature. These models with various component structural features showed different thermodynamic properties, viscosities, and cohesive energy densities. Different specific simulation protocols comprising the constant-NVT and constant-NPT MD procedures within the studied temperature range were employed.

By adopting initial configurations appropriate for the experimental densities, constant-NVT MD simulations at the nanosecond scale can reveal many interesting results on local structure. The three asphalt systems exhibit reasonable features which are in agreement of temperature dependency properties demonstrated by typical radial distribution functions and mean square displacement.

Specially, the calculated results of radial distribution functions (RDFs) and mean squared displacements (MSDs) also indicated the important roles of model compositions, saturates, and resins with respect thermodynamical properties and mechanical properties of asphalt model systems. It is worth noting that 1 ns is long enough to obtain accurate

relative results of local structure and short-time dynamics from the equilibrated initial configurations.

The characteristics of bitumen at a particular temperature are determined by both the constitution (chemical composition) and the structure (physical arrangement) of the molecules in the bitumen. Changes to the constitution, structure or both will result in a change to the thermodynamic and mechanical properties. Thus, to understand changes in bitumen viscosity and cohesive properties, it is essential to understand how the structure and constitution of bitumen interact to influence the viscosity and cohesive properties.

Further work is expected in exploring these simulated results presented here using bigger size of system and higher conversion. Moreover, it is greatly desirable to compare these simulated results to the corresponding experimental data in the future.

Chapter 6
Advanced Image Characterization of the Multiscale Interface

6.1 Introduction

Experimental techniques that enable one to probe the multiscale properties of materials and structures have significantly developed. In particular, a rich set of experimental tools suitable to probe the materials behavior at micro- and nanometer lengthscales are now available. Since many fundamental deformation mechanisms operate at different scales, these approaches provide us with the opportunity to understand material theories and simulation results from multiscales.

Until more than 20 years ago, the scales accessible to mechanical testing of materials was largely limited to millimeter scales. Certainly, material properties of individual molecules or assemblies of molecules could not be determined. The early 1990s marked a decade of many new developments that enabled the study of material properties at ultra-small scales. The experimental analysis of such multiscale properties from nanoscale to macroscale is possible with techniques such as the High Resolution Optical Microscopy (HROM), Atomic Force Microscope (AFM) and environmental scanning electron microscope (ESEM), Focused Ion Beam (FIB), and Transmission Electron Microscopy (TEM). These techniques are based on the development of finer instrumentation and control mechanisms that enable one to characterize interface and surface morphology.

A key aspect in the analysis of the properties of asphalt concrete materials is the ability to test properties experimentally and to enable proper guidance to interpretation of the results. The combination of experimental testing with computational and theoretical

concepts has proven to be a particularly fruitful strategy, for both scientific discovery and for technological innovations and applications.

Mechanical properties are of interest throughout a range of lengthscales and timescales, and for a variety of applications. At larger scales, pavements must withstand enormous pressures and temperature ranges and different loading conditions. At smaller scales, reaching micrometers and scales much below, mechanical properties are quite important for reliability of devices.

Previously, optical, electron and scanning probe microscopy techniques have all been used to observe the structure of the asphaltene phase. Simple reflected or transmitted light microscopy has not normally been successful due to the black or dark brown color of bitumen, which prevents any contrast between the asphaltene and maltene phase from being observed.

Scanning electron microscopy (SEM) has been used successfully to characterize the structure of the asphalt phase. Although the resolution of electron microscopes is excellent, they do have some shortcomings. For example, SEM requires the use of a vacuum and depressed temperature, which can cause a change in the asphalt structure compared to that at ambient temperature and pressure; the volatility of the bitumen in the vacuum of the microscope observation chamber, its extreme susceptibility to electron beam damage. These problems have restricted the resolving power available for probing bitumen microstructure.

ESEM is a relatively new SEM technique that offers an approach to study this failure mode. The primary advantage of the ESEM over conventional SEM is that the ESEM does not require the test sample to be under high vacuum. Thus, wet, oily, dirty, or nonconductive samples can be examined in their natural state without modification or preparation. The sample environment can be varied through a range of pressures and temperatures. These factors combine to make the ESEM a powerful tool to investigate the asphalt-aggregate interface.

TEM is also employed to characterize the nanoscale interface in this dissertation. Although transmission electron microscopy (TEM) has been used to examine the dispersion of polymers in bitumen, no literature was found on the use of TEM for examining the structure of the asphalt-aggregate interface. The major advantage of TEM

in this application is that the bitumen sample requires little pretreatment that may affect the original dispersion of asphalt at the bitumen-rock interface. The FIB is used to prepare the sample to a required size and shape, which cannot be recognized by human eyes.

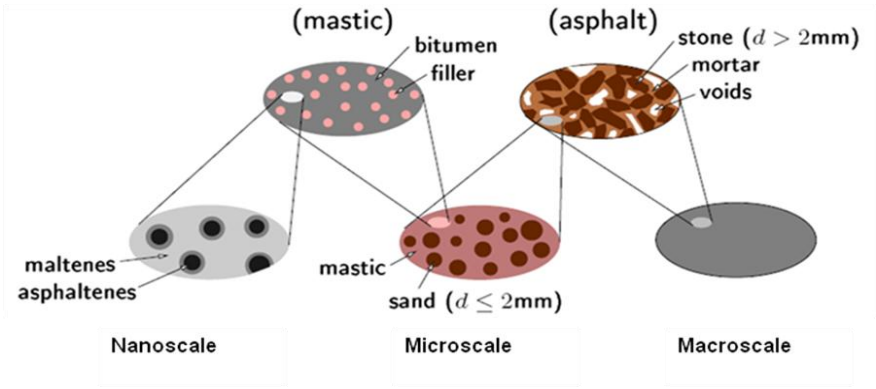

Figure 6-1 Multiscale model for determination of bitumen-rock interface morphology [96]

In order to account for the wide range of lengthscales of asphalt-aggregate interface, a multiscale scheme is proposed in Figure 6-1. It allows one to predict the mentioned temperature-dependent material functions by upscaling of information from finer scales of observation towards the macroscale. In Figure 6-1, four additional observation scales are introduced below the macroscale, namely (1) the nano-scale or atomistic, (2) the meso-scale or phase field morphology, (3) the micro-scale (bitumen and fine aggregate phase components), and (4) the macro-scale (mastic and aggregate).

At each scale of observation, the characteristics (such as structure and material properties) of the constituents present at this scale are obtained either from the next-finer scale by upscaling or need to be specified by respective experiments. Start from the lowest scale of observation, e.g. the nano-scale, this research deals with the identification of structures and material properties at the nano-scale. In the context of the multiscale model shown in Figure 6-1, the obtained results can serve as input for upscaling material parameters of bitumen towards the next-higher scale.

Note that the sample preparation is quite challenging for multiscale characterization and fabrication. Binder is a soft, heat sensitive, visco-elastic-plastic, semi-liquid material. However, aggregate is a solid mineral rock material. Chemical

composition of binder and aggregate can be determined by ESEM chemistry map. A lot of different physical, chemical and mechanical properties occur at the interfaces.

The research objectives of multiscale image characterization are to: characterize multiscale structure and composition of the interface in the asphalt-aggregate system using advanced image characterization technologies, e.g. HDOM, ESEM, AFM, FIB, and TEM. Start from the top scale, the 3D high definition optical microscopy is used to evaluate structure and homogeneity of interface morphology at macroscale. Then AFM is employed to characterize the mesoscale interface plot with contact mode. It is followed by determining the microscopic interfacial adhesion behavior from the ESEM data. Then FIB is adopted to characterize the microscopic interface and fabricate the nanoscale sample for TEM use. Finally, the most powerful tool, TEM, is used to determine the nanoscale morphology of the amorphous-crystal interface down to the atomistic scale. With the multiscale characterization of asphalt-aggregate interface, we may have better understanding of the interfacial deformation and failure behaviors, which stem from the tiny nanoscale and then upscale to the highest macroscale. The broader impact of this study is that it may result in significant saving of financial and other resources that are currently used to combat pavement distresses originating from interface failure.

6.2 Multiscale Interface Characterization Devices

In this study, the most advanced nanoscale characterization and fabrication devices are employed. A brief review of the instruments is illustrated as follows:

6.2.1 High Resolution Optical Microscope

The HRMS device used is the HIROX KH-7700 3D digital video microscope, shown in Figure 6-2. It is an optical inspection microscope used to image objects with rough surfaces or irregular topology, do optical comparisons, measure feature sizes in 2 dimensions and view objects from multiple perspectives. The optics is optimized for digital imaging, and it has a significantly larger depth of field than conventional optical microscopes.

Figure 6-2 HIROX KH-7700 3D digital video microscope at NCFL, Virginia Tech

6.2.2 Atomistic Force Microscope

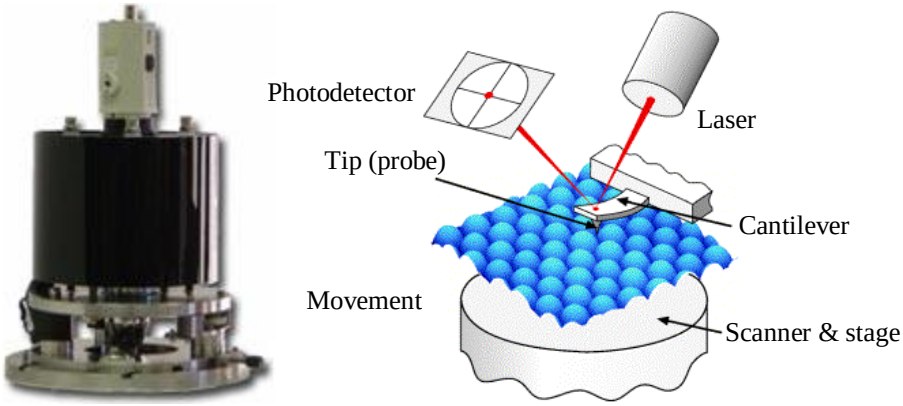

Figure 6-3 The ESPM 3D AFM at Center for Smart Infrastructure (CSI), VTTI

For the identification of properties at the meso-scale, the AFM is employed. During AFM measurements, the specimen surface is scanned by a silica or silica-nitride cantilever with a small tip (AFM tip) at the free end. The deflection w_s of the cantilever is detected by an optical lever method. Based on w_s, a picture representing properties at the specimen surface is obtained. Hereby, depending on the mode of measurement (contact versus pulsed-force mode), the surface topography can be identified.

When using AFM, the forces between the tip and the sample are governed by the attractive Van der Waals forces and the repulsive Pauli exclusion forces. In the case of asphalt there are also colloidal forces due to the presence of adsorption layers (resins on asphaltenes). These total interacting forces can therefore be repulsive or attractive, depending on the distance between the tip and the sample. When the atoms are not

strongly bound in the lattice, forces can destroy the organic sample. Therefore, if the oil phase in the asphalts is not bound, additional attraction between the cantilever and the oil can occur, thus leading to adhesion of the tip to the sample. Surface topography also needs to be as smooth as possible as any sudden change causes oscillation of the cantilever.

AFM can be operated in two different modes: height mode or force mode. In the height mode the force between the tip and sample is kept constant so that information on the topography of the sample can be obtained. With the force mode the tip scans the sample at constant height and force variations are recorded. Where different phases are present in the sample, interacting forces between each phase and tip can be different; therefore, local phase information can also be obtained with the force mode.

The ESPM 3D AFM is a specialized atomic force microscope, shown in Figure 6-3, for surfaces molecular patterning designed specifically for material science and nanoscience applications. It is capable of imaging in environments with temperature control. It can be used for spatial identification and mapping of molecules structures and studies of material composition. The results presented in this research used ESPM 3D AFM, located at the Center for Smart Infrastructure (CSI) in Virginia Tech Transportation Institute.

Schematically, in the imaging mode, a sharp tip is scanned over a surface and some surface parameter is monitored. Traditionally, the deflection of a cantilever holding the tip is monitored by a photodiode. When the tip scans across the surface, it will interact with the latter, and deflect according to the interaction: if there is an attractive interaction between the surface and the tip, the tip will be deflected towards the surface, whereas deflection away from the surface will occur in the case of a repulsive tip-surface interaction. In the most frequently used AFM technique, the deflection is kept constant through a feed-back loop, and the z-movement of the stage needed for accomplishing is monitored. From this, one essentially obtains an interaction map, which under certain conditions may be translatable to a topographic map.

The technique has many advantages, including capability of high resolution, no need for sample treatment or coating, no need for vacuum, and possibility for quantitative measurements of sample form, distribution and roughness over a range of magnifications.

Since there are many types of tip-surface interactions, different types of interaction maps may be obtained. Furthermore, different types of maps require slightly different tip-surface positioning: sometimes the tip is scanned in contact with the surface and sometimes it is scanned in non-contact. The contact mode is used in this study.

6.2.3 Environmental Scanning Electron Microscope

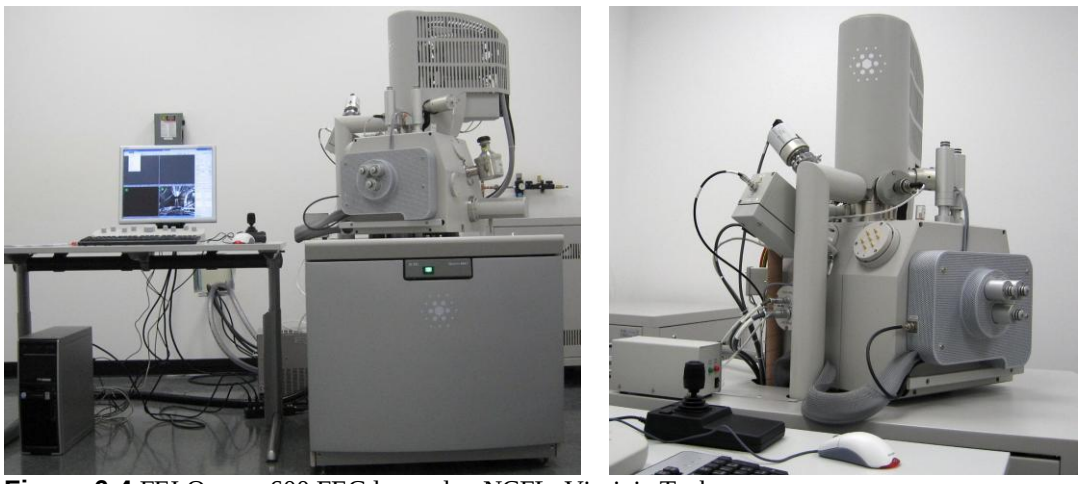

Figure 6-4 FEI Quanta 600 FEG located at NCFL, Virginia Tech

The FEI Quanta 600 FEG, shown in Figure 6-4, located in NCFL at Virginia Tech, is an environmental SEM that can operate in high-vacuum and low-vacuum modes. It is used to image samples that are difficult to impossible to image in high vacuum SEMs; in situ experiments such as hydrating, dehydrating and heating samples are possible with the ESEM. It can operate with pressures around the sample up to 4000 Pa and in conjunction with a Peltier stage can image fully hydrated samples, a critical advantage for imaging biological samples.

The FEI Quanta 600 FEG is equipped with:

- High-vacuum, low-vacuum, and extended vacuum modes

- A heating stage to 1000 C
- Bruker EDX with a Silicon Drifted Detector

Basically, an ESEM employs a scanned electron beam and electromagnetic lenses to focus and direct the beam on the specimen surface in an identical way as a conventional SEM. A very small focused electron spot (probe) is scanned in a raster form over a small specimen area. The beam electrons interact with the specimen surface layer and produce various signals (information) that are collected with appropriate detectors. The output of these detectors modulates, via appropriate electronics, the screen of a monitor to form an image that corresponds to the small raster and information, pixel by pixel, emanating from the specimen surface.

6.2.4 Focused Ion Beam

The focused ion beam (FIB) microscope has gained widespread use in fundamental materials studies and technological applications over the several years because it offers both high-resolution imaging and flexible micro-fabrication in a single platform.

The FIB instrument is similar to a scanning electron microscope (SEM), except that the beam that raster over the sample is an ion beam rather than an electron beam. Secondary electrons are generated by the interaction of the ion beam with the sample surface and can be used to obtain high-spatial-resolution images. In most commercially available systems, Ga ions are used, and their sputtering action enables precise fabrication of samples. In conjunction with the gas-injection capabilities on these systems, which enable ion-beam-activated deposition and enhanced etching, a range of sample fabrication schemes are possible.

During the last 25 years, FIB instrumentation has become an important technology for a wide array of materials science applications, from circuit editing and transmission electron microscopy (TEM) sample preparation to microstructural analysis and prototype nano-fabrication.

Most modern FIB instruments become a powerful platform for imaging, material removal, and deposition at length scales of a few nanometers to hundreds of microns. The FIB instrument becomes a powerful tool for nano-manipulation and fabrication through

the augmentation of an FIB instrument with micromanipulators and gas injection for local chemical vapor deposition (CVD).

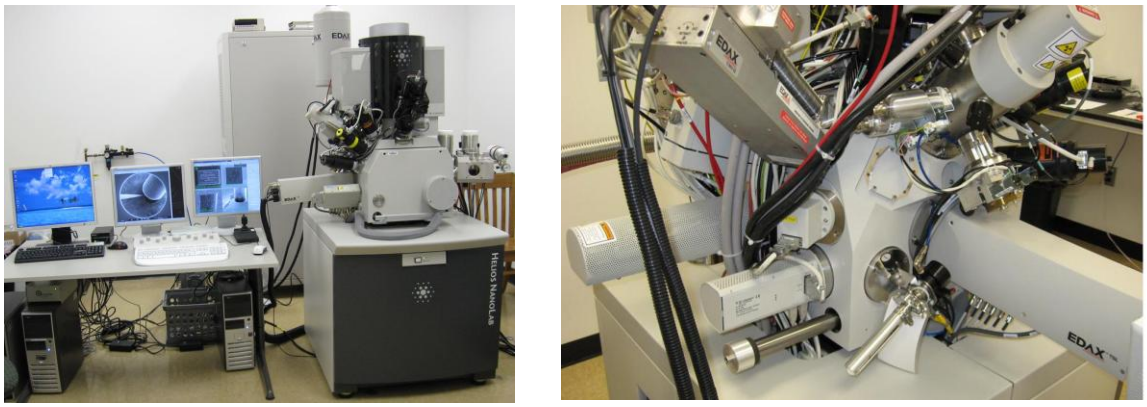

Figure 6-5 FEI Helios 600 NanoLab, located in NCFL at Virginia Tech

The FEI Helios 600 NanoLab, shown in Figure 6-5, located in NCFL at Virginia Tech, is a dual-beam workstation that combines a high-resolution SEM and a focused ion beam. It is used to dissect or deposit material at a micro- to nano-meter size scale. The instrument is capable of nanoscale lithography, deposition, and tomography, and it has a manipulator for precisely probing, straining, picking up and placing nanometer sized objects cut from or deposited on a larger samples.

The sample is mounted on a grounded stage with three-axis translation, rotation, and tilt capabilities. The stage is designed to have a eucentric point (e.g. a well centered point such that the field of view is maintained when tilting the specimen) at the location where the two beams cross (or at the working distance of the ion beam, in the case of a single-beam FIB). The region of interest on the sample is moved to the eucentric point using translation and rotation and then tilted for the desired angle of beam incidence. The total current on the sample (sum of the incoming ion or electron beam and all emitted charged particles) is measured at the stage.

Depending on the application, the various emitted particles or radiation can be detected with appropriate detectors in the sample chamber. The ions sputtered from the sample can also be detected using a variety of detectors such as charge electron multipliers, and mass selection of the sputtered charged particles is also possible.

The local deposition of material also enables sophisticated micromanipulation

within the FIB chamber, made possible through micromanipulation accessories and the ability of the FIB to cut (sputter), paste (deposit), and watch (image) during a manipulation process within the chamber. The result is a system that can image, analyze, sputter, and deposit material all with very high spatial resolution and controlled through one software program. In a large part, it is this multifunctional versatility that has made FIB instruments popular among materials researchers.

6.2.5 Transmission Electron Microscope

TEM has played a critical role in unraveling the microstructural and compositional origins of the rich variety of novel behavior exhibited by multilayer thin films. The TEM techniques that have been applied to the analysis of these materials range from simple bright-field imaging to determine parameters such as layer thickness in cross section, to electron holography, used to probe the electronic structure of the multilayer film.

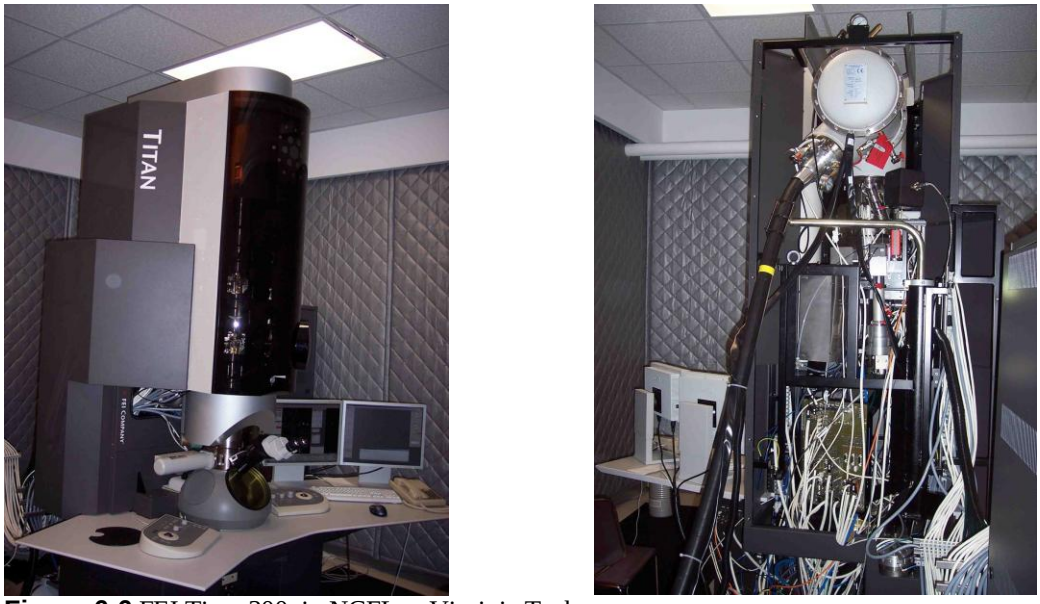

Figure 6-6 FEI Titan 300, in NCFL at Virginia Tech

The FEI Titan 300, shown in Figure 6-6, in NCFL at Virginia Tech, is a Scanning Transmission Electron Microscope that uses interactions between an electron beam and a thin sample to extract information about the structure and chemistry of materials. The instrument can image the arrangement of atoms within solids with sub-angstrom

resolution - the highest resolution available with any microscopy technique. It is used to study the nature of internal defects and interfaces that influence the mechanical, chemical, electrical, magnetic, and optical properties of solids.

6.3 Specimen Preparation

Specimen preparation techniques are very material dependent, therefore, it is important to initially select the technique that is most beneficial for the individual specimen. The multiscale characterization experiments need to prepare specimen from various scales.

Start from the macroscale, we cut one inch size interface sample from an asphalt-aggregate mixture compacted sample at low temperature. In order to prevent the asphalt layer from melting at the interface area, low speed cutting is maintained during the procedure. Then the sample is mounted on bracket of optical microscopy. The AFM sample is made from a piece of that sample, since no special treatment is need for AFM testing.

For ESEM characterization, samples are cut or cleaved into a suitable size for mounting. The selected sample was subsequently mounted on a pre-cooled ESEM shuttle. The shuttle with the sample was then plunged into a preformed temperature at -20 ℃ and transferred into the preparation chamber of a VG Microtech LT 7400 Cryo-Prep module (vacuum) at 10^{-4} Pa. Generally the specimen is about 4mm wide X 6-8 mm long. For site specific specimens, area of interest (AOI) should be about 1mm away from bottom edge. The integrated circuit devices and thin film specimens are commonly encapsulated on the top surface.

The specimen was subsequently coated with 1 nm of Pt, from a sputter head using ultrapure argon gas. Finally, the shuttle was transferred to a cold stage at -20 ℃. A VG Microtech anti-contaminator cold shroud -50 ℃ was located about 4 mm above the specimen. The temperature difference between the cold-shroud and the specimen surface ensured minimum deposition of contaminating molecules onto the observation surface. All the observations were performed at -20 ℃ using an accelerating voltage between 2 and 5 kV.

To limit contamination and creep of the original fracture surface morphology, the temperature of the sample was maintained as low as possible during the sample preparation. This ensured good reproducibility of sampling and subsequent analysis. During the sample preparation, the low temperature that creep effect does not drastically affect the morphology of the interface obtained at -20 ℃.

The goal of TEM specimen preparation is to produce high-quality micrographs which illustrate the microstructure accurately. So the sample should be free of artifacts and unaltered in any way. The coating should be thin over a large area. It should be clean and free of contamination, non-magnetic and conductive. For clarification, a sample preparation procedure chart is presented in Figure 6-7, as follows:

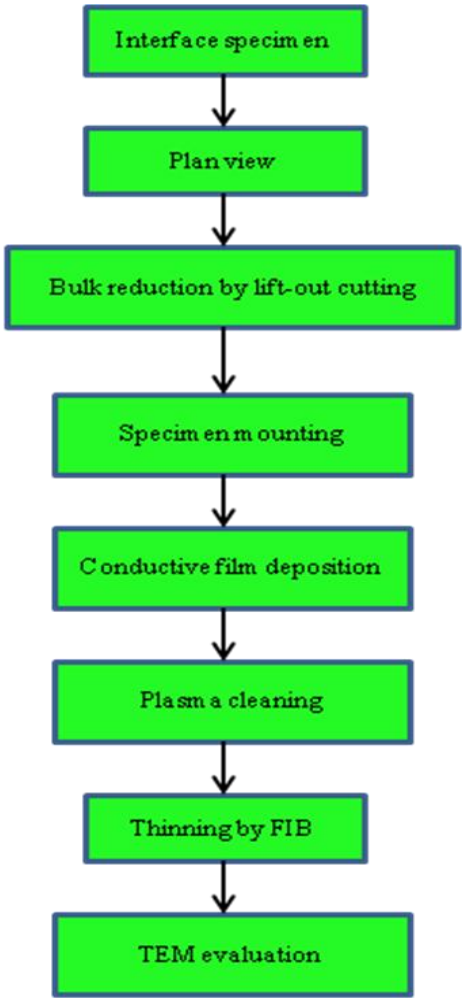

Figure 6-7 TEM sample Preparation Flow Chart

Once the specimen is mounted, conductive film deposition is made on the sample

surface. FIB is used to make a lift-out cutting preparation which includes an asphalt-aggregate interface structure.

6.4 Results and Discussion

With these series of techniques, a visual investigation on a large or small scale, into bitumen-mineral interfaces that have different chemical compositions and structures can now be made. It is interesting to note that, although asphalt and aggregate are homogeneous on a macro scale, the micro structures are highly heterogeneous. Although through human eye, perfect bonding interfaces can be observed on macroscale, when viewing asphalt aggregate at a variety of smaller scales, they show very imperfect interface structures.

6.4.1 High Resolution Optical Microscopy

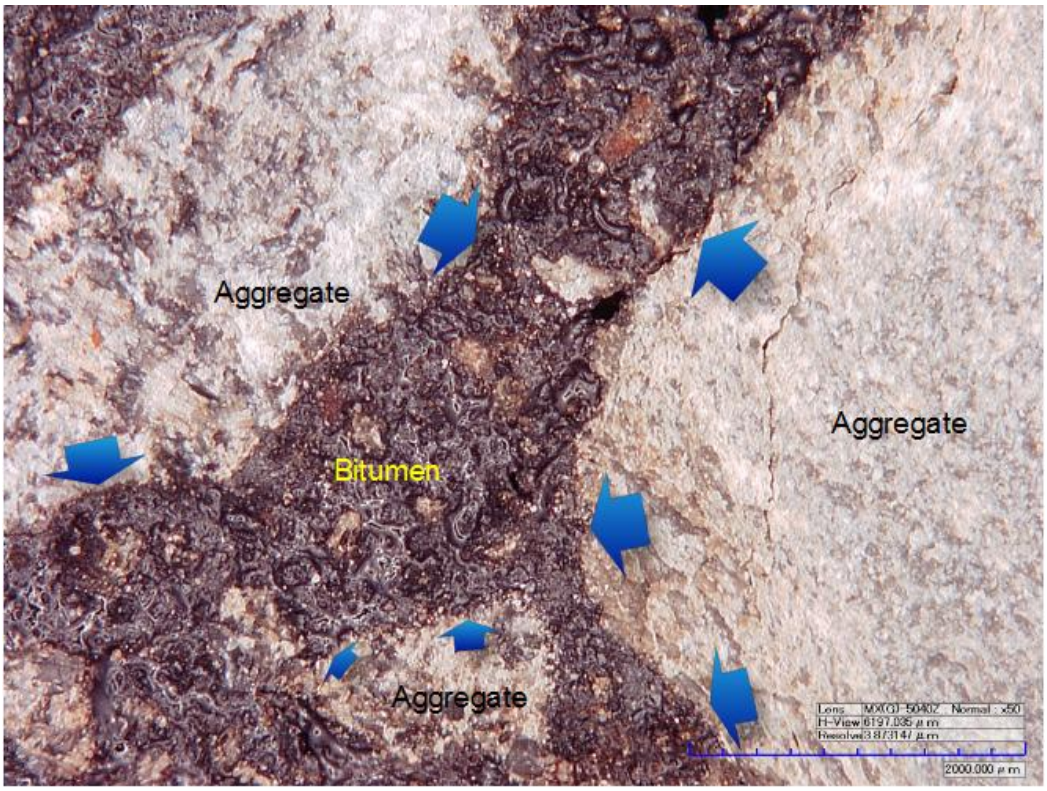

Figure 6-8 Digital Optical Microscope Image at Interface with X50, by 3D Digital Video Microscope at VT

Figure 6-8 illustrates a digital optical microscope image at the asphalt-aggregate interface with a magnification of X50. This is an overview of interface structure. As can be seen, large aggregates are scattered throughout this region and mastics fill the spaces between the gaps. The rough aggregate interfaces bonded very well with the bitumen at most places. Nevertheless, one hole is present at the edge along the interface.

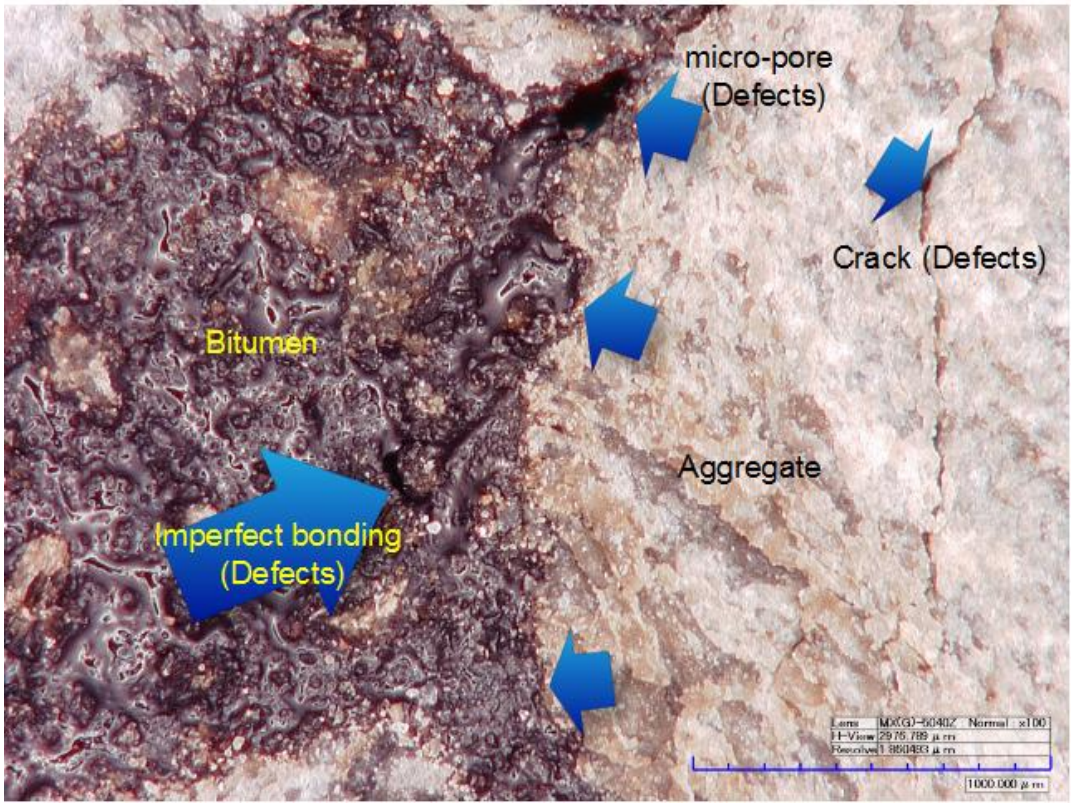

Figure 6-9 Digital Optical Microscope Image at Interface with X100

When we use a larger magnification, as shown in Figure 6-9, one can view a micro-pore in much more detail. This defective micro-pore could be due to the narrow space that exists between a micro-stone and the aggregate. Another imperfect bond can also be detected by viewing this image. A micro crack is located within the bitumen phase, and, in contrast to the micro-pore, it is not round, but linear. This crack could be due to the shrinkage within the asphalt phase. One interesting note is that a long and narrow crack also appeared in the aggregate phase. It appears as if the crack occurred naturally when the rock mineral was growing. Fortunately, this will not affect the interface behaviors.

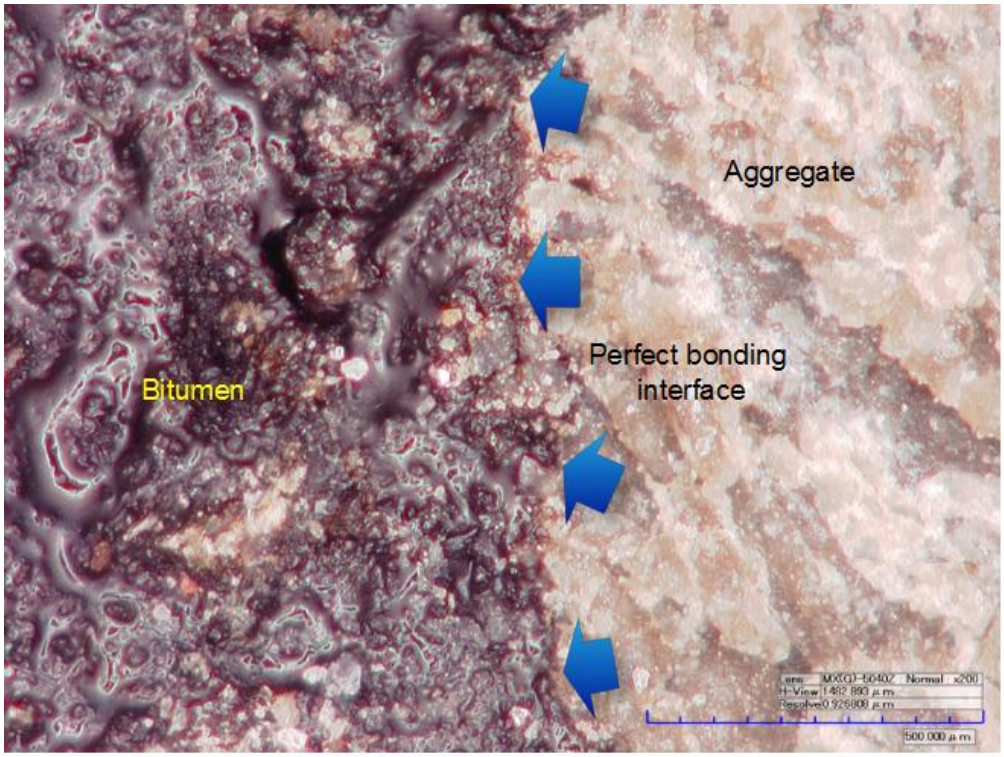

Figure 6-10 Digital Optical Microscope Image at Interface with X200, by 3D Digital Video Microscope at VT

Figure 6-10 illustrates a perfect bonding interface of bitumen-aggregate with a magnification of X200. As one can see, this interface is void of any micro-pores, cracks, or other defects.

6.4.2 Atomic Force Microscope

Mesoscale experimental studies of asphalt provide results on nanoscale properties. Atomic force microscopy (AFM) is gaining popularity for examining bitumen samples. One of the advantages of AFM is that it requires no sample preparation and operates under ambient conditions. Loeber et al. [97] and Pauli et al. [98] used AFM to observe bee-like structures of bitumen on the surface of a film, which they attributed to asphaltene networks. AFM was also used to measure mechanical force on asphalt [99] as a function of indentation over small distances. Comparable forces can be calculated from simulations. This scale is larger than that attainable from direct molecular simulations and sets an upper bound on the length scales over which properties can be considered uniform.

During AFM measurements employed the contact mode, the oscillation of the AFM cantilever, described by the amplitude corresponding to free oscillation A_0 [V], is reduced by both attraction and repulsion forces when approaching the bitumen surface. Using the aforementioned AFM equipment, these measurements were conducted with a frequency f [Hz] equal to the resonance frequency of the cantilever, f = 270 kHz.

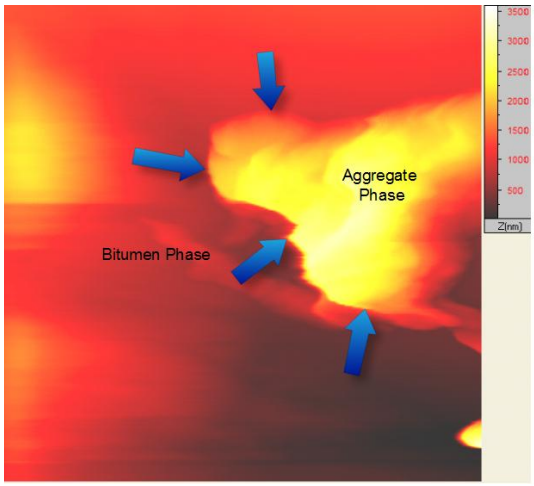

Figure 6-11 Morphology Image of Bitumen-Rock Interface Region, general view (1 μm x 1 μm), Different Darkness Represent Deflection Variation

Figure 6-11 shows the structure of bitumen-rock interface using AFM. Upon the first scan of the asphalt samples, one can see a general picture of the interface structure. This is followed by a more finer-grained scannings at higher magnifications. Different levels of darkness represent variation in deflection.

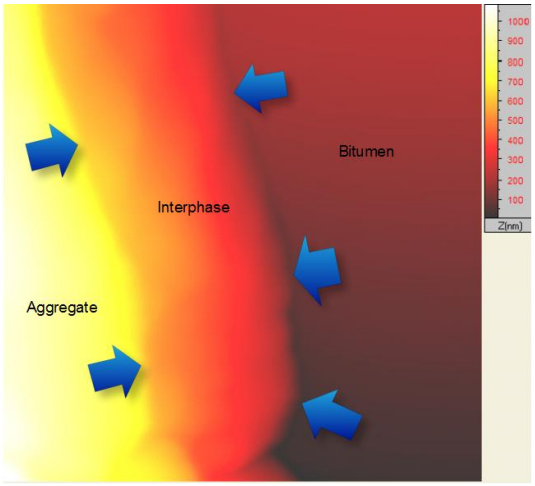

Figure 6-12 AFM Image of Bitumen-Rock Interface Region, zoom-in window (200 nm x 200 nm), Different Darkness Represent Deflection Variation. AFM image of the same interface position, but with

higher magnification, taken by the contact mode after scanning is made. The boundary structure can be concerned by color.

Figure 6-12 shows an AFM image from a probe of the interface specimen taken at room temperature. The dark area represents the bitumen phase, while the lightest region shows the aggregate. The area between them could be bitumen or aggregate, but it's hard to discern from the AFM characterization. So we conceptualized it as an interphase area, which may have formed from interfacial diffusion.

6.4.3 Environmental Scanning Electron Microscope

The sample is examined under the Environmental Scanning Electron Microscope along the asphalt-aggregate interface to identify positions to observe. For these characterizations, the ESEM pressure was 665 PA (5 mmHg) and the beam energy was 15 keV.

The presence of the oil phase prohibits observations in a conventional SEM unless the oil phase is removed from the specimen. In contrast, the high-pressure condition of the ESEM allows for direct observation of the polymer structure without any sample preparation. Figure 6-13 shows the general overview of an asphalt-aggregate specimen with magnification of 22X

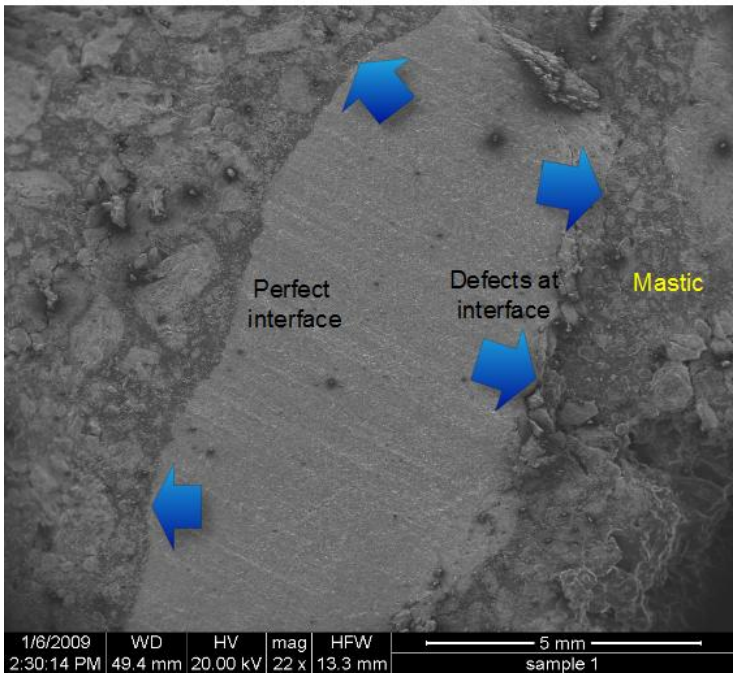

Figure 6-13 ESEM micrographs showing interface characteristic between bitumen and aggregate interface, this is an overview Digital Image at Interface with Magnification 22X, by ESEM at VT

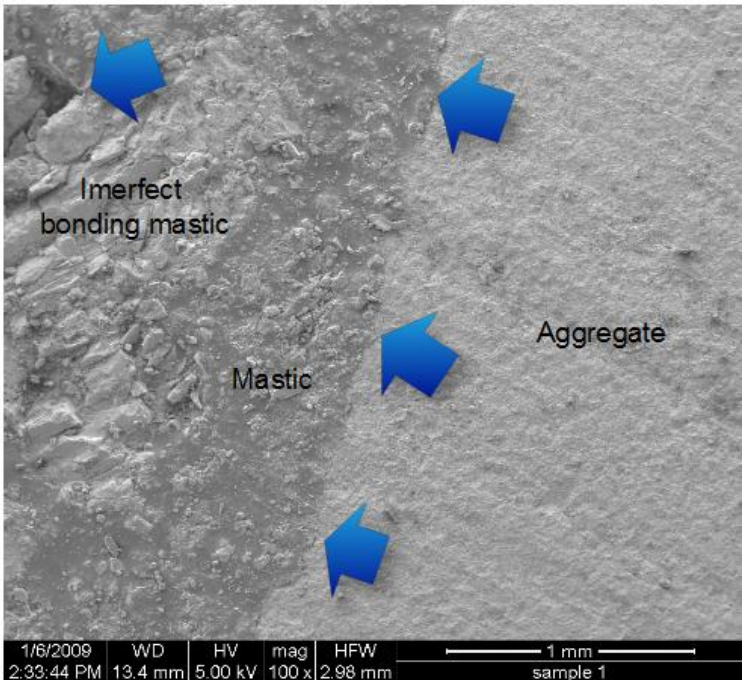

Figure 6-14 Digital Image at Interface with Magnification 100X, by ESEM at VT

Figure 6-14 depicts an interface region with magnification of 100X. From this microscale image characterization, a clear interface can be discerned. On the top left of the image, imperfect bonding mastic region is also shown.

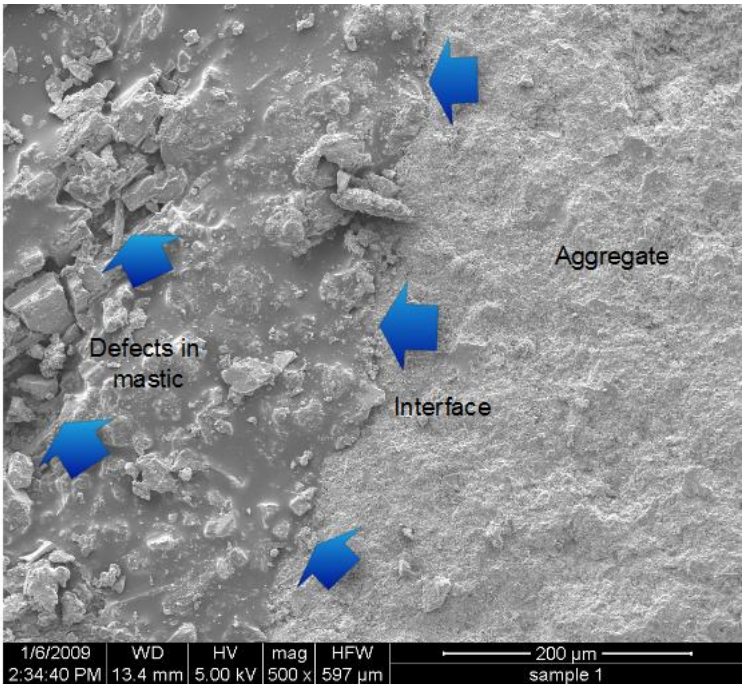

Figure 6-15 Digital Image at Interface with Magnification 500X, by ESEM at VT

Figure 6-15 demonstrates a magnified interface image with 500X. From the 200 μm scale, a clear interface is illustrated with a few micro-stones scattered throughout the asphalt phase. At the top-left of this image, defects can be seen clearly. These defects could have been caused by the cutting procedure.

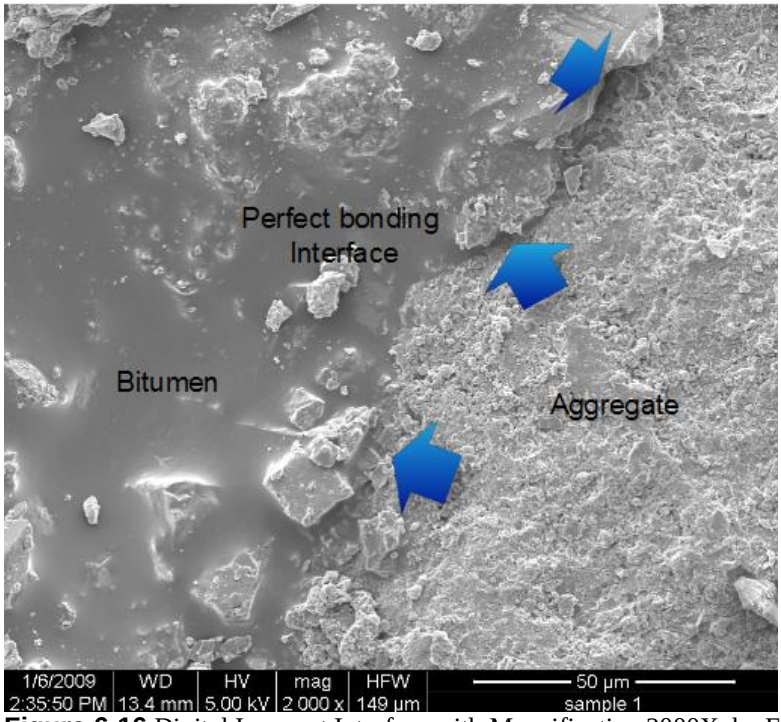

Figure 6-16 Digital Image at Interface with Magnification 2000X, by ESEM at VT

Figure 6-16 illustrates a perfect bonding interface region. As one can see, bitumen acts as glue to stick the aggregates together.

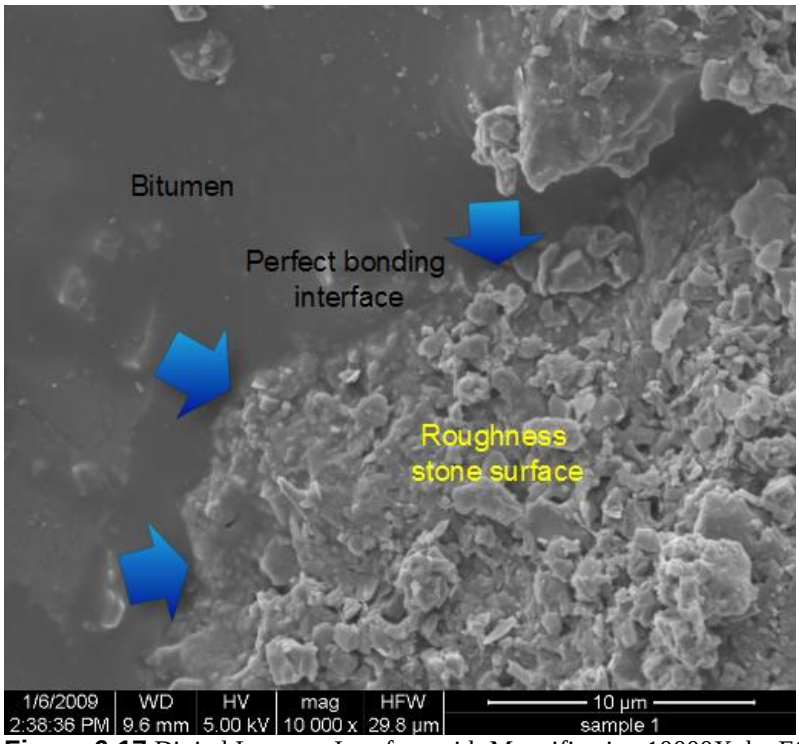

Figure 6-17 Digital Image at Interface with Magnification 10000X, by ESEM at VT It can be seen that bitumen and rock interface bonded perfectly

Figure 6-17 shows a perfect bonding interface region. From this image, the roughness morphology of the aggregate surface is clearly illustrated, while the bitumen phase looks very smooth. The interface region bonded perfectly; there appear to be no evidence of micro-pores or any other defects.

Figures 6-13 through 6-17 show a series of Environmental Scanning Electron Microscope micrographs of the interface of the specimen. As shown in Figure 6-17, the aggregate has a rough surface, which contributes to its increased absorption of asphalt binder. The same section of the aggregate specimen was further investigated under high magnification as shown in Figure 6-17. As can be seen, the aggregate bonds tightly and continuously with the asphalt binder, and its rough surface pores allow penetration of the asphalt binder to form a strong bond.

Moreover, Figure 6-16 shows the interlocking mechanism between aggregate and the mastic filler. The presence of sufficient surface texture provides the interlocking site for asphalt binder and the aggregate that result in an excellent interfacial zone.

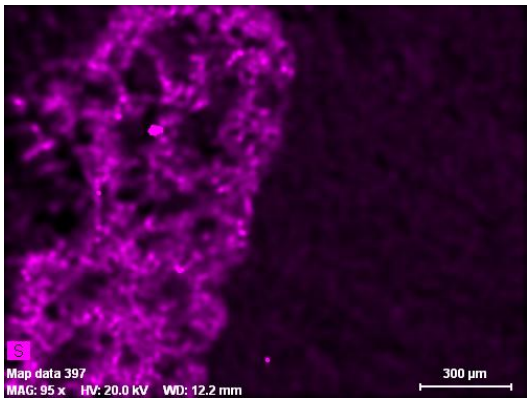

Chemistry map of S

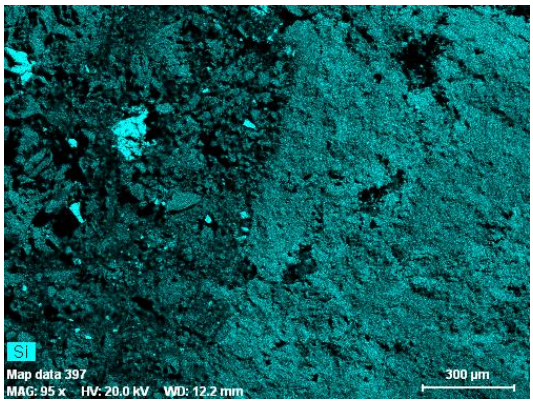

Chemistry map of Si

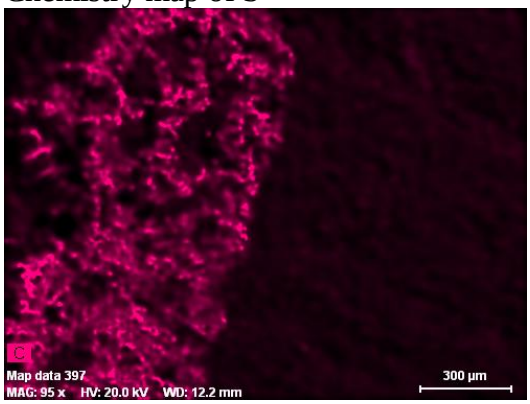

Chemistry map of C

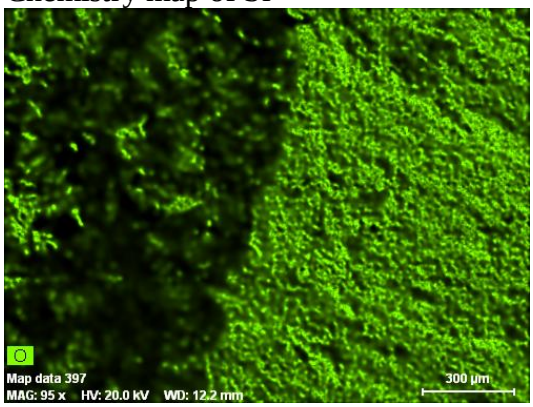

Chemistry map of O

Figure 6-18 Separated chemistry map of S, Si, C, and O

Furthermore, this particular observation region was also used to make a chemistry spectrum analysis using the ESEM. The presence of Oxygen, Sulphur, Silicium, and Carbon at the interface sample was determined. Trace amounts of other elements were also observed and recorded. Results were shown in Figure 6-18 depict a chemical map of the interface. Carbon and Sulphur are the most prevalent elements in the asphalt phase, while Silicium and Oxygen are spread throughout the aggregate region. It is also important to note that the Silicium and Oxygen scattered throughout the asphalt region are due to the mastic filler which is mixed into the asphalt.

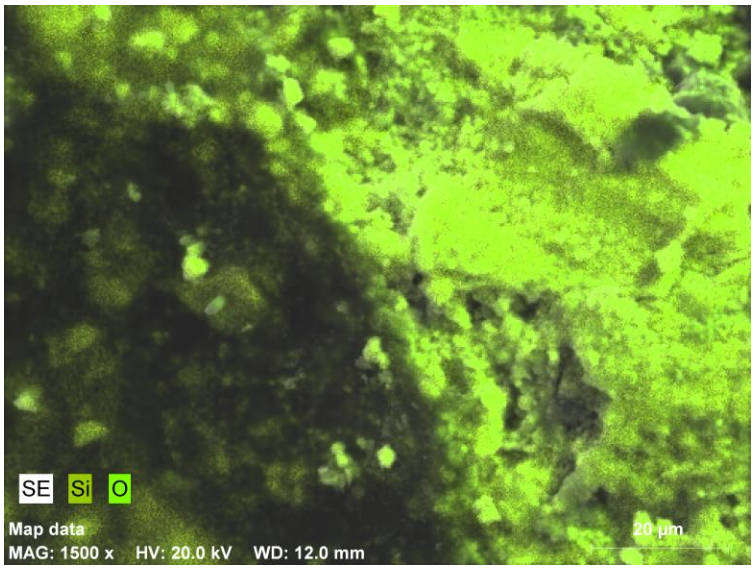

Figure 6-19 Chemistry combination Si and O

Figure 6-19 demonstrates a combined chemistry map of Silicium and Oxygen. The asphalt and aggregate interface are shown in dark and light green, respectively. On the right part of Figure 6-19, the light green area is primarily composed of Silicium and Oxygen. This is the reason why quartz is chosen to represent the aggregate and built into our interface structure model.

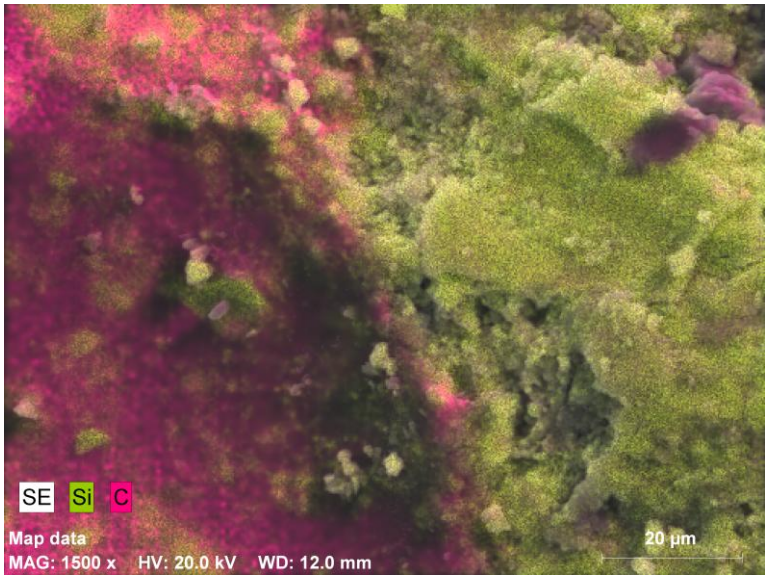

Figure 6-20 Chemistry combination Si and C

Figure 6-20 illustrates a combined chemistry map of Silicium and Carbon. The

light green area is primarily composed of Silicum. The red area is mainly composed of Carbon.

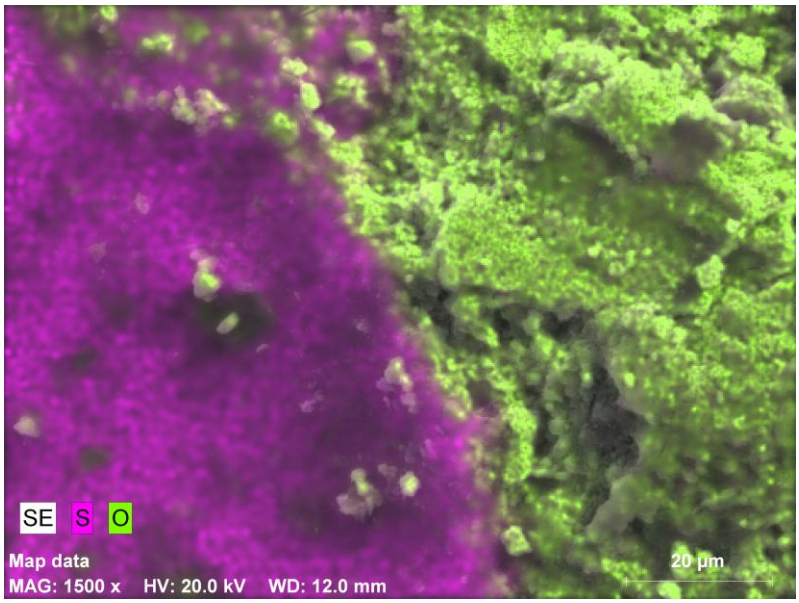

Figure 6-21 Chemistry combination S and O

Figure 6-21 shows a combined chemistry map of Sulphur and Oxygen. The light green area represents Oxygen and the red shows Sulphur. The building of our asphalt-aggregate interface model is discussed in Chapter7, based on these interface chemical analyses.

6.4.4 Focused Ion Beam

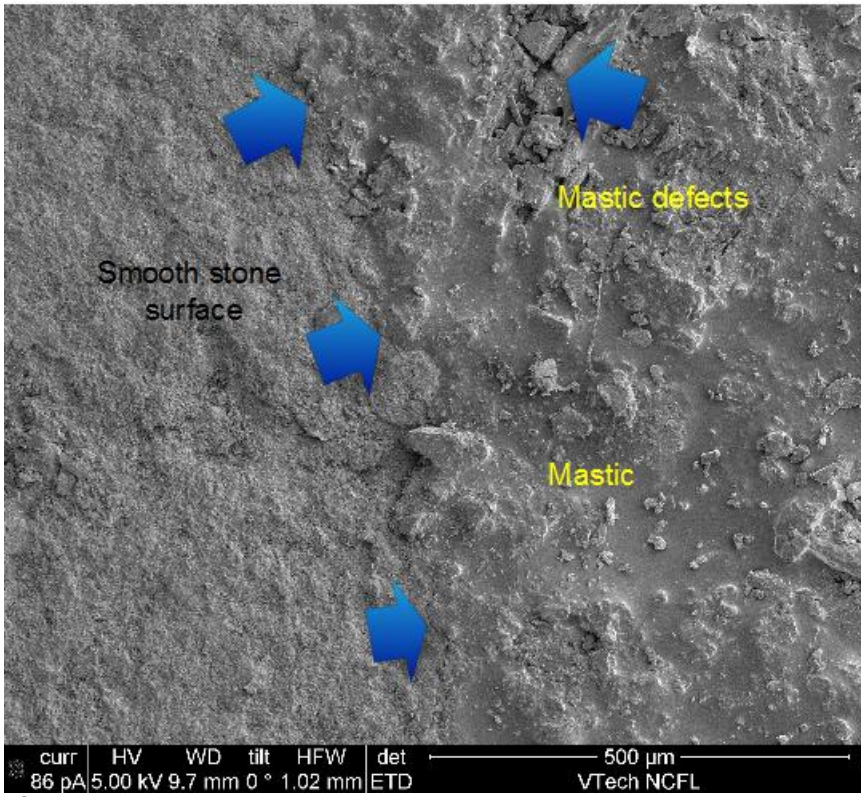

Figure 6-22 FIB overview at the interface, by FIB at VT

Focused Ion Beam was also used to characterize the interface in a similar manner as the ESEM, shown in Figure 6-22.

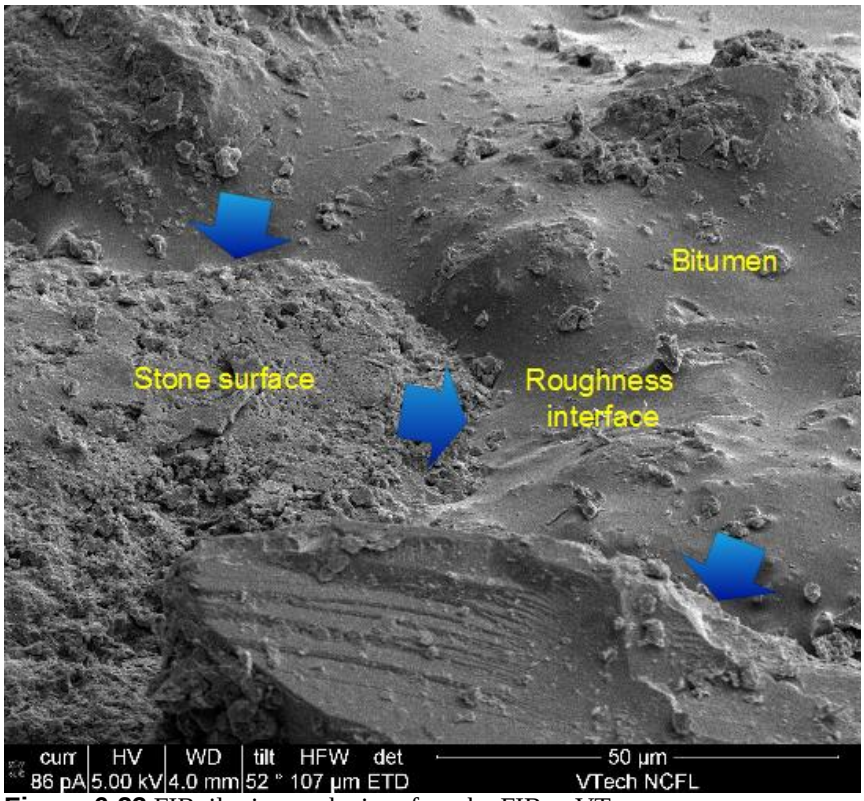

Figure 6-23 FIB tilt view at the interface, by FIB at VT

While Figure 6-21 shows an image taken from above, Figure 6-23 illustrates a tilted view of the interface. Roughness interface structures can be discerned from this image.

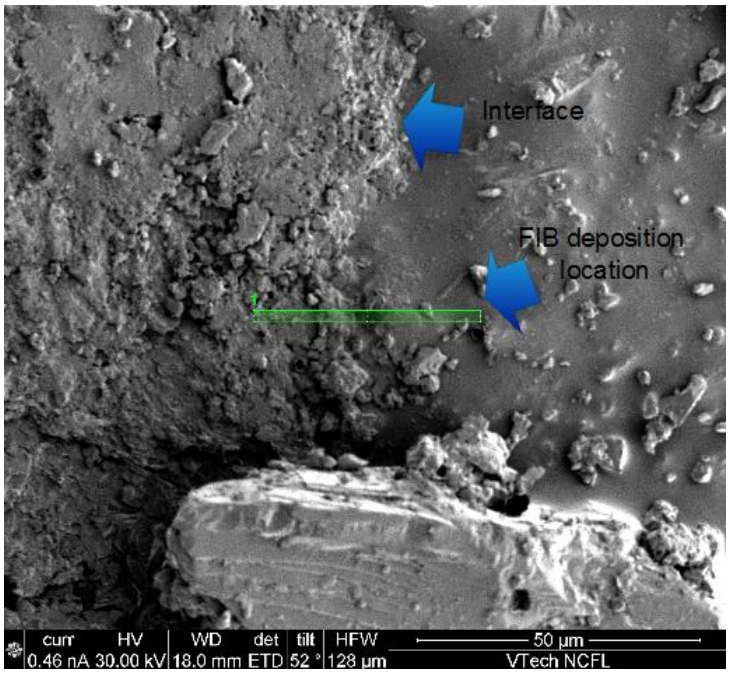

Figure 6-24 FIB tilt view, to locate the cutting position, by FIB at VT

Figures 6-22 through 6-23 are all images taken using surface probe technology. In contrast, Figure 6-24 demonstrates a procedure of locating the sample cutting position. The sample is cut by the FIB in order to explore the internal microstructure of the interface.

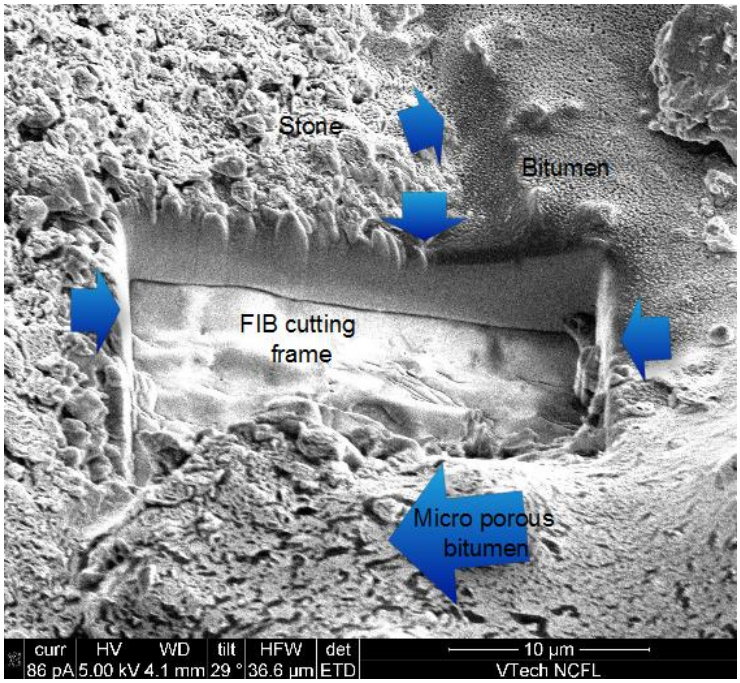

Figure 6-25 Asphalt-rock perfect interface (tight binding) micro-structure, by FIB at VT

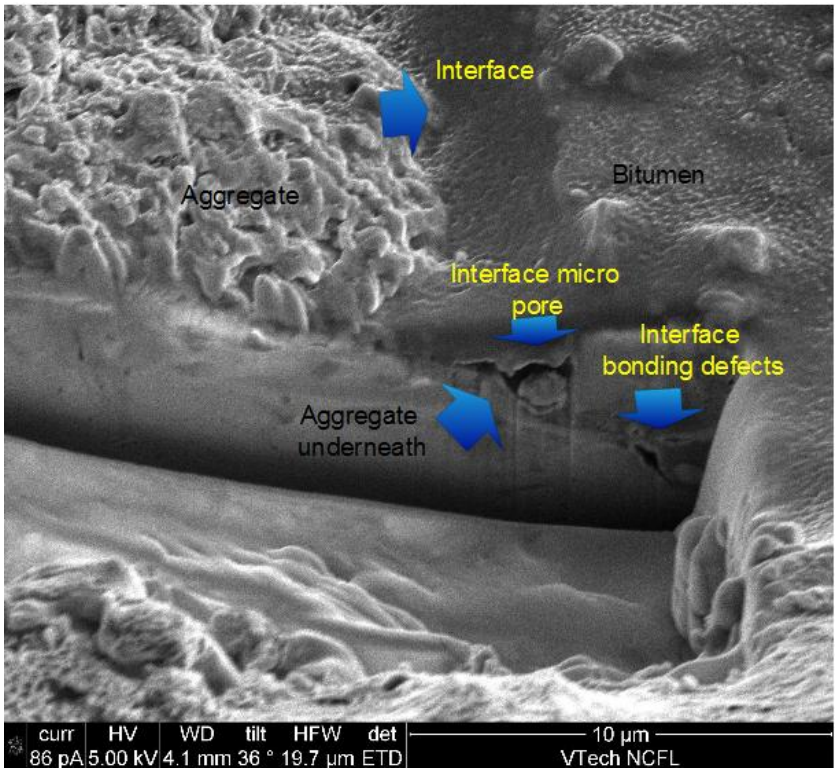

Figure 6-26 Micro-pores located at asphalt phase along the asphalt-rock interface, by FIB at VT

Figure 6-25 and 6-26 depict the cutting frame at the interface. We can observe that

the interfacial micro-pore and interface bonding defects are both underneath the thin asphalt layer. This is in agreement with our expectation that imperfectly bonded interfaces are highly prevalent.

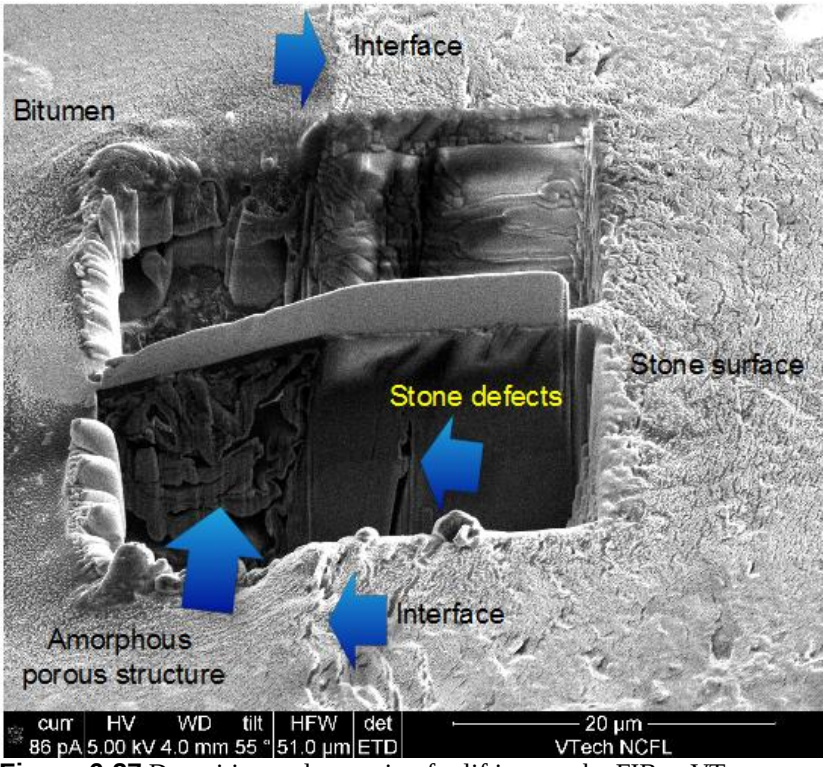

Figure 6-27 Deposition and preparing for lifting out, by FIB at VT

Besides image characterization, FIB is also used to produce TEM sample. Figure 6-27 illustrates a lift-out cutting procedure. At the cut thin layer interface sample, an amorphous porous structure can be viewed in the asphalt phase, while in the aggregate region, the morphology changes dramatically. The asphalt amorphous layer structure has a lot of micro-voids, while the stone phase is free of micro voids, except for a natural internal crack.

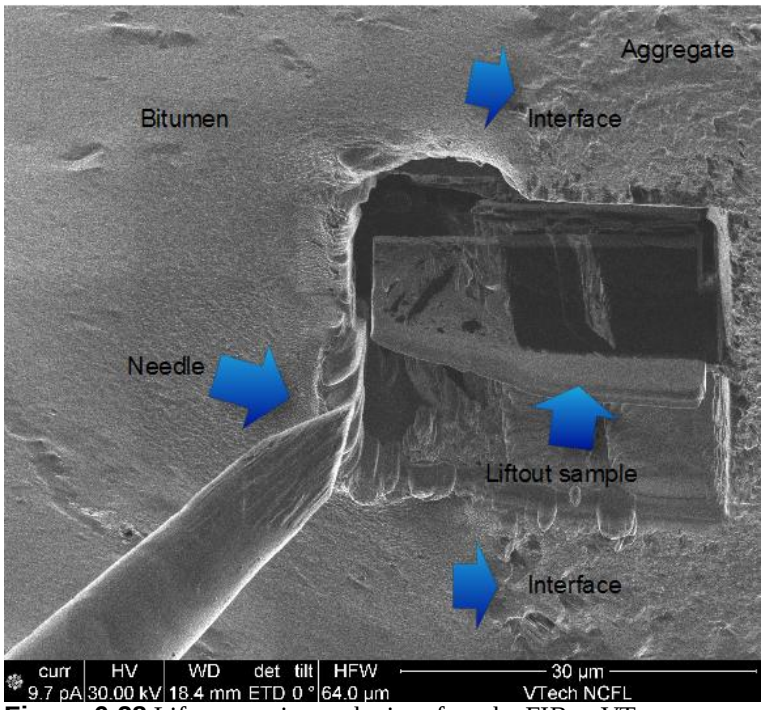

Figure 6-28 Lift out cutting at the interface, by FIB at VT

After the cutting sample is made, a carrying needle will be used to glue the sample to the needle tip. Figure 6-28 shows a carrying needle is lifting out a sample.

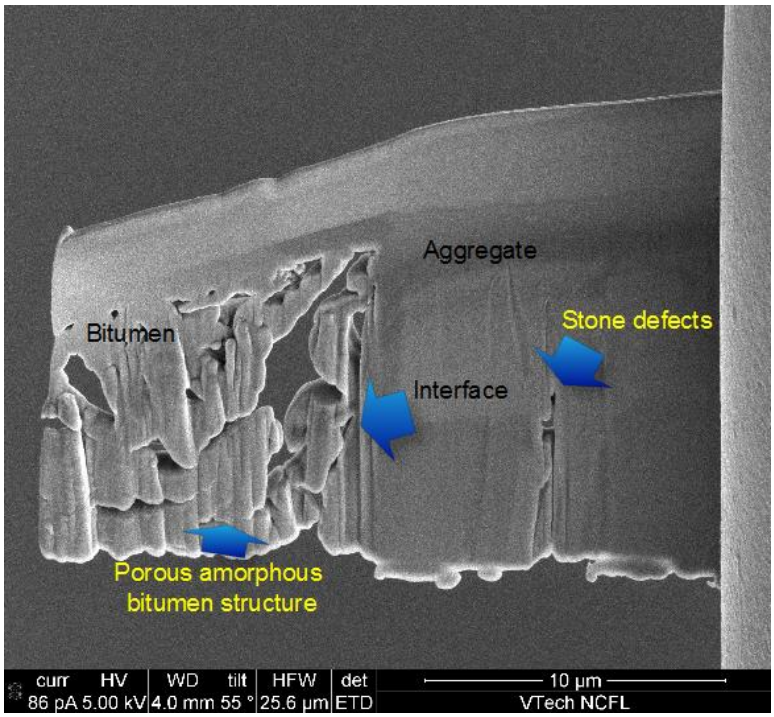

Figure 6-29 Excises sample from the interface, by FIB at VT

Figure 6-29 depicts the original lift-out sample from the FIB. It is clear that the asphalt while amorphous, still exists a porous structure. There are a lot of micro-voids spread throughout the bitumen structure. The aggregate phase appears perfect but it has a natural micro-crack. This sample was also excised by TEM observation.

6.4.5 Transmission Electron Microscopy

The morphology of the asphalt-aggregate interface was observed by using a transmission electron microscopy (TEM), formally referred to as Titan. TEM imaging requires thin samples that partly transmit the electron beam. However, for a poorly-ordered structure, the thickness of the sample is likely to cause errors, as it is very difficult to eliminate the superimposition of lattice fringes.

In the present study, the sample was produced by the FIB lift-out cutting technique for TEM observation. Several pictures were taken from different spots to obtain a general view. The transmission electron microscope was also equipped with an anti-contamination trap, a computerized imaging system for analysis.

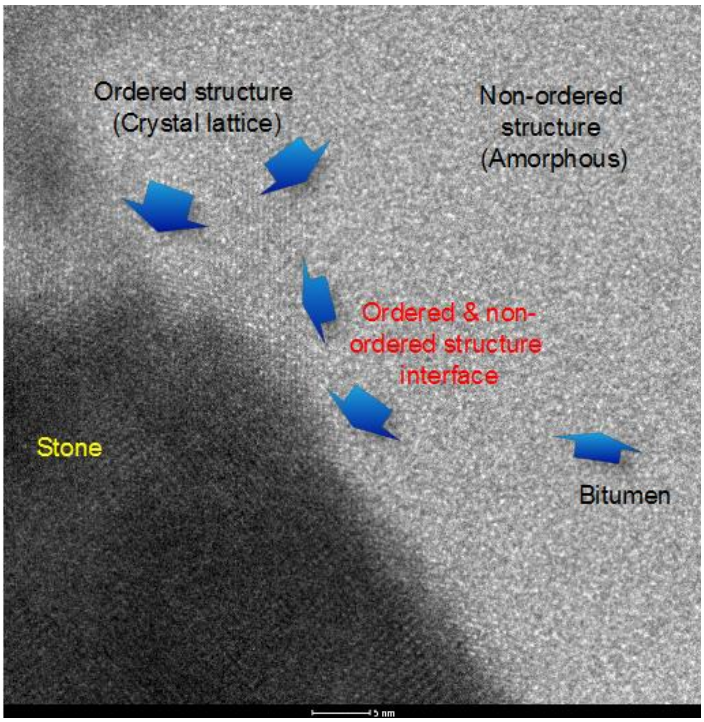

Figure 6-30 Titan_Region_1 Smooth interface

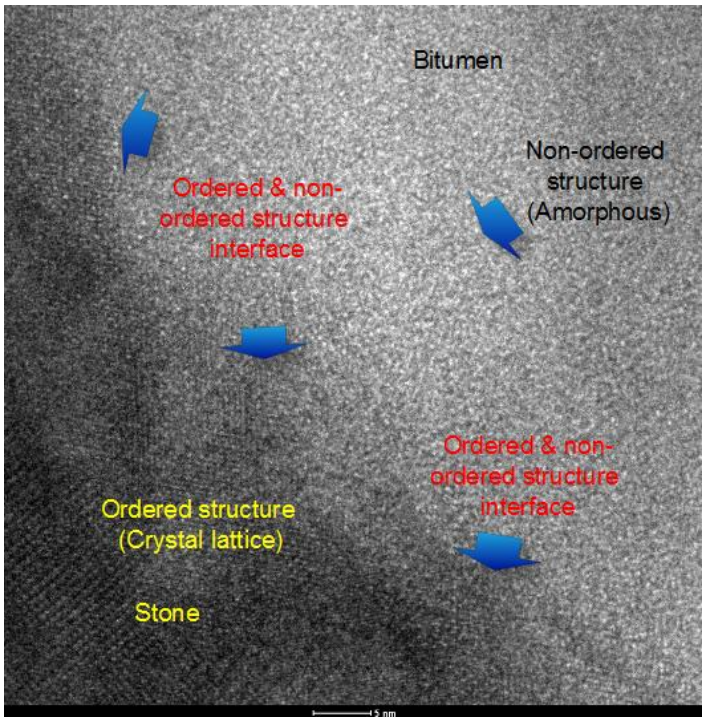

Figure 6-31 Titian_Region_2 Smooth interface

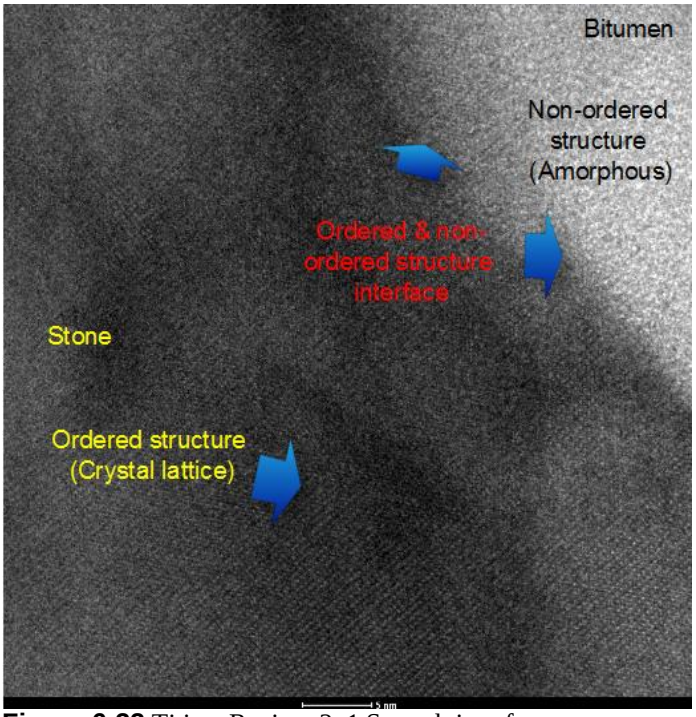

Figure 6-32 Titian_Region_2_1 Smooth interface

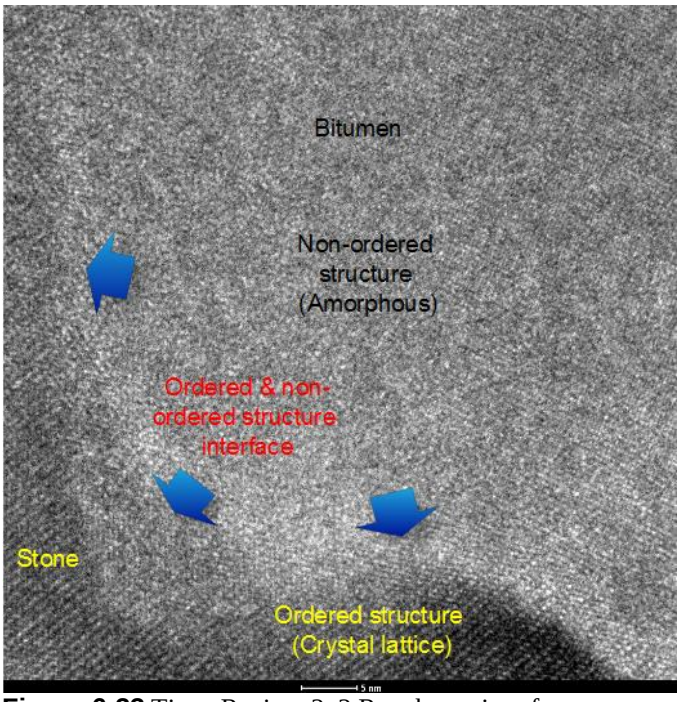

Figure 6-33 Titan_Region_2_2 Roughness interface

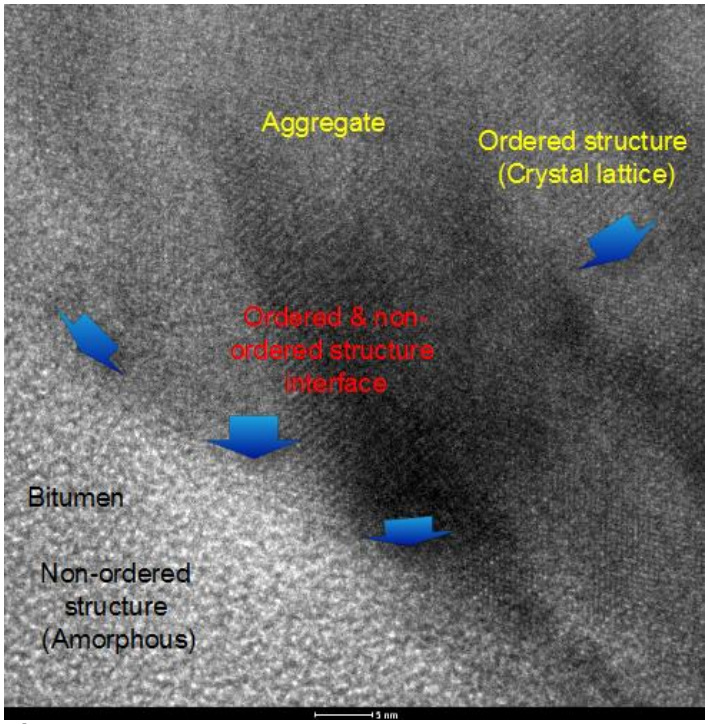

Figure 6-34 Titan_Region_3 Smooth interface

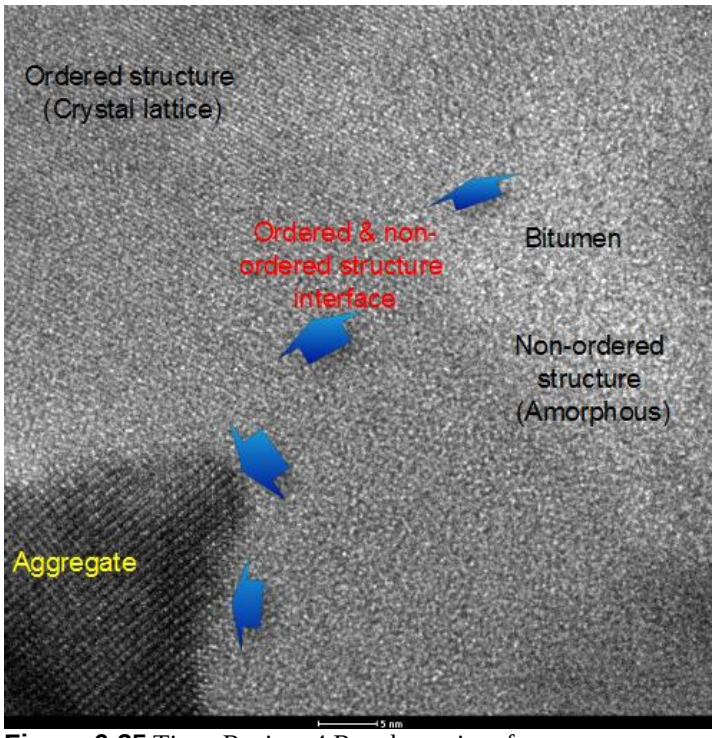

Figure 6-35 Titan_Region_4 Roughness interface

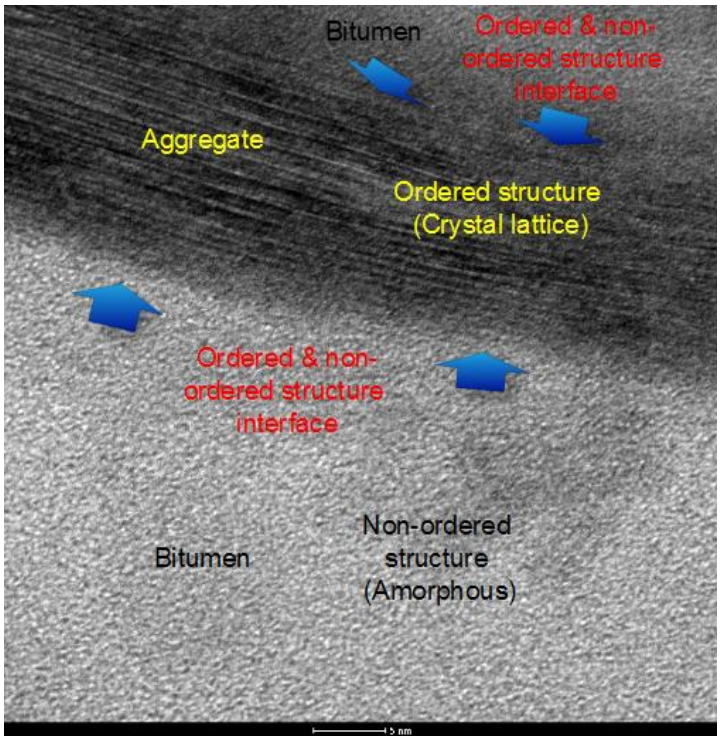

Figure 6-36 Titan_Region_5 Smooth interface

Figures 6-30 through 6-36 illustrate representative TEM images obtained from the

nanoscale interface specimen. Long range periodic orders present in all of the TEM images depict the rock mineral's crystal structure, while the asphalt phase is characterized by nonperiodic order. In Figure 6-36 we present representative micrographs taken from the nanoscale interface sample.

The morphology observed by Titan indicates that the bitumen molecules and the mineral crystals display a condensed contact at the interface region, especially along the boundary of stone surface. However, such perfect binding areas are not located everywhere in the asphalt concrete body; nanoscale defects, such as voids, cracks, and slots can also be found throughout the interface.

The identification of material atomistic structure at the nano-scale in the context of multiscale modeling of asphalt was been throughout this paper. Based on these observations, we can conclude that stacking disruption of amorphous structures is pervasive. Unfortunately, long range order is largely absent in the majority of asphalt interface regions.

6.5 Summary

This study was carried out to characterize the multiscale morphology characteristics of the amorphous asphalt-aggregate interfaces. Based on the laboratory characterizations and analyses from this study, the following conclusions can be made:

The use of HROM, AFM, ESEM, FIB, and TEM for observing the asphalt-aggregate interface structure is influenced by the chemical nature of the bitumen, and this varies depending on the source of the bitumen.

High-resolution images of asphalt atomistic interfacial morphology and structural information of their distribution at the interfaces have been obtained.

As generally stated, all of the 5 different microscale observation methods, HROM, AFM, ESEM, FIB, and TEM, are inter-correlated by scales. Optical microscope gives us a big picture of the macro-scale interface structure; while a complete and real asphalt structure can be viewed by the AFM which does not need any preparation method; the ESEM can't be used to observe the oil phase, but it has a very good resolution for the asphalt and aggregate structure. Moreover, the ESEM chemistry map

provides a clear identification of chemical composition at the bitumen phase, mineral phase, and interface region. The TEM gives us a straight forward method which can access directly into the atomistic structure of the interface. In addition, the FIB not only provides a clear identification approach in a similar manner as the ESEM, but also serves as a nanoscale fabrication tool for the TEM sample preparation.

With the multiscale characterization at the asphalt-aggregate interface, we may have a better way to understand the interfacial composition and configuration from various scales. Because the macroscale deformation and failure at the interfaces stem from the bottom nanoscale, then upscale to the highest macroscale. The broader impact of this study is that it may result in significant saving of financial and other resources that are currently used to combat pavement distresses originating from interface failure.

Chapter 7
Modeling of Asphalt-Aggregate Interface Tensile Strength

7.1 Introduction

As demonstrated in Chapter 5, asphalt is a product of the fractional distillation of petroleum. Asphalts vary in consistency from solid materials at room temperature to materials whose consistency is practically the same as water at high temperature. For road mixes, too solid asphalt lacks the necessary fluidity for workability and is susceptible to low temperature cracking, whereas too soft asphalt may bleed to the surface or develop potholes and rutting under traffic. It is critical to have adequate consistency to ensure good workability and performance during service.

The mineral aggregate components of pavements are distributed throughout a mixture and range in size from coarse to fine. Properly compacted asphalt mixtures produce a structure whose stability, stiffness, and wearing properties are dependent on the interlocking of the aggregate particles and the cohesiveness of the binder. Only the portion of the mineral filler consisting of particles thicker than the asphalt film contributes to the interlocking of the aggregate. The other portion of the filler, the fine particles that smaller than the thickness of the asphalt film, is suspended in the asphalt and is part of the binder component of the mixture.

The asphalt-aggregate interaction is a thin-film phenomenon. A number of testing procedures have been used to attempt to measure rheological properties of thin films. It is important to investigate the asphalt-aggregate interaction in the interfacial region to determine if this interaction relates to pavement distresses such as moisture damage, tender mix, permanent deformation, fatigue cracking, and low temperature cracking.

It is hypothesized that fine aggregate particles (mineral fillers) function as more than just inert particles in asphalt, and that physico-chemical interactions occur between asphalt and mineral fillers may affect pavement performance. Further, it is speculated that these physico-chemical interactions are three-way interdependent interactions of fine particles, asphalt, and larger aggregates. It is expected that the adhesion of the fine particle-asphalt binder to larger aggregate particles would be affected by the compositional characteristics and quantity of the fillers. With the use of larger quantities of fine particles or with the use of improper fine particles, adhesion may be critically affected, particularly when the paving mixture is exposed to the action of water. In such an environment, the bond between asphalt binder and mineral aggregate may be weakened or even destroyed. This would lead to a poorly performing paving mixture.

It is assumed that contact between mineral fines and asphalts results in migration of polar organic asphalt molecules to polar sites on mineral surfaces. This aggregate induced interaction results in changes within asphalt microstructures. Currently, no standard binder test is in use to determine the aggregate-induced effects of asphalt microstructure on the properties of asphalt binder adhesion, nor is there a mixture test that determines the contribution of these physico-chemical effects on the properties of asphalt-aggregate mixtures.

The objective of this chapter is devoted to investigate into a nanoscale asphalt-aggregate interface model that enables the interactions between thin asphalt layers and aggregate surfaces to be predicted.

7.2 The Interface Region

Cohesively bonded interfaces play a significant and important role in a variety of products, commonly based on layered thin film substrates and adhered layer systems, such as composite material systems.

The reliability of asphalt-rock composite is often compromised by the occurrence of interfacial separation processes (or delamination). Dedicated experiments to measure interface performance are being developed in industry and academia. Unfortunately, the results clearly reveal that a macroscopic approach to this problem does not enable the

development of truly predictive insights under different loading conditions or classes of interfacial function.

The key problem resides in the fact that the total fracture energy encompasses contributions from physical de-bonding processes and micro-scale dissipation processes in the bonded material, which cannot be obtained without a multiscale approach.

In pavement industry, the cohesively bonded asphalt-aggregate systems of interest typically involve bitumen and a substrate of mineral materials. The adhesion between the layers in such systems has been the subject of industrial interest. Due to the complexity and limitations of computing power, industry currently is still largely relying on trial-and-error experimental procedures for the complex interfacial system to be designed or optimized.

The thickness of the films or layers often is in the range of 2 nm up to 1 μm and more in layered pavement materials. In most cases, the debonding of asphalt-aggregate interface is a ductile separation. Ductile separation, namely failure, has been studied by taking into account the visco-plastic dissipation mechanisms in the adjacent sections of material near the interface in question. Such adhesive failure has been investigated using classical fracture mechanics with small scale separations.

The classical reasoning in addressing the ductile separation problem is to study the adhesion on the basis of the physic-chemical bonding of the layers at the separating interface. Although this provides clear answers in brittle interfaces, it constitutes a major problem for cohesive interfaces, because during interfacial separation, a considerable amount of energy is dissipated in breaking chemical bonds, disrupting, rearranging, and deforming the adjacent material. As a result, different experimental configurations or tests do not provide consistent measurements of the work of adhesion at an interface, since the measured fracture energy consists of a contribution from (1) actual de-bonding at the surface, (2) dissipative deformation in the bonded material adjacent to the interface, (3) the interaction between both previous mechanisms, and (4) stress- or energy-induced chemical changes in the materials at the interface. Hence, the interfacial strength is generally affected by both chemical and mechanical bonding between the asphalt and the rock minerals. While chemical bonding arises from the formation of new phases, mechanical bonding occurs by interlocking of constituent in composites.

Interface failure mechanism typically involves the pull-out and separation of molecules. These are processes which can be accurately studied using atomistic modeling approach, since molecular dynamics can simulate its atomic motion allowing the investigation of the deformation and ductile failure process.

In this work, we chose CVFF-aug forcefield for atomistic model construction and simulation. This force-field describes intra-molecular and intermolecular interactions in the chemical system. The bond stretching energy, valence angle bending energy and the dihedral torsion energy included in the bonding terms are used in the energy expression of CVFF-aug. In the nonbonding terms, van der Waals interaction energy and Coulomb interaction energy terms are considered.

7.3 Model of the Interface System

Chapter 5 demonstrates the configuration of the internal structure of bitumen. The configuration is largely determined by the chemical constitution of the molecular species present. Bitumen is a complex chemical mixture of molecules that are predominantly hydrocarbons with a small amount of structurally analogous heterocyclic species and functional groups containing sulphur, nitrogen, and oxygen atoms[100].

Before modeling, representative chemical elements which can characterize the typical object performance properties are required. Otherwise, even if the model is constructed, materials' critical properties can't be represented by the model.

Modeling interface need to have some fundamental elements which can characterize interfacial transition zone morphology and performance under damaged state. Currently available fundamental elements include interfacial shear zone, micro-void, and micro-crack. But it's not enough to characterize the interface. Fortunately, Chapter 6 characterized the asphalt-aggregate interface structure, size, chemical compositions, etc. by using advanced multiscale characterization devices, e.g. ESEM, FIB, and TEM. In accordance with the obtained real interface nanoscale structure, atomistic modeling is the approach adopted in this chapter.

Figure 7-2 illustrates an asphalt-quartz interface proposed in the present set of simulations. This interface structure is built by adopting a mix_1 asphalt model presented

in Chapter 5 and a quartz lattice structure constructed in Chapter 4. Since an orthogonal geometry is needed for loading purpose, the quartz supercell subsurface needs to be cut into an orthogonal shape with P1 space group. The cleaved quartz (001) surface structure is given in Figure 7-1. The lattice parameters are shown as follows: a=24.55 Å, b=27.01 Å, c=20.62 Å, α=90°, β=90°, and γ = 90 °.

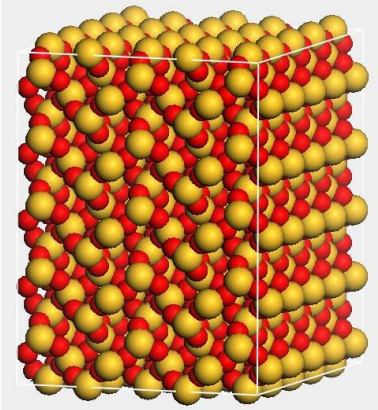

Figure 7-1 Cleaved orthogonal crystal structure of quartz

According to the methodology described above, a bitumen-quartz interface system is successfully generated, as shown in Figure 7-2.

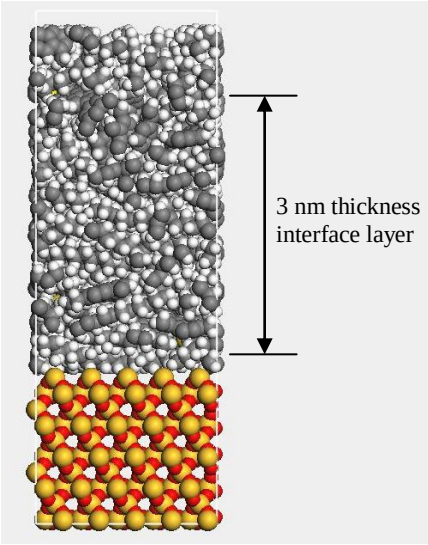

Figure 7-2 Front view of asphalt-quartz interface atomistic model

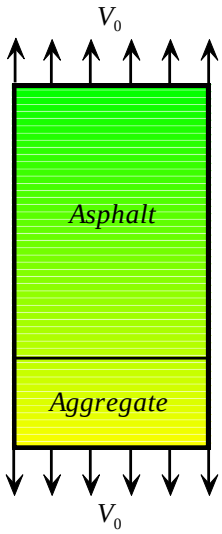

Figure 7-3 Loading scheme consisting of velocity-specified boundary

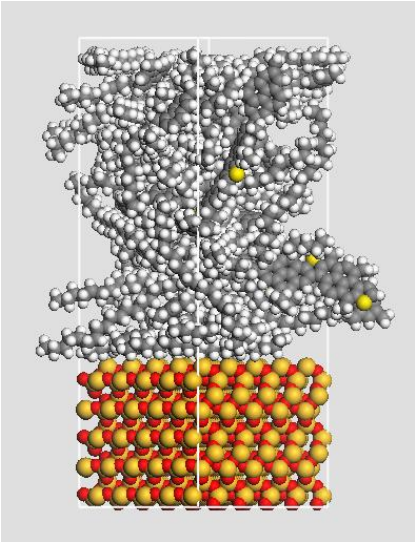

Figure 7-4 Side view of asphalt-quartz interface atomistic model

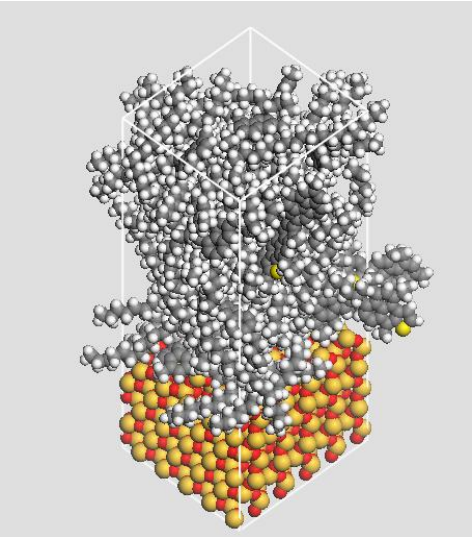

Figure 7-5 Top side view of asphalt-quartz interface atomistic model

After construction of the interface model, the last row of atoms in the ± Z direction is constrained to create planar rigid surfaces. These rigid surfaces are designated as the loading planes. In this work, the interface displacement is calculated as the sum of the absolute displacement of each of the loading planes. Periodic boundary conditions are applied to surfaces in the X and Y directions. These boundary conditions allow the application of a near uniaxial state of stress within the interface region during tensile deformation sequences prior to free surface localization deformation originating at the free surfaces.

Because the quartz structure is quite rigid in comparison to the asphalt and the quartz geometric structure of each atom is already in an optimized position, the atom constraints algorithm to fix the atomic coordinates of selected atoms (quartz atoms) is employed during simulations. Fixing atoms simplifies the energy expression, because the interactions between the fixed atoms are constant and can be ignored. This decreases the computational expenses.

In addition, we are able to precisely control the rate and displacement of the loading surfaces. With the introduction of loading surfaces in Z direction, a number of previous authors have shown that a lot of valuable information regarding deformation characteristics on the nanoscale may be obtained with these boundary conditions. Prior to

deformation, the interface model is equilibrated to 298 K, allowing for atomic movement along the quartz-asphalt interface and creating the idealized asphalt amorphous structure.

7.4 NPT Ensemble & Nose-Hoover Thermostat at Equilibrium

As a result of required numerical approximations in MD simulations, especially the use of cut-off distances in potentials to reduce the computational requirements, the energy in the system can drift over time. Therefore, methods must be implemented to maintain thermodynamic constraints from the effect of cumulative errors. In this simulation, an isothermal and isobaric (NPT) ensemble is chosen for proper deformation. Because constraining the volume (NVT) would not account for any change in density during deformation and could lead to inaccurate pressures on free surfaces of the simulation cell.

Nose [101] implemented an external thermal bath to thermostat a system. The thermal bath controls its associated momentum to permit the energy in the system to fluctuate, while maintains a NVT or NPT ensemble using time and distance scaling. The non-equilibrium NPT ensemble is employed in this simulation which is proposed by Melchionna et al. [102]. The non-equilibrium NPT ensemble is an extension to the Nose-Hoover ensemble, which is in order to more precisely sample the NPT ensemble. This ensemble is available natively in LAMMPS and is used throughout this research.

The NPT integration has already been used by other researchers (see [102]) to update the positions and velocities of each timestep for atoms in a specific group with a Nose-Hoover temperature thermostat [103] and Nose-Hoover pressure barostat [104]. Where P denotes pressure and T denotes temperature. This creates a system trajectory that is in consistent with the isothermal-isobaric ensemble.

The thermostat is applied to only the translational degrees of freedom for the particles. The translational degrees of freedom can also have a bias velocity removed from them before thermostatting takes place. The desired temperature at each timestep is a ramped value during the simulation from Tstart (step of start) to Tstop (step of stop). The Tdamp parameter is specified in time units and determines how rapidly the temperature is relaxed.

The NPT ensemble regulates the system temperature and pressure with external temperature and pressure baths. Dampening parameters are used to adjust the flux between the simulation system and the baths. The parameters need to be set so that the system temperature and pressures are damped enough to prevent severe oscillations, so that the system reaches its quasi-equilibrium point not too slowly, especially for the high strain-rate deformation simulations.

The atoms in the fix thermostat group are the only ones whose velocities and positions are updated by the velocity/position update portion of the NPT integration.

For pressure calculations, there are two methods. First, regardless of what atoms are in the fix thermostat group, a global pressure is computed for all atoms to monitor the system thermodynamic properties. Second, when the size of the simulation box is changed, all atoms are re-scaled to new positions, in which case only the atoms in the fix thermostat group are re-scaled. Then, the pressure is calculated using all atoms after rescaled to new positions. The latter can be useful for leaving the coordinates of atoms in a solid substrate unchanged and controlling the pressure of asphalt layer. Therefore, the second method is employed is this simulation.

7.5 Procedure for Imposing Deformations

Prior to any deformation simulation, the initial configuration is relaxed to ensure that the system is in relative equilibrium. An NPT ensemble is used to maintain a constant temperature, typically at 298 K. furthermore, the NPT ensemble is used to allow the system volume to change so that the relaxed density is achieved at an external pressure of 1 ATM. The relaxation runs for 500 ps with an integration time step of 1.0 fs. The potential and kinetic energies as well as the temperature, volume, and pressure are extracted from LAMMPS normal output file.

To deform the interface model, a velocity displacement is applied to each atom in the upper loading plane. The displacement drives the loading plane in an opposite direction to the substrate quartz. Various displacement rates are applied normally to the interface in + Z direction, which subject the interface model to tension state. Throughout the deformation procedure, the system temperature is maintained approximately at 298

and 273 K, respectively, using the Nosé-Hoover thermostat.

Figure 7-2 depicts the interface model considered in this work. A couple of displacement rates ranging from 0.5 to 10 m/s are applied to the loading planes of the asphalt-aggregate interface supercell model for tensile deformation. The magnitudes of applied displacement rates are altered in order to investigate the stress-strain curves under different strain rates. It is noteworthy that for the interface model, image forces will still play a role in the deformation process.

Figure 7-3 shows the deformation scheme for the simulation. Tensile deformation rates are chosen to identify regions of deformation rate-dependent behaviors within the interface model. For all deformation rates, initial samples were identical in terms of structure and thermal equilibration.

Note that the magnitudes of the applied tensile displacements are chosen to subject the interface model to a tensile strain of 0.7, the peak of each deformation. Here, strain is calculated from the reference and current positions of the loading planes. Thus, the interface model under different deformation rates at altered temperature may be compared to draw conclusions regarding to the temperature dependency and the deformation rate-dependent behaviors.

In LAMMPS, each time step begins with the NPT calculations to determine the pressure derived displacements to the faces normal to the X and Y directions. It is followed by the prescribed displacements to the faces normal to the Z direction. All of the atoms in the simulation box are moved proportional to their distances from the displaced faces, resulting in prescribed deformation. By default LAMMPS is only capable of deforming the simulation cell at a constant deformation rate.

Since amorphous molecules are big and there are substantial differences between intermolecular and intramolecular forces, the size of the simulation cell could have an effect on the continuity of the results. The larger the size of the simulation cell with the appropriate density, the more likely that configuration will represent a continuum. However, larger simulation sizes take much more computational time. One of the initial goals was to find out the smallest size of a system that still maintains the deformation behavior of larger systems in the hope of minimizing computational requirements while reducing size effects.

Another concern is the consistency between simulations with different initial velocity distributions. At the start of a MD simulation, the atoms must be assigned velocities in a manner that ensures the kinetic energy of the system conforms to the desired temperature. In LAMMPS, the initial velocities are assigned randomly to each atom through the use of a Boltzmann distribution. The velocity distributions were modified by changing the random number generator seed.

Other MD parameters that must be considered for their effects on the deformation behaviors are the integration time step size, the frequency of scaling the simulation box to correspond with the desired deformation rate, and the values of the temperature and pressure dampening parameters. Small integration time steps result in more accurate dynamics, but at a computational cost. Increasing the integration time steps too much can result in numerical instabilities. For example, if two atoms are approaching one another at a high enough velocity, a large integration time step could permit the atoms to overlap during the next integration step resulting in a numerical singularity for typical pair potentials. In order to find the largest time step while maintaining the desired accuracy and stability, the integration time steps of 0.5, 1.0, and 2.0 fs were evaluated. An integration time step of 2.0 fs occasionally caused numerical instabilities which resulted in crashes of LAMMPS. There were no significant differences between the 0.5 and 1.0 fs integration steps. Therefore, the integration time step of 1.0 fs is used throughout this research.

During the deformation process, the MD simulation box must be rescaled to represent the change in shape of the simulation box. Since this rescaling requires computational time to reposition all of the atoms, the rescaling should only be performed as frequently as necessary. The stress-strain behavior was evaluated with the simulation box being rescaled every 1, 10, and 20 time steps. Since there were not any significant differences between the stress-strain behaviors due to the frequency of the rescaling, the simulation cell is rescaled every 20 time steps.

7.6 Simulation Procedure

Simulations are performed with Periodic Boundary Conditions (PBCs) imposed

on the supercell in three dimensions. For the interface supercell, first energy minimization is performed using conjugate gradient and line search algorithms, until there is no significant change in the total energy. After energy minimization, MD equilibration with a time-step of 1 fs/step is performed in two different ensembles: (1) isothermal-isobaric (NPT) ensemble for equilibration at 1 ATM pressure at 298 K or 273 K temperature until the volume of the supercell being equilibrated has stabilized, and there are minimal pressure fluctuations; (2) canonical (NVT) ensemble for equilibration at 298 K and 273 K until the fluctuations in the temperature subside. The termination criterion for equilibration is: when there is no significant change in the supercell volume and mean pressure of 1 ATM with mean temperature of 298 K or 273 K are achieved. During NPT equilibration, flexible cell flag is used to allow cell dimensions to change independently in three orthogonal directions and the resulting equilibrated structure is then used for deformation study in the NPT ensemble.

The stress-strain curve is plotted based on the well established procedure defined in Chapter 3. In order to obtain stress-strain plots for the interface layer supercell, 6 displacement rates range from 0.5 to 10 m/s is applied to loading planes of the asphalt-aggregate interface supercell model under tensile deformation. The stress tensor during the simulation is calculated in accordance with the stress appears at each displacement rate level.

7.7 Results and Discussion

The analyses focus on understanding the correlations among factors such as the structural arrangement, the stress-strain curve during deformation, deformation contour of each atom position deviation, and the peak interfacial strength. It is important to understand at this point that the simulations are classical MD in nature and, therefore, analyses do not focus on the fundamental bond breaking mechanisms at the localized length scale of individual chemical bonds. Accordingly, the insights offered mainly focus on overall mechanistic understanding without providing details regarding the manner of individual chemical bond breaking mechanisms.

The primary stages of tensile deformation and failure are illustrated in the

supercell model at different frames, as shown in Figure 7-6. Atomic arrangements and structure of the sample under loading are shown in the snapshots. It is found that the 2-layer interface structure undergoes significant structural change during the deformation and failure process.

It can be observed that the asphalt molecules start cleaving off the quartz surface at strains corresponding to the peak stress point of tensile stress-strain curve in all of the loading rates. After the peak stress point been passed through, the asphalt molecules start to loose, as shown in Figure 7-6.

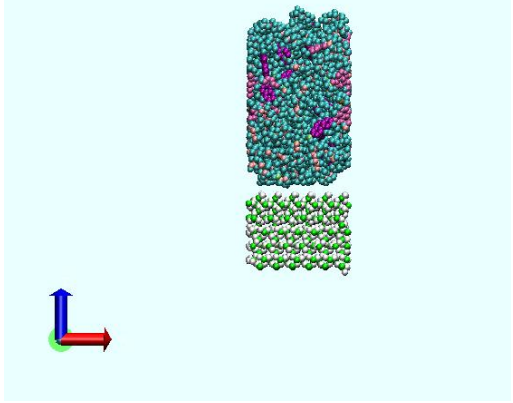

a

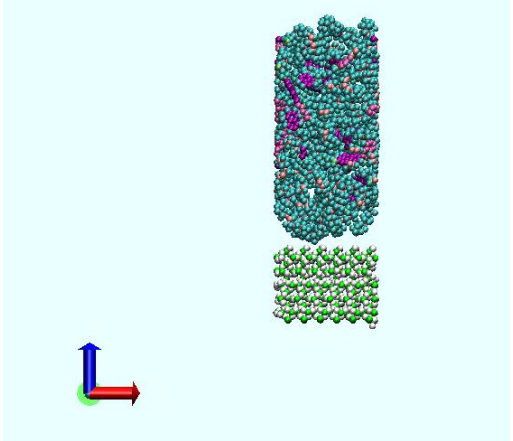

b

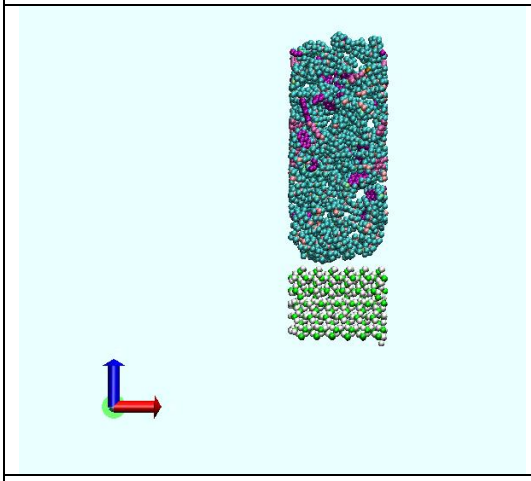

c

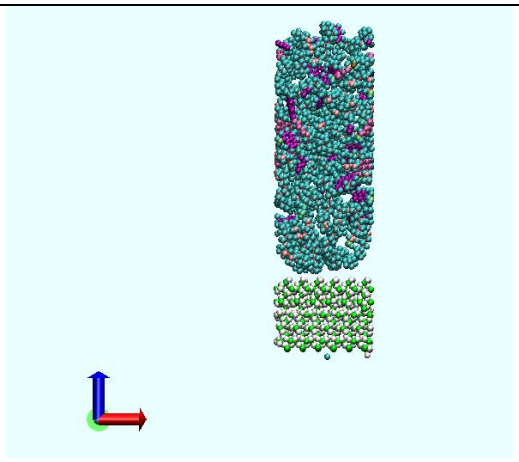

d

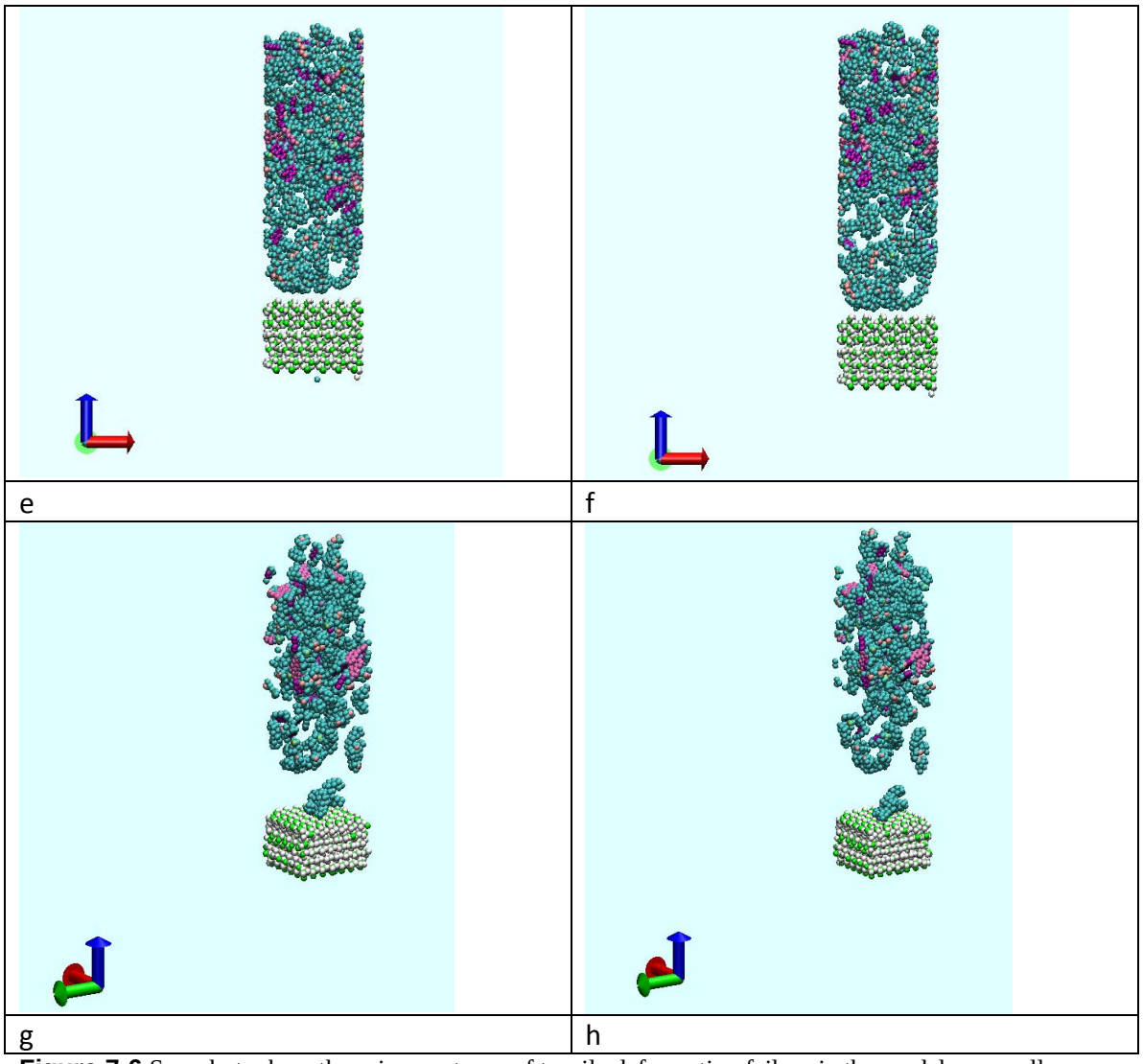

Figure 7-6 Snapshots show the primary stages of tensile deformation failure in the model supercell. Almost, invariably the peak of the stress–strain curves coincides with the asphalt molecules cleaving off from the Asphalt-quartz interface.

Since mix_1 asphalt model is a mixture of flexible chain-like molecules and rigid asphaltene molecules, it elongates on applied deformation till it is fully stretched. Soon afterwards it cleaves off the asphalt-quartz interface, such cleavage results in a local nanoscale interfacial failure. The cleavage is also accompanied with the tensile breakage of the asphalt interface region nano-voids, which is in corresponding to the peak stress value as illustrated in Figure 7-6 (e) and Figure 7-6 (f).

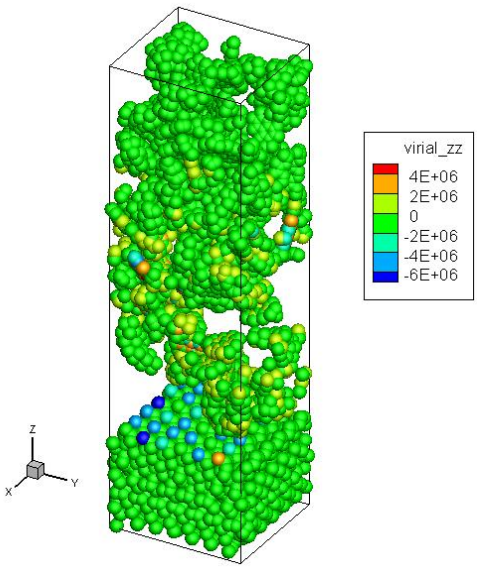

virial_zz when the interface strength reduced

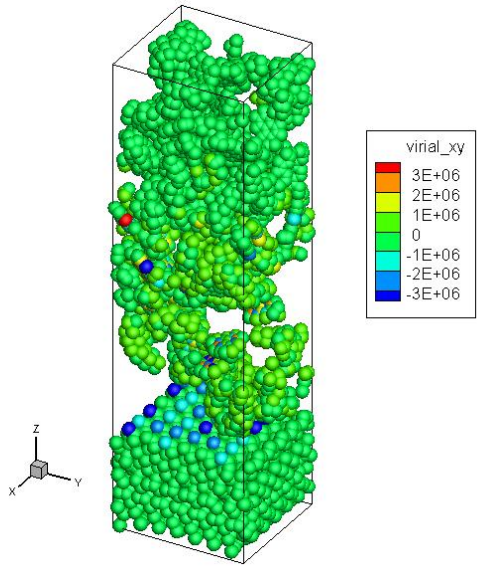

virial_xy when the interface strength reduced

Figure 7-7 Virial contour when the interface strength reduced

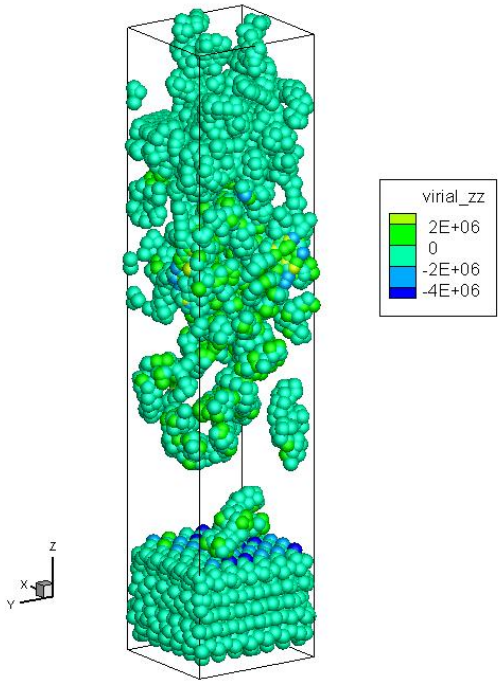

virial_zz when the interface totally failure

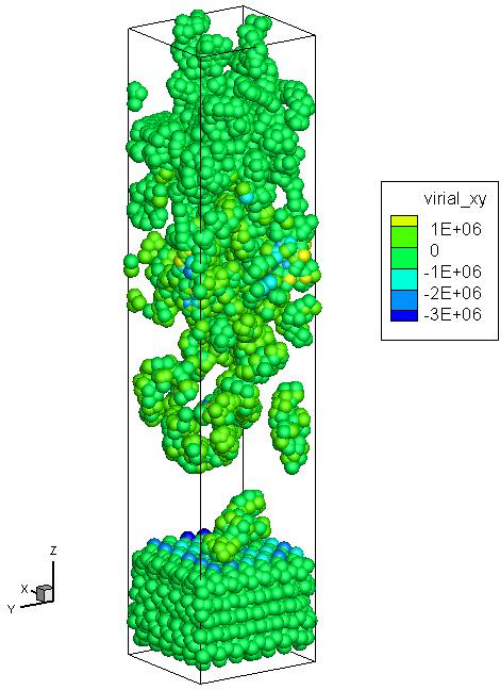

virial_xy when the interface totally failure

Figure 7-8 Virial contour when the interface totally failure

Figure 7-7 and Figure 7-8 illustrate the virial potential energy values appear at the

time the interface strength reduced, and when the interface is totally failure. The peak value of virial_zz shown in Figure 7-7 is 4.0×10^6 kcal/mol, while the peak value of virial_zz depicted in Figure 7-8 drops to 2.0×10^6 kcal/mol. In a similar manner, the peak value of virial_xy illustrated in Figure 7-7 is 3.0×10^6 kcal/mol, while the peak value of virial_xy shown in Figure 7-8 is reduced to 1.0×10^6 kcal/mol. It's clear that the interface interaction keeps decreasing with the increasing of interfacial deformation. Additionally, the originally condensed interfacial asphalt layer becomes loose and nano-voids appear with the deformation increases. The interatomic interaction drops down gradually both in normal and tangential directions. An interesting note is that two asphaltene molecules remain adhered to the substrate surface after the interface tension failure. This could be due to the cohesion strength weakness appearing somewhere at the interfacial region. This phenomenon is in agreement with the failure theory that adhesion and cohesion failure may combine together and may hardly to be discerned.

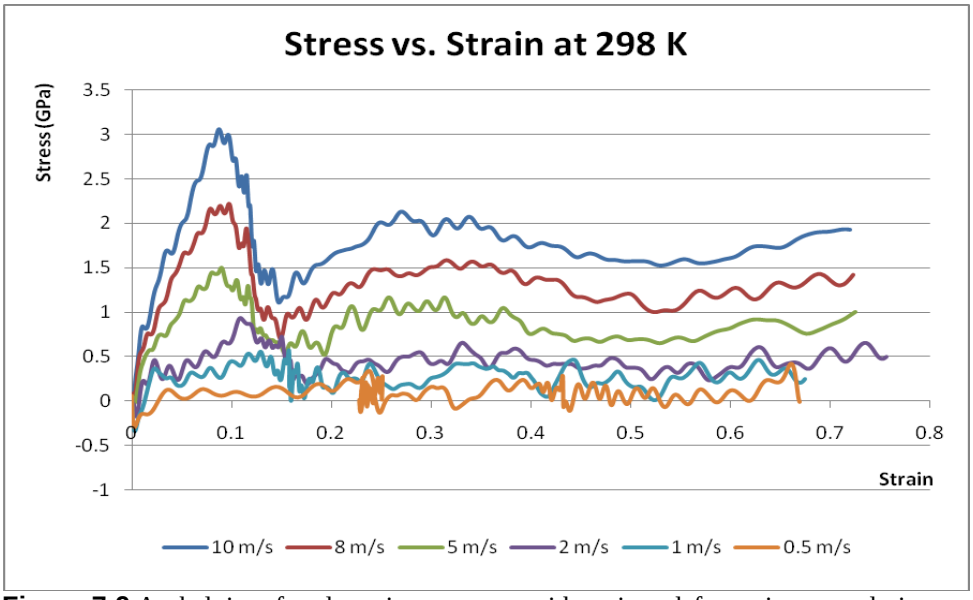

Figure 7-9 Asphalt interface layer instant stress with various deformation rates during tensile at 298 K

The stress-strain relations of the asphalt-quartz interface model under tensile loading, at temperature T = 298 K, and with various deformation rates is plotted in Figure 7-9.

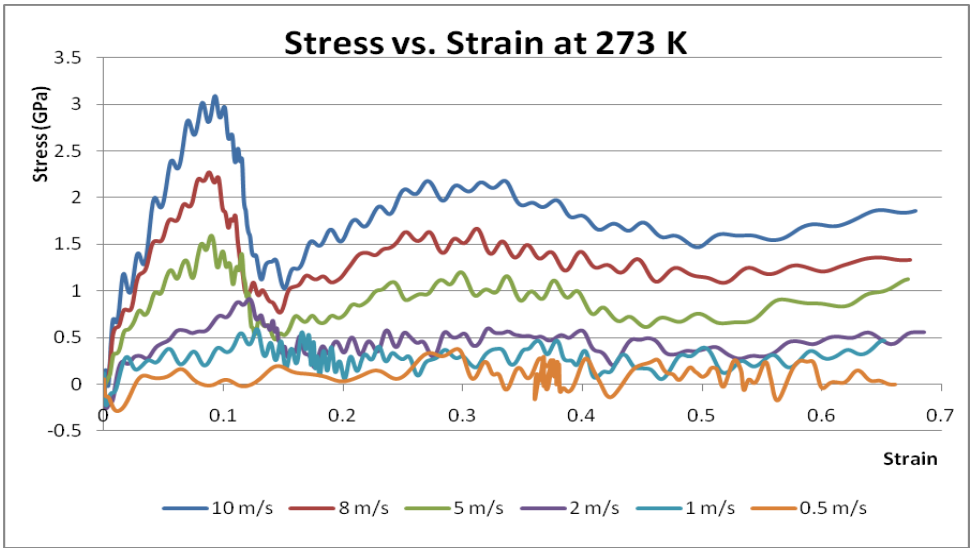

Figure 7-10 Asphalt interface layer instant stress with various deformation rates during tensile at 273 K

From the instantaneous stress-strain behavior at a deformation rate of 10 m/s shown in Figure 7-9, the first local peak value of 3.05 GPa with a strain of 0.1 shows a loosen state of interface layer. After reaching this highest stress point, the interface stress fluctuates suddenly, which means the start of failure progress at the interface region. The interface stress fluctuates thereafter and leads to a total interface failure. Thus, the yield strain and stress obtained at the strain rate of 10 m/s is 0.1 and 3.05 GPa, respectively.

Beyond the highest stress point at a strain of $\varepsilon_{zz} = 0.1$, the interface asphalt layer, a 30 Angstrom thick layer, is not able to hold the structure anymore and the plastic deformation starts to take place in order to accommodate the applied strain. The interface layer enters into a ductile state from then on and thereafter. During this process, ductile property of the interface layer commences and the plastic flow forms. At the same time, the nano-voids and holes appear simultaneously.

From the instant snapshots given in Figure 7-6, the condensed binding interface layer appears to be void of any defects at the beginning of tensile loading. It is followed by the appearance of a few loose regions, named nano-voids, along with the loading process at about T = 15 ps. After it passes over the highest stress point, the interface layer loses strength gradually. In accordance with the fluctuating stress state, the number of nano-voids increases rapidly and the size of nano-voids grows up as well. Followed by the growing of the sizes, nano-voids gradually connect to each other. Consequently, the

loading procedure will lead to an adhesive failure at the asphalt-rock interface. It is named a dynamical interfacial adhesive failure.

For the purpose of comparison at various deformation rates, Figure 7-9 shows that a stress slope goes up quickly and reaches the stress peak of 3.05 GPa appearing at the strain of 0.1. This is the tensile strength peak at a specific deformation rate of 10 m/s. After passing over the peak stress point, the stress curve goes down quickly and leads to the first valley at a strain of 0.15. At the same time, the stress reaches down to 1.0 GPa. The stress valley may in corresponding to the present of nano-pores. Then the stress rises up again and climbs up to a value of 2.2 GPa at a strain of 0.3. This time, however, the stress curve rises smoothly and decays gradually to 1.5 GPa in the strain of 0.7. The second peak stress should be in agreement with amorphous structure rearrangement and make itself a better resistance to external constraints.

The situation also happens at deformation rates of 8 m/s and 5m/s. But the stresses are a little bit lower than the one shown at the rate of 10 m/s. Those are reasonable results. One interesting discovery is that interface peak and valley stresses of all 3 deformation rates appear at the same strain of 0.1 and 0.15, respectively. That phenomenon means the failure strain of interface can be measured by any of these 3 deformation rates.

As to the deformation rate at 2 m/s, the curve fluctuates throughout the loading procedure. The relative peak occurs at a strain of 0.11 with a stress of 0.8 GPa. Then the curve drops down instantly and it decays thereafter. There is no obvious valley and second peak appear after the weak peak stress. Considering the stress-strain curve at 2 m/s, we can predict that the interface under relatively low deformation rate will decrease the strength. This behavior is in good agreement with the rheological nature of the asphalt materials.

For the other 2 deformation rates, 1 m/s and 0.5 m/s, the rheological properties are both illustrated obviously. 1 m/s has the global peak stress of 0.6 GPa and other local peak of abound 0.4 GPa. It seems the peak and valley share the same stress. With the drop down of peak stress, the corresponding strain moves to 0.13. On the contrary, 0.5 m/s represents a totally non-peak and non-valley properties. The stress at this deformation rate decay smoothly and no strength can be obtained.

Comparing with the stress-strain curves at 298 K shown in Figure 7-9, the interface shows no difference at 273 K, as given in Figure 7-10. Thus temperature dependency properties of asphalt cannot be captured in the above two figures. The reason of this discrepancy could be the temperature difference is relatively small, because physically asphalt is measured with almost the same mechanical properties at 298 K and 273 K.

7.8 Summary

The connection between the simulations of the atomistic strain-stress and the macroscopic strain-stress is very useful. Basically, this work examines the effect of nanoscale interfacial interactions between the asphalt molecules and mineral aggregate phases, as well as the effect of structural hierarchy on mechanical strength of asphalt-quartz composite materials in different loading environments. Such analyses could bring forth important evidence on the role of interfacial arrangement, structural hierarchy, and chemical environment in pavement materials interface failure.

The atomistic modeling is employed to calculate the deformation, failure, and strength of asphalt-aggregate interface. A series of calculations of different mechanical loading types is performed to gain insight into the deformation and failure behaviors of interface. Figure 7-9 and Figure 7-10 shown in this chapter provide an overview of the strength properties of asphalt-aggregate interface, summarizing the relative quantitative strength under different rates of loading.

These simulation results show that the distribution of initial velocities (initial temperature) does not have a significant effect on the deformation behavior. In addition, the results suggest that a critical outcome of these studies is the observation that the interface structure is at an increasingly large tensile stretch with a higher loading rate. Such information about the interface failure behavior of asphalt-aggregate may be essential to understand the role of asphalt components in pavement materials. Furthermore, the results provide useful estimations of the failure and deformation strength for different types of loading rates, as well as enable a comparison of different relative strengths.

The practical result of this study hopefully will be an improvement in the prediction of hot-mix-asphalt (HMA) performance by better characterization of the asphalt-aggregate interface behaviors, which is known to vary significantly with the compositions of both asphalt and aggregate.

Chapter 8
Modeling of Interface under Confined Shear Strength

8.1 Introduction

In Chapter 7, we explored the tensile strength of an asphalt-aggregate interface system. Normally, the nanoscale interface is always under two fundamental loading mechanisms. One is the tensile, another is the shear. In this chapter, asphalt-aggregate interface shear strength is investigated by atomistic modeling.

As demonstrated in Chapter 7, asphalt-aggregate interface system is a thin film structure. Our knowledge of such thin films has increased greatly in recent years due to the development of high performance computers and newer experimental techniques such as Surface Force Apparatus (SFA). Many MD simulations have been performed for confined fluids between two planes in the effort to mimic the SFA experiments.

Interface shear is an extremely complex phenomenon, which is common to many technological, geological, and biological applications. In order to understand the interface shear, one needs to be able to characterize what is going on the molecular level.

To understand the atomic processes occurring at the interface of two interfacial materials when they are brought together or moved with respect to one another is central to many technological problems, including adhesion, lubrication, and friction. Although our understanding of static interfaces have advanced considerably, very little is known about dynamic interfacial behaviors at the molecular level. The classical continuum theorem has historically provided most of the theoretical and computational tools for engineers. However, technology is now reaching to nanoscale dimensions where the continuum picture is no longer valid. Molecular simulation and microscopic experimental

techniques provide excellent opportunities to tackle these interfacial friction problems [105-106]. On the theoretical front, several molecular dynamics simulations have been carried out to study properties of thin films under shear [107-108]. On the experimental front, the Surface Force Apparatus is recently employed to study both static and dynamic properties of liquid thin films sandwiched between two smooth surfaces.

Molecular dynamic simulations provide an effective approach to analyze this phenomenon at the molecular level. Those previous MD studies on model systems have helped us to understand liquid layer under nano-confinement and the nature of transitions between 'smooth' and stick-slip sliding.

However, a direct comparison between simulation and experiment still remains impossible. This is because the lowest shear rates accessible by MD are at least four orders of magnitude larger than those typically used in experiments. This limitation directly stems from the MD method. In MD simulations, properties are averaged over the steady state, which becomes very noisy for low shear rates. Having a large signal-to-noise ratio (and hence subjecting the asphalt to large shear rates) is therefore crucial to obtain the meaningful averages in the steady state. This basically prevents accessing the interface interaction for realistic shear rates. Thus, current MD methods are therefore unable to shed light on a number of recent experimental measurements on films of about 5~8 molecular layers.

8.2 Confined Shear Model

This chapter aims to shear the asphalt-quartz interfacial atomistic system at different shear rates between two quartz walls and calculate the interfacial shear stress. In confined shear simulations, the interfacial shear stress can be expressed as horizontal forces at the interface. The interfacial shear velocity profiles are also calculated for monitoring the interface shear system instantly.

Based on the above goals, a 3-layer asphalt-quartz atomistic model is constructed in Figure 8-1. Note that Figure 8-1, Figure 8-2, and Figure 8-3 illustrate the front view, top view and top-side view of the 3-layer interface system, respectively. The entire confined shear model system contains 6276 atoms, 4082 bonds, 7756 angles, and 11121

torsions. The cell size is of a=24.565 Å, b=27.03 Å, and c=112.21 Å in length and the angles are α=90°, β=90°, and γ = 90 °(orthogonal cell). Shear loading direction is applied along the X-axis (along a direction).

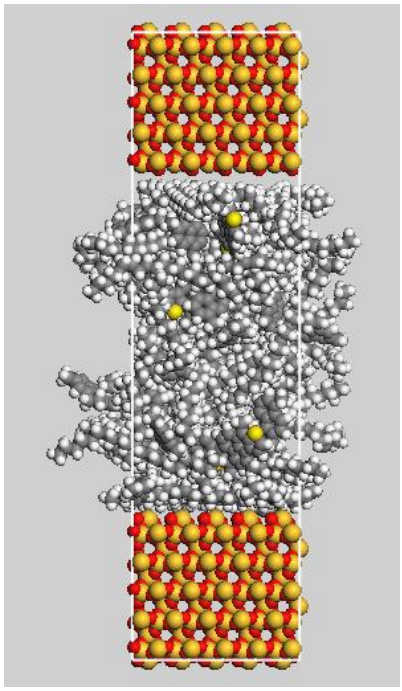

Figure 8-1 Asphalt_mix1 layer confined between two layers of quartz wall (front view)

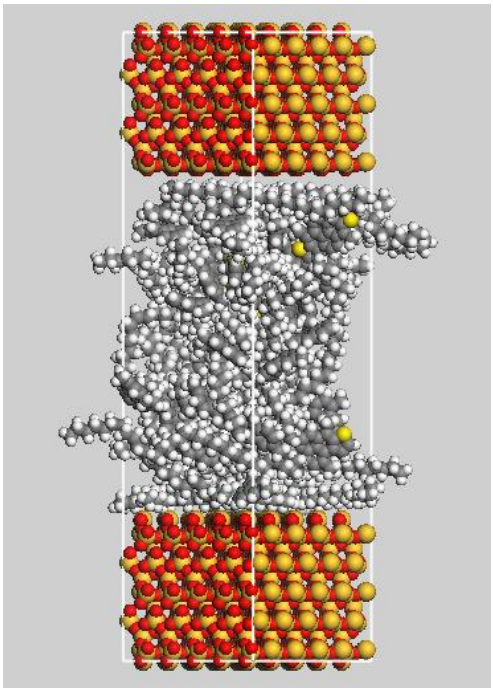

Figure 8-2 Asphalt_mix1 layer confined between two layers of quartz wall (side view)

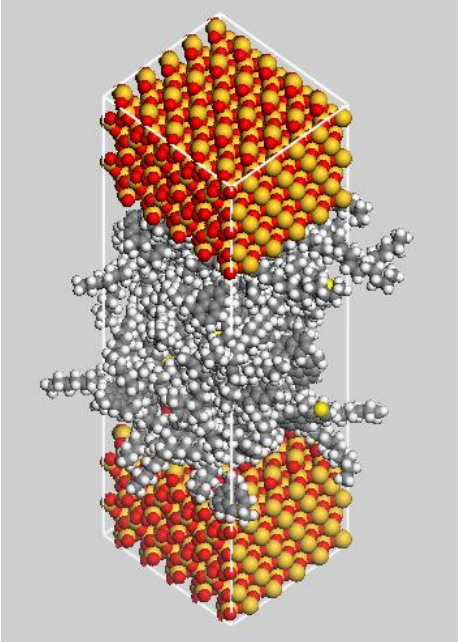

Figure 8-3 Asphalt_mix1 layer confined between two layers of quartz wall (top-side view)

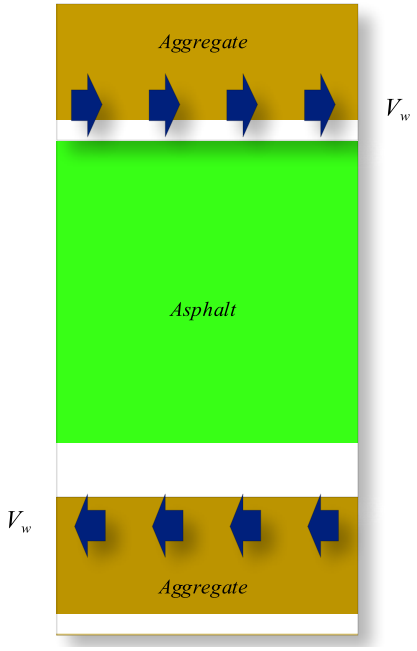

Figure 8-4 Loading scheme of asphalt_mix1 layer confined between two layers of quartz wall

As shown in the 3-layer sandwich model, CVFF-aug forcefield is used to characterize the interatomic interaction and simulations are performed using LAMMPS. In order to simulate the confined shear of the systems as described above, the whole system was divided in three parts. The top quartz layer was moved as a rigid body with a given velocity in OX direction, its movement was confined to the OX directions, all forces in the OX direction were set to zero. The bottom quartz layer was held frozen in its starting position. The middle asphalt layer was left completely flexible.

The quartz surface was constructed from unit cells of quartz and multiplied until the cell length in X and Y direction had appropriate size. The asphalt layer was chosen from the asphalt_mix1 model in Chapter 4 and been confined in between the two layers. The whole system equilibrated using LAMMPS molecular dynamics with both quartz layers kept rigid before applying shear. The system was equilibrated for 5000 ps in order to fully possible adhesion of the asphalt towards the mineral surface. Then shear simulations were performed at various shear rates in order to determine the shear stress dependency on the shear velocities.

The simulation results obtained include the structure of the asphalt under shear

conditions, adhesion towards the quartz surface, and of course the shear stress at different shear rates. The results from the LAMMPS molecular dynamics study agree well with our expectations.

8.3 Simulation Details

Figure 8-4 shows the overall loading scheme of the confined shear simulation cell in the interfacial shear simulation. Asphalt molecules are confined between the two walls. The top and bottom walls have opposite shear direction and the shear direction is along the X axis.

The 3-dimensional periodic boundary conditions were applied to the entire simulation cell except for confined asphalt in the Z direction. This guaranteed that atoms moved out of the simulation cell on one side would re-enter the system on the other side along the X direction. Atoms in the quartz walls experienced both normal and tangential forces. These atoms mutually interacted with atoms in the rest of the sliding system across the wall–asphalt boundary through interatomic forces. Consequently, heat was transported across the sample and into the walls.

The sliding at the interface will generate heat, which will gradually raise the local temperature of the sample. When asphalt is under applied shear, work done on the system is converted into heat. The heat can diffuse away from the interface and the asphalt is a heat sensitive material. Hence proper methods should be used to remove the overheating. There are two approaches for shear flow simulations that could be used: in one case, the sheared asphalt is not thermostated and only the confining walls are maintained at a constant temperature; while in the other case, a suitable thermostat is employed to keep the entire mass of the fluid at a constant temperature. The first approach, appropriate coupling to a thermostat, is employed in this research to remove the heat.

Therefore, in this simulation, a fitful form of thermostat has to be applied to prevent overheating. Nose-Hoover thermostat technique is employed in these simulations. Specifically, the thermostat is applied to the Y and Z components of the velocities of the asphalt molecules.

The initial configuration of the system was chosen from the asphalt mix1 model

built up in Chapter 5. For the rest of the simulations, the initial configurations of the 3-layer confined model were taken from the aforementioned run. The NVT ensemble is used to make the temperature of the system steady. The NVT thermostat kept the whole cell at a desired constant temperature at 273 K and 298 K, respectively. Before the shear applied, the original built system is equilibrated for 50000 steps, in order to prevent the system energy blowing out.

8.4 Results and Discussion

The 3-layer asphalt mix1 with 2 quartz walls model subject to confined shear was performed in this study. In the simulations with shear loading, we use loading boundary conditions in a steered molecular dynamics protocol. For the purpose of fully control of every asphalt molecules, we use displacement boundary conditions, continuously displacing particles in the boundary. The simulations are carried out by MD simulation to equilibrate the potential energy as the external strain is applied.

We try to make the shear displacement as large as possible, so the simulation time duration altered with respect to different shear velocity. Snapshots of the confined shear simulation at shear velocity of 15 m/s and 1 m/s are shown in Figure 8-5 and Figure 8-6, respectively. Figure 8-5 depicts that the interface slides very quickly at high shearing velocity and it was totally debonding at 120 ps, while it took 1 ns for just half debonding at low shearing velocity. However, the shape and profile of two sheared asphalt systems seems with only a little difference.

Generally, the two loading cases illustrated that the interface boundary is the weak region of the model, because all simulations finally fail at the interface boundary and all of the failures belong to interfacial sliding failure mode.

Microstructure changes during shear can also be observed in Figure 8-5 and Figure 8-6. The rigid asphalt molecules in mix1 model deforms a little under shear. This may be because the condensed asphalt phase is composed of rigid asphaltenes and long chain resins, which results in semi-rigid characteristics and makes it not easy to deform. There are no nano-voids or nano-pores appeared in the asphalt layer throughout the simulation process. A sheared asphalt system illustrated in Figure 8-5 shows a sheared

structure of the asphalt layer, after applying the confined shear simulation in order to determine the shear stress state.

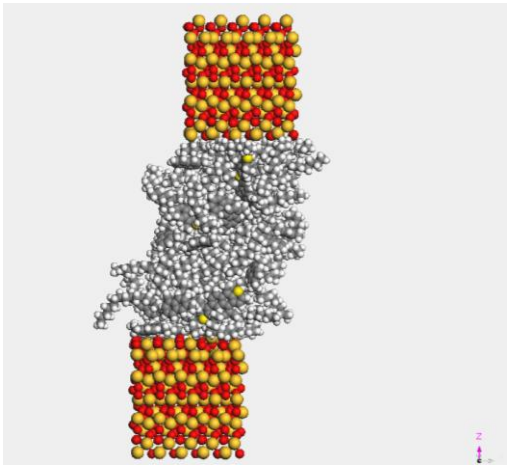

Time = 10 ps

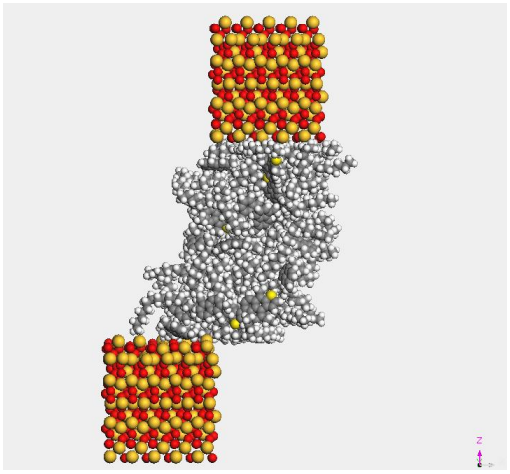

Time = 60 ps

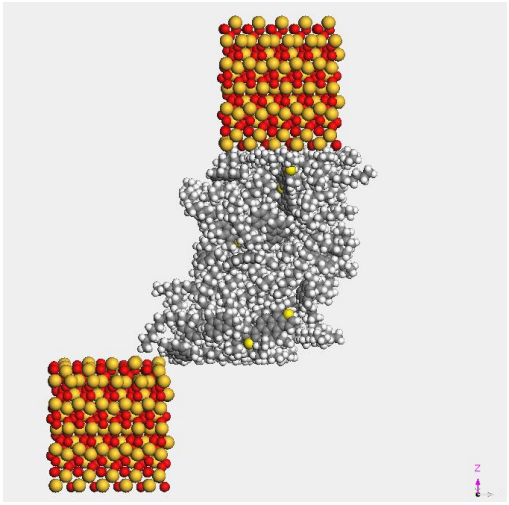

Time = 120 ps

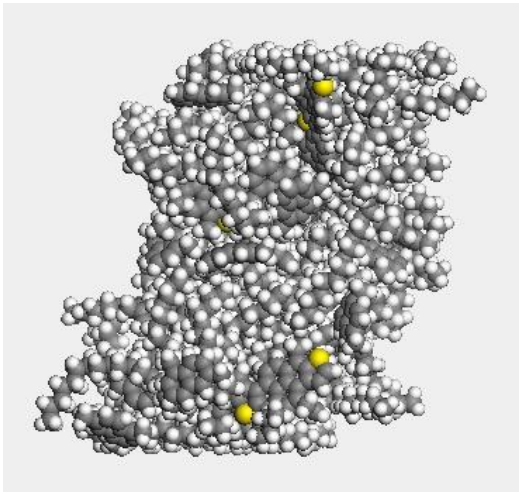

Sheared asphalt system after 120 ps MD simulation

Figure 8-5 Snapshot of confined shear at V=15 m/s

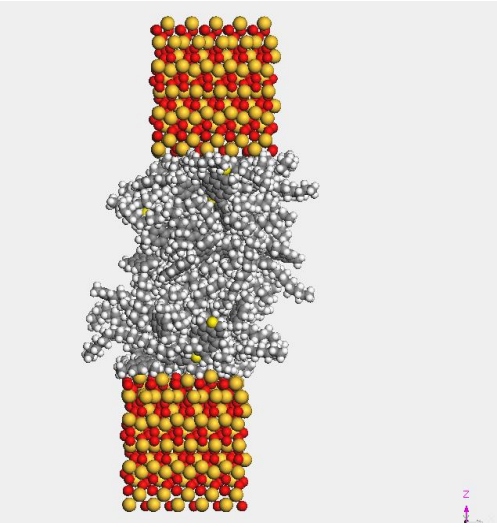

Time = 100 ps

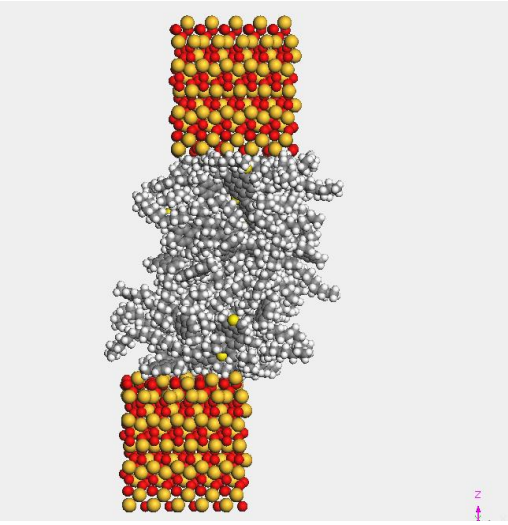

Time = 300 ps

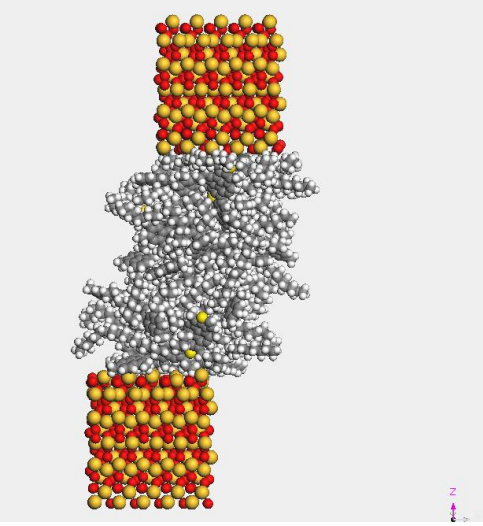

Time = 500 ps

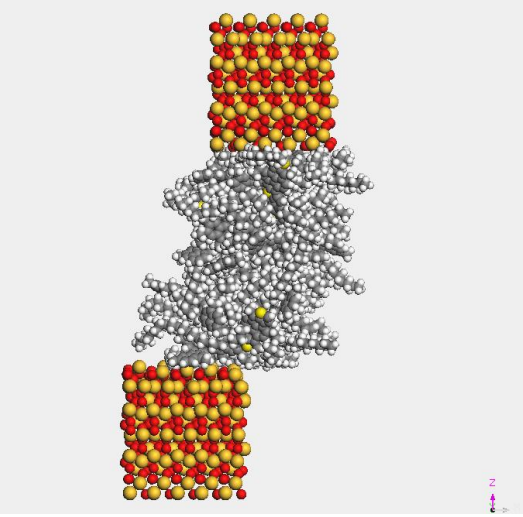

Time = 800 ps

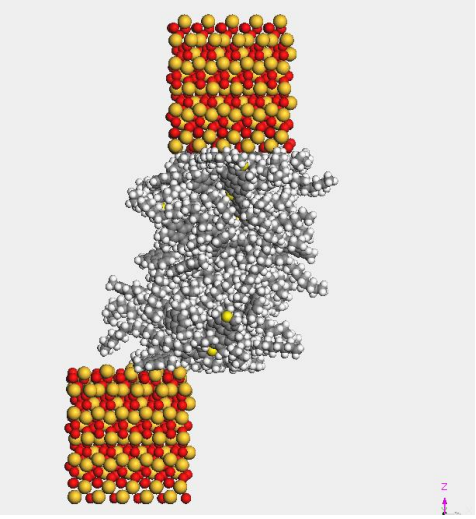

Time = 1000 ps

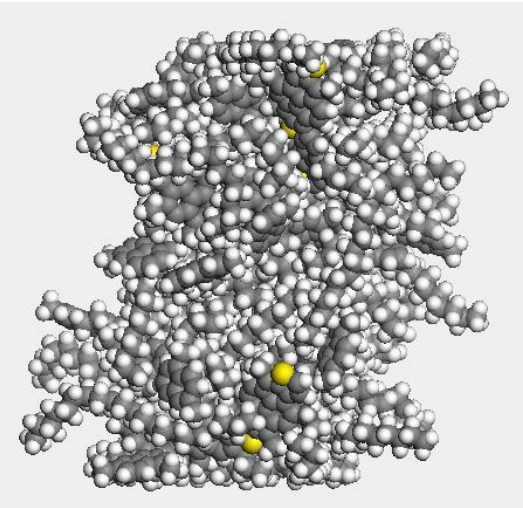

Sheared asphalt system after 1 ns MD simulation

Figure 8-6 Snapshot of confined shear at V=1 m/s

After deformation progresses, the atoms associated with each molecule are repositioned. This implies that the deformation associated with sliding remains confined to the weakened boundary zone and that shear is localized in the interface layer. Hence, the layer in the sliding interface region is responsible for the interfacial shear characteristics of the confined shear system. This is consistent with experimental observations, where failure surface was always found between and around the bi-material interface.

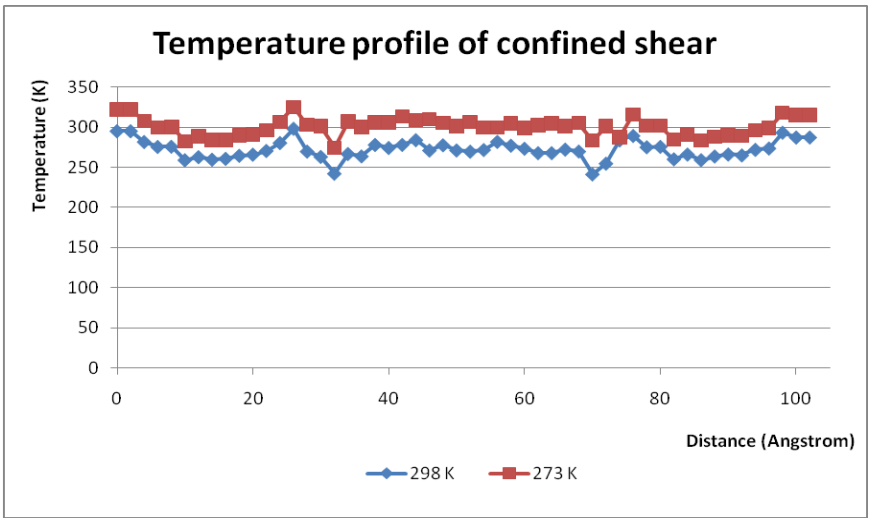

Figure 8-7 Temperature profile of the confined shear supercell

The temperature distribution across the simulation cell for 273 K and 298 K cases is indicated in Figure 8-7. From this profile, it was obvious that the shift of the sliding interface happened very soon after sliding was initiated. This is in consistent with our expectation that the temperature of both asphalt set and the wall sets maintained steady by NVT ensemble combined with Nose thermostat.

Based on the system configurations at different simulation time steps, the velocity profiles associated with all atoms in the simulation cell were also plotted. Two such velocity profile plots (at T = 273 K and T = 298 K, respectively) are shown in Figure 8-8 and Figure 8-10.

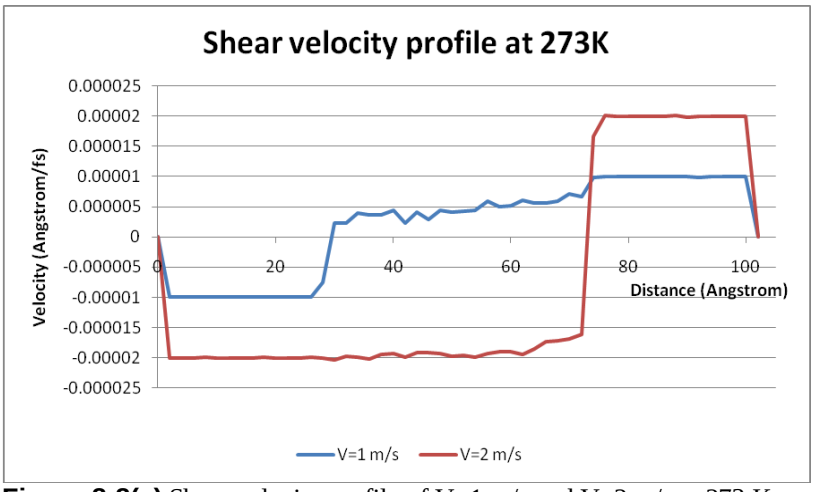

Figure 8-8(a) Shear velocity profile of V=1 m/s and V=2 m/s at 273 K

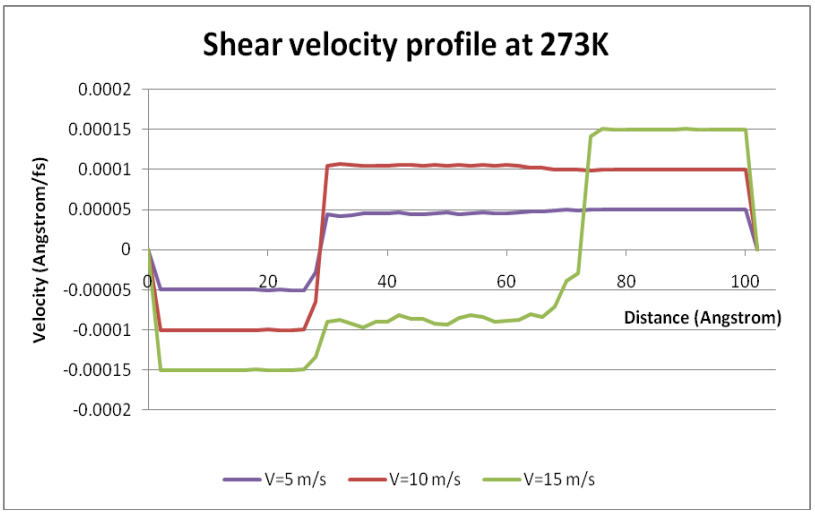

Figure 8-8(b) Shear velocity profile of V=5 m/s, V=10 m/s, and V=15 m/s at 273 K

Figure 8-8 plots the shear velocity profile of the interface at 273 K. For the purpose of clear demonstration, five shear velocities profile are separated into two groups and plotted in two figures, respectively. In Z direction of the simulation cell, 2 quartz walls are occupying the position range of (0 ~ 27) and (75~ 102) Angstrom. The asphalt layer is located in between them. Constant shear velocity is applied along the X axis and two walls are shearing towards opposite direction. At low velocity, e.g. V=1 m/s, the asphalt layer has relatively longer time for relax with each displacement step. Thus, a velocity ramp could be seen between the range of (27~75) Angstrom. This results in a most deformed asphalt shape comparalbe to other shear velocities. However, the velocity ramp disappears with higher velocities, e.g. V=2 m/s, V=5 m/s, and V=10 m/s conditions. This phenomenon is due to the higher velocity that only leaves limited time for the apshalt layer to relax. This leads to the fact that the intermolecule de-cohsive interaction is larger than the asphalt-quartz de-adhesion interaction. Thus the asphalt molecules slide along one of the walls (depends on the interaction strength of each side) at the start of shearing and without the occurance of any velocity ramp.

Such velocity ramp phenomenon is more obviously present for simulation at 298 K, shown in Figure 8-8. The steepest velocity ramp occurs at the lowes velosity of V=1 m/s. With the velocity increases, the ramp decreases gradually at V=2 m/s and V=5 m/s. Thereafter, little ramp can be seen for V=10 m/s and V=15 m/s.

One interesting observation, abnormally, as shown in Figure 8-8 is that a ramp occurs in V=10 m/s, and velocity appears in the V=2 m/s profile. This could be the roughly equilivant shear forces appeared at these two interfaces from the beginning of the simulation. Thus, there is no relatively weak interface for the shear cleavage. From the thermodynamical standpoint of view, asphalt-quartz interface bonded better (performs better) in the case at 273 K, a relatively lower temperature. One note that the asphalt at lower temperature has larger cohesive energy and bigger interaction force, which are already demonstrated in Chapter 5.

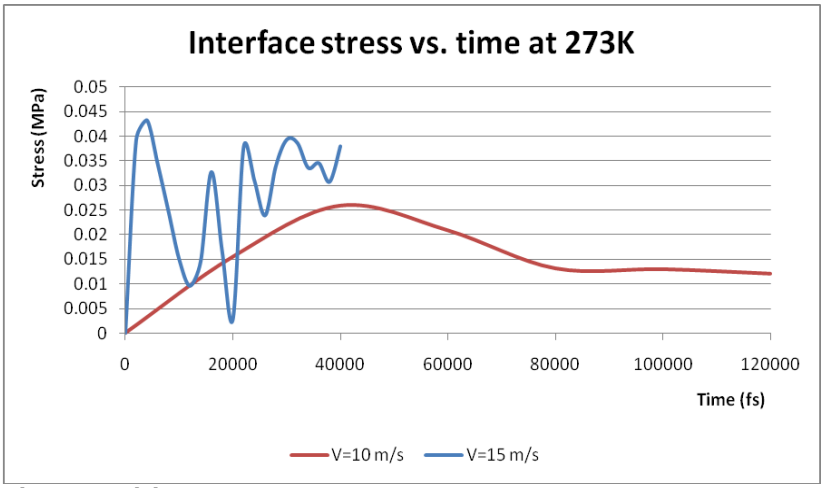

Figure 8-9(a) Shear stress profile of V=10 m/s and V=15 m/s at 273 K

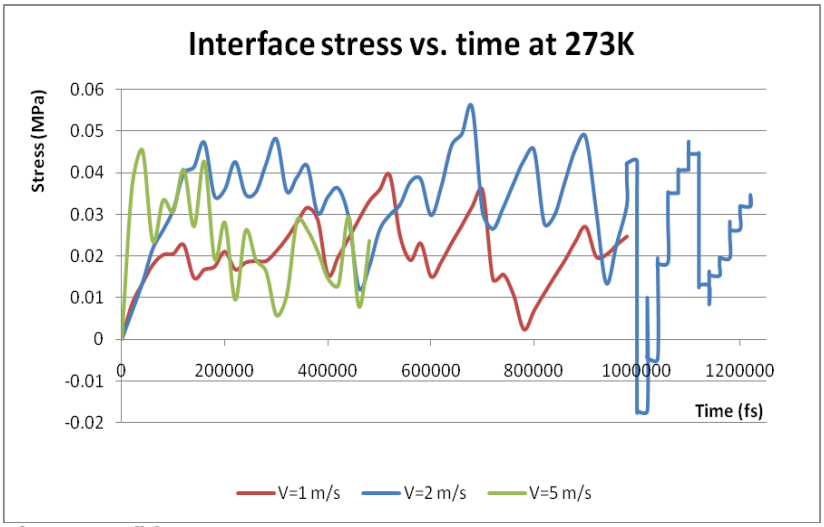

Figure 8-9(b) Shear stress profile of V=1 m/s, V=2 m/s, and V=5 m/s at 273 K

Figure 8-9 depicts the interface shear stress during the shear process. The fluctuation features are shown throughout the simulation advances and the stress peaks range from 0.2 to 0.5 MPa. Typically, each interface debonding appears at the start of sliding. In other words, the interface shear failure occurs just after the first stress peak. From then on, some stress peaks may appear, but they may be caused by other factors, e.g. the atoms inter-lock during sliding.

As demonstrated in Figure 8-9, observations can be drawn that the shear strength of V=1 m/s is 0.04 MPa and it appears at 450 ps, while the strength of V=1 m/s is 0.045 MPa with appears at 20 ps. For condition of V=5 m/s, the peak stress shows 0.48 MPa at 160 ps. For condition of V=10 m/s, the peak stress shows 0.43 MPa at 20 ps.

Nevertheless, the condition of V=15 m/s shows low stress of 0.25 MPa and decays quickly. This may be due to the high velocity sliding wall destroyed the interface bonding at the very beginning of simulation and there is no atomic interlock can reduce the shear slide. Hence, the shear strength decreased at a higher sliding speed. Also, at high shear speeds, the curves for shear stress of the different velocity converged. That is caused by the effect of structure on interfacial adhesion was more pronounced at lower shearing speeds. There is no apparent velocity dependency can be drawn from the available results.

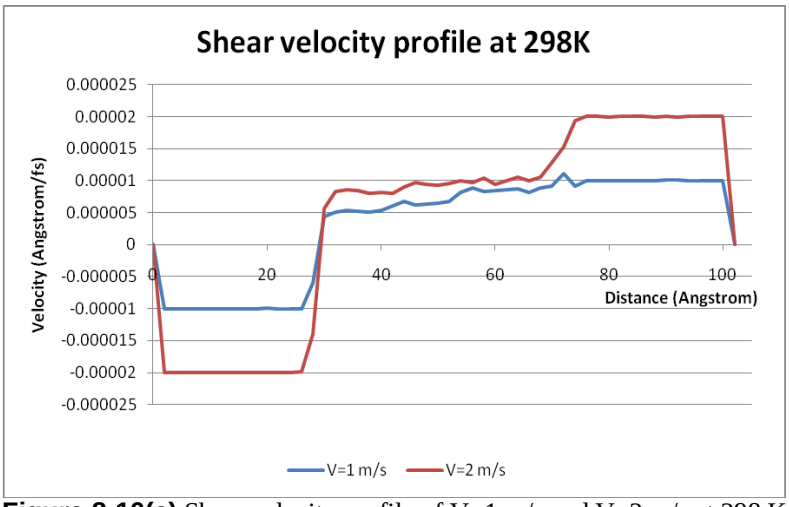

Figure 8-10(a) Shear velocity profile of V=1 m/s and V=2 m/s at 298 K

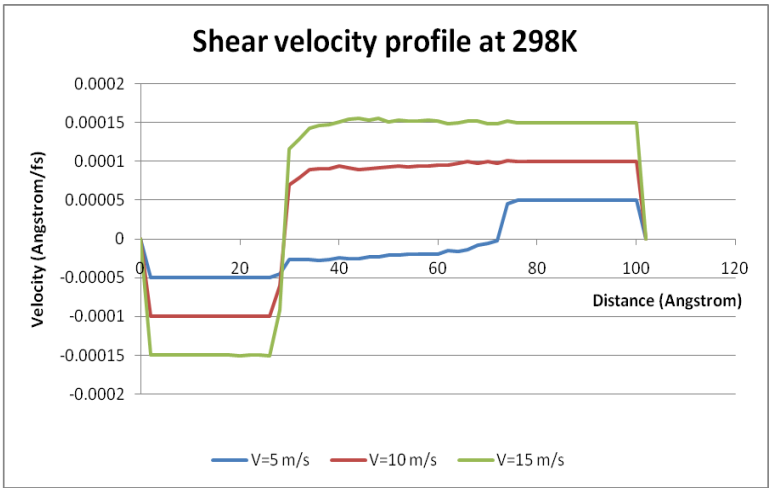

Figure 8-10(b) Shear velocity profile of V=5 m/s, V=10 m/s, and V=15 m/s at 298 K

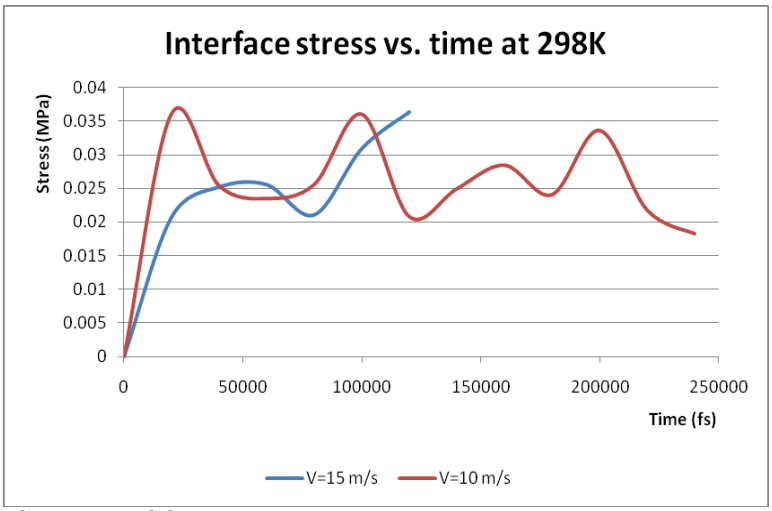

Figure 8-11(a) Shear stress profile of V=10 m/s and V=15 m/s at 298 K

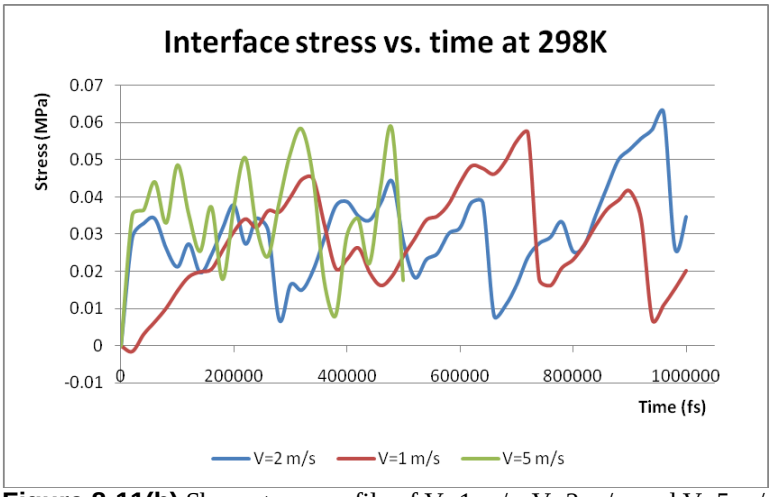

Figure 8-11(b) Shear stress profile of V=1 m/s, V=2 m/s, and V=5 m/s at 298 K

In comparison with the plots in Figure 8-11, the same fluctuation trend can also be observed with those shown in Figure 8-9. However, there seems no temperature dependency properties can be observed from the confined shear stress. Probably, the interface interaction along shear direction is too weak to be concern, which is led by the MD simulation noise effects.

8.5 Summary

In this chapter, we carried out the constant-velocity MD simulations of asphalt

confined between quartz surfaces under shear. Various properties of the confined asphalt, including velocity profiles, stress profile, and temperature profiles were calculated and compared with different temperature. Interfacial slide failure was found in all shear simulations.

The simulation consists of an equilibration stage, followed by a production stage during which data are collected. Shearing of the asphalt appears by moving the top wall in the positive X direction and the bottom wall left fixed, with the upper wall moving at a specified velocity. During the shear process, the wall atoms are allowed to fluctuate about equilibrium positions, to which they are attached. Heat generated by the shearing process is removed by thermostatting only the wall atoms, thereby assuring a realistic simulation in which the thermal conductivity of the asphalt and shear forces together determine the asphalt temperature. Data collection consists of the calculation of velocity, temperature, and wall shear stress profiles, with averaging intervals specified. The wall temperature is the temperature of the thermostatted walls. The wall velocity is to specify the velocity of the walls in meter/second.

In all cases, the shear strength decreased at a higher sliding speed. Also, at high speeds, the curves for shear stress for the different velocity converged. That is, the effect of structure on interfacial adhesion was more pronounced at lower shearing speeds. However, there is no apparent velocity dependency that can be drawn from the available results. The reason lies in the fact the asphalt molecules themselves tend to agglomerate led by cohesive potential, so the mix1 model shows relatively rigid properties under shearing.

Materials composition is associated with velocity, which may be related to local structural changes on the sliding interface. In the slide of asphalt layer, asphalt molecules near a sliding interface deforms most. Shear localization is induced by formation of a weakened layer in MD simulations for composites containing small molecules of asphalt. This is consistent with experimental observations.

As pointed out earlier, direct comparison between simulation and experiment is still difficult. A noticeable issue is the inappropriate configuration of experiments. As all other simulations, however, current MD simulations were carried out at a high shearing speed.

Chapter 9

Atomistic Modeling of Moisture Damage

9.1 Introduction

Asphalt pavements are susceptible to moisture induced damage, which is caused by moisture interaction with asphalt-aggregate bonds. Although moisture-induced damage in asphalt concrete has been studied for over 70 years, two very fundamental questions remain unanswered: Can the conditions that cause moisture-induced damage be accurately predicted? How can moisture-induced damage be mitigated? The foremost difficulty lies in the fact that the moisture interaction with asphalt-aggregate bonds is a phenomenon that appears at the atomic or nano-scale level. This Chapter offers a novel approach to understand and quantify moisture interactions with asphalt-aggregate bonds at the nano-scale, and relating these interactions to the moisture-induced damage at the Macro-scale.

9.1.1 Definition of Moisture Sensitivity

Moisture-related problems are due to

- Adhesive failure—stripping of the asphalt film from the aggregate surface, or
- Cohesion failure—loss of mixture stiffness.

These mechanisms can be associated with the aggregate, the binder, or the interaction between the two ingredients. Moisture-related distresses are also accelerated by mix design or construction issues, including those factors given in Table 9-1.

Moisture damage can be defined as the loss of strength and durability in asphalt mixtures due to the effects of moisture. Moisture damage can occur because of a loss of bond between the asphalt cement or the mastic (asphalt cement plus the mineral filler and

smaller aggregate), the fine, and the coarse aggregate. Moisture damage also appears because moisture weakens the mastic, making it more susceptible to moisture during cyclic traffic loading. The literature [13, 109-110] refers to at least five different mechanics of stripping: detachment, displacement, spontaneous emulsification, pore pressure, and hydraulic scour.

Table 9-1 Factors that can contribute to moisture-related distress

MIX DESIGN	• Binder and aggregate chemistry • Binder content • Air voids • Additives
PRODUCTION	• Percent aggregate coating and quality of compaction • Temperature at plant • Excess aggregate moisture content • Presence of clay
CONSTRUCTION	• Compaction—high in-place air voids • Permeability—high values • Mix segregation • Changes from mix design to field production (field variability)
CLIMATE	• High-rainfall areas • Freeze–thaw cycles • Desert issues (steam stripping)
OTHER FACTORS	• Surface drainage • Subsurface drainage • Rehab strategies—chip seals over marginal HMA materials

9.1.2 Moisture-Related Distress Manifestations

Moisture-related distress is similar in many ways to distress caused by other factors, e.g. materials, design, and construction. Moisture tends to accelerate the presence of the distress types. The types of distress that can be related to moisture, or the other factors, are described below:

- Bleeding, cracking, and rutting: These distresses are caused by a partial or complete loss of the adhesion bond between the aggregate surface and the asphalt. This may be caused by the presence of water in the mix due to poor compaction, inadequately dried or dirty aggregate, poor drainage, and poor aggregate–asphalt

chemistry. It is aggravated by the presence of traffic and freeze-thaw cycles and can lead to early bleeding, rutting, or fatigue cracking.

- Raveling: Progressive loss of surface material by weathering or traffic abrasion or both. It is another manifestation of moisture-related distress. It may be caused by poor compaction, inferior aggregates, low asphalt content, high fines content, or moisture-related damage, and it is aggravated by traffic.
- Localized failures: This type of distress can be the end result of either of the types discussed above. It is progressive and can be due to the loss of adhesion between the binder and the aggregate or the cohesive strength in the mix itself.
- Structural strength reduction: This is a result of a cohesive failure causing a loss in stiffness in the mixture.

9.2 Causes of Moisture-related Distress

The detrimental effect of moisture in asphalt mixtures, called moisture damage, is one of the main reasons for early rehabilitation of asphalt pavements. Moisture plays a special role in the degradation of asphalt mixtures since it is not only the main source of weathering but also a major contributor to the evolution of other distresses. Moisture damage in asphalt mixtures is a complex phenomenon involving thermodynamic, chemical, physical, and mechanical processes. At a microscopic level, it can be defined as the progressive loss of functionality of the material due to loss of the adhesive bond between the aggregate surface and the mastic (a matrix comprising asphalt binder and the fine portion of the aggregates); or loss of the cohesive resistance within the asphalt binder.

Figure 9-1 illustrates a cohesive failure appearing at the asphalt phase without moisture. Figure 9-2 shows an adhesive fracture occurring at the aggregate-asphalt interface region without the penetration of water. The difference between adhesive failure and cohesive fracture lies in the crack location. Hence the crack location determines the fracture mode. Figure 9-3 illustrates the moisture immerged interface under slowly moisture damage, namely stripping failure. Moisture induced pavement failure can be seen from Figure 9-4, which depicts the early failures due to lack of adhesion caused by

climate effects.

Figure 9-1 Cohesive Failure

Figure 9-2 Adhesive Failure

Figure 9-3 Water Invades the Interface – Stripping

Figure 9-4 Early failures due to lack of adhesion and climate effects

During the last decade, the understanding of the various mechanisms that lead to moisture damage at the micro-scale has proceeded. Consequently, new experiments and analytical models have been proposed to reflect moisture damage due to one or more of these mechanisms [10]. Micromechanical modeling of moisture damage in asphalt mixtures becomes an efficient tool to understand the dynamics of the interaction of all damage mechanisms and to provide guidance for the development of continuum moisture damage models.

The main objective of this Chapter is to present the fundamentals and application of the atomistic modeling method that couples the effect of moisture diffusion and mechanical loading on the nanoscale structure asphalt mixtures interface. The first part of this Chapter discusses the damage mechanisms that are considered in the model. Next, the atomistic simulation of the model is described. Finally, the last section of the paper

explains how the model is used to study the damage produced in a series of 3D nano-mechanical representation of moisture induced asphalt-aggregate interface cohesive and adhesive models subject to mechanical loading.

Numerous factors can contribute to moisture sensitivity problems in asphalt pavements. Some of these factors are discussed briefly in this section.

9.2.1 Moisture-Sensitive Aggregates

Aggregates can greatly influence whether a mixture will be moisture sensitive or not. The aggregate surface chemistry and the presence of clay fines are important factors affecting the adhesion between the aggregate and the asphalt binder. In pavement industry, common methods of combating these factors are through the use of antistrip agents such as liquids or lime and by the elimination of detrimental clay fines through proper processing or specification.

9.2.2 Asphalt Binder Sensitivity

The asphalt binder can influence both the adhesion between it and the aggregate and the cohesion of the mastic. Adhesion is influenced by the chemistry of the asphalt as well as by the stiffness of the binder. The cohesive strength of the asphalt matrix in the presence of moisture is also influenced by the chemical nature of the binder and processing techniques. The fundamentals of binder sensitivity to water are also treated in this chapter on chemical and mechanical processes.

9.2.3 Presence of Water and Traffic

Moisture-related problems do not occur without the presence of water and traffic, which provides energy to break the adhesive bonds and cause cohesive failures. Repeated freeze-thaw cycles can also accelerate the distress in the pavement. Moisture comes from rain infiltration or from beneath the surface. Once the moisture is in the pavement, it can affect either the adhesive bond or cohesive strength.

9.3 Contributing Mechanisms to Moisture Damage

9.3.1 Detachment

Detachment is the separation of an asphalt film from an aggregate surface by a thin film of water without an obvious break in the film. Theories that explain adhesive bond energy provide the rationale to understand detachment. Several factors are involved in detachment. First of all, it is necessary to develop a good bond between the asphalt and the aggregate. Such a bond is initially dependent on the ability of the asphalt to coat the aggregate. Coating ability of aggregate increases as the surface tension or free surface energy of adhesion decreases [111]. According to the reference [111], if a three-phase interface consisting of aggregate, asphalt, and water exists, water reduces the free energy of the system more than asphalt to form a thermodynamically stable condition of minimum surface energy. Surface energy measurements at Texas A&M University [12] have established that when the free energy at the asphalt-aggregate interface is calculated in the presence of water, energy is released, meaning that the aggregate surface has a strong preference for water over asphalt. The larger the value, the stronger is the preference for detachment of asphalt from aggregate in the presence of water.

Most asphalts have relatively low polar activity and the bond that develops between the aggregate and asphalt is chiefly due to relatively weak dispersion forces. On the other hand, water molecules are highly polarities and can replace the asphalt at the asphalt-aggregate interface. Chemical reaction theory can be used to explain stripping as a detachment mechanism [112].

9.3.2 Displacement

Displacement differs from detachment because it involves displacement of asphalt at the aggregate surface through a break in the asphalt film [113]. The source of the break or disruption may be incomplete coating of the aggregate surface, film rupture at sharp aggregate corners or edges, micro-holes originating in the asphalt film because of aggregate coatings, etc. Some authors describe film rupture as a separate mechanism of moisture damage, but it can be incorporated as part of the displacement mechanism.

The process of displacement can proceed through changes in the pH of the water at the aggregate surface that enters through the point of disruption. These changes alter the type of polar groups adsorbed, leading to the buildup of opposing, negatively charged, electrical double layers on the aggregate and asphalt surfaces. The driving force to reach equilibrium attracts more water and leads to physical separation of the asphalt from the aggregates.

9.3.3 Environmental Effects

Terrel and Shute [114] report that factors such as temperature, air, and water have a profound effect on the durability of asphalt concrete mixtures. In mild climates where good-quality aggregates and good-quality asphalt cements are available, the major contribution to deterioration is traffic loading and the resulting distress manifestations. Premature failure may result when poor materials and traffic are coupled with severe weather. Terrel and Al-Swailmi [115] identify a number of environmental factors of concern: water from precipitation of groundwater sources, temperature fluctuations (including freeze-thaw conditions), and aging of the asphalt. They identify traffic and construction techniques, which are external to the environment, as important factors. Factors considered by Terrel and Shute to influence water sensitivity in asphalt mixtures are given in Table 9-2.

Table 9-2 Factors Influencing Response of Mixtures to Water Sensitivity [114]

Variable	Factor
Existing condition	Compaction method Voids Permeability Environment Time Water content
Materials	Asphalt Aggregate Modifiers or additives
Conditioning	Curing Dry versus wet Soaking Vacuum saturation

	Freeze–thaw Repeated loading Drying
Other	Traffic Environmental Age

9.4 Adhesive Failure and Cohesive Failure

Damage in asphalt mixtures can appear within the mastic (cohesive failure) or at the aggregate-mastic interface (adhesive fracture or failure). Whether or not a cohesive or adhesive failure occurs depends on the nature of the mastic and the relative thickness of the mastic around the coarse and fine aggregate. Lytton [116] used micromechanics to assess the 'thickness' of the asphalt film at which adhesive failure gives way to cohesive failure. The cohesive and adhesive bond strength determined from cohesive and adhesive surface energies versus thickness of the asphalt binder or mastic. The theory essentially states that asphalt mixtures with thin asphalt films fail in tension by adhesive bond rupture, while those with thicker asphalt films (or mastic films) fail because of damage within the mastic (cohesive failure) as opposed to interfacial debonding. The thickness that differentiates these two types of failure is dependent on the rheology of the asphalt (or mastic), the amount of damage the asphalt or mastic can withstand prior to failure, the rate of loading, and the temperature at the time of testing.

Consider an example, when asphalt or mastic coatings are thin, adhesive strength controls performance. In this stage, the adhesive bond strength in the presence of water determines mixture strength and is the critical condition. On the other hand, when asphalt or mastic coatings are relatively thick, cohesive properties limit or control damage resistance. Therefore, in this situation, the impact of moisture intrusion into the mixture may be the key to assessing moisture damage of the mixture. In this case it may be more important to consider the impact of how much moisture the mastic holds and the impact on cohesion of this infused water than to consider adhesive bond strength in the presence of water.

Realistically, it is necessary to consider both adhesive bond and cohesive strength

properties of the mixtures as mastic coatings range from relatively thin to relatively thick throughout the mixture. Mixture strength then becomes a question of the statistical distribution of conditions where adhesion or cohesion strengths control. Thus the effects of moisture on adhesive bond strength and cohesive mastic strength are perhaps equally important.

9.4.1 Adhesion Theories

Terrel and Shute [114] describe four theories that are often used to explain the adhesion between asphalt and aggregate: (a) chemical reaction, (b) surface energy, (c) molecular orientation, and (d) mechanical adhesion. Most likely a combination of mechanisms occurs synergistically to produce adhesion, and no one theory describes adhesion. They explain that the four theories are affected by the following factors: surface tension of the asphalt cement and aggregate, chemical composition of the asphalt and aggregate, asphalt viscosity, surface texture of the aggregate, aggregate porosity, aggregate cleanliness, and aggregate moisture content and temperature at the time of mixing with asphalt cement.

9.4.2 Surface Energy and Molecular Orientation

From a simplistic viewpoint, surface energy may be described in terms of the relative coating ability of aggregate surfaces by water or asphalt. Water is a better wetting agent than asphalt due to lower viscosity and a lower surface tension. However, the concept of using surface energy to calculate the cohesive strength of the asphalt mastic and the adhesive bond energy between aggregate and the asphalt cement or between aggregate and the mastic is much more complex.

Molecular orientation is coupled with surface energy because both are a part of a theory that considers structuring of asphalt molecules at the asphalt-aggregate interface and assumes that adhesion between asphalt and aggregate is facilitated by a surface energy reduction at the aggregate surface as asphalt is adsorbed to the surface. Kringos et al. [13] describes molecular orientation and surface energy as synergistic processes. They also mention the observations of researchers regarding surface phenomenon. For example, how aggregates that impart a relatively high pH to contact water or that have a

relatively high stripping or debonding potential.

9.4.3 Cohesion Theories

Cohesion develops in the mastic and is influenced by the rheology of the filled binder. As will be discussed in more detail subsequently, Kim [117] describe how the resistance of a mastic to microcrack development is strongly influenced by the dispersion of mineral filler. Thus, the cohesive strength of the mastic is controlled not by the asphalt cement alone, but by the combination and interaction of the asphalt cement and the mineral filler. Terrel [114] indicates that water can affect cohesion in several ways, including weakening of the mastic due to moisture saturation and void swelling or expansion. Cohesion properties would influence the properties in the mastic beyond the region where interfacial properties dominate. An interesting result of this is the work of Schmidt and Graf [118], who show that an asphalt mixture will lose about 50 percent of its modulus upon saturation. The loss may continue with time, but upon drying, the modulus can be completely recovered.

Cheng et al. [119] describe the severe weakening of asphalt mixtures when they are subjected to moisture conditioning. They demonstrate the strength loss in a repeated load triaxial test when subjected to 85% saturation. The results indicate that this strength loss is predictable when one compares the wet adhesive bond strength between the asphalt and the aggregate with the much higher dry adhesive bond strength. But they go on to demonstrate that the rate of damage in various mixtures is also related to the diffusion of water into the asphalt mastic, and that the asphalts that hold the greatest amount of water accumulate damage at a faster rate.

9.5 Effect of Asphalt Composition on Adhesion

9.5.1 Asphalt Composition

The chemistry of asphalt is complex. This brief overview is certainly a simplification of the complex nature of asphalt and is meant to provide descriptions of

basic asphalt components, which are used in discussion throughout this chapter.

9.5.2 Elemental Composition

Asphalt molecules are comprised primarily of carbon and hydrogen (between 90% and 95%) by weight. However, the remaining atoms, called heteroatoms, are very important to the interaction of asphalt molecules and hence the performance of asphalt. They include oxygen, nitrogen, sulfur, and iron.

9.5.3 Molecular Structure

Asphalt atoms are linked together to form molecules. Perhaps the simplest is the aliphatic carbon-carbon chain saturated with hydrogen bonds. The carbon-carbon bonds can also form rings saturated with hydrogen. These saturates are essentially nonpolar and interact primarily through relatively weak Van der Waals forces. A second class of asphalt molecules involves aromatics. This molecule has six carbon atoms in the form of a hexagonal ring. This ring possesses a unique bond with alternating single and double bonds between carbon atoms.

9.5.4 Bonds in Asphalt Molecules

Strong covalent bonds link atoms together to form asphalt molecules. These molecules interact with one another through much weaker bonds: pi-pi bonds, hydrogen or polar bonds, and Van der Waals bonds [120]. Pi-pi bonds are unique to aromatic molecules. They provide polarity and the ability of aromatic molecules to link together in unique configurations, including a stacked arrangement. Heteroatoms among asphalt molecules develop polarity and link together by forming hydrogen bonds. Van der Waals bonding is the weakest of the secondary bonds. They form when molecules cool or stress is removed. Van der Waals bonding is responsible for the free-flowing nature of asphalt at high temperatures versus the semi-solid nature at lower temperatures [120]. As a point of reference, it is important to understand that covalent primary bonds within the molecule are from 10 to 100 times stronger than secondary bonds.

9.5.5 Polar Versus Nonpolar Molecules

Polar molecules form ‘networks’ through hydrogen and pi-pi bonds that give asphalt its elastic properties. Nonpolar materials form the body of the material in which the network is formed and contribute to the viscous properties of asphalt [120]. Degree of polarity is the most important property of polar molecules, while degree of aromaticity is the second most important. Highly polar and highly aromatic molecules form the most interactive and strongest molecular networks.

Nonpolar molecules do not interacting strongly enough to form networks, but they do substantially influence asphalt performance. The molecular weight of nonpolar molecules is related to low temperature performance [120]. A majority of high-molecular weight nonpolar molecules will lead to asphalts that stiffen and perform poorly at low service temperatures. If nonpolars are waxy, they will crystallize at low temperatures and become crack susceptible. Nonpolar and polar molecules must interact in an acceptable manner, in other word, compatible. If polar and nonpolar molecules are relatively similar in chemistry, they will be compatible; however, if they are very different, the polar network will not stay in solution, and phase separation can be a substantial problem.

9.5.6 Asphalt Model

Asphalt is a two-phase system. The polar molecules interact with each other through polar-polar or hydrogen bonding. These bonds form associations that create a network within the nonpolar solvent molecules. However, as explained by Jones [120], both phases make a significant contribution to asphalt performance.

9.5.7 Asphalt Chemistry and Adhesion

Polarity or separation of charge within the organic molecules promotes attraction of polar asphalt components to the polar surfaces of aggregates. Although neither asphalt nor aggregate has a net charge, components of both have non-uniform charge distributions, and both behave as if they have charges that attract the opposite charge of the other material. Curtis et al. [121] have shown that aggregates vary widely in terms of surface charge and are influenced by environmental changes. Adhesion between asphalt and aggregate arises between the polar of the asphalt and the polar surface of the aggregate. However, polarity alone in asphalt is not sufficient to achieve good adhesion

in pavements because asphalt is affected by the environment. Asphalt has the capability of incorporating and transporting water. Absorption of water varies with asphalt composition and changes further as asphalt is oxidized. Cheng et al. [122] have shown that a substantial quantity of water can diffuse through and be retained in a film of asphalt cement or an asphalt mastic, substantially changing the rheology of the binder. At the molecular level in asphalt, basic nitrogen compounds tend to adhere to aggregate surfaces consistently. Carboxylic acids are easily removed from aggregate in the presence of water if the acids form a monovalent salt by interaction at the aggregate surface, but calcium salts of acids are much more resistant to the action of water.

9.6 Influence of Aggregate on Stripping

Both siliceous and calcareous aggregates can be strippers, but both can also be non-strippers. Characteristics other than their bulk composition influence this behavior. Scanning electron microscopy (SEM) [121] showed that the surfaces of different aggregates have very different textures, ranging from smooth to rough. The siliceous aggregate has smooth areas, which may give rise to stripping, while roughness may help to promote bonding.

The surface charge of the aggregate determines, to some degree, the extent of attraction and adsorption of the asphalt. This surface charge can be quantified by measuring the streaming potential [123] or Zeta potential of the aggregate. Consequently, the aggregate surface can be suitably modified to effect favorable attraction between the asphalt and aggregate.

Electron transfer from the asphalt at the interface relies on the ability of aggregates to accept or donate these electrons. The electron donor and electron acceptor properties of two aggregates, ranging from quartz to calcite, show a wide range of activities. Aggregates composed of calcareous exhibit the strongest acceptor character, while silicate materials are less strong. Asphalt is composed of such a variety of chemical species that it most likely will also have a continuum of electron donor and acceptor behavior, the exact range of which is dependent on its chemistry. The matching of the electron donation and accepting abilities of the aggregates and asphalts, respectively, may

lead to improvements in asphalt concrete performance.

One factor affecting the coating of the aggregate surface by asphalt depends on the interfacial tension between the asphalt and the aggregate. Some additives can be extremely beneficial by reducing the surface tension, promoting coating, and facilitating close contact between the asphalt and the aggregate surface.

9.7 Stripping Model

Stripping is the major distresses within asphalt concrete pavements caused due to penetration of water within the interface of asphalt-aggregate. Mechanical interlocking, physical adhesion, and chemical bonding are the three main mechanisms responsible for stripping/debonding. The force of water intrusion within asphalt and aggregate can destroy the pavements.

Sensitivity to water is a key factor in the adhesion of asphalt to aggregate. Water penetrates into the pavement and changes the environment from an organic medium adsorbed onto a solid to a system that may resemble an emulsion, in which the asphalt and the water are mixed and competing for the aggregate surface.

The separation force of water intrusion between asphalt and aggregate can destroy pavements. Field and experimental data show that stripping occurs from many different modes of action. Water can attack the asphalt-aggregate bond by diffusing through the asphalt film, then reaching the surface and competing for the active sites on the aggregate. Water may also invade by seeping through cracks in the asphalt or by being present in aggregate pores and diffusing outward. Other points of failure exist under wet conditions. Adhesive failure can appear in both the asphalt and aggregate at the interface, while cohesive failure can appear only in the asphalt.

Figure 9-5 illustrates attraction based on affinity to charged aggregate surface active sites, which adsorb polar and nonpolar functionalities of asphalt. The interface chemistry interactions majorly comprise electro static force, hydrogen bonding, and vDW interaction, as shown in Figure 9-6.

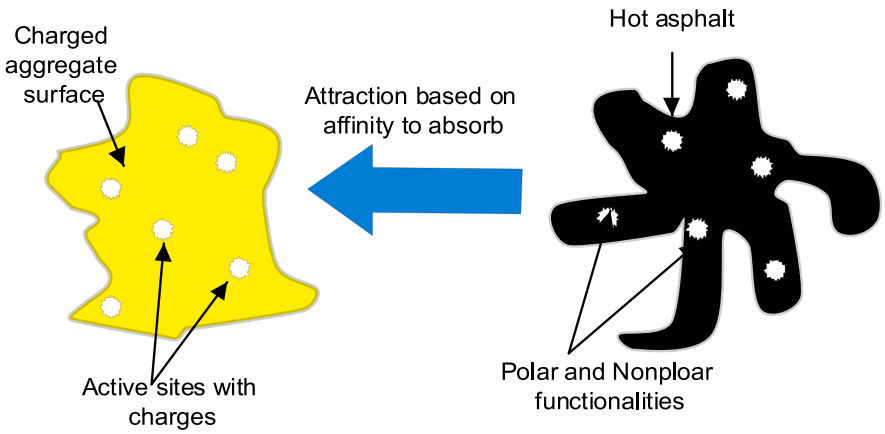

Figure 9-5 Interface attraction based on affinity of active sites on aggregate and polar functionalities on asphalt

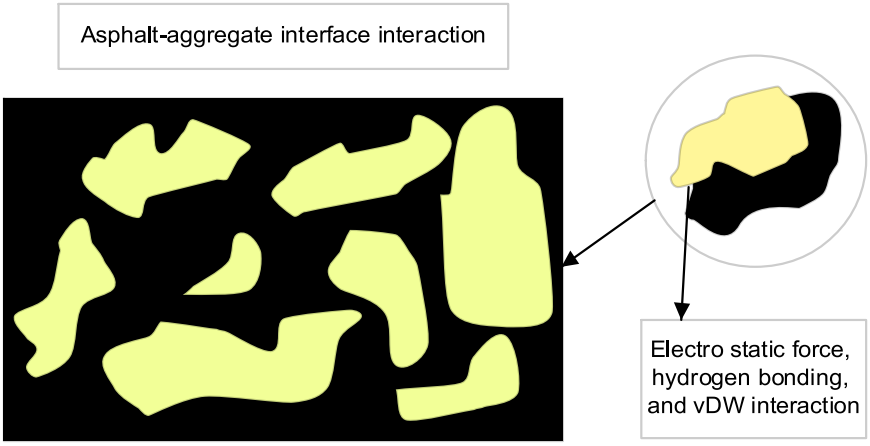

Figure 9-6 Asphalt-aggregate interface chemistry interaction

Figure 9-7 illustrates that water can destroy asphalt-aggregate bond by diffusing through the asphalt film and then reaching the surface and competing for the active sites present on the aggregate surface.

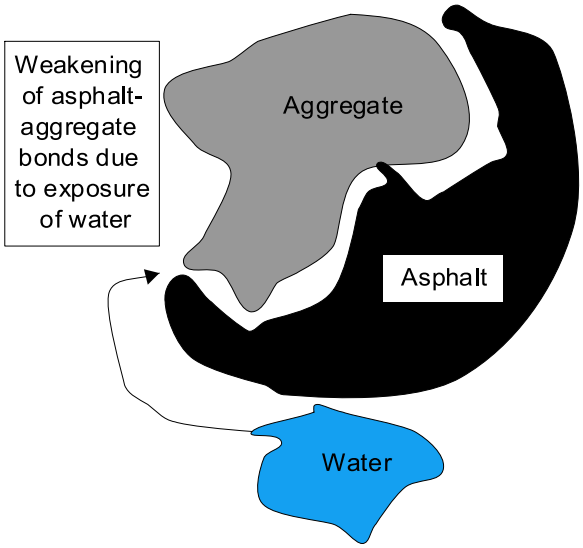

Figure 9-7 Moisture exposures within asphalt concrete mix due to environmental factors

As stated before, aggregates can be mainly divided as siliceous and calcareous types. Both siliceous and calcareous aggregates can be strippers as well as nonstrippers. There are many other characteristics of aggregates other than bulk composition which affect their behavior. It is evident that the different aggregates have different surface textures, ranking from smooth to rough. The siliceous aggregates are generally slick and smooth at the surface, while calcareous aggregates are little bit rough and hence it might promote bonding between aggregate and asphalt.

Once the asphalt has coated the aggregate surface, some of its organic chemical functionalities enter into bond formation with the aggregate constituents. The functional groups frequently combine with alkali metals present on the aggregate surface to form water-soluble salts. These asphalt-aggregate bonds being ionic in nature will weaken or solubilize over time with exposure to moisture.

There are various methods of preventing stripping within asphalt concrete mixtures. Typically this is done by adding antistripping agent within asphalt-aggregate mixture. One such agent is hydrated lime. It has been observed that some lime treated aggregates tend to form stronger, more robust, and durable bonds with asphalt. This is believed to be caused by the insensitivity of these bonds to the action of water. The bonds formed in this case are strong, insoluble bonds. Also the effect of fines within asphalt-aggregate mixture plays a critical role. The presence and amount of fines determine the

extent of stiffening of the asphalt near the aggregate surface by having a bridging effect between the bulk asphalt and aggregate surface [124]. Also the number of active sites on aggregate surfaces can be increased by the addition of agents enriched in cations of iron, magnesium, and calcium. Specific asphalt aggregate pairs can be promoted for either adsorption or increased resistivity to water.

9.8 Interface Interaction in Asphalt-Aggregate Systems

The role of asphalt binder in an asphalt mixture is to uniformly coat the aggregate and bind the aggregate together. Essentially, asphalt binder behaves as an adhesive. Therefore, the theory of adhesion is applied to study Hot Mix Asphalt (HMA) bond strength [125-126]. Consider two aggregates coated with a thin film of asphalt binder and attached to each other by the asphalt film, as shown in Figure 9-8.

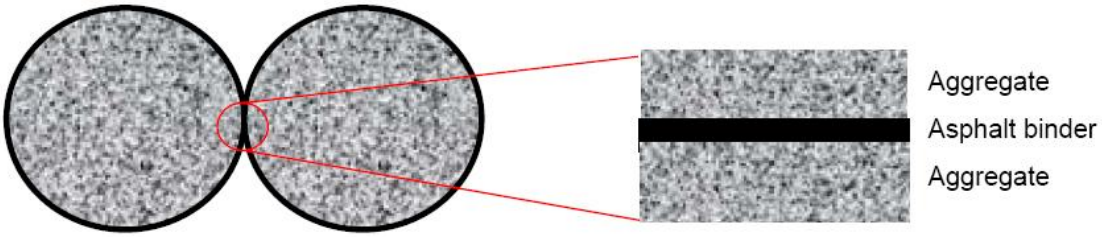

Figure 9-8 Asphalt-coated Aggregate Idealized as an Adhesive Joint

The bond between asphalt and aggregate can be idealized as an adhesive joint, where the binder is the adhesive and the aggregate is the adhered [127]. Failure can occur within the asphalt binder (loss of cohesion) or near the interface between the asphalt binder and aggregate (loss of adhesion). The device used in reference [128], performed the pull-off strength is determined by measuring the maximum tensile force that a surface area can bear before asphalt binder is separated from aggregate.

9.8.1 Two-layer Adhesive Interface Model

According to the various moisture conditions, substrate constituents, and asphalt models, totally 8 two-layer asphalt-aggregate adhesive interface models are constructed in this chapter.

These interface models are built in different ways to quantify adhesion/stripping between the bitumen and aggregate. The three different ways of using the MD simulation explored in this subsection are as follows:

- To calculate the surface free energies of asphalt mixtures and aggregate substrates, this is then used to determine the adhesion energies of asphalt-aggregate interfaces.
- To measure the total reduction in adhesion energy of the asphalt-aggregate system when water penetrates into the clean dry asphalt-aggregate interface system.
- To measure the susceptibility to water stripping of the aggregate-bitumen system composed by different mixtures and different aggregate substrates.

This Chapter presents a description of the MD simulation methodology and results for the above three applications for various combinations of interface materials. Comparisons between results based on surface energy calculation and the results from the moisturized adhesion energy indicates that the surface free energy evaluation approach can be used to calculate various adhesion parameters related to the moisture sensitivity of the asphalt mixes with adequate sensitivity.

9.8.2 Surface Free Energy Theory

Physical adhesion between bitumen and aggregate is an important factor that determines the durability of HMA mixtures in the presence of moisture. For the bitumen aggregate composite matrix to function durably a high bond energy between the aggregate and bitumen is desirable. This adhesion also ensures proper coating of the aggregate surface by the bitumen during the mixing process increasing the mechanical interlock between the aggregate surface and the binder.

The bond strength between bitumen and aggregate can be quantified using surface energy components of these materials. As the same situation for predicting stripping, a profound understanding can be made from investigating adhesive failure based on surface energy to understand the stripping process between bitumen and aggregate in the presence of moisture. Cheng et al. [129] present a detailed methodology by which to measure the surface energies of asphalt and the surface energies of aggregates using the

universal sorption device (USD). They show how to compute the adhesive bonding energy between the bitumen and the aggregate both in a dry state and in a wet state. Their results demonstrate that the adhesive bond calculated per unit area of aggregate is highly dependent on the aggregate and asphalt surface energies and that the values of the adhesive bond vary over a significant range. They further point out that the affinity of the aggregate for water is far greater than it is for asphalt, so that if water has access to the aggregate interface it is likely to replace the asphalt (a strip mode), and the rate of replacement is a function of the aggregate–asphalt bond strength.

Therefore, in the presence of moisture, there is an overall decrease in the free energy of the system favoring water to displace bitumen from the aggregate surface. The magnitude of free energy released quantifies the affinity to water to displace bitumen from the aggregate surface. A low magnitude of free energy released indicates better resistance to moisture damage. The absolute values of bond energy between aggregate and bitumen in the dry condition and the free energy released in presence of moisture can be calculated from surface energy components.

The surface free energy values for asphalt, γ_A, and aggregate, γ_S, are used to calculate the total adhesive bond energy, ΔG_{AS}, as follows [125]:

$$\Delta G_{AS} = \gamma_A + \gamma_S - \gamma_{AS} \tag{9-1}$$

where γ_{AS} is the interfacial surface energy between asphalt and aggregate. The subscripts A, S, and W represent bitumen, aggregate, and water, respectively.

An advanced method for determining thermodynamic equilibrium adhesion (i.e. bond strength) between asphalt-aggregate pairs in the presence of water has been developed [122, 129]. The interfacial surface energy of the asphalt-aggregate system in the presence of water is determined based on the individual surface energies of the components. Water, denoted ‘W’, can displace asphalt binder from the aggregate surface and the work of debonding of asphalt from aggregate by water, ΔG_{ASW}, may be determined [130] by:

$$\Delta G_{WAS} = \gamma_{AW} + \gamma_{SW} - \gamma_{AS} \tag{9-2}$$

where γ_{AW} is the surface energy between asphalt and water and γ_{SW} is the surface energy between aggregate and water.

The interfacial surface free energy between asphalt and aggregate is denoted by γ_{AS}. The above equation is used to determine the energy required to displace a unit area of the asphalt-aggregate interface by water creating a unit area of asphalt-water interface (AW) and aggregate-water interface (SW).

The magnitude of ΔG_{ASW} may be used to determine the potential for water to displace asphalt from the aggregate interface. A larger magnitude indicates a larger reduction in free energy and implies a greater potential for water to displace asphalt at the aggregate surface [131]. Both ΔG_{AS} and ΔG_{ASW} are used to evaluate moisture sensitivity of materials and predict moisture damage in asphalt mixtures [10, 14, 109, 129-131].

The thermodynamic equilibrium bond strength is only one component of the actual bond strength between asphalt and aggregate. Bond strength at the asphalt aggregate interface is a function of not only interfacial forces, but also the mechanical properties of the interfacial zone and the bulk phases of the components. Equations above do not account for the influence of the viscoelastic nature of the asphalt binder on the adhesive energy. In addition, the plastic work by the binder in the asphalt-aggregate system may be orders of magnitude higher than G_{ASW} at the interface. The stress necessary to detach asphalt film from a substrate is a function of material properties such as bulk modulus, film thickness, and elastic energy due to stored strain energy, work expended in plastic deformation and interfacial work of adhesion.

The mechanical interlock or bond strength of asphalt and aggregate mainly depends on the physical properties of the aggregate. These properties include: surface area and texture, surface coatings, particle size, and porosity or absorption [115]. A stronger bond between asphalt and aggregate is created with a rough, porous aggregate with large surface area. Physicochemical surface properties of mineral aggregate are more important for moisture induced stripping as compared to the properties of the asphalt binder.

Comparison of moisture sensitivity of mixes between different groups of HMA mixes is also possible with the inclusion of other parameters such as coating ability and

specific surface area of the aggregates.

9.9 Asphalt-aggregate Interface Moisture Damage Modeling

9.9.1 CVFF-aug Forcefield Parameters for Moisture Interaction

Since water molecules are included in the atomistic simulation, the interaction between atoms comprises bonded and nonbonded interactions. The augmented consistent valence force field (CVFF-aug) is employed to characterize the various asphalt, water and aggregate interactions. The total potential energy can be expressed by:

$$E = \sum_b H_b \left\{1-\exp\left[-a(b-b_0)\right]\right\}^2 + \sum_\theta \left(\theta-\theta_0\right)^2 + \sum_\phi H_\phi \left[1+\cos\left(n\phi-\phi_0\right)\right] + \sum_i \sum_{j>i} \left[\frac{A_{ij}}{r_{ij}^{12}} - \frac{B_{ij}}{r_{ij}^{6}} + \frac{Z_i Z_j}{r_{ij}}\right] \quad (9\text{-}3)$$

Here, each term describes the bonded potential (H_b =bond energy, a =force constant, b = bond length, b_0 = bond length at minimum energy), the angle of bending (H_θ = force constant, θ = bending angle, θ_0 = bending angle at minimum energy), the torsion angles (H_ϕ = force constant, n = order of rotation axis, ϕ = torsion angle, ϕ_0 = torsion angle at minimum energy). The van der Waals and the coulomb charge forcefield parameters are shown in Table 9-3 potentials, respectively. The bonded interaction force-field parameters used here are summarized in Table 9-4.

Note that the SiO2 crystal structure is composed by atom of type 2 (Siz) & type 1 (Oz). The average asphalt molecules are comprised by atom types 5 (C3), 7 (Cp), 8 (C2), 9 (C=), 10 (C), 11 (S) and 6 (H).

Table 9-3 vDW and electrostatic parameters of CVFF-aug Forcefield

Atom name	Atom type	Force field charge (e)	Atomic mass (g/mol)	Hybridization	R(min) Sigma (Ang)	Ebsinong (kcal/mol)	Radius for bond calculation (Ang)
H	4 (h*)	0.41000	1.01	Sp3	0.00000	0.00000	0.46

O	3 (o*)	-0.82000	16.00	Sp3	3.553176	0.155416	0.75
O	1 (oz)	-1.2000	16.00	Sp3	12.654358	0.00000	0.75
Si	2 (Siz)	2.4000	28.09	Sp3	8.185887	0.00000	1.18
C	5 (c3)	-0.30000	12.01	Sp3	4.35000	0.039000	0.85
H	6 (h)	0.10000	1.01	Sp3	2.75000	0.038000	0.46
C	7 (cp)	-0.1000	12.01	Sp2	4.06000	0.148000	0.85
C	8 (c2)	-0.2000	12.01	Sp3	4.35000	0.039000	0.85
C	9 (c=)	-0.1000	12.01	Sp2	4.06000	0.148000	0.85
C	10 (c1)	-0.1000	12.01	Sp3	4.35000	0.039000	0.85
S	11 (s)	-0.0564	32.07	Sp3	3.780177	0.042976	1.14

Table 9-4 Bonded potential parameters used in the simulation

Tension/compression parameters			
	b_0 **(Å)**	H_b **(kcal/mol)**	**A (1/Å)**
C-C	1.526	88.000	1.975
C-H	1.105	108.600	1.771
Angle parameters			
	θ_0 **(deg)**	H_0 **(**$kcal \cdot mol^{-1}\deg^{-2}$**)**	
C-C-C	110.5	46.6	
C-C-H	110.0	44.4	
H-C-H	106.4	39.5	
Torsion			
	H_ϕ **(kcal/mol)**	**n**	ϕ_0 **(deg)**
C-C-C-C	1.4225	3	0.0
C-C-C-H	1.4225	3	0.0
H-C-C-H	1.4225	3	0.0

9.9.2 Interfacial Moisture Adhesion Models

Physical and chemical properties at the micro scale are surface free energy and specific surface area of the aggregates. These properties directly influence the nature and durability of the bond between the aggregates and the bitumen in wet and dry conditions. This in turn affects the durability of the asphalt mix in terms of its resistance to moisture induced damage and fatigue cracking.

With water enters the pavement from the granular base, pavement will be deteriorated. In some cases, water can also infiltrate through the surface cracks and ground water seepage from the sides due to hydraulic gradient. Water enters the interface of asphalt and aggregate in various ways. Diffusion across the bitumen film, seepage

through the voids, wear and tear of the binder film, existing moisture in the pores of aggregates, diffusion from the pores to the interface, and direct contact with the aggregate due to its partial coating are some of the common ways by which moisture can migrate into the interface [132].

It has become necessary to seek a more fundamental understanding of the moisture damage process by carefully considering the micro-mechanisms that influence the adhesive interface between aggregate and asphalt that results in the cohesive strength and durability of the mastic. To this end, a fundamental approach to calculating adhesive bond strength in asphalt mixtures in the presence of water based on the surface free energy calculation is carried out in this subsection.

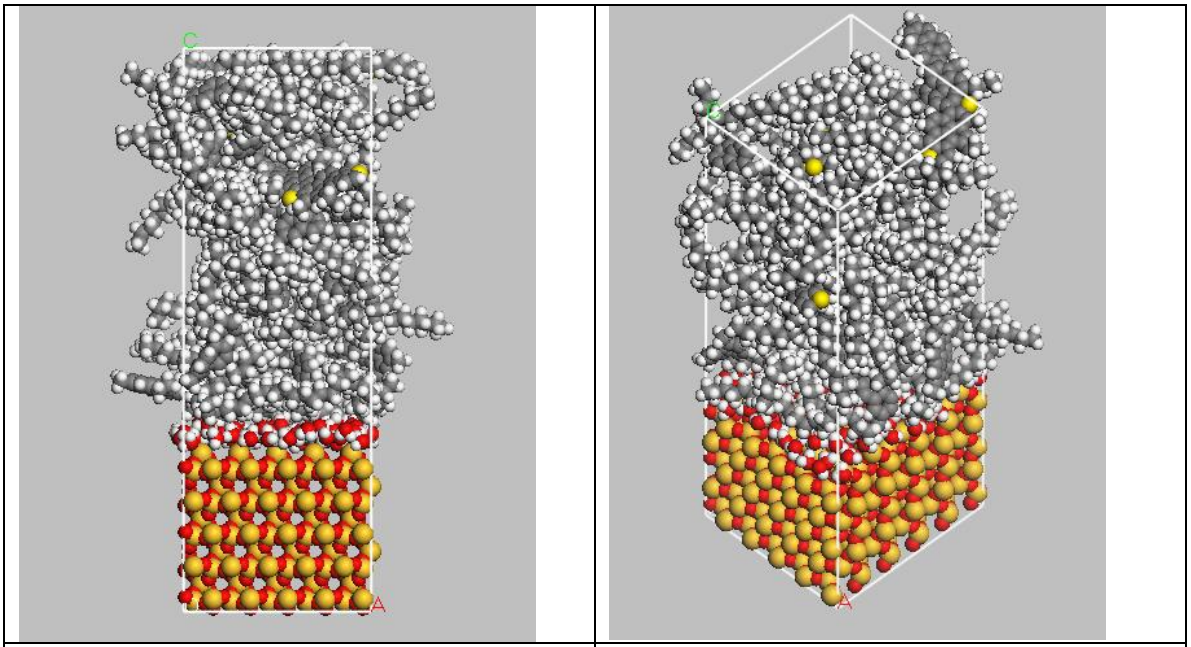

front view of asphalt-quartz interface water100 model	top-side view of asphalt-quartz interface water100 model

Figure 9-9 Hydrated asphalt-quartz interface model

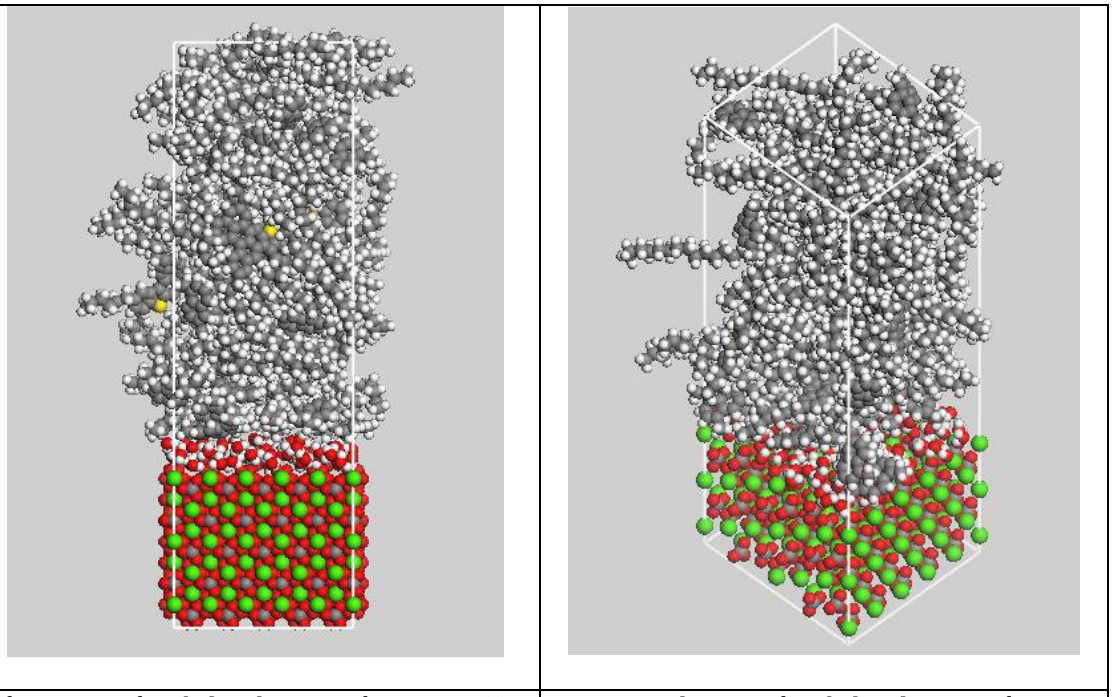

front view of asphalt-calcite interface water100 model	Top-side view of asphalt-calcite interface water100 model

Figure 9-10 Hydrated asphalt-calcite interface model

For the purpose of better explaining the adhesion phenomenon, totally 8 interfacial atomistic models are built according to various adhesion properties with respect to aggregate and asphalt type.

The asphalt mix1 adhered to quartz substrate is a basic dry adhesion model, named ‘mix1_quartz_dry adhesion’ model. Accordingly, an asphalt mix1 adhered to quartz substrate with a water layer between them is the dry model’s corresponding moisturized model. It is named the ‘mix1_quartz_moisture adhesion’ model. Based on the same rule, the asphalt mix1 adhered to calcite substrate, named the ‘mix1_calcite_dry adhesion’ model is also built. Accordingly, its moisture model is named ‘mix1_calcite_moisture adhesion’. This is for the purpose of studying the affinity properties of different aggregate substrates. Additionally, in order to investigate adhesion properties of different asphalt materials, asphalt mixture2 is also used to build the adhesion models in a similar manner to the asphalt mixture1 models.

Figure 9-9 illustrates the ‘mix1_quartz_moisture adhesion’ model proposed for calculating interface adhesion energy. This interface structure is built by adopting an

interface tensile loading model built in Chapter 7 and then injecting a 100 water molecules layer at the interface region. The final size of 'mix1_quartz_moisture_adhesion' model is in an orthogonal box with lattice parameters are shown as follows: a=24.54998, b=27.010, c=73.0688. The final size of 'mix1_calcite_moisture_adhesion' model, as shown in Figure 9-10, is also in an orthogonal box with lattice parameters are: a=24.57, b=27.03, c=80.31. Here we use larger simulation cell, smaller density, and higher temperature when building the asphalt mixture. Then use high pressure or move atoms operation in simulation and squeeze the Z direction of the simulation cell size to get the real asphalt mixture density and cell size.

9.9.3 Results and Discussion

In this simulation, an isothermal and isobaric (NPT) ensemble is chosen for equilibration. Constraining the volume (NVT) would not account for any change in density during moisturize and could lead to inaccurate pressures on free surfaces of the simulation cell. Thus, the non-equilibrium NPT ensemble combined with the Nose-Hoover thermostat is used. After the system pressure reaches a stable value, the constant-NVT ensemble is employed to perform the moisturized interface adhesion simulation.

According to the surface free energy theory, γ_A, γ_S, γ_{AS}, ΔG_{AS} and ΔG_{ASW} are all calculated for each of the 8 model. Table 9-5 depicts the 'mix1_qaurtz' and 'mix1_calcite' models interfacial with dry/moisture adhesion energy at 298 K. For 'mix1_qaurtz' model, the dry adhesion energy, ΔG_{AS}, is 2029.14 kcal/mol, whereas the moisturized adhesion energy, ΔG_{AS}, is 1237.70 kcal/mol. So the 'mix1_quartz' interface adhesion energy decreases sharply with the presence of water layer. As to the 'mix1_calcite' model, the dry adhesion energy, ΔG_{AS}, is 2674.94 kcal/mol, while the moisturized adhesion energy, ΔG_{AS}, is 2557.99 kcal/mol. It's clear, the 'mix1_calcite' interface energy drops a little with the presence of water layer. From the results obtained, the aggregate adsorption to asphalt mix1 property can be drawn. Calcite is more prone to adsorb asphalt mix1 even with the presents of water may only affect the adsorption property a little. This is in agreement with pavement industry observations that lime (calcite is the major component) has bigger adhesive properties than granite (quartz is the

major component).

Table 9-5 Mix1_qaurtz and Mix1_calcite models interfacial dry/moisture adhesion energy at 298 K

Model ID	**mix1_quartz_dry adhesion**	**mix1_calcite_dry adhesion**	**Units**
γ_A	7996.89	8845.73	kcal/mol
γ_S	-78162.97	-105581.65	kcal/mol
γ_{AS}	-72195.23	-99410.85	kcal/mol
ΔG_{AS}	2029.14	2674.94	kcal/mol
Model ID	**mix1_quartz_moisture adhesion**	**Mix1_calcite_moisture adhesion**	
γ_A	8800.69	8810.46	kcal/mol
γ_S	-79542.10	-105581.63	kcal/mol
γ_{AS}	-71979.11	-99329.16	kcal/mol
ΔG_{AS}	1237.70	2557.99	kcal/mol
γ_{AW}	3447.603111	5333.775246	kcal/mol
γ_{SW}	-92000.80034	-123346.7504	kcal/mol
ΔG_{WAS}	-16574.08	-18683.82	kcal/mol

Table 9-6 illustrates ‘mix2_qaurtz’ and ‘mix2_calcite’ models interfacial with dry/moisture adhesion energy at 298 K. For ‘mix2_qaurtz’ model, the dry adhesion energy, ΔG_{AS}, is 2022.39 kcal/mol, whereas the moisturized adhesion energy, ΔG_{AS}, drops to 1280.53 kcal/mol. So the ‘mix2_quartz’ interface adhesion energy decreases sharply with the presence of water. As to the ‘mix2_calcite’ model, the dry adhesion energy, ΔG_{AS}, is 4462.40 kcal/mol, while the moisturized adhesion energy, ΔG_{AS}, drops to 2838.52 kcal/mol. The ‘mix2_calcite’ interface energy decreases also sharply with the presence of water layer. It is clear that the aggregate adsorption properties to asphalt mix2 property can be drawn. Calcite is more prone to adsorb asphalt mix2 than quartz even with the presents of water, because the adhesion energy of moisturized ‘calcite_mix2’ interface is higher than the dry ‘quartz_mix2’ interface.

Furthermore, the adhesion strength between quartz and two types of asphalt mixtures are roughly similar with each other, both for dry and moisturized conditions.

However, the calcite is more sensitive to asphalt mixture type. For dry adhesion, the 'calcite_mix2' model is at 4462.40 kcal/mol in adhesion energy, whereas the 'calcite_mix1' model is of only 2674.94 kcal/mol. For hydrated condition, 'mix2_calcite' is 2838.52 kcal/mol, which is still higher than that of 2557.99 in 'mix1_calcite' model. Hence, the asphalt affinity can be drawn that asphalt mix2 has more adhesive property to calcite. This is in accordance with our observations in Chapter 5 that asphalt mixture2 model has bigger adhesive/cohesive energy density than asphalt mixture1 model.

Table 9-6 Mix2_qaurtz and Mix2_calcite models interfacial dry/moisture adhesion energy at 298 K

Model ID	**mix2_quartz_dry adhesion**	**mix2_calcite_dry adhesion**	
γ_A	5637.01	5844.96	kcal/mol
γ_S	-67345.19	-105671.55	kcal/mol
γ_{AS}	-63730.57	-104288.98	kcal/mol
ΔG_{AS}	2022.39	4462.40	kcal/mol
Model ID	**mix2_quartz_moisture adhesion**	**mix2_calcite_moisture adhesion**	
γ_A	5542.42	5686.75	kcal/mol
γ_S	-67313.96	-105581.08	kcal/mol
γ_{AS}	-63052.07	-102732.85	kcal/mol
ΔG_{AS}	1280.53	2838.52	kcal/mol
γ_{AW}	-50.166794	2061.831598	kcal/mol
γ_{SW}	-79494.87461	-123444.9942	kcal/mol
ΔG_{WAS}	-16492.97	-18650.31	kcal/mol

Generally, the interface adhesion or anti-moisture damage properties can be reached from the results obtained. The affinity property between different types of asphalts and aggregates can be drawn as follows:

Quartz < calcite

Mixture1 < mixture2

Considering the water susceptibility, the magnitude of ΔG_{ASW} is compared among each moisture model. Table 9-5 demonstrates that model 'mix1_quartz_moisture

adhesion' has a ΔG_{ASW} value of -16574.08 kcal/mol, whereas the 'mix1_calcite_moisture adhesion' model is -18683.82 kcal/mol. It is obvious that the magnitude of ΔG_{ASW} for calcite is larger than quartz model. The same trend also exists in mix2 models. Table 9-6 depicts that model 'mix2_quartz_moisture adhesion' has a ΔG_{ASW} value of -16492.97 kcal/mol, while the 'mix2_calcite_moisture adhesion' model is -18650.31 kcal/mol. Therefore, calcite substrate has larger potential for water to detach asphalt from the aggregate interface. Clearly, it shows that the mix2 asphalt model is less susceptible to water displacement, since a larger magnitude of ΔG_{ASW} value indicates a larger reduction in free energy and implies a greater potential for water to detach asphalt at the aggregate surface. Therefore, the moisture sensitivity property between different types of asphalts and aggregates can be drawn as follows:

Quartz < calcite

Mixture2 < mixture1

It is also evident that the asphalt components that have a better affinity for the aggregates also have less sensitivity to water. Adsorption of asphalt from water and subsequent desorption of the asphalt by water are dependent on both the asphalt composition and on the aggregate chemistry and morphology.

The aggregate composition and surface chemistry appear to have a much more substantial effect on the amount of asphalt adsorbed and desorbed than does the asphalt compositions. The amount of asphalt adsorbed for the calcite doubled the surface energy for the quartz. Water sensitivity also appeared to be strongly dependent on the chemistry of the aggregate. For some aggregates that show substantial water sensitivity, the asphalt chemistry seemed to have a much larger influence on the amount of asphalt desorbed and retained than on those aggregates that did not show substantial sensitivity to water.

Hence, much more moisture sensitivity is exhibited by siliceous aggregate but not by calcareous aggregate. Different siliceous aggregates exhibited a variety of moisture sensitivity levels. Lime aggregate has better adhesion and better anti-moisture damage property than granite. Based on the data, we can say that the limestone ranks it ahead of the granite in terms of bonding energy per unit area.

In general, by using the proposed adhesion mechanism and surface energy between asphalt binder and aggregate, the stripping mechanism can observed. Surface energy theory suggested that the different amount of interfacial tension and work of separation between pure asphalt, water, and aggregate resulted in an adhesion failure between the asphalt and aggregate. Why stripping was observed more in quartz than limestone is answered by the differential surface free energies between the asphalt and aggregate. Water is a polar molecule and asphalt is either non-polar or weakly polar. In addition, molecules of silicates have high dipole moments (higher than that of water), and carbonate mineral rocks are also polar to limited degree. Thus, siliceous aggregates such as quartz can absorb more water than asphalt because of the attraction between the polar mineral molecules and the polar water molecules. Furthermore, on a relatively non-polar surface, such as limestone, the cohesive forces in the water are greater than the adhesive forces between water and limestone. Therefore, a weak polar substance such as asphalt does not preferentially strip from limestone and is held to the surface primarily by van der Waal's forces.

9.10 Moisture Adhesion Damage Illustration in Simplified Atomistic Model

9.10.1 Nanoscale Interface Adhesion/Debonding Model

For the purpose of illustrating the fundamental moisture damage mechanism, the simplified atomistic adhesion models are built. We use calculated adhesive bond energy to predict moisture damage through stripping. The simulation geometry of the atomistic studies discussed in this section is schematically shown in Figure 9-12. The atomistic interface dry adhesion model is shown in Figure 9-11. In this model, an average asphalt molecule is located on top of the quartz substrate. Since an orthogonal geometry is needed for loading purpose, the quartz supercell's surface needs to be cut into an orthogonal shape with P1 space group. The lattice parameters are shown as follows: a=39.304, b=32.431, c=93.417, α=90°, β=90°, and γ = 90 °. The adhesion model is

composed by 2447 atoms, 3093 bonds, 6030 angles, and 8835 dihedrals.

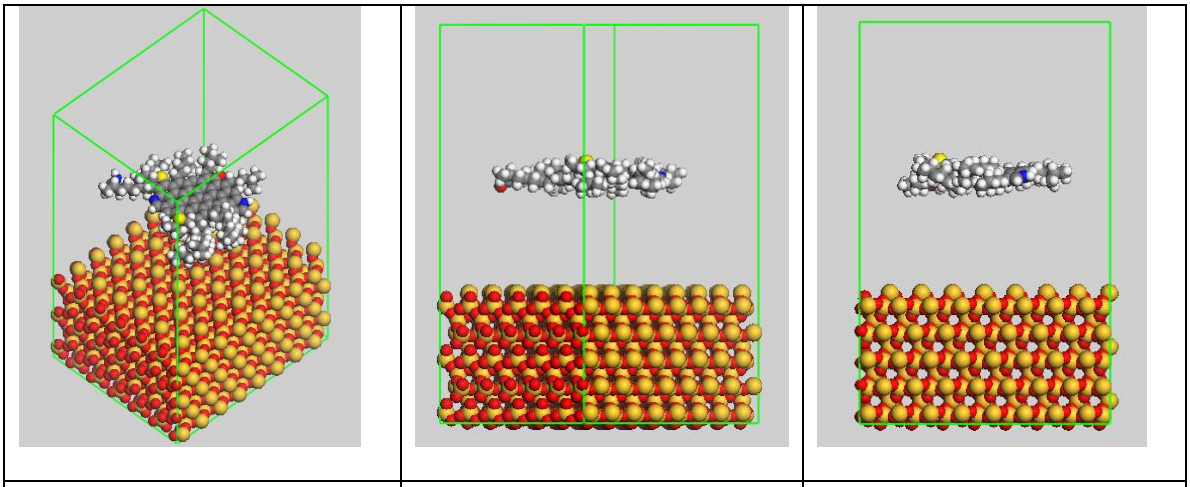

Front view	Side view	Top-side view

Figure 9-11 Simple atomistic model of the average asphalt-quartz interface dry adhesion

In MD simulations, we model the asphalt part using CVFF-aug forcefield interaction, and we treat the interface between the two parts using the Buckingham potential to model the vdW adhesion interactions. The quartz substrate is kept to be fixed. The expressions for the interatomic potentials, as well as the overall simulation method, including the expressions for adhesion energy and debonding energy are identical to the procedure described above. Studies of variations of adhesion temperature dependency properties are also achieved through various thermostats to maintain the system temperature in simulations.

To the purpose of measuring the interface adhesion energy and force, MD simulations are carried out. Schematically, a constant force is applied to each atom in the asphalt molecule to drag it towards the direction opposite to the quartz substrate. Then calculate the interaction force and potential energy between the asphalt and the substrate. The interaction force will first grow up then drop down and decay to 0. Typically, the largest adhesion force will be the peak value of the interaction force curve, as is the similar manner for the interatomic interaction potential.

The magnitude of the force is specified along Z direction, whereas in X and Y directions will be set un-restrained. If an atom is closer than a distance delta to the point,

then the force is not applied. It means do not include that X and Y dimension in the distance calculation or force application. This method allows one to achieve a smoothly interface adhesion interaction simulation through the molecular dynamics.

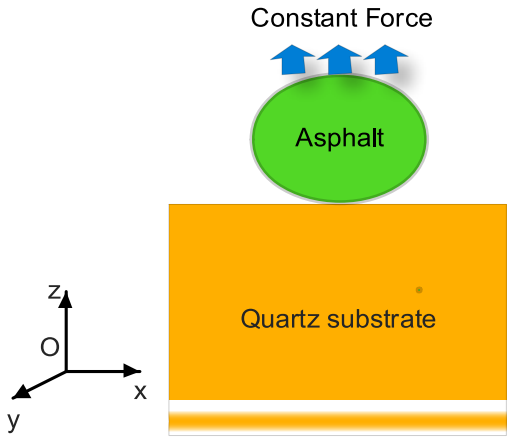

Figure 9-12 The schematic of the model used for studies of asphalt-aggregate interface adhesion. The model represents an average asphalt molecule attached to a quartz substrate.

Molecular dynamics simulations of the average asphalt molecule and water molecule adsorbed on (001) surfaces of quartz provide new insight into the relationships between the substrate structure and composition and the molecular-scale structure and properties of asphalt-aggregate interface with the presence of interfacial water.

For the three phases studied here, the differences in the structural charge on the octahedral sheet, charge distributions, and the orientations of asphalt groups all affect the surface water structure. The density profiles of water molecules perpendicular to the surface are very similar, due to the prevalent importance of H-bond between the surface and the water and to their similar layered crystal structures.

However, the predominant orientations of the surface asphalt molecule and the detailed two-dimensional near-surface structure are quite different. The atomic density profiles and other structural characteristics of asphalt at the two surfaces are very different, because the asphalt is hydrophobic in nature whereas the quartz (001) surface is hydrophilic.

9.10.2 Simple Atomistic Model of the Moisture Damage Mechanism

Interaction between water and asphalt-aggregate interfaces can substantially affect the properties of asphalt-aggregate adhesion, including the structure and dynamics of the near surface water and functionality of the substrate surface [133-134]. These interactions are, thus, of significant interest in pavement materials industry. In geochemistry and environmental science, water-asphalt-aggregate interactions are important factors controlling such processes.

Mineral-water-asphalt interactions are largely controlled by the atomistic structure, composition, and surface charge distribution, which vary widely among minerals. The substrate surface structure provides the basic framework for interface water adsorption. Local variation of near-surface structural charge due to structural substitutions or defects provides negatively or positively charged surface sites which can orient the water dipoles and which can significantly influence formation of donating or accepting hydrogen bonds with the surface.

Rock minerals in pavement environments often have particle sizes as small as few nanometers and expose several surfaces simultaneously. Surface defects, absorbents including inorganic and organic ions and molecules, and solution chemistry can complicate the interfacial interactions.

The effects of mineral surface structure and composition on the structure and dynamics of the near-surface water fluids are, however, difficult to study and incompletely understood. In addition to the natural complexity of near-surface fluids, the water phase is statically and dynamically disordered, and there are fewer applicable experimental techniques to probe its properties in situ than are available for probing mineral surfaces [135]. It is, thus, instructive to first attempt to understand somewhat idealized systems, starting with the interaction of water with perfect mineral surfaces and simple asphalt molecule structure without considering, for instance, internal defects.

MD simulations are efficient in obtaining detailed fundamental information about the behavior of such well-defined systems on the molecular time- and length- scales. Such insight into the structure of interfacial water is essential to improved understanding of asphalt surface experimental data. Computational studies of different oxide and hydroxide surfaces show quite different near-surface water structures and suggest that different surface functional groups can play different roles in developing the interfacial

hydrogen bonding networks that are keys to understanding near-surface water structure.

Detailed and systematic investigations of these issues are essential to further advance our understanding of the ways in which the competing molecular-scale phenomenon control the structural and dynamic properties of asphalt-aggregate interfacial water.

In this subsection, we present a molecular dynamics (MD) computer simulation study of the interaction of water with the ideal asphalt-aggregate interface. The study is designed to clarify the fundamental molecular-scale relationships between the substrate mineral structure and composition and the asphalt molecular structure, thermodynamic properties, mechanical properties of water between the asphalt-mineral surfaces.

The quartz mineral structure is chosen based on the following criteria. (1) It is representative of important types of mineral surfaces. (2) It has relatively simple and well-known chemical compositions and crystal structures, making the construction of the representative computational MD models tractable.

The results of our simulations show that substrate composition, structure and charge distribution directly affect the structure, adhesion/cohesion properties, as well as distribution and diffusion rates of the interfacial water.

9.10.3 Molecular Models of Asphalt-mineral-water Interfaces

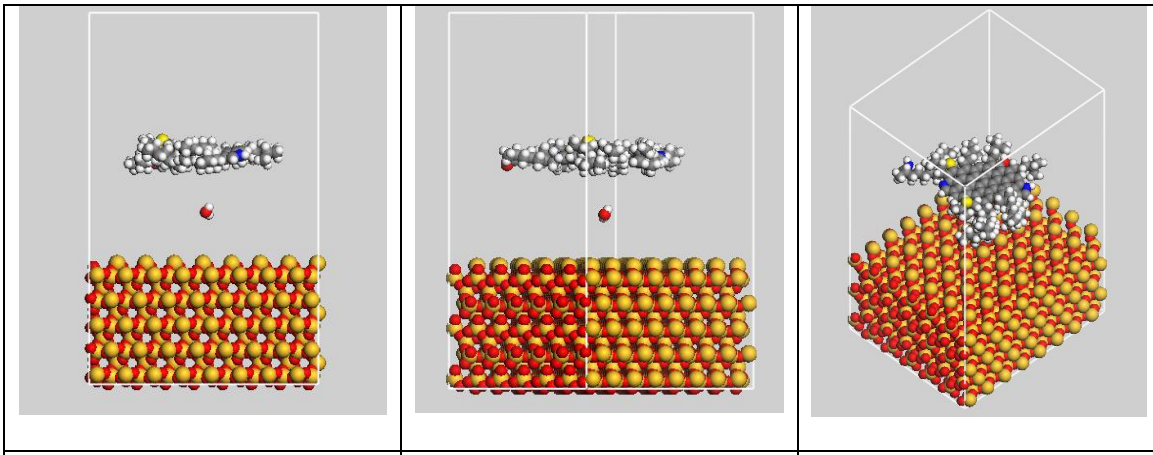

Front view	Side view	Top-side view

Figure 9-13 Simple atomistic model of the average asphalt-quartz interface moisture damage

For the purpose of obtaining the moisture damage effects at the interface, one water molecule is injected into the interface adhesion model proposed in Figure 9-11. The hydrated interface adhesive model is shown in Figure 9-13.

Figure 9-13 shows that the final rectangular simulation supercell has x, y, and z dimensions of value at a=39.304 Å, b=32.431 Å, c=103.4171 Å, respectively. The simplified adhesion model is composed by 2450 atoms, 3095 bonds, 6031 angles, and 8835 dihedrals. A water molecule was inserted between the asphalt-quartz interfaces.

The CVFF-aug forcefield is used for all asphalt-mineral-water interfacial simulations described here. The simulations were performed at ambient conditions (T = 298 K; P = 0.1 MPa) and used the LAMMPS software, and previously described MD simulation procedures.

Prior to modeling water adsorption on the mineral surfaces, MD simulations at constant-NPT ensemble were carried out to test the performance of our methods and models with respect to the bulk crystal structures of the minerals. These simulations reproduce the experimentally determined bulk crystal structures very well, yielding unit cell dimensions of the experimental values in all dimensions.

Periodic boundary conditions were applied to the resulting mineral-asphalt-water interfaces models in all three dimensions, and the simulation supercells contained volumes representing both the quartz phase and water. For the quartz part, the a, b, and c crystallographic dimensions computed in the initial NPT-ensemble MD simulations for each bulk phase are obtained to get the correct size.

9.10.4 Moisture Damage Simulations

9.10.4.1 Interface Structure Squilibration

In this simulation, all interatomic interactions in the interface structure should be initially identified and evaluated for each possible interatomic coordinates.

The MD simulations were performed using periodic boundary conditions, Ewald summation to calculate long-range electrostatic contributions to the potential energy, and a ‘cutoff’ method to calculate short-range van der Waals interactions. Two stages of energy minimization were applied to the initial model. First, we fixed the positions of

atoms in the orthogonal quartz section and allowed only the average asphalt molecule to relax, since its initial position and orientation are most likely to be significantly different from the optimum configurations. Energy minimization was then applied to the entire system with no constraints.

The energy of the dry interface model system was allowed to converge to its minimum within a 0.001 kcal/mole convergence criterion, and this optimized structure was then used as the starting configuration for NPT-ensemble MD simulation at 298 K and 0.1 MPa with a time step of 1.0 fs. The system was allowed to relax and equilibrate for 100 ps of MD simulation. To ensure thermodynamic equilibrium, the convergence of total energy and its components, as well as temperature, density, and atomic radial distribution functions were carefully monitored during this equilibration period.

This moisturized interfacial model is followed by inserting a water molecule at the interface area. Further structural relaxation of interface model containing water molecule with these predetermined supercell parameters was achieved in four stages. First, the positions of all atoms in the substrate were fixed, and only the positions and orientations of water and average asphalt molecules were allowed to relax in an energy minimization procedure. This was followed by a relatively short (10-50 ps) NVT-ensemble MD run. Then the atoms in the substrate were released, and in the last two stages the energy minimization and MD steps were repeated with all atoms of the system free to relax. These optimized structures were then used as the starting configurations for the final MD simulations, which were all performed in the NVT-ensemble. Since all atoms in each system were completely free to move during these simulations, the constant-volume modeling approach with a fixed cell shape does not introduce significant limitations on the resulting interfacial structure, dynamics, and energetics of water. A time step of 1.0 fs was used for all MD simulations, and each system was allowed to equilibrate for 500 ps of MD simulation. The equilibrium dynamic trajectory for each model was finally recorded for statistical analysis at 50 fs intervals during the next 500 ps of MD simulation.

9.10.4.2 Pullout loading for Modeling of Adhesive/Moisture Damage

Asphalt-aggregate-water molecule system will be performed in a simulation

procedure that accounts for interaction with interfacial pullout and temperature dependence. The simulation output will be used to relate molecule structure to the nano-mechanical properties. A relationship of molecule structure versus adhesion force and deformation is obtained.

Pullout/adhesion force and interaction potential energy will be calculated from molecular model by first isolating a single asphalt molecule, fixing all atoms in the quartz section, and applying a constant force to one of its C atoms in space up to Z direction, allowing the water molecule to freely move between the interface layer, and performing a molecular dynamics simulation while slowly increasing the distance between the asphalt molecule and the fixed quartz atoms.

A time step of 1.0 fs was used for all MD simulations. All final MD simulations were performed at constant temperature and volume in the statistical NVT ensemble. To achieve the desired pressure at a given temperature for this interface model, the densities and cell dimensions were determined in a series of preliminary calculations consisting 50 ps of NVT MD and 100 ps NPT MD at a certain temperature for the model system. The last 50 ps of the trajectories resulting from the NPT MD simulations were used to determine the densities and supercell dimensions. As shown in Figure 9-14 and Figure 9-15, the average asphalt molecule is adsorbed onto the quartz surface at equilibrium. We suppose this is the tight binding adhesion model.

This is schematically shown in Figure 9-12. In order to make a comparison between the two interface systems, pull-out simulations are both performed on the dry adhesive model and the moisture interface system.

9.10.5 Results and Discussion

9.10.5.1 Dry Interface Adhesion Model

The large quart with average asphalt molecule adhesion model subject to pull-out is performed. We try to make the pull-out displacement as low as possible, so the dynamic effects can be removed from the debonding simulation process. With various system temperatures, interface bonding temperature dependency properties are indicated respect to different adhesion forces and potential energy.

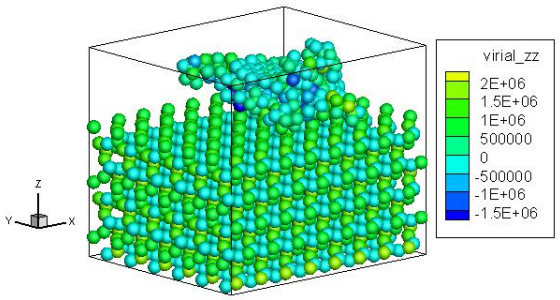

Figure 9-14 Virial_zz value contour of the adhesion system at the equilibrated state

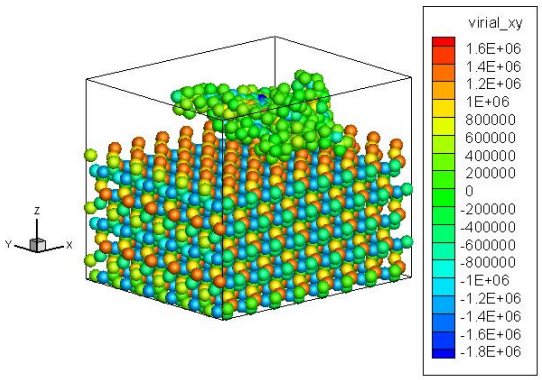

Figure 9-15 Virial_xy value contour of the adhesion system at the equilibrated state

Virial value contours of the adhesion system after equilibrium is shown in Figure 9-14 and Figure 9-15. Figure 9-14 indicates that the per-atom virial interaction energy in Z direction is roughly uniform with each other in a magnitude of 2.0×10^{6} kcal/mol. Figure 9-15 illustrates that the distribution of virial energy in tangential direction along XY plane varied. The red atoms, majorly Silicon, possess larger interaction potential role at a magnitude of 1.6×10^{6} kcal/mol. This demonstrates that the substrate quartz adsorb the asphalt molecule strongly not only in the normal direction but also in the tangential direction. This result is in agreement with the results shown in Chapter 7 and Chapter 8 that the tension and shear strength are both appear at the interface region.

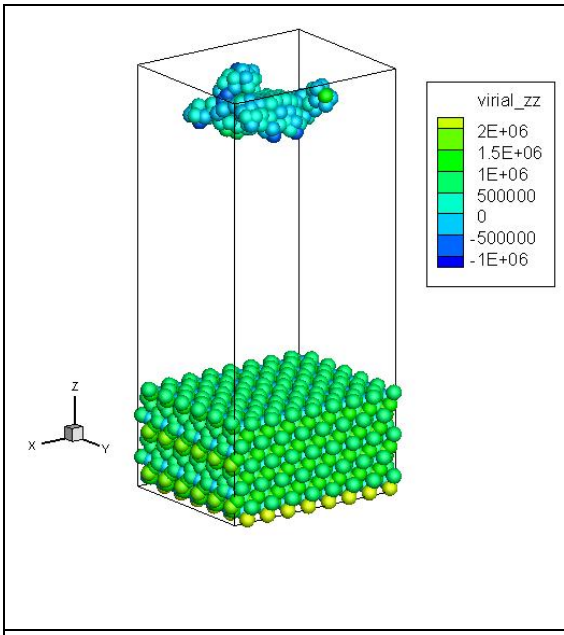

Figure 9-16 Virial_zz value contour of the adhesion system after pull-off (interface debonding simulation)

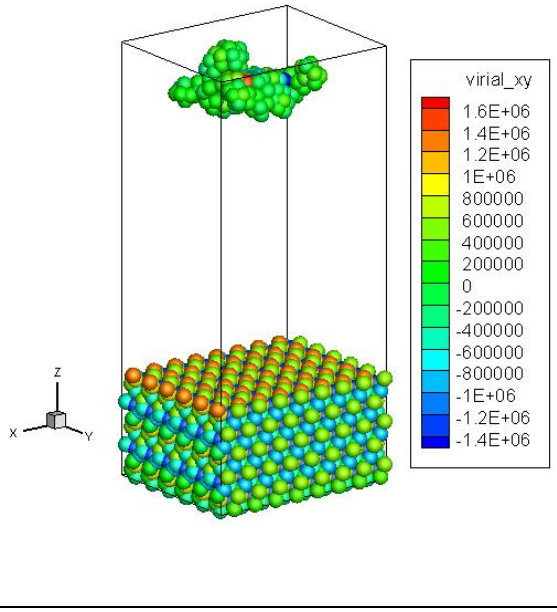

Figure 9-17 Virial_xy value contour of the adhesion system after pull-off (interface debonding simulation)

After the interface system equilibrium reached, a constant force is applied to drag the asphalt molecule upward in Z direction. Figure 9-16 and Figure 9-17 show the virial value contour of the interface structure under debonding process. They indicate that the shape of average asphalt molecule vary differently during the drag process, because the asphalt molecule keeps changing its shape to make the total potential energy minimum. Figure 9-17 shows the Silicon atoms have larger virial_xy potential energy than the Oxygen atoms. It could be due to the Silicon has larger atomic radius and adsorption force, which lead to bigger interaction forces with asphalt molecule.

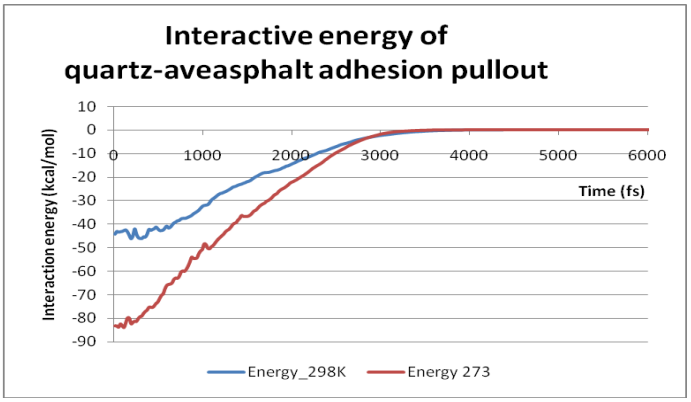

Figure 9-18 Instant interactive energy curve of quartz-aveasphalt adhesion pullout

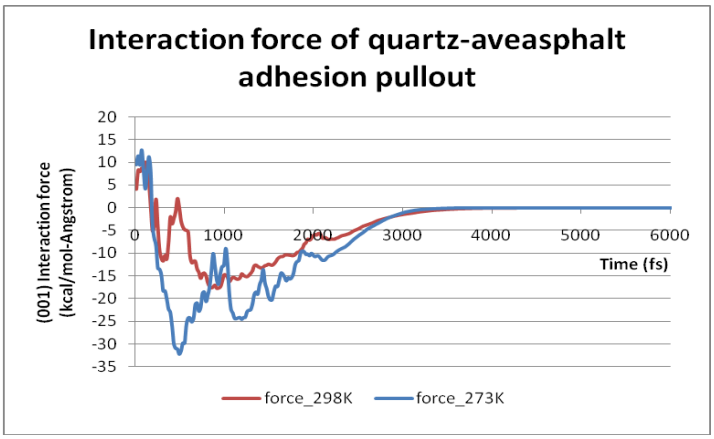

Figure 9-19 Instant interactive force curve of quartz-aveasphalt adhesion pullout

Figure 9-18 shows the instant interaction energy curve of the quartz-asphalt adhesion interface under pull-out. The results indicate that the energy is dependent on system temperature. The interaction energy starts from -80 kcal/mol at 273 K, whereas it is of 44 kcal/mol at 298K. Initially, the energy is in a steady state. It is followed by a fluctuating dropping down. Both temperature curves drop down quickly and they merged together at the 3500 steps. This is in agreement with the interatomic interaction characterization that the interactomic potential drops down quickly with the increase of the distance.

Figure 9-19 shows the maximum adhesion strength as a function of the system temperature. The same observation can be drawn from the interaction force curve. With the temperature increase, the adhesion force increases. The adhesion strength is obtained

from pullout simulation that it is -32 $kcal/mol \cdot Angstrom^{-1}$ at 273 K, whereas it is -18 $kcal/mol \cdot Angstrom^{-1}$ at 298 K.

These observations allow drawing conclusions about the adhesion: The results indicate that interface adhesion can be achieved at not only normal direction but also at tangential direction. With respect to variations in temperature, keeping a strong adhesion force can only be achieved at lower temperature. Generally, all cases illustrated that the atomistic interface interaction is the control role of adhesion, and the adhesion strength has a strong dependency on the system temperature and the surface chemistry of the adhesion element.

9.10.5.2 Hydrated Interface Adhesion

Hydrated interface adhesive interaction mechanism is depicted in Figure 9-20 and Figure 9-21. Figure 9-20 and Figure 9-21 illustrate the virial_xx and virial_zz contour of the average asphalt, water and quartz system during MD equilibration. The largest interactive energy occurs at the asphalt molecule whereas the water molecule and quartz have relatively smaller potential energy.

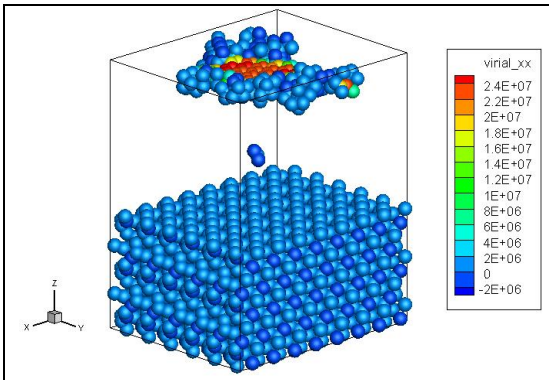

Figure 9-20 Timestep=6000, Virial_xx stress of large_quartz_water_1 system during equilibration

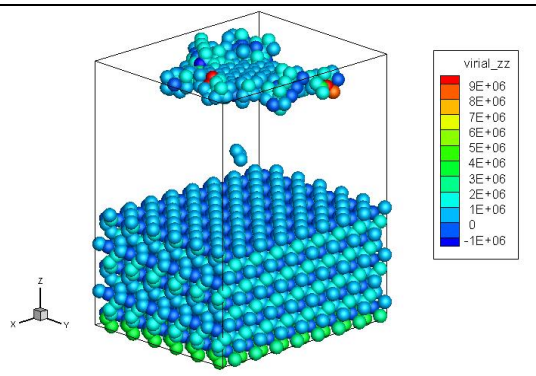

Figure 9-21 Timestep=6000, Virial_zz stress of large_quartz_water_1 system during equilibration

With the simulation advancing, water molecule is adsorbed onto the quartz surface whereas the asphalt molecule is approaching to the quartz substrate. At this time, the virial_zz decreased from the initial value of magnitude of 9.0×10^6 kcal/mol, shown

in Figure 9-21 to the 2.0×10^{6} kcal/mol Figure 9-23. This is a representation of the interaction among asphalt, water and quartz decreased and this is in good agreement of the system energy equilibration process.

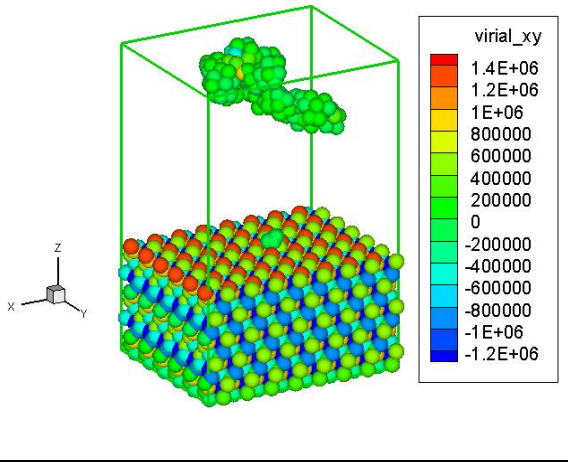

Figure 9-22 Virial_xy value contour of large_quartz_water_1 system during equilibration

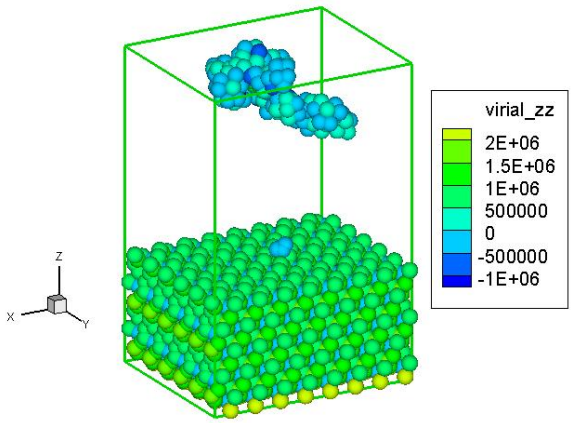

Figure 9-23 Virial_zz value contour of large_quartz_water_1 system during equilibration

Figure 9-24 and Figure 9-25 illustrate the equilibrated moisture asphalt-aggregate interface. The water molecule is located between the asphalt-aggregate interface structures. From the virial_xy, shown in Figure 9-24, and virial_zz, shown in Figure 9-25, the total energy of this three-phase system is a little bit lower than the debonding model in dry adhesion model, shown in Figure 9-14 and Figure 9-15. This could be due to the appearance of water molecule in between, which is in agreement with the introduction section of this chapter. If a three-phase interface consisting of aggregate, asphalt, and water, water reduces the free energy of the system more than asphalt to form a thermodynamically stable condition of minimum surface energy.

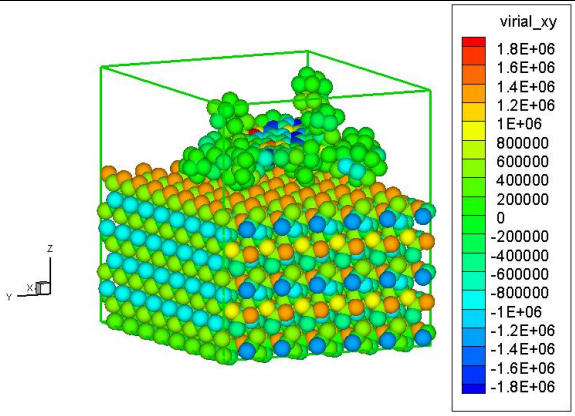

Figure 9-24 Virial_xy value contour of equilibrated large_quartz_water_1 system

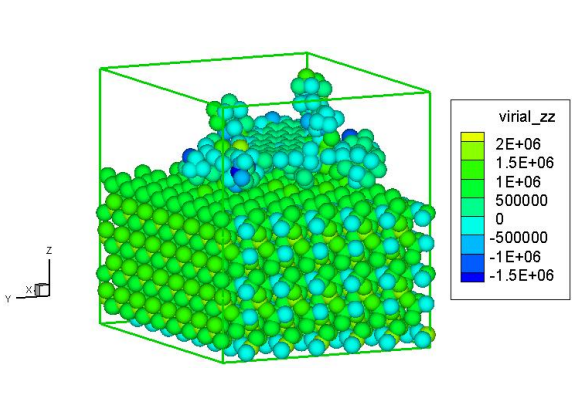

Figure 9-25 Virial_zz value contour of equilibrated large_quartz_water_1 system

In order to evaluate the hydrated quartz-average asphalt interface adhesion strength, in other words, moisture damage possibility. Pullout loading simulations are carried out at 273 K and 298 K, respectively. Results presented in Figure 9-26 show the interaction energy between the average asphalt molecule and quartz substrate at 273 K and 298 K, respectively. The interaction energy starts from a value of 50 kcal/mol. Then it goes down to 0 with the increase of distance between the aveasphalt molecule and quartz substrate. At the beginning, the interaction energy of 273 K is greater than that of 298K. This is in agreement with the fact that semi-liquid asphalt has larger cohesive energy at lower temperature.

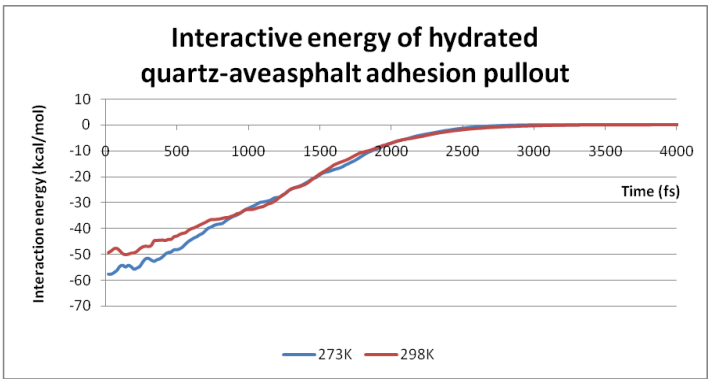

Figure 9-26 Interaction energy between aveasphalt molecule and quartz substrate at 273 K and 298 K

Figure 9-27 depicts that the quartz-asphalt interactive force is approaching to 0 at the beginning of pullout, because the interface system is equilibrated to a minimum

energy state. With the distance increasing, the asphalt-quartz interaction force grows up. Then the interaction force reaches the peak value at 25 for 273K and 21 for 298K, respectively. The attractive force keeps increasing, before it reaches the peak. Whereas the attractive force decay slowly and fluctuating to 0, after the highest attraction force. As to the temperature dependent effect, the peak attractive force of 273 K is a little bit larger than that at 298 K. This is in accordance with the interaction energy results shown in Figure 9-26 that the asphalt molecule appears to be more attractive at low temperature than high temperature.

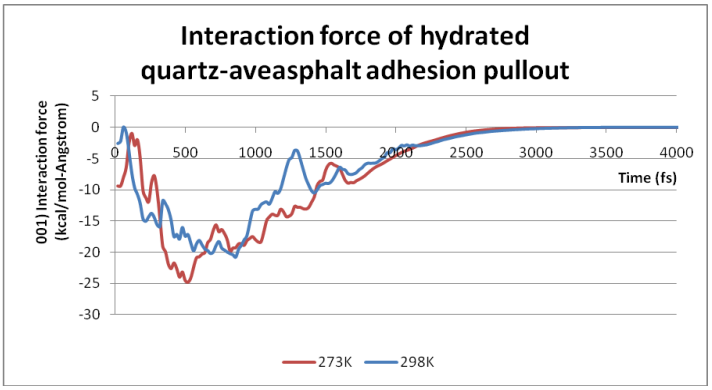

Figure 9-27 Interaction force between aveasphalt molecule and quartz substrate at 273 K and 298 K

Analytic comparison is made between the hydrated quartz-aveasphalt pullout and dry adhesion pullout simulations. With the presents of water molecule at the asphalt-quartz interface region, the total adhesion interaction energy and force decreased. The reason is that water reduces the system adhesion energy of the system more than asphalt to form a thermodynamically stable condition of minimum surface energy. The pullout simulation illustrates a mechanism that mimics the moisture damage by external loading applied on hydrated asphalt-aggregate interface. The mechanical damage procedure performed on hydrated interface is roughly the same as the dry interface. Nevertheless, the hydrated interface needs smaller external energy and force than dry interface. This result is in agreement with the moisture damage appears in the pavement industry as we observed. If a pavement is always affected by moisture environment, it will result in any of the failure mode, e.g. rutting, fatigue, raveling, with traffic loads.

This study demonstrates the atomistic mechanism of interface moisture damage. In the presence of water, the adhesion mechanism can change significantly because water

can displace asphalt molecule from aggregate surface sites, and because polar surface shows an affinity of their own for water molecules.

To be able to compare these simulation results with experiment requires that either the simulations must be performed on much larger systems or the experiments must be performed on nanometer thick systems. The result indicates that the interface adhesion energy and force determine adhesive failure is an important part of how to think about adhesive failure particularly at the molecular scale.

9.11 Moisture Cohesion Damage Illustration in Simplified Atomistic Model

9.11.1 Asphalt Cohesion Damage

Asphalts are complicated materials formulated so they meet specified criteria for physical properties under extreme pavement temperature conditions. A detailed molecular understanding of mechanisms by which chemical cohesion damage, particularly affect physical property is not yet fully understood. This limits asphalt suppliers in designing new modified asphalts which satisfy the chemical and physical demands of real-world exposure.

Even though cohesive failure of asphalt has been regarded as a less important factor in the definition of moisture damage of HMA, Khattak et al. [136] suggested that the probability of cohesive failure was much greater than adhesive failure. This was also demonstrated by work of Kanitpong and Bahia [137], which is supported by the observation of failure surfaces in asphalt mixtures obtained from the Tensile Strength Ratio (TSR) test, where the failure was visually observed within the binder coating without evidence of apparent loss of adhesion to the aggregate particles.

This cohesive failure can be partially explained by emulsification of water in the asphalt phase, which is different to conventional emulsified asphalts in which the asphalt is emulsified in a water phase [138]. Fromm's work [138] showed that water could enter into the asphalt film and form a water-in-asphalt emulsion. This emulsification of water

in the asphalt film causes asphalt particles to separate from the asphalt film (cohesive failure) and ultimately leads to an adhesive failure at a critical time when this emulsification boundary propagates to the aggregate surface.

However, since the mechanism of cohesive failure leads, ultimately, to an adhesive failure, most instances of cohesive failure may only be inferred rather than observed, and the final mechanism (i.e., adhesive) is reported as the cause [115]. Thus, even though the definition of moisture damage in HMA has been regarded as the failure of adhesive and cohesive bonds between the asphalt and the aggregates in the presence of water, it has proven difficult to distinguish between the two modes of failure in predicting failure mode unless the failure surface of HMA is visually inspected [115].

Cohesion between bitumen and de-cohesion in the presence of water are key factors that influence the moisture sensitivity of an asphalt mix from a materials point of view.

We have described the development of an evaluation method to estimate the surface free energy components of aggregates. These values can be combined with the surface free energy components of bitumen to quantify the moisture sensitivity of asphalt mixes. When surface free energy is used to compute the work of adhesion between the aggregate and bitumen and their work of debonding in the presence of water, it accounts for the contribution of the physical cohesion between these materials.

In this subsection, MD simulation is applied on two cohesive asphalt models, one dry and one hydrated, respectively. The dry model is to calculate the inter asphalt molecule interaction potential between them. Pullout simulation is also performed to calculate the cohesive strength. The same simulations are also applied on the hydrated cohesive model, which a water molecule is injected into the gap between two asphalt molecules.

9.11.2 Mechanism of Dry Asphalt Cohesive Failures

In this task, two average asphalt molecule structures will be incorporated in a simulation procedure that accounts for interaction with each other. The simulation output will be used to relate molecule structure to the nano-mechanical properties. Using the MD techniques, the instant interactive mechanical behavior will be determined.

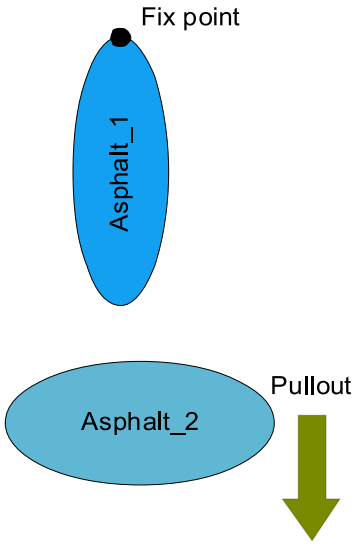

Figure 9-28 Schematic diagram of asphalt molecule pullout simulation

Pullout/cohesion force will be calculated from molecular model by first isolating a single average asphalt molecule from the binder, fixing one of its atoms in space, allowing the other side of its atoms to chemically bond to an another average asphalt molecule, and performing a molecular dynamics simulation while slowly increasing the distance between the motion group and the fixed atom. This is schematically shown in Figure 9-28. The pullout forces measured from these calculations will be obtained to understand inter asphalt molecule cohesive energy.

Here, we use a molecular dynamic simulation where one carbon molecule passes through an asphalt molecule along the perpendicular direction. The simulation output is cohesion energy/force of the two asphalt molecule groups shows the change of the cohesion energy as a function of simulation steps. This result gives us an atomistic picture of fundamental cohesive mechanism of asphalt.

9.11.3 Inner Bitumen Cohesion Modeling

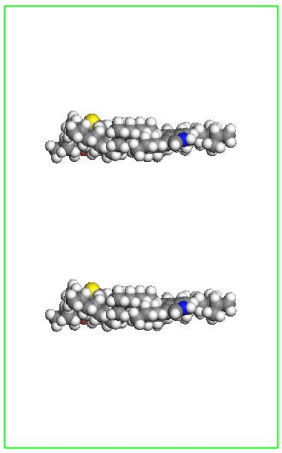

Side-view of Two average asphalt molecules adhesive model

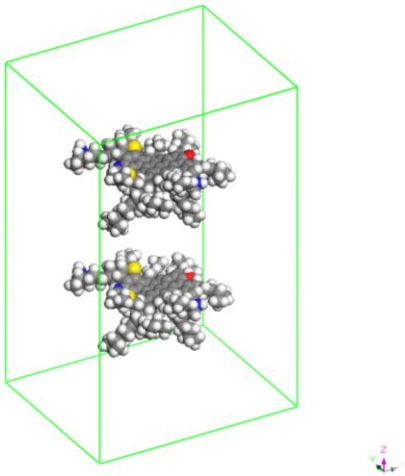

Top-side view of Two average asphalt molecules adhesive model

Figure 9-29 Dry two average asphalt molecules adhesive model

The cohesion model consisting of two average asphalt molecules is constructed as shown in Figure 9-29. It comprises 574 atoms, 618 bonds, 1212 angles, and 1926 dihedrals. In order to apply external loading and produce a full cohesive energy curve, the orthogonal simulation box is set to be the size of (39.304 X 32.4312 X 83.42) Angstrom. Comparatively, a moisture cohesive model consisting of 577 atoms, 620 bonds, 1213 angles, and 1926 dihedrals is also constructed.

In MD simulations, CVFF-aug forcefield interaction is also used to characterize interatomic interaction. When the cohesive model is under pullout, one of the C atoms belongs to the lower asphalt molecule will be fixed. The expressions for the interatomic potentials, as well as the overall simulation method, including the expressions for adhesion energy and de-cohesion energy are the same as used in adhesion model.

In order to measure the inner-asphalt cohesion energy and force, the pullout simulation is carried out. In this subsection, a constant force is applied to each atom in the asphalt molecule to drag it towards the direction opposite to each other. When calculating the interaction force and potential energy between the asphalt molecules, the interaction force will first grow up then drop down and decay to 0. Accordingly, the largest adhesion force will be the peak value of the interaction force curve, as is the same thing for interaction potential.

The magnitude of the force is specified along Z direction whereas in X and Y

directions will be set un-restrained. If an atom is closer than a distance delta to the point, then the force is not applied. It means do not include that X and Y dimension in the distance calculation or force application. This method allows one to achieve a smoothly interface adhesion interaction simulation through the molecular dynamics.

For hydrated cohesion model, the appearance of water molecule leads to a change of the cohesion system. The calculation method adopted is the same as in dry cohesion pullout. Perform calculation to get the interaction force and potential energy between the asphalt molecules which is disturbed by the water molecule.

9.11.4 Simulation Details

In this simulation, we define a computation that calculates the total energy and force interaction between two groups of atoms: the compute group and the specified group2. The interaction energy is defined as the pairwise energy between all pairs of atoms where one atom in the pair is in the first group and the other is in the second group. Likewise, the interaction force calculated by this compute is the force on the compute group atoms due to pairwise interactions with atoms in the specified group2.

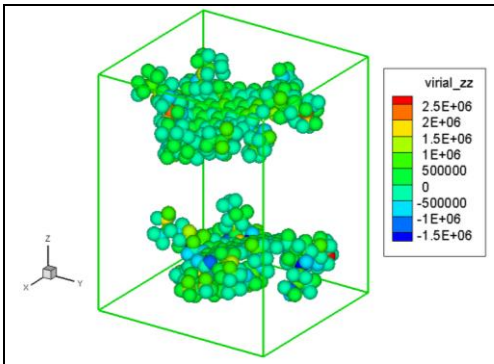

Figure 9-30 timestep=7000 two_aveasph stress_zz

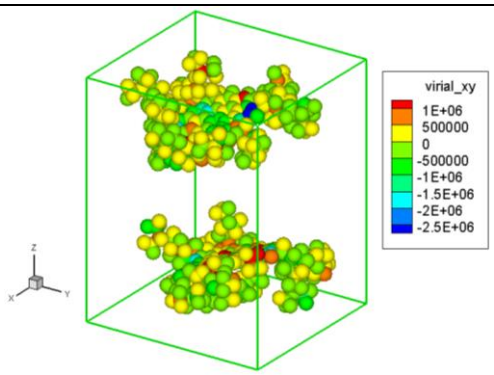

Figure 9-31 timestep=7000 two_aveasph stress_xy

The two molecules are put at the center of the simulation box with a distance of 15 Angstrom in between. In Figure 9-30 and Figure 9-31, the virial energy contours at the timestep of 7000 are plotted. Virial_zz value is bigger than that of virial_xy value. This cohesive bonding occurs in 100 ps to reach the equilibration. Each atom of the two

asphalt molecules is allowed to move within their local neighborhood. The energy and force are calculated by looping over a neighbor list of pairwise interactions. Thus it can be inefficient to compute this quantity too frequently.

Simulations under pullout are performed. Pullout deformation mode is achieved by moving one atom of the average asphalt_1 at constant velocity in the +Z directions.

9.11.5 Dry Cohesion Asphalt Results

Figure 9-32 and Figure 9-33 show the equilibrated cohesive model. We assume that the two asphalt molecules are fully binding to each other. The magnitude value of virial_zz is 3.5×10^6 kcal/mol, whereas that of virial_xy is 1.4×10^6 kcal/mol. Peak virial values are located at the S atom, O atom and N atom, because they have relatively bigger adsorption energy than Carbon and Hydron atoms. Thus, heteroatoms play a significant role in cohesion interaction.

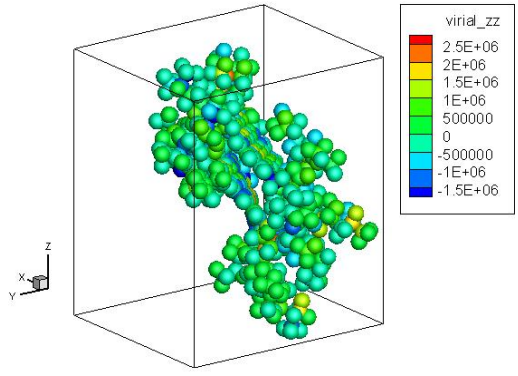

Figure 9-32 Virial contour of equilibrated cohesive model, virial_zz of the peak at 2000 fs

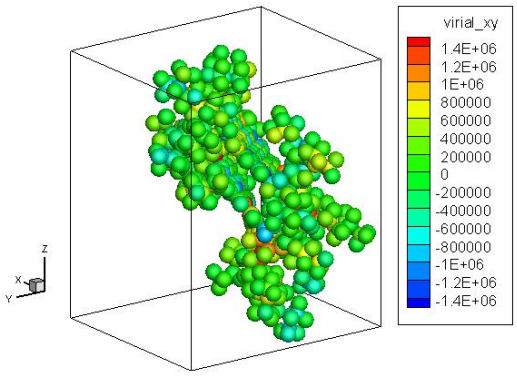

Figure 9-33 Virial contour of equilibrated cohesive model, virial_xy at the peak at 2000 fs

Figure 9-34 and Figure 9-35 illustrate the pullout simulation at the middle of this process. From the virial_zz contour, with the increase of intermolecule distance the interaction potential decreases. The magnitude of virial_zz drops down from the tight binding state of 3.5×10^6 kcal/mol to the loosened 2.0×10^6 kcal/mol, while the magnitude of virial_xy goes down from the cohesive state of 1.4×10^6 kcal/mol to 1.2×10^6 kcal/mol. Peak virial values are located at the central aromatic ring area where C atom are compacted, this may due to the high energy double of connected aromatic C

rings.

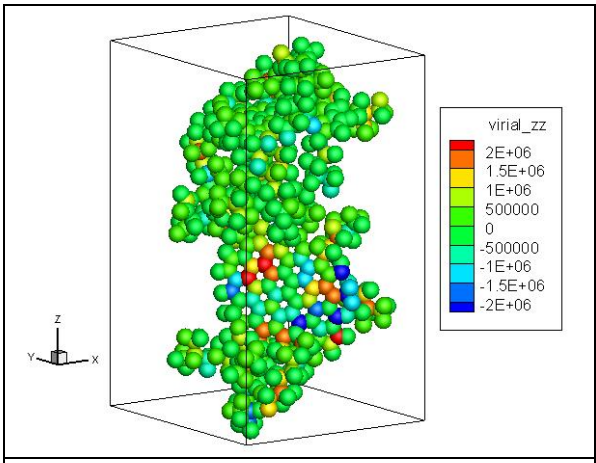

Figure 9-34 Virial contour at the start of pullout simulation, virial_zz of the separating point at 3500 fs

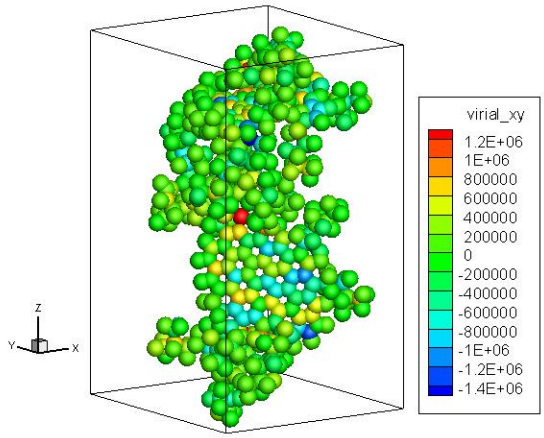

Figure 9-35 virial_xy of the separating point at 3500 fs

Figure 9-36 and Figure 9-37 illustrate the state that the two aveasphalt molecules are separated apart from each other. From the virial_zz contour, with the increase of intermolecule distance the interaction potential keeps decreasing. Figure 9-38 and Figure 9-39 demonstrate the pullout simulation at the end of this process.

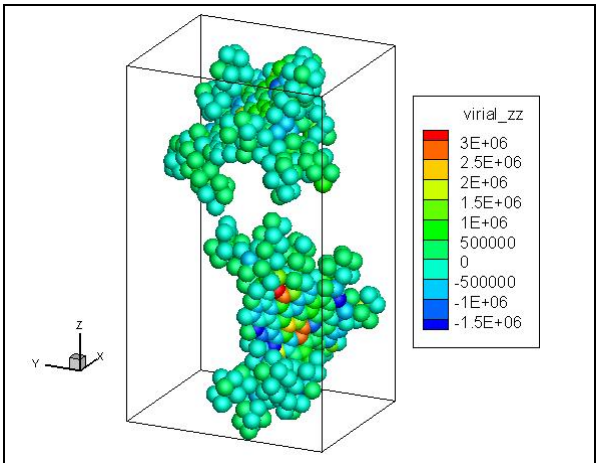

Figure 9-36 Virial contour at the end of pullout simulation, virial_zz of the separating point at 4500 fs

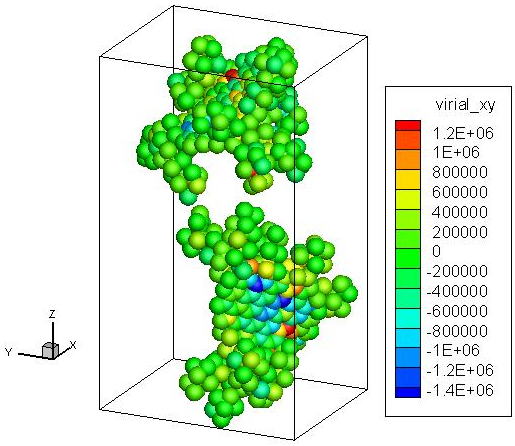

Figure 9-37 virial_xy of the separating point at 4500 fs

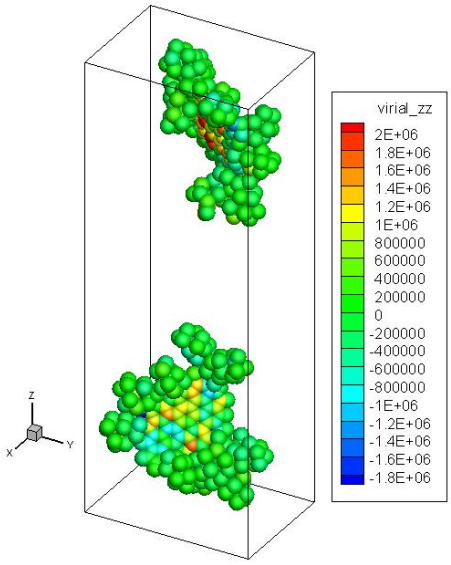

Figure 9-38 virial_zz after the total separating at 7000 fs

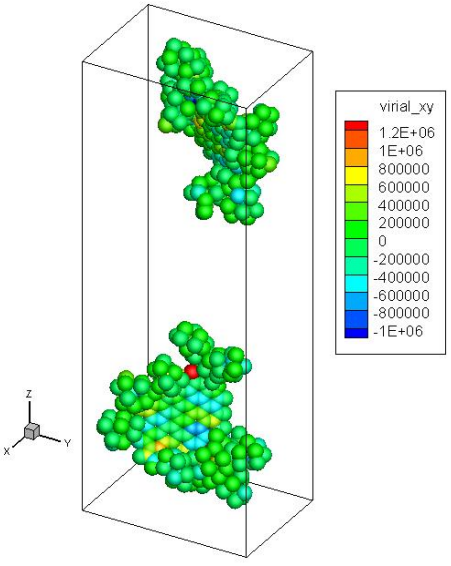

Figure 9-39 virial_xy after the total separating at 7000 fs

Figure 9-40 illustrates the interaction energy curve of two average asphalt molecules pullout simulation. The two interaction energy curves fluctuate at the start of pullout loading and decay with the distance increases. The results indicate that the energy of 273K is a little bit bigger than the one at 298K. The temperature dependent property of the cohesive system is not that obvious. Because the system is relatively small and the fluctuation noise may immerse the typical curve into a noise sea.

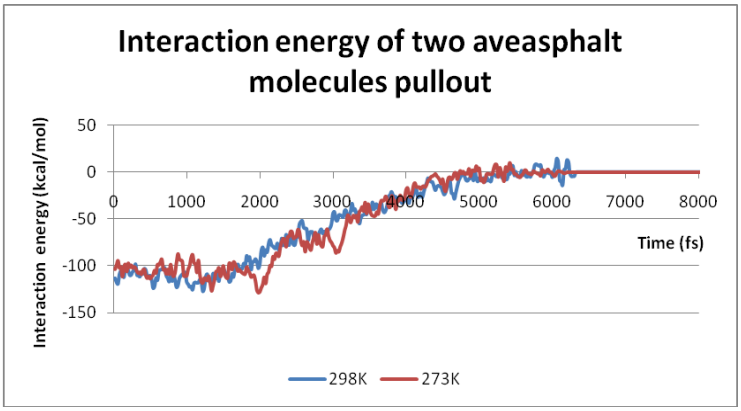

Figure 9-40 Interaction energy of two average asphalt molecules pullout

Figure 9-41 shows the maximum adhesion strength as a function of the system temperature, although the system fluctuation immerses some of the critical features. The

same observation can be drawn from the interaction force curve. With the temperature decreases, the adhesion force increases. The adhesion strength is obtained from pullout simulation that it is -28 $kcal/mol \cdot Angstrom^{-1}$ at 273 K, whereas it is -27 $kcal/mol \cdot Angstrom^{-1}$ at 298 K.

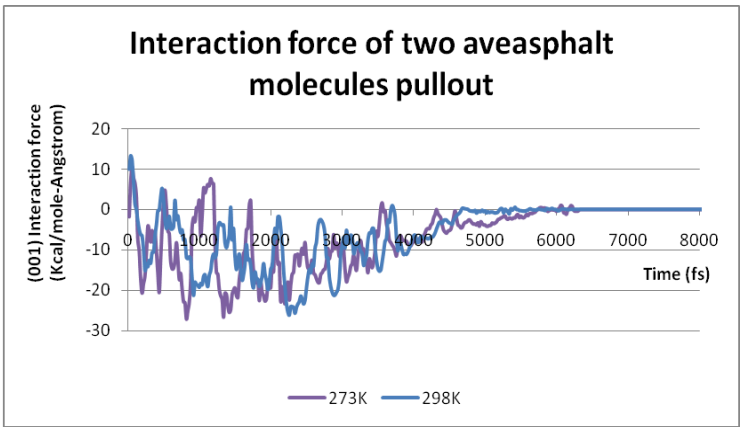

Figure 9-41 Interaction force of two average asphalt molecules pullout

These observations allow drawing conclusions about the cohesion: The results indicate that inter-asphalt cohesion can be achieved at not only normal direction but also at tangential direction. With respect to variations in temperature, keeping a strong cohesion force can only be achieved at lower temperature. Generally, all cases illustrated that the atomistic interaction is the control role of cohesion, and the cohesion strength has a strong dependency on the system temperature and the chemistry of the adhesion element.

9.11.6 Hydrated Asphalt Molecules Cohesive Property

The hydrated two average asphalt molecules cohesive interaction model is also constructed and shown in Figure 9-42. As illustrated in the middle of this figure, a water molecule is inserted between the two asphalt molecules. The moisture cohesive model is as the same simulation box size with the dry cohesive model.

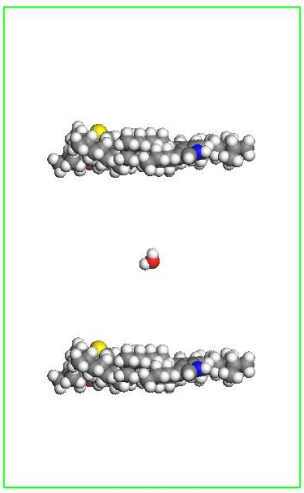

Front view of hydrated two-asphalt moisture system

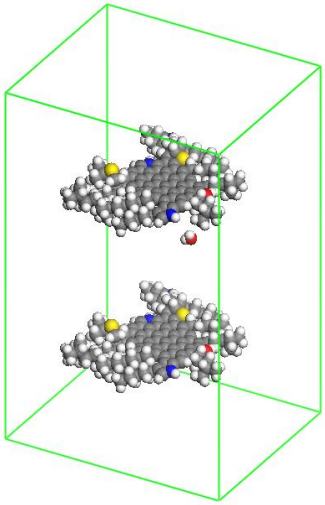

Top-side view of hydrated two-asphalt moisture system

Figure 9-42 Hydrated two-asphalt moisture system

If the MD simulation runs enough long time, the water molecule will be propelled out of the two asphalt system. This is in agreement with the experimental fact that asphalt materials have strong hydrophobic property which makes asphalt materials have water proof features. Because water is a polar molecule, while the average asphalt molecule may have non-polar or weak-polar properties.

Figure 9-43 and Figure 9-44 illustrate the virial_zz and virial_xy values of the hydrated two average asphalt systems at the start of pullout loading. The largest interactive energy occurs at the asphalt molecule whereas the water molecule and quartz have relatively smaller interaction potential energy.

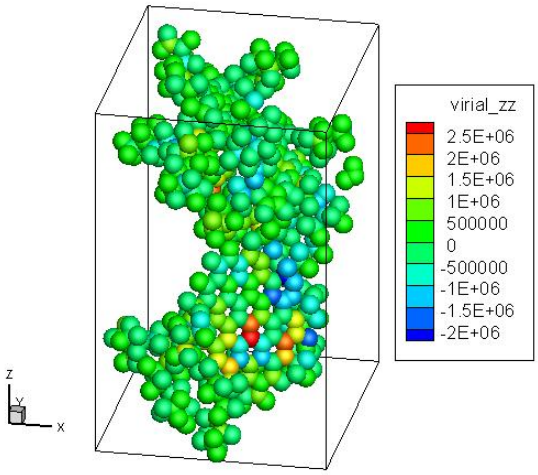

Figure 9-43 Virial_zz plot of the hydrated cohesive model at 5000 fs

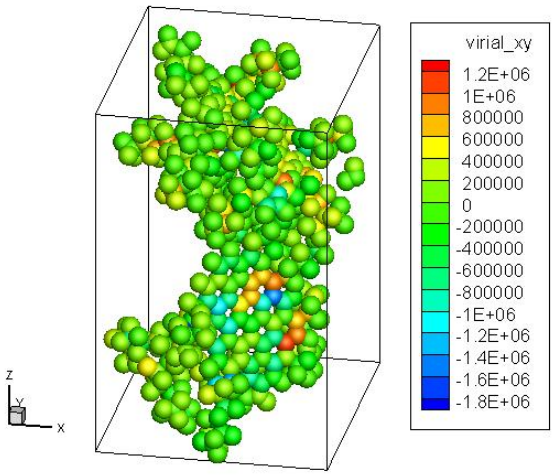

Figure 9-44 Virial_xy plot of the hydrated cohesive model at 5000 fs

With the simulation advancing, the water molecule does not adsorb onto any of the asphalt molecule but repelled between them. We name this phenomenon hydrophobic property because the water molecule has not any trend to approach to the asphalt molecules.

Then pullout simulations are performed on the hydrated two average asphalt molecules system, and monitor the instant interactive energy and force. Consequently, a comparison is made between the moisture/dry two-average asphalt systems.

In order to investigate the hydrated two average asphalt system adhesion strength, in other words, moisture damage possibility caused by cohesion loss. Pullout loading simulations are carried out at 273 K and 298 K, respectively. Results illustrate in Figure 9-45 show the cohesion energy between the two aveasphalt molecules at 273 K and 298 K, respectively. The interaction energy of 273 K starts from a value of 48 kcal/mol and it is followed by rising to a peak at 76 kcal/mol. Then it goes down to 0 with the increase of distance between the two aveasphalt molecules. A strong fluctuation is always accompanied with the whole process. As to the 298 K case, the adhesion energy has the same trend as that of 273 K, but it always has lower cohesion energy than that of 298 K. The peak cohesion energy is 48 kcal/mol which is lower than that of 76 kcal/mol at 273

K. This is in agreement with the fact that semi-liquid asphalt has larger cohesive energy at lower temperature.

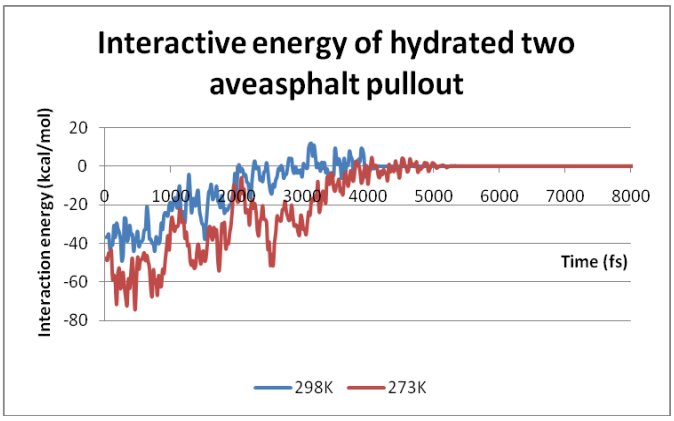

Figure 9-45 Interactive energy of hydrated two aveasphalt pullout

Figure 9-46 depicts that the two asphalt cohesive force is approaching to 0 at the beginning of pullout, because the interface system is equilibrated to a minimum energy state. With the distance increasing, the cohesive force grows up. Then the interaction force reaches the peak value at 19 for 273K and 17 for 298K, respectively. The attractive force keeps increasing, before it reaches the peak. Whereas the attractive force decay quickly and fluctuating to 0, after the highest attraction force. As to the temperature dependent effect, the peak attractive force of 273 K is a little bit larger than that at 298 K. This is in accordance with the interaction energy results shown in Figure 9-45 that the asphalt molecule appears to be more attractive at low temperature than high temperature.

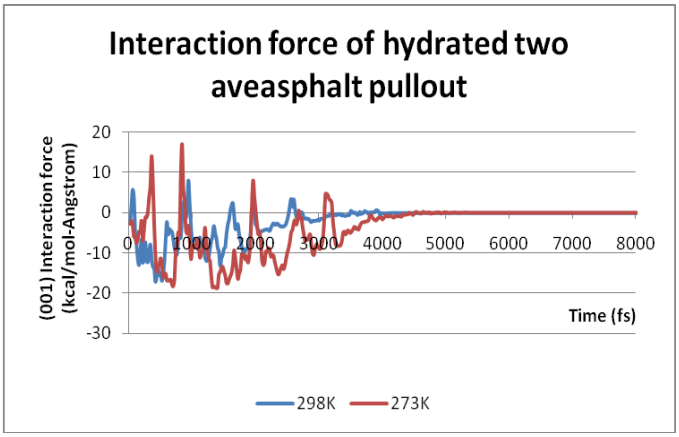

Figure 9-46 Interactive force of hydrated two aveasphalt pullout

Analytic comparison is made between the hydrated/dry two aveasphalt adhesion pullout simulations. With the presents of water molecule at the two asphalt interface region, the total cohesion energy and force decreased. The reason is that water reduces the system cohesion energy of the system more than asphalt to form a thermodynamically stable condition of minimum surface energy. Moreover, the water molecule will be repelled away from the two asphalt molecules system. This phenomenon is named hydrophobic feature. Due to the hydrophobic nature, the hydrated two-asphalt system cannot reach an energy stable state, which leads to a stronger cohesion energy and force fluctuation, shown in Figure 9-45 and Figure 9-46.

The pullout simulation illustrates a mechanism that mimics the moisture damage by external loading applied on dry/hydrated two average asphalt molecules interface. The mechanical damage procedure performed on hydrated interface is roughly the same as the dry interface. Nevertheless, if only water can appear in the asphalt binder, the hydrated asphalt binder needs smaller external force to de-cohesion than dry asphalt. This result is in agreement with the moisture damage appears in the pavement industry as we observe. If a pavement is always affected by moisture environment, it will result in any of the failure mode, e.g. rutting, fatigue, raveling, with traffic loads.

This study demonstrates the atomistic mechanism of cohesive loss induced moisture damage. In the presence of water, the cohesion mechanism can change significantly because water can displace asphalt molecule from each other, and because polar water molecules shows a hydrophobic feature which may de-cohesion the asphalt binder.

To be able to compare these simulation results with experiment requires that either the simulations must be performed on much larger systems or the experiments must be performed on nanometer thick systems. The result indicates that the asphalt cohesion energy and force determine cohesion loss induced failure is an important factor of how to think about cohesion failure particularly at the molecular scale.

9.12 Summary

This Chapter focused on developing a nanoscale modeling system for reliable prediction of moisture damage in asphalt concrete interface. For this purpose, a couple of atomistic models, e.g. quartz-mix1-water, calcite-mix2-water, and calcite-mix1-dry, etc. are constructed. Interface adhesion modeling procedures developed for adhesion energy and cohesion energy using surface free energy method were performed to the atomistic models. Simulation results are in agreement with macroscale observations that the asphalt-aggregate is susceptible to moisture. Quartz surface is more susceptible to moisture than Calcite, whereas the mix1 is more susceptible to moisture than mix2. Because quartz is an acid substrate, whereas calcite has an alkaline inclination which makes it has larger affinity to asphalt and less susceptible to water. In addition, different asphalt mixture also affects adhesion energy. Based on the comparison between mix1 and mix2, the cohesion and adhesion forces provide by mix2 is significantly larger than those of mix1. Mix2 sample is relatively soft with good ingredients and fraction of molecules therefore it has larger adsorption potential energy than mix1.

Moreover, in order to investigate the fundamental mechanisms of moisture adhesion/cohesion, a series of simplified atomistic models are constructed to perform pullout simulations to calculate adhesion/cohesion forces. The MD simulation results presented here provide improved understanding on how mineral substrate structure and hydrated environment affect the molecular-scale structure and properties of asphalt-aggregate interface.

The atomic profiles of water and asphalt are largely controlled by the mineral surface structure. The orientations of these molecules, however, are dominantly influenced by quartz surface hydrophilicity, surface charge distribution, and the ability to form polar interactions with adsorbed water molecules. The molecular layer of water and asphalt at the surface is well ordered and absorbed parallel to the surface, reflecting the substrate crystal structure and composition. The mobility of adsorbed water molecules are controlled by mineral surface charge and hydrophilicity/hydrophobicity.

The mineral-asphalt-water interfaces considered here represent only a few idealized cases of perfect surfaces in contact with pure liquid water. Detailed quantitative

analysis of the effects of mineral substrate structure and asphalt composition on the structure, dynamics, and energetics of interfacial water within the framework of a single force field model are highly instructive, because the fundamental structural and dynamical conclusions seem to be quite informative and generalizable to systems containing mineral surfaces with similar compositions and structures.

In the future, incorporation of inorganic and organic additives and mineral surface defects will bring the molecular models closer to the complex mineral aggregate and asphalt reality. Advanced, atomistically detailed surface specific experimental data will also be essential. These are subjects of future investigations. The progress in this direction would eventually provide a solid molecular-scale picture of moisture mineral-asphalt interfaces that should be complementary to the common macroscopic asphalt-aggregate double layer models.

1. The atomistic modeling method employed in this research offers a convenient way to calculate surface free energies of different aggregates and predict moisture resistance of potential mixes when combined with surface energies of various bitumens.

2. The dispersive component and base components of aggregate surface energy play a significant role in adhesion with bitumen. The two aggregates, e.g. quartz and calcite, discussed in this Chapter have widely different base components of surface energy which are the primary contributors to the differences in the compatibility with any given bitumen.

3. Adhesion energy calculations based on aggregate and bitumen surface energies corroborate well with previous theories suggesting that most bitumens are weak to silicate substrates, but calcarious aggregates provide stronger interactions between bitumen for adhesion.

4. The results obtained demonstrate the ability of this methodology to generate a useful guide for all possible combinations of these materials based on the surface energy components of each material. This MD simulation protocol may be used as a materials selection tool to select combination of asphalt binder and aggregate that will yield optimal performing asphalt mixes.

Chapter 10
Conclusions

10.1 Overview

In this dissertation, we established a multiscale modeling method to bridge the gap between nanoscale materials features and civil engineering materials deformation and failure mechanisms. The specific technologies such as high performance parallel MD simulation, results visualization, and 3D high definition multiscale digital microstructure characterization devices are all employed in this dissertation. The main achievements are summarized as follows. In the area of interface deformation and failure behaviors modeling:

1. Characterized multiscale features of asphalt concrete materials by using nanoscale characterization & fabrication devices, e.g. High Resolution Optical Microscope (HROM), Environmental Scanning Electron Microscope (ESEM), Transmission Electron Microscope (TEM), Focused Ion Beam (FIB), and Atomistic Force Microscope (AFM).
2. Developed 3D atomistic models to calculate the bulk elastic constants of the stone-based mineral aggregate, e.g. Granite, Quartz, Calcite, and Kaolinite. Elastic Stiffness constants, elastic Compliance constants, Young's modulus, Poisson ratios, Lame constants, bulk and shear modulus of the 4 minerals are obtained by molecular mechanics method.
3. Developed 3D one average asphalt molecular model and 2 mixing asphalt molecular models to perform MD simulation and predicted static property (e.g. RDF, concentrate profile), thermodynamic properties (e.g. potential energy, bonded energy, and nonbonded energy, MSD), and nano-transportation/mechanical

properties (e.g. the stress autocorrelation function, viscosity, as well as the cohesive energy density).

4. Developed 3D 2-layer atomistic models to characterize asphalt concrete interface structures. Performed nanoscale uniaxial tension simulation on the asphalt-aggregate interface model. Calculated the interfacial deformation and failure behaviors, as well as performed the parameter analysis on deformation rates.
5. Developed a 3D 3-layer (aggregate-asphalt-aggregate) confined shear atomistic model and performed interface confined shear simulations. Asphalt-aggregate interface temperature profiles, shear stress profiles, and shear velocity profiles are obtained to characterize the interfacial interaction in tangential direction.
6. Developed several computer programs to analyze and interpret atomistic trajectories in macro scale, according to statistical mechanics and statistical thermodynamics. The author developed a high performance parallel distributive computing algorithm. Based on this algorithm, a parallel computing program --- MPI_multistress is developed to implement the multiscale understanding/predicting materials mechanical behaviors. Simulation results are all visualized by using advanced visualization software, e.g. VMD and Atomeye, to figure out the materials deformation and failure phenomena.

In the area of asphalt concrete interfacial moisture damage modeling:

1. Various dry/wet interface models are constructed, including mix1/mix2 and quartz/calcite. Surface free energy theory is employed to investigate the adhesion/cohesion energy at the interface. Water susceptibility of each pair of combination is also calculated. Interface interaction phenomenon, e.g. asphalt affinity, mineral surface adsorption, interface adhesion/stripping, hydrophobic and hydrophilic properties, etc. are all investigated with nanoscale atomistic modeling and simulation methods.
2. Simplified adhesion/cohesion asphalt-aggregate interface dry/wet models are constructed and pullout simulations are performed to explore the fundamental mechanisms of moisture adhesion/cohesion strength. Temperature-dependency properties are also investigated. Asphalt binders are susceptible to moisture. This

trend is in agreement with pavement industry observations. Based on the wet/dry adhesion/cohesion forces and virial values in the simplified mechanism models, it is shown that the asphalt binders are susceptible to moisture damage and they have strong temperature dependency properties compared to rock minerals.

10.2 Summary of Conclusions

Asphalt-aggregate interfacial deformation and failure behaviors are complex process in which asphalt binders undergo important nanoscale rearrangement of their structure through processes, e.g. ordering of similar molecules due to temperature, loading, air, and other environmental factors. These nanoscale characteristics have dramatic effects on binder and mixtures' mechanical properties such as stiffness, viscosity, adhesion, and cohesion, etc.

Understanding how and what structures and components affect the asphalt binder and mixtures' mechanical properties has remained unexplored, because these interactions occur at the atomistic to molecular scales. This research provides a fresh perspective to the deformation and failure behaviors that can be brought through a fundamental study of the mechanisms of asphalt concrete through multiscale characterization and atomistic modeling of asphalt-aggregate interface.

This dissertation offers a novel approach to provide the link between interface atomistic structure and mechanical behavior through nanoscale experimentation and advanced molecular modeling. MD simulations are performed on full atomistic models to determine the interaction in molecular structure under the influence of mechanical factors such as temperature, loading, and moisture.

The objective of this research was to develop models and methods to bridge atomistic and continuum models of deformation processes in asphalt-aggregate interface composite materials systems. Particularly, focuses on the identification of composite materials' phenomena at the atomistic level and the interpretation of these results into the continuum level. The research presented here has met this goal by providing a foundation for multi-scale modeling of deformation processes in composite materials, composed by both organic and inorganic materials. Atomistic tools, e.g. molecular mechanics and

molecular dynamics, are both successfully used to perform simulations in a nanoscale model framework. The successful bridging of moisture damage from atomistic to continuum models is a specific application of this process that serves as a direction for similar bridging of other materials phenomena.

There are both conceptual and technical challenges to studying deformation and failure with an atomistic approach. One must overcome the intrinsic small length- and time-scale limitations and be able to focus on the controlling mechanisms. The first challenge is that physical laws valid at larger scales may become invalid when features reach the nano-scale. In terms of mechanical response, conventional descriptions such as stress-field characterizations may be no longer applicable, and one must come up with new descriptions based on nanoscale behaviors that would remain valid down to the nano-meter. Another major challenge is the lack of reliable interatomic potentials to carry out the simulation. Empirical potentials do not have to be highly accurate, but it is essential for them to be able to work reasonably well in many different atomistic environments.

These calculations constitute one of the first attempts to conduct fully atomistic simulations on a multi-component asphalt mixture whose chemical composition is chosen to be reflective of compounds found in real asphalts. Different molecules were chosen to reflect saturate, naphthene aromatic, and asphaltene components. The ultimate model mixtures displayed properties in simulations that were qualitatively similar to those of real asphalts but not quantitatively the same. Initial calculations focused on small molecules and simple mixtures to assess the accuracy of the methods and force field. It was found that the CVFF-aug force field provides sufficient accuracy for predicting the asphalt-aggregate interface models. The potential is fitted to the cohesive energy, the lattice constants, and the elastic constants of all the component systems. The potential predicts the mechanical and thermodynamic properties of the component systems in qualitatively agreement with experimental measurements.

Based on the finding of this study, the following conclusions are made:

Through a combination of molecular dynamics and molecular statics, mechanical properties, e.g. elastic constants, modulus, poison's ratio are all calculated for 4 mineral crystals. In all minerals analyzed, the Young's modulus is higher than that for the

corresponding mineral crystal materials. The tension strengths of asphalt-aggregate interface structures approach the ideal shear strengths of their confined shear structure. The observations reported here provide important data and insights for formulating continuum relations for multi-component composite materials with nanosize mechanisms.

The interface tensile strength simulation is able to predict interface interactions between asphalt and aggregates with different deformation rates. Factors identified as significant through analysis of variance performed on the results were consistent with expectations. The confined shear simulations are also performed and the results obtained are for characterizing the interfacial interaction in tangential direction.

High-resolution images of asphalt atomistic interfaces morphology and information on their distribution within the interfaces have been obtained. Generally, all of the 5 different microscopical observation methods, e.g. HROM, AFM, ESEM, FIB and TEM, are correlated among scales. In the modeling chapters, all of our atomistic models are based upon these advanced multiscale image characterizations.

The last topic is moisture damage. Moisture damage in asphalt mixes is a complex process that involves two primary interfacial phenomena, cohesion/adhesion. First, water can interact physically/chemically with the asphalt cement to cause a reduction in cohesion with an associated reduction in stiffness and strength of the mixture. Second, water can get between the asphalt film and the aggregate and break the adhesive bond between the asphalt film and the aggregates, thus ‘stripping’ the asphalt from the aggregate. Stripping or moisture damage can be reduced when strong adhesive bonds are present.

For the first time in asphalt concrete interface area, this study has used atomistic modeling and simulation approach to determine the adhesion/cohesion forces in wet/dry asphalt aggregate system. The technique can be considered as a nanoscale tool that can address directly the roles that different atomistic interactions of asphalt, aggregate, and water play in influencing the intermolecular adhesion/cohesion force due to moisture-induced damage.

This research focused on developing an approach to evaluate the susceptibility of aggregates and asphalts to moisture damage by understanding the nano-mechanisms.

These nanoscale mechanisms may influence the adhesive bond between aggregates and asphalt, as well as the cohesive strength and durability of the asphalt. The results were compared to actual reported field performance and further used to predict which combinations of asphalt and aggregate will produce superior in-service performance. A summary of the work accomplished in this study and main findings is presented along with procedures that can be used to select the optimum combinations of aggregates and binders that will reduce moisture susceptibility.

In this study, surface free energy theory is employed to evaluate the moisture adhesion energy at the asphalt-aggregate interfaces. This study developed a nanoscale simulation protocol to evaluate the susceptibility of asphalt mixes to moisture damage. A critical parameter to these processes is bond strength failure between asphalt and aggregate in the presence of water. Bond strength is determined via a pullout simulation. In this study, the methodologies for preparing atomistic interface model and conducting nanoscale pullout simulations using CVFF-aug forcefield are established. Determination of adhesion between asphalt-aggregate interface and inner asphalt cohesion force are challenging. This is because asphalt is a sticky soft material compared to other hard materials, and asphalt is a complicated composite material in atomistic scale which has various types of molecular structure based on the sources. Simulation results for bond strength are linked to moisture adhesion properties and, for the first time, bond strength, water susceptibility as a factor of the aggregate types and asphalt components is established. Based on this relationship, the fundamental mechanisms of asphalt concrete moisture adhesion/cohesion damage that occurs over time in regards to the amount of moisture can be elucidated. Comparisons of pull-out tensile strength to binder permanent deformation results highlight the need for an evaluation method that can properly calculate binder adhesive/cohesive characteristics when subjected to moisture conditions.

10.3 Contributions and Implications

Atomistic simulations build a bridge between experimental macroscopic behavior and molecular level, which offer us an insight into the local distributions of atomistic rearrangements and stresses that occur during deformation and failure. In this way, new

information can be gained that is difficult or impossible to obtain from experiments. Simulations may provide crucial input for the construction of macroscopic models. Establishing connections between molecular and macroscopic properties lies in the mechanical performance of asphalt-aggregate interface systems.

In this dissertation, large-scale molecular dynamics simulations are carried out to study the deformation and failure processes of asphalt binder and rock mineral aggregate. We show that the MD method combined with visualization tools is well suited for gaining mechanistic insights into the interfacial failure processes at various conditions.

This research has yielded a clear understanding of the influence of the structures on mechanical behavior through the development of atomistic scale materials models based on the nanoscale attributes of asphalt-aggregate interfaces, particularly the evolution of the asphalt-aggregate interface under tensile, confined shear, and moisture damage. The ultimate goal of the research is to develop methods to determine macroscale model parameters largely from molecular level models, reducing the need for experimental derivation of these parameters while providing additional capability for material design. To this end, a significant step toward this goal has been completed.

It is concluded that such an atomistic modeling based methodology can be applied to the study of failure in the interfacial regions of asphalt composites and this study represents an initial step in using these methods to provide a fundamental understanding of the atomistic scale materials behavior.

A thorough investigation of the application of molecular dynamics methods to simulate the deformation of interfaces has been completed. The sensitivity of the molecular dynamics method to the various model parameters and the interface system initial configurations has been determined. The confirmation of the molecular dynamics method is essential in ensuring that the remaining atomistic simulations can be trusted.

These contributions will have a significant impact in the field of asphalt concrete mechanics by shedding light on the relationship between nanoscale structures and macroscopic behaviors as well as providing methods to quantitatively link these scales. For the purposes of asphalt mixture design, the relationships obtained between nanoscale morphology and the resulting deformation and failure behaviors of asphalt-aggregate interface can support optimization and robust design methods to determine the

compositions for specific uses.

Furthermore, the determination of moisture damage model structures and parameter values based on atomistic models would facilitate prediction of mechanical behavior and morphology evolution of novel asphalt concrete materials without the need to synthesize them. Additionally, these methods, in conjunction with parametric studies, will permit the robust design of novel asphalt concrete that will meet desired mechanical behavior and anti-failure properties.

10.4 Recommendations of Future Research

This research is the first computer simulation studies focused on mechanistic aspects of the asphalt-aggregate composite materials interface, more exploration can be addressed on all aspects of interface deformation to varying contents.

Asphalt aging is a complex phenomenon, which involves physical and chemical changes to asphalt molecules. These changes have dramatic effects on asphalt binder and asphalt concrete properties such as viscosity, and adhesion/cohesion. The aging of asphalt concrete is another major failure cause. The aging of asphalt-aggregate mixtures is influenced by both the asphalt and the aggregate. However, aging of the asphalt alone does not appear to be an adequate means of predicting mix performance because of the apparent mitigating effect the aggregate has on aging. Moreover, the specific nanoscale mechanism of asphalt aging still remains unknown. Therefore, we suggest investigate the changes in molecular structure and composition of an asphalt binder due to aging, and relates these molecular structure and composition to mechanical behavior at nanoscale technologies.

In addition, the focus of this research is in the range of perfect atomistic structure deformation. For the simulation of asphalt concrete with high loading rates, atomistic simulations may be used with initial defects structure to study the performance of the asphalt concrete under cyclic loading with a large number of repetitions. Typically, the nanoscale model simulation requires real atomistic components and structures which contains nano-voids, defects, vacancies, and pores. If more applications of atomistic modeling are anticipated for predicting various mechanical, chemical and physical

properties, high definition real structure atomistic model should be constructed. In order to overcome these limitations, new 3D nanoscale image characterization techniques should be developed.

Furthermore, molecular modeling of real pavement materials interfaces often requires the description of complex and incompletely or poorly characterized crystal structures, low symmetries, large unit cells, variable compositions, and complex and variable interlayers and interfaces. The numerous parameters of a bonded force field are not easily transferred from relatively simple and well-known structures to systems with complex and ill-defined bond structures. For such systems, the application of a currently available forcefield is problematic because it can easily lead to lack of the experimental data to constrain all the force field parameters necessary to describe interatomic interactions. Thus, a specific forcefield for modeling pavement materials is highly necessary. We suggest to develop a specific forcefield for characterizing molecular simulations of hydrated mineral crystals compounds and their interactions with asphalt molecules component elements, including heteroatoms.

Appendix

Derivation of RDF Simulation Expression

The radial distribution function is defined by

$$\rho g(\mathbf{r}) = \frac{1}{N}\left\langle \sum_{i}^{N}\sum_{j\neq i}^{N} \delta\left[\mathbf{r} - \mathbf{r}_{ij}\right] \right\rangle \tag{A-1}$$

Here N is the total number of atoms, $\rho = N/V$ is the number density, $\mathbf{r}_{ij}$ is the vector between centers of atoms i and j, and angular brackets represent a time average. For homogeneous uniform substances, the structural arrangement of atoms depends only on the distance r between atoms and is independent of the orientation of the separation vector $\mathbf{r}$, so it reduces to

$$\rho g(r) = \frac{1}{N}\left\langle \sum_{i}^{N}\sum_{j\neq i}^{N} \delta\left[r - r_{ij}\right] \right\rangle \tag{A-2}$$

Now this double sum contains $N(N-1)$ terms; however, the distance r_{ij} is invariant under interchange of labels i and j, so only $\frac{1}{2}N(N-1)$ of those terms are unique. Therefore, we can write it as

$$\rho g(r) = \frac{2}{N}\left\langle \sum_{i}^{N}\sum_{j<i}^{N} \delta\left[r - r_{ij}\right] \right\rangle \tag{A-3}$$

The normalization of $g(r)$ is obtained by integrating over all possible separations of two atoms,

$$\rho \int g(r) d\mathbf{r} = \frac{2}{N}\left\langle \sum_{i}^{N}\sum_{j<i}^{N} \int \delta\left[r - r_{ij}\right] d\mathbf{r} \right\rangle \tag{A-4}$$

On the rhs, we have interchanged the order of time average, summation, and integration. The normalization condition of the δ symbol is

$$\int \delta\left[r - r_{ij}\right] d\mathbf{r} = 1 \tag{A-5}$$

so the above reduces to

$$\rho \int g(r) d\mathbf{r} = N - 1 \approx N \tag{A-6}$$

This equation says that if we sit on one atom and count the atoms in the system, we find $N-1$ other atoms. This equation also serves as the basis for a probabilistic interpretation of $g(r)$. $\frac{\rho}{N-1} g(r) V(r, \Delta r)$ is the probability that an atomic center lies in a spherical shell of radius r and thickness Δr with the shell centered on another atom.

Here $V(r, \Delta r) = \Delta \mathbf{r}$ is the volume of the spherical shell. The radial distribution function shows how the presence of one atom influences, on a time average, the positionis of neighboring atoms. For separations less than about one atomic diameter, $g(r) = 0$. For large separations in fluids, one atom should have no influence on the position of another, the density will then be uniform, and $g(r) = 1$.

To obtain an expression for evaluating $g(r)$ from simulation data, we start by rewriting (A-4) using a small but finite shell thickness Δr,

$$\rho \sum_{\Delta r} g(r) V(r, \Delta r) = \frac{2}{N} \sum_{\Delta r} \left\langle \sum_{i}^{N} \sum_{j<i}^{N} \delta\left[r - r_{ij}\right] \Delta \mathbf{r} \right\rangle \tag{A-7}$$

The double sum on the rhs of (A-7) represents a counting operation.

$$\sum_{i}^{N} \sum_{j<i}^{N} \delta\left[r - r_{ij}\right] \Delta \mathbf{r} = N(r, \Delta r) \tag{A-8}$$

where $N(r, \Delta r)$ is the number of atoms found in a spherical shell of radius r and thickness Δr, with the shell centered on another atom. The equation that results from putting (A-8) into (A-7) must be satisfied term by term; that is, it should be obeyed for each spherical shell, so we find

$$g(r) = \frac{\left\langle N(r, \Delta r) \right\rangle}{\frac{1}{2} N \rho V(r, \Delta r)} \tag{A-9}$$

Writing the time average explicitly over a total of M time-steps gives

$$g(r) = \frac{\sum_{k=1}^{M} N_k(r, \Delta r)}{M(\frac{1}{2}N)\rho V(r, \Delta r)} \tag{A-10}$$

where N_k is the result of the counting operation (A-8) at time t_k in the run. Physically, (A-10) can be interpreted as the ratio of a local density $\rho(r)$ to the system density ρ. The choice of a value for shell thickness Δr is a compromise: it must be small enough to resolve important features of $g(r)$, but it must also be large enough to provide a sufficiently large sampling population for statistically reliable results.

References

1. Cleri, F., et al., *Atomic-scale mechanism of crack-tip plasticity: Dislocation nucleation and crack-tip shielding.* Physical Review Letters, 1997. **79**(7): p. 1309-1312.
2. Abraham, F.F., et al., *Instability dynamics in three-dimensional fracture: An atomistic simulation.* Journal of the Mechanics and Physics of Solids, 1997. **45**(9): p. 1461-1471.
3. Bulatov, V., et al., *Connecting atomistic and mesoscale simulations of crystal plasticity.* Nature, 1998. **391**(6668): p. 669-672.
4. Farkas, D., et al., *Multiple-dislocation emission from the crack tip in the ductile fracture of Al.* Philosophical Magazine a-Physics of Condensed Matter Structure Defects and Mechanical Properties, 2001. **81**(5): p. 1241-1255.
5. Abraham, F.F., et al., *Simulating materials failure by using up to one billion atoms and the world's fastest computer: Brittle fracture.* Proceedings of the National Academy of Sciences of the United States of America, 2002. **99**(9): p. 5777-5782.
6. Rice, J.R., *DISLOCATION NUCLEATION FROM A CRACK TIP - AN ANALYSIS BASED ON THE PEIERLS CONCEPT.* Journal of the Mechanics and Physics of Solids, 1992. **40**(2): p. 239-271.
7. Gumbsch, P., et al., *Controlling factors for the brittle-to-ductile transition in tungsten single crystals.* Science, 1998. **282**(5392): p. 1293-1295.
8. Argon, A.S. and B.J. Gally, *Selection of crack-tip slip systems in the thermal arrest of cleavage cracks in dislocation-free silicon single crystals.* Scripta Materialia, 2001. **45**(11): p. 1287-1294.
9. Tsai, D.H., *The virial theorem and stress calculation in molecular dynamics.* The Journal of Chemical Physics, 1979. **70**(3): p. 1375-1382.
10. Caro, S., et al., *Moisture susceptibility of asphalt mixtures, Part 2: characterisation and modelling.* International Journal of Pavement Engineering, 2008. **9**(2): p. 99 - 114.
11. Copeland, A.R., J. Youtcheff, and A. Shenoy, *Moisture sensitivity of modified asphalt binders - Factors influencing bond strength.* Transportation Research Record, 2007(1998): p. 18-28.
12. Cheng, D.X., et al. *Moisture damage evaluation of asphalt mixtures by considering both moisture diffusion and repeated-load conditions*. in *82nd Annual Meeting of the Transportation-Research-Board*. 2003. Washington, D.C.
13. Kringos, N., et al. *Determination of Moisture Susceptibility of Mastic-Stone Bond Strength and Comparison to Thermodynamical Properties*. in *Technical Session of the Association-of-Asphalt-Paving-Technologists*. 2008. Philadelphia, PA.
14. Bhasin, A. and D.N. Little. *Methods to quantify interfacial adhesion and debonding in bitumen-aggregate systems in dry and wet conditions*. in *International Conference on Advanced Characterisation of Pavement and Soil Engineering Materials*. 2007. Athens, GREECE.

15. Fini, E.H., et al. *Interfacial Fracture Energy: An Indicator of Bituminous Material Adhesion*. in *Technical Session of the Association-of-Asphalt-Paving-Technologists*. 2008. Philadelphia, PA.
16. Raab, C. and M.N. Partl, *Investigation into a long-term interlayer bonding of asphalt pavements.* Baltic Journal of Road and Bridge Engineering, 2008. **3**(2): p. 65-70.
17. Wu, S.P., et al. *Temperature sensitivity of Asphalt-aggregate Adhesion via Dynamic Mechanical Analysis*. in *7th International Conference on Fracture and Damage Mechanics*. 2008. Seoul, SOUTH KOREA.
18. Mo, L.T., et al., *Ravelling investigation of porous asphalt concrete based on fatigue characteristics of bitumen-stone adhesion and mortar.* Materials & Design, 2009. **30**(1): p. 170-179.
19. Airey, G.D., et al. *Asphalt mixture moisture damage assessment combined with surface energy characterization*. in *International Conference on Advanced Characterisation of Pavement and Soil Engineering Materials*. 2007. Athens, GREECE.
20. Zimmerman, J.A., et al. *Calculation of stress in atomistic simulation*. in *7th United States National Congress on Computational Mechanics*. 2003. Albuquerque, NM.
21. Zhou, M., *A new look at the atomic level virial stress: on continuum-molecular system equivalence.* Proceedings of the Royal Society of London Series a-Mathematical Physical and Engineering Sciences, 2003. **459**(2037): p. 2347-2392.
22. Wallin, M., et al., *Multi-scale plasticity modeling: Coupled discrete dislocation and continuum crystal plasticity.* Journal of the Mechanics and Physics of Solids, 2008. **56**(11): p. 3167-3180.
23. Cleveringa, H.H.M., E. Van Der Giessen, and A. Needleman, *Comparison of discrete dislocation and continuum plasticity predictions for a composite material.* Acta Materialia, 1997. **45**(8): p. 3163-3179.
24. Penumadu, D., et al., *Mechanical properties of blended single-wall carbon nanotube composites.* Journal of Materials Research, 2003. **18**(8): p. 1849-1853.
25. Grujicic, M., G. Cao, and W.N. Roy, *Atomistic modeling of solubilization of carbon nanotubes by non-covalent functionalization with poly (p-phenylenevinylene-co-2,5-dioctoxy-m-phenylenevinylene).* Applied Surface Science, 2004. **227**(1-4): p. 349-363.
26. Grujicic, M., G. Cao, and W.N. Roy, *Atomistic simulations of the solubilization of single-walled carbon nanotubes in toluene.* Journal of Materials Science, 2004. **39**(7): p. 2315-2325.
27. Abraham, F.F., et al., *Simulating materials failure by using up to one billion atoms and the world's fastest computer: Work-hardening.* Proceedings of the National Academy of Sciences of the United States of America, 2002. **99**(9): p. 5783-5787.
28. Roth, J., F. Gahler, and H.R. Trebin, *A molecular dynamics run with 5 180 116 000 particles.* International Journal of Modern Physics C, 2000. **11**(2): p. 317-322.
29. Haile, J.M., *Molecular Dynamics Simulation : Elementary Methods*. 1997, New York: Wiley-Interscience.

30. Goldstein, H., et al., *Classical Mechanics*. 2002, San Francisco: Addison Wesley.
31. Landau, L.D. and E.M. Lifshitz, *Mechanics*. 1978, Oxford, New York: Pergamon Press.
32. Liu, W.K., et al., *An introduction to computational nanomechanics and materials.* Computer Methods in Applied Mechanics and Engineering 193 (2004), 2004. **193**(17-20): p. 1529-1578.
33. Tersoff, J., *New empirical approach for the structure and energy of covalent systems.* Physics Review. B, 1988. **37**: p. 6991 - 7000.
34. Los, J. and A.Fasolino, *Monte Carlo simulations of carbon-based structures based on an extended Brenner potential.* Computer Physics Communications, 2002. **147**(178).
35. Brenner, D.W., et al., *A second-generation reactive empirical bond order (REBO) potential energy expression for hydrocarbons.* J. Physics: Condensed Matter, 2002. **14**: p. 783-802.
36. Scheiner, S. *Calculating the properties of hydrogen bonds by ab initio methods*. in *Reviews in Computational Chemistry*. 1991. New York: VCH Publishers, Inc.
37. Dauber–Osguthorpe, P., et al., *Structure and energetics of ligand binding to proteins: E. coli dihydrofolate reductase–trimethoprim, a drug–receptor system.* Proteins: tructure, Function and Genetics, 1988. **4**: p. 31–47.
38. Allen, M.P. and D.J. Tildesley, *Computer simulation of liquids*. 1987, Oxford [England], New York: Clarendon Press; Oxford University Press. xix, 385 p.
39. Gropp, W., E. Lusk, and A. Skjellum, *Using MPI : portable parallel programming with the message-passing interface*. 1994, Cambridge, Mass.: MIT Press. xx, 307 p.
40. Plimpton, S., *FAST PARALLEL ALGORITHMS FOR SHORT-RANGE MOLECULAR-DYNAMICS.* Journal of Computational Physics, 1995. **117**(1): p. 1-19.
41. Gao, H. and P. Klein, *Numerical simulation of crack growth in an isotropic solid with randomized internal cohesive bonds.* Journal of the Mechanics and Physics of Solids, 1998. **46**(2): p. 187-218.
42. Smith, R.W. and D.J. Srolovitz, *Void formation during film growth: A molecular dynamics simulation study.* Journal of Applied Physics, 1996. **79**(3): p. 1448-1457.
43. Hu, S.Y., Y.L. Li, and K. Watanabe, *Calculation of internal stresses around Cu precipitates in the bcc Fe matrix by atomic simulation.* Modelling and Simulation in Materials Science and Engineering, 1999. **7**(4): p. 641-655.
44. Horstemeyer, M.F. and M.I. Baskes, *Atomistic finite deformation simulations: A discussion on length scale effects in relation to mechanical stresses.* Journal of Engineering Materials and Technology-Transactions of the Asme, 1999. **121**(2): p. 114-119.
45. Irving, J.H. and J.G. Kirkwood, *The Statistical Mechanical Theory of Transport Processes. IV. The Equations of Hydrodynamics.* The Journal of Chemical Physics, 1950. **18**(6): p. 817-829.
46. Schofield, P. and J.R. Henderson, *STATISTICAL-MECHANICS OF INHOMOGENEOUS FLUIDS.* Proceedings of the Royal Society of London

Series a-Mathematical Physical and Engineering Sciences, 1982. **379**(1776): p. 231-246.
47. Cheung, K.S. and S. Yip, *ATOMIC-LEVEL STRESS IN AN INHOMOGENEOUS SYSTEM.* Journal of Applied Physics, 1991. **70**(10): p. 5688-5690.
48. Machova, A., *Stress calculations on the atomistic level.* Modelling and Simulation in Materials Science and Engineering, 2001. **9**(4): p. 327-337.
49. Weiner, J.H., *Statistical mechanics of elasticity*. 1983, New York: Wiley. xii, 439 p.
50. Dupuy, L.M., et al., *Finite-temperature quasicontinuum: Molecular dynamics without all the atoms.* Physical Review Letters, 2005. **95**(6).
51. Gao, H.J. and B.H. Ji. *Modeling fracture in nanomaterials via a virtual internal bond method*. in *Workshop on Fundamentals and Applications of Cohesive Models*. 2002. Germany.
52. Jiang, H., Y. Huang, and K.C. Hwang, *A finite-temperature continuum theory based on interatomic potentials.* Journal of Engineering Materials and Technology-Transactions of the Asme, 2005. **127**(4): p. 408-416.
53. Chen, Y.P., *Local stress and heat flux in atomistic systems involving three-body forces.* Journal of Chemical Physics, 2006. **124**(5).
54. Zimmerman, J.A., *Continuum Definitions for Stress in Atomistic simulation*, in *Other Information: PBD: 1 Dec 2002*. 2002. p. Medium: ED; Size: 79 pages.
55. Yoshimoto, K., et al., *Mechanical Heterogeneities in Model Polymer Glasses at Small Length Scales.* Physical Review Letters, 2004. **93**(Copyright (C) 2010 The American Physical Society): p. 175501.
56. Hill, R., *Continuum micro-mechanics of elastoplastic polycrystals.* Journal of the Mechanics and Physics of Solids, 1965. **13**(2): p. 89-101.
57. Walpole, L.J., *On the overall elastic moduli of composite materials.* Journal of the Mechanics and Physics of Solids, 1969. **17**(4): p. 235-251.
58. Torquato, S., *Random Heterogeneous Media: Microstructure and Improved Bounds on Effective Properties.* Applied Mechanics Reviews, 1991. **44**(2): p. 37-76.
59. Nemat-Nasser, S. and M. Hori, *Micromechanics : overall properties of heterogeneous materials*. 1993, Amsterdam ; New York: North-Holland. xx, 687 p.
60. Theodorou, D.N. and U.W. Suter, *ATOMISTIC MODELING OF MECHANICAL-PROPERTIES OF POLYMERIC GLASSES.* Macromolecules, 1986. **19**(1): p. 139-154.
61. Brown, D. and J.H.R. Clarke, *MOLECULAR-DYNAMICS SIMULATION OF AN AMORPHOUS POLYMER UNDER TENSION .1. PHENOMENOLOGY.* Macromolecules, 1991. **24**(8): p. 2075-2082.
62. Berendsen, H.J.C., et al., *MOLECULAR-DYNAMICS WITH COUPLING TO AN EXTERNAL BATH.* Journal of Chemical Physics, 1984. **81**(8): p. 3684-3690.
63. Parrinello, M. and A. Rahman, *STRAIN FLUCTUATIONS AND ELASTIC-CONSTANTS.* Journal of Chemical Physics, 1982. **76**(5): p. 2662-2666.
64. Cain, T. and J.R. Ray, *Third-order elastic constants from molecular dynamics: Theory and an example calculation.* Physical Review B, 1988. **38**(12): p. 7940.

65. Brigatti, M.F. and P. Davoli, *Crystal-structure refinements of 1M plutonic biotites.* American Mineralogist, 1990. **75**(3-4): p. 305-313.
66. Levien, L., C.T. Prewitt, and D.J. Weidner, *STRUCTURE AND ELASTIC PROPERTIES OF QUARTZ AT PRESSURE.* American Mineralogist, 1980. **65**(9-10): p. 920-930.
67. Humphrey, W., A. Dalke, and K. Schulten, *VMD: Visual molecular dynamics.* Journal of Molecular Graphics, 1996. **14**(1): p. 33-&.
68. Gale, J.D., et al., *An ab Initio Study of the Structure and Properties of Aluminum Hydroxide: Gibbsite and Bayerite.* The Journal of Physical Chemistry B, 2001. **105**(42): p. 10236-10242.
69. VANORIO, et al., *Elastic properties of dry clay mineral aggregates, suspensions and sandstones*. Vol. 155. 2003, Oxford, ROYAUME-UNI: Blackwell. 8.
70. Amorosi, A. and S. Rampello, *An experimental investigation into the mechanical behaviour of a structured stiff clay.* Geotechnique, 2007. **57**(2): p. 153-166.
71. Huang, E., et al., *Compression studies of gibbsite and its high-pressure polymorph.* Physics and Chemistry of Minerals, 1999. **26**(7): p. 576-583.
72. Sato, H., A. Yamagishi, and K. Kawamura, *Molecular simulation for flexibility of a single clay layer.* Journal of Physical Chemistry B, 2001. **105**(33): p. 7990-7997.
73. Sato, H., et al., *First-principles studies on the elastic constants of a 1 : 1 layered kaolinite mineral.* American Mineralogist, 2005. **90**(11-12): p. 1824-1826.
74. Speight, J.G., *The chemistry and technology of petroleum*. 4th ed. 2007, Boca Raton: CRC Press/Taylor & Francis. 945 p.
75. Hortal, A.R., et al., *Molecular-weight distributions of coal and petroleum asphaltenes from laser desorption/ionization experiments.* Energy & Fuels, 2007. **21**(5): p. 2863-2868.
76. Badre, S., et al., *Molecular size and weight of asphaltene and asphaltene solubility fractions from coals, crude oils and bitumen.* Fuel, 2006. **85**(1): p. 1-11.
77. Groenzin, H. and O.C. Mullins, *Molecular Size and Structure of Asphaltenes from Various Sources.* Energy & Fuels, 2000. **14**(3): p. 677-684.
78. Mullins, O.C., B. Mart ńez-Haya, and A.G. Marshall, *Contrasting Perspective on Asphaltene Molecular Weight. This Comment vs the Overview of A. A. Herod, K. D. Bartle, and R. Kandiyoti.* Energy & Fuels, 2008. **22**(3): p. 1765-1773.
79. Groenzin, H. and O.C. Mullins, *Molecular size and structure of asphaltenes.* Petroleum Science and Technology, 2001. **19**(1-2): p. 219-230.
80. Schneider, M.H., et al., *Asphaltene molecular size by fluorescence correlation Spectroscopy.* Energy & Fuels, 2007. **21**(5): p. 2875-2882.
81. Yen, T.F. and G.V. Chilingar, *Asphaltenes and asphalts*. 1994, Amsterdam ; New York: Elsevier Science. v.
82. Mullins, O.C., *Asphaltenes, heavy oils, and petroleomics*. 2007, New York: Springer. xxi, 669 p.
83. Groenzin, H. and O.C. Mullins, *Asphaltene molecular size and structure.* Journal of Physical Chemistry A, 1999. **103**(50): p. 11237-11245.
84. Read, J., D. Whiteoak, and Shell Bitumen., *The Shell Bitumen handbook*. 5th ed. 2003, London: Thomas Telford. xii, 460 p.
85. Redelius, P.G., *Solubility Parameters and Bitumen.* Fuel, 2000. **79**: p. 27-35.

86. Redelius, P.G., *Bitumen Solubility Model using Hansen Solubility Parameter.* Energy Fuels, 2004. **18**: p. 1087-1092.
87. Storm, D.A., et al., *Molecular Representations of Ratawi and Alaska North Slope Asphaltenes Based on Liquid- and Solid-State NMR.* Energy Fuels, 1994. **8**: p. 561–566.
88. Kowalewski, I., et al., *Preliminary results on molecular modeling of asphaltenes using structure elucidation programs in conjunction with molecular simulation programs.* Energy & Fuels, 1996. **10**(1): p. 97-107.
89. Storm, D.A., et al., *Molecular Representations of Ratawi and Alaska North Slope Asphaltenes Based on Liquid- and Solid-State NMR.* Energy & Fuels, 1994. **8**(3): p. 561-566.
90. Storm, D.A., et al., *UPPER BOUND ON NUMBER AVERAGE MOLECULAR-WEIGHT OF ASPHALTENES.* Fuel, 1990. **69**(6): p. 735-738.
91. Artok, L., et al., *Structure and Reactivity of Petroleum-Derived Asphaltene.* Energy & Fuels, 1999. **13**(2): p. 287-296.
92. Rogel, E. and L. Carbognani, *Density Estimation of Asphaltenes Using Molecular Dynamics Simulations.* Energy Fuels, 2003. **17**: p. 378-386.
93. Mullins, O.C., *Rebuttal to Strausz et al. Regarding Time-Resolved Fluorescence Depolarization of Asphaltenes.* Energy & Fuels, 2009. **23**(5): p. 2845-2854.
94. Leach, A.R., *Molecular modelling : principles and applications*. 2nd ed. 2001, Harlow, England ; New York Prentice Hall.
95. Schelling, P.K., S.R. Phillpot, and P. Keblinski, *Comparison of atomic-level simulation methods for computing thermal conductivity.* Physical Review B, 2002. **65**(14).
96. Stangl, K., A. Jager, and R. Lackner. *Microstructure-based identification of bitumen performance*. in *2nd Meeting of the European-Asphalt-Technology-Association (EATA)*. 2006. Meriden, ENGLAND.
97. Loeber, L., et al., *New direct observations of asphalts and asphalt binders by scanning electron microscopy and atomic force microscopy.* Journal of Microscopy-Oxford, 1996. **182**: p. 32-39.
98. Pauli, A.T. and W. Grimes, *Surface morphological stability modeling of SHRP asphalt.* Abstracts of Papers of the American Chemical Society, 2003. **225**: p. 5-PETR.
99. Pauli, A.T., et al., *Surface energy studies of SHRP asphalts by AFM*, in *Am. Chem. Soc., Petrol. Chem. Div. Prepr.* 2003.
100. Saal, R.N.J. and J.W.A. Labout, *Rheological Properties of Asphaltic Bitumen.* The Journal of Physical Chemistry, 1940. **44**(2): p. 149-165.
101. Nose, S., *A UNIFIED FORMULATION OF THE CONSTANT TEMPERATURE MOLECULAR-DYNAMICS METHODS.* Journal of Chemical Physics, 1984. **81**(1): p. 511-519.
102. Melchionna, S., G. Ciccotti, and B.L. Holian, *HOOVER NPT DYNAMICS FOR SYSTEMS VARYING IN SHAPE AND SIZE.* Molecular Physics, 1993. **78**(3): p. 533-544.
103. Hoover, W.G., *Canonical dynamics: Equilibrium phase-space distributions.* Physical Review A, 1985. **31**(Copyright (C) 2010 The American Physical Society): p. 1695.

104. Hoover, W.G., *Constant-pressure equations of motion.* Physical Review A, 1986. **34**(Copyright (C) 2010 The American Physical Society): p. 2499.
105. Rakesh, L., *Modeling and Bio molecular Self-assembly via Molecular Dynamics and Dissipative Particle Dynamics.* Numerical Analysis and Applied Mathematics, Vols 1 and 2, 2009. **1168**: p. 832-835.
106. Priezjev, N.V., *Shear rate threshold for the boundary slip in dense polymer films.* Physical Review E, 2009. **80**(3).
107. Sofos, F., T. Karakasidis, and A. Liakopoulos, *Variation of Transport Properties Along Nanochannels: A Study by Non-equilibrium Molecular Dynamics.* Iutam Symposium on Advances in Micro- and Nanofluidics, 2009. **15**: p. 67-78.
108. Hansen, J.S., P.J. Daivis, and B.D. Todd, *Viscous properties of isotropic fluids composed of linear molecules: Departure from the classical Navier-Stokes theory in nano-confined geometries.* Physical Review E, 2009. **80**(4).
109. Kim, Y.R., et al., *Evaluation of moisture damage mechanisms and effects of hydrated lime in asphalt mixtures through measurements of mixture component properties and performance testing.* Journal of Materials in Civil Engineering, 2008. **20**(10): p. 659-667.
110. Kringos, N. and A. Scarpas. *Simulation of combined physical-mechanical moisture induced damage in asphaltic mixes*. in *International Conference on Advanced Characterisation of Pavement and Soil Engineering Materials*. 2007. Athens, GREECE.
111. Majidzadeh, K. and F.N. Brovold., *State of the Art: Effect of Water on Bitumen–Aggregate Mixtures*, in *HRB, National Research Council*. 1968: Washington, D.C.
112. Sides, S.W., G.S. Grest, and M.J. Stevens, *Surface-tethered chains entangled in a polymer melt: Effects on adhesion dynamics.* Physical Review E, 2001. **64**(Copyright (C) 2010 The American Physical Society): p. 050802.
113. Kringos, N. and A. Scarpas, *Physical and mechanical moisture susceptibility of asphaltic mixtures.* International Journal of Solids and Structures, 2008. **45**(9): p. 2671-2685.
114. Terrel, R.L. and J.W. Shute, *Summary report on water sensitivity*, in *Strategic Highway Research Program*. 1989, National Research Council: Washington, D.C.
115. Terrel, R.L. and S. Al-Swailmi, *Water Sensitivity of Asphalt – Aggregate Mixes: Test Selection*, in *Strategic Highway Research Program*. 1994, National Research Council: Washington, D.C.
116. Lytton, R.L., *Personal Communication*, T.A.M.U. Department of Civil Engineering, Editor. 2001: College Station, TX.
117. Kim, H. and W.G. Buttlar, *Discrete fracture modeling of asphalt concrete.* International Journal of Solids and Structures, 2009. **46**(13): p. 2593-2604.
118. Schmidt, R.J. and P.E. Graf, *The effect of water on the resilient modulus of asphalt treated mixes*, in *Proceedings of the Association of Asphalt Paving Technologiests*. 1972. p. 118-162.
119. Cheng, D.X., et al., *Use of surface free energy properties of the asphalt-aggregate system to predict moisture damage potential.* Journal of the Association of Asphalt Paving Technologists, Vol 71, 2002: p. 59-88.

120. Jones, H.G., *Plants and microclimate : a quantitative approach to environmental plant physiology*. 2nd ed ed. 1992, Cambridge: Cambridge University Press. xxiv, 428 p.
121. Curtis, C.W., *INVESTIGATION OF ASPHALT-AGGREGATE INTERACTIONS IN ASPHALT PAVEMENTS.* Abstracts of Papers of the American Chemical Society, 1992. **204**: p. 29-FUEL.
122. Cheng, D.X., et al. *Surface energy measurement of asphalt and its application to predicting fatigue and healing in asphalt mixtures*. in *81st Annual Meeting of the Transportation-Research-Board*. 2002. Washington, D.C.
123. Lyklema, J. and H.P.v. Leeuwen, *Fundamentals of interface and colloid science*. 1991, San Diego: Academic Press. v. <1-5>.
124. Tarrer, A.R. and V.P. Wagh, *INNOVATIVE TESTS TO PREDICT THE STRENGTH AND TYPE OF ASPHALT-AGGREGATE BONDS.* Petroleum Science and Technology, 1992. **10**(4): p. 457 - 474.
125. Bhasin, A., et al., *Limits on adhesive bond energy for improved resistance of hot-mix asphalt to moisture damage.* Bituminous Paving Mixtures 2006, 2006(1970): p. 3-13.
126. Khalid, H.A. and O.K. Monney, *Moisture damage potential of cold asphalt.* International Journal of Pavement Engineering, 2009. **10**(5): p. 311-318.
127. Harvey, J.A.F. and D. Cebon, *Failure mechanisms in viscoelastic films.* Journal of Materials Science, 2003. **38**(5): p. 1021-1032.
128. Gubler, R., et al., *Influence of water and temperature on mechanical properties of selected asphalt pavements.* Materials and Structures, 2005. **38**(279): p. 523-532.
129. Cheng, D.X., et al. *Use of surface free energy properties of the asphalt-aggregate system to predict moisture damage potential*. in *Technical Sessions of the Association-of-Asphalt-Paving-Technologists*. 2002. Colorado Springs, Co.
130. Bhasin, A. and D.N. Little, *Characterization of aggregate surface energy using the universal sorption device.* Journal of Materials in Civil Engineering, 2007. **19**(8): p. 634-641.
131. Bhasin, A., et al. *Limits on adhesive bond energy for improved resistance of hot-mix asphalt to moisture damage*. in *85th Annual Meeting of the Transportation-Research-Board*. 2006. Washington, DC.
132. Taylor, M.A. and N.P. Khosia, *STRIPPING OF ASPHALT PAVEMENTS: STATE OF THE ART.* Transportation Research Record 911, 1983: p. 150-158.
133. Henderson, M.A., *Surface stabilization of organics on hematite by conversion from terminal to bridging adsorption structures.* Geochimica et Cosmochimica Acta, 2003. **67**(5): p. 1055-1063.
134. Brown, C.A. and S. Siegmann, *Fundamental scales of adhesion and area-scale fractal analysis.* International Journal of Machine Tools & Manufacture, 2001. **41**(13-14): p. 1927-1933.
135. Fenter, P., et al., *Observation of molecular-scale interfacial structures with X-ray Reflection Interface Microscopy.* Geochimica et Cosmochimica Acta. **70**(18, Supplement 1): p. A169-A169.
136. Khattak, M.J., G.Y. Baladi, and L.T. Drzal, *Binder rheology, morphology and adhesion effects on asphalt mixtures.* Geotechnical Engineering for Transportation Projects, Vol 1, 2004(126): p. 925-937.

137. Kanitpong, K. and H.U. Bahia, *Role of adhesion and thin film tackiness of asphalt binders in moisture damage of HMA.* Journal of the Association of Asphalt Paving Technologists, Vol 72, 2003: p. 502-528.
138. Hefer, A.W., D.N. Little, and R.L. Lytton, *A synthesis of theories and mechanisms of bitumen-aggregate adhesion including recent advances in quantifying the effects of water.* 2005 Journal of the Association of Asphalt Paving Technologists: From the Proceedings of the Technical Sessions, Vol 74, 2005. **74**: p. 139-195.